Swansea University E-Theses

Finite element modelling and experimental validation in radiative heat transfer.

Vujicic, Mile R

How to cite:

Use policy:

UNIVERSITY OF WALES SWANSEA

SCHOOL OF ENGINEERING

FINITE ELEMENT MODELLING

AND EXPERIMENTAL VALIDATION

IN RADIATIVE HEAT TRANSFER

BY

Mile R. Vujičić DIPL.-ING., MSc

Thesis submitted to the University of Wales
for the award of the degree of PhD

January 12, 2006

ProQuest Number: 10805416

ProQuest 10805416

Acknowledgements

I would like to thank all the people who have helped me in one way or another during my time at University of Wales Swansea. First I would like to express my sincere gratitude to my supervisor, Dr. Steve Brown, who sparked my interest in radiative heat transfer and provided support and encouragement at key times. He was always there with stimulating discussions and new suggestions, yet also willing to let things develop in unexpected ways. His ongoing confidence in me was essential to the completion of this work.

Next I would like to thank Dr. Nick Lavery, who worked directly with my sponsors (Defence, Science and Technology Laboratory) and the development of computer code 'Pharo'.

I would also like to thank Savani Sameer from Defence, Science and Technology Laboratory (DSTL) for making my research possible.

I give my thanks to my fellow students, particularly those working towards their EngD at the Materials Research Centre for their good company and assistance.

I owe a great debt to technicians at both the Machwoods workshops at the School of Engineering, with a special thanks to Peter Matthews, Tony Green and Steve Jones, who worked very hard to ensure that my experimental rig was completed in time.

I would also like to thank Professor R. Lewis for making the time to discuss my papers with me.

I would like to thank my parents, Rajko and Dragica Vujičić, my sisters Dobrila and Rada for their love, support, and guidance over the years.

I would also like to thank my parents-in-law, William Pryce and Mary Pope, for their love and encouragement.

My deepest gratitude goes to my wife, Kate. She supported me in times of doubt, and has enriched my life beyond measure.

This thesis is dedicated to my father

Rajko Djordjo Vujičić

and my son

Joe Rajko Vujičić

Abstract

The work presented in this thesis can be divided into two parts: numerical modelling and experimental validation.

The first part considers a finite element computer code called **Pharo** which has been developed to simulates heat transfer exchanged in an enclosure via thermal radiation and conduction. This finite element heat transfer code has been written for the **Defence, Science and Technology Laboratory (DSTL)**.

Face to face (zonal) thermal radiation which operates with diffuse surface properties of materials without a participating media is analyzed and included in **Pharo**. To analyze the net heat exchanged within an enclosure several methods for view factor calculation, such as the Monte Carlo and Hemi-cube methods were included in **Pharo**. During heat transfer simulations a better accuracy of results has been demonstrated using a new approach called the **Multiple Reflection of View Factors 'MRV'** method.

Transient heat flow is solved using both finite difference and finite element time stepping. Also, an analysis of transient heat flow using different solvers (direct and iterative) to find the most appropriate one was carried out.

The second part of the work considers experimental validation of numerical results obtained using **Pharo**. Special attention was given to the analysis of the relationship between view factors and measured heat transfer. To make the experimental data complete the measurements of surface properties including emissivity, reflectivity for different wavelengths as well as roughness of materials is presented. These experimental results can be used as experimental benchmark data for model users and developers.

Contents

List of Figures

List of Tables

Nomenclature

A = surface area, $[m^2]$

BCG = bi-conjugate gradient

$BCGSTAB$ = bi-conjugate gradient stabilized

CGS = conjugate gradient squared

c_0 = speed of light in vacuum, ($c_0 = 2.9979 \cdot 10^8$ $[m/s]$)

c = speed of light in any other medium

CPU = computational process unit

DDR = diffuse directional spectral reflectivity

DHR = directional hemispherical spectral reflectivity

$e_\lambda b(\lambda, T)$ = hemispherical spectral emissive power, $[W/(m^2 \cdot \mu m)]$

F_{12} = view (configuration) factor between surfaces 1 and 2

HDR = hemispherical directional spectral reflectivity

HE = hemispherical spectral emissivity

h = Planck constant, ($h = 6.6260755 \cdot 10^{-34}$ $[J \cdot s]$)

h = convection heat transfer coefficient - convection, $[W/(m^2 K)]$

$i_{\lambda b}(\lambda)$ = spectral intensity

$\mathbf{J}$ = Jacobian matrix

k = Boltzmann constant - radiative heat transfer, ($k = 1.380658 \cdot 10^{-23}$ $[J/K]$)

k = thermal conductivity - thermal conduction, $[W/mK]$

$\mathbf{K}$ = conductance (coefficient stiffness) matrix - finite element technique

$LSCG$ = least square conjugate gradient

m = number of rays which hit another surface (the Monte Carlo method)

$\mathbf{M}$ = capacitance (mass) matrix - finite element technique

N = total number of rays used in the Monte Carlo method

N = resolution of a hemi-cube, $N_{tot} = 3N^2$ - total number of pixels per a hemi-cube

$N_1(\xi, \eta)$ = shape (interpolation) function of node 1 in 2D- finite element technique

$N_1(\xi, \eta, \zeta)$ = shape (interpolation) function of node 1 in 3D- finite element technique

$n = \frac{c_0}{c}$ = index of refraction - radiative heat transfer

PCG = preconditioned conjugate gradient

$Q_{1 \rightleftharpoons 2}$ = net heat flux exchanged between surfaces 1 and 2, $[W]$

$random[0]$ = uniformly distributed random number

r_1 = radius of disc 1

SDR = specular directional spectral reflectivity

t = temperature defined in Celsius (centigrade) scale, $[^{o}C]$

T = temperature defined in Kelvin scale, $[K]$

$\dot{T}$ = temperature differentiated with respect to time

$tc1r$ = temperature of the thermocouple 1 of the receiver, $[^{o}C]$

$tc1e$ = temperature of the thermocouple 1 of the emitter, $[^{o}C]$

t_{amb} = ambient temperature, $[^{o}C]$

W = weight function - finite element technique

$c/D = (distance)/(Diameter\ of\ the\ disc\ emitter)$ distance ratio between a disc as an emitter and a square plate as a receiver

$c/L = (distance)/(Length\ of\ the\ square\ emitter)$ distance ratio between a square plate as an emitter and a plate as a receiver

$c/d = (distance)/(Diameter\ of\ the\ cylinder\ emitter)$ distance ratio between a cylinder as an emitter and a square plate as a receiver

α_1 = hemispherical total absorptivity of surface 1 independent of temperatures

α_2 = hemispherical total absorptivity of surface 2 independent of temperatures

$\alpha_\lambda(\lambda, \theta, \varphi, T_A)$ = directional spectral absorptivity

$\alpha(\theta, \varphi, T_A)$ = directional total absorptivity

$\alpha_\lambda(\lambda, T_A)$ = hemispherical spectral absorptivity

δ_{kj} = Kronecker delta

ε_1 = total hemispherical emissivity of surface 1 independent of temperatures

ε_2 = total hemispherical emissivity of surface 2 independent of temperatures

$\varepsilon_\lambda(\lambda, \theta, \varphi, T_A)$ = directional spectral emissivity

$\varepsilon(\theta\varphi, T_A)$ = directional total emissivity

$\varepsilon_\lambda(\lambda, T_A)$ = hemispherical spectral emissivity

θ_1 = angle between normal to A_1 and connecting line between A_1 and A_2

θ_2 = angle between normal to A_2 and connecting line between A_1 and A_2

θ_i = an angle of incident measured from a normal of an element

θ_r = an angle of reflection measured from a normal of an element

θ = value and name of the method for time stepping

λ = wavelength, $([\mu m]$ or $[\mathring{A}])$

ν = frequency, $[Hz]$

ϱ_1 = total hemispherical reflectivity of surface 1 - radiative heat transfer

ϱ_2 = total hemispherical reflectivity of surface 2 - radiative heat transfer

ϱ^d = diffuse reflectivity - radiative heat transfer

$\varrho^s =$ specular reflectivity - radiative heat transfer

$\rho_\lambda(\lambda, \theta_r, \varphi_r, \theta, \varphi) =$ bidirectional spectral reflectivity

$\rho(\theta_r, \varphi_r, \theta, \varphi) =$ bidirectional total reflectivity

$\rho_\lambda(\lambda, \theta, \varphi) =$ directional-hemispherical spectral reflectivity

$\rho(\theta, \varphi) =$ directional-hemispherical total reflectivity

$\rho_\lambda(\lambda, \theta_r, \varphi_r) =$ hemispherical-directional spectral reflectivity

$\rho(\theta_r, \varphi_r) =$ hemispherical-directional total reflectivity

$\rho_\lambda(\lambda) =$ hemispherical spectral reflectivity

$\varrho =$ density of material - thermal conduction, $[kg/m^3]$

$\sigma =$ Stefan-Boltzmann constant, $(\sigma = 5.5704 \cdot 10^{-8} \; [W/m^2 K^4])$

$\neq$ thickness of the plate, $[mm]$

Chapter 1

Introduction

Heat transfer, as a science, seeks to understand and predict many effects in nature, such as the energy transfer between a body at a higher temperature to a body at a lower temperature by direct contact or by thermal radiation.

High powered machines, furnaces, boilers, gas turbine combustors, heat apparatus design, ceramics and glass forming technology, solar energy utilization, cryogenic insulation and high temperature phenomena in hypersonic flight all require knowledge of heat transfer laws.

It is known that heat transfer includes conduction, convection and thermal radiation. Other than in a few simple cases all these heat transfer mechanisms are usually taking place in heat transfer analysis.

Before the 1960's, when work on radiative heat transfer expanded, significant contribution to the analysis and understanding of this heat transfer mode was made by H.C. Hottel, G. Poljak and J. R. Oppenheim.

In the 1960's a tremendous amount of research started at universities and research centres across whole the USA. The most remarkable centres were the University of Minnesota at Minneapolis (Professor E. R. G. Eckert, E. M. Sparrow, R.C. Birkebac, K. E. Torrance, R. P. Bobco etc.), NASA Lewis Research Center (R. Siegel), the University of California at Berkeley (Professor R. A. Seban), the University of Texas at Austin (Professor J. R. Howell, M. Perlmutter etc.), the Purdue University (Professor R. J. Viskanta) and the University of Kentucky (Professor R. M. Drake, Jr). Also, Professors J. R. Mahan from Virginia Polytechnic Institute and State University and M. Modest from the Pennsylvania State University made a great contribution in radiative heat transfer analysis.

At the same time in Europe, the most recognized work in radiative heat transfer has been carried out under the leadership of Professor J. F. Sacadura (France).

The results of their work, and that of their students, were used by many

software companies and materialized in the development of commercial codes.

These days, there are many commercial codes based on finite difference, finite element (Ansys, Elfen, Maya, Radioss-CFD, CFD++, Adina, Abaqus, Nastran etc.), boundary element (Linflow etc.), finite volume (Ansys CFX, Star-CD, Fluent, Phoenics etc.), and other techniques which have been developed to solve heat transfer problems including radiative heat transfer. In some of them, for example Elfen, radiative heat transfer is considered very poorly. On the other hand Ansys CFX, Fluent and Phoenics have more advanced tools to calculate radiative heat exchanged within an enclosure. However, to adapt these codes to work on personal computers some approximations have been made (for the example an introduction of macro surfaces). Sometimes, these approximations can cause the loss of very important details. On the other hand, detailed analysis causes an increase in CPU time and computer storage.

1.1 Objectives

Collaboration between Materials Research Centre of School of Engineering Swansea and the Survivability & Platform Technology Group at Defence, Science and Technology Laboratory (DSTL) Farnborough started several years ago. The subject of the interest for DSTL was the signature prediction of vehicle platforms. In infra-red signature prediction the thermal characteristics of an aircraft for a given flight condition, including its exhaust gas flow must be determined. A result of this collaboration has been the development of a finite element heat transfer code named **Pharo**.

The primary objective of this work was to develop **Pharo**, and to set up experiments whose results could be used to validate **Pharo**.

Since 2002, step by step **Pharo** has been developed dramatically, and now, it can work in complex geometry, using state of the art numerical and computational techniques. The development of **Pharo** is presented in the section that follows. During this research my curiosity took me in, what was for me, new areas of research into iterative solvers.

A second, important outcome of the work to validate **Pharo** was to obtain reliable experimental data, which can be used as a benchmark for model users and developers. Since the 1960's when Professor E. R. G. Eckert established the state of the art laboratory for heat transfer analysis at the University of Minnesota in Minneapolis, a huge number of papers have been published. Radiative heat transfer experiments, including measurements of surface properties, were carried out under the supervision of Professor E. M. Sparrow. Hundreds of papers written by him and his former students have

been published in the Journal of Heat Transfer. A logical question should be: What is new in my research that can give a high mark to this thesis? The contribution of my research, to already existing knowledge, is information that combines both view factor information and heat transfer effects simultaneously.

1.2 Code development

Until 2002, only integration methods for view factor calculation, which plays a crucial role in calculations of net radiative flux exchanged between surfaces, were used. It had been found that integration methods have a lack of flexibility to deal with complex geometries, especially when the presence of obstacles takes place. This was the main reason for focussing attention towards other more flexible methods for the view factor calculation. The first method analyzed was the Monte Carlo method. From 2003, this method took the main place for view factor calculation in **Pharo**. The advantages as well as disadvantages of the Monte Carlo method are analyzed and presented in Chapter 2. Since, early 2005 a new method for view factor calculation, called the Hemi-cube method, has been successfully applied in **Pharo**. The results of analysis of the Hemi-cube method are presented in Chapter 2.

Until 2002, equation (2.12) was used for the calculation of net radiative heat flux exchanged between two surfaces. A comparison between results obtained using equation (2.12) and experimental data showed that this equation gives low accuracy, particularly when surfaces with high reflectivity are included in the enclosure. To ensure greater accuracy of results obtained the simple radiosity face to face equation (2.54) was introduced. Finally, I proposed a new approach called Multiple Reflection of View Factors (MRV) method for the radiative heat transfer simulation. An analysis of MRV method is presented in Chapter 2, while a comparison between the results obtained using the MRV method and experimental data is given in Chapter 6. The MRV method has also been implemented into **Pharo**.

1.3 Thesis Structure

It is desirable to present a fully sequential text, with everything following from what has gone before. However, with a number of aspects overlapping and referring to one another in their own development there is necessarily a certain amount of forward referencing. The structure adopted attempts to keep this to a minimum.

Special attention in this thesis has been given to thermal radiation (radiation exchange in an enclosure composed of diffuse-grey surfaces containing radiatively *nonparticipating* media). It is for this reason that this thesis started with numerical methods for view factor calculation. After a review of numerical methods including Integration, the Hemi-cube and the Monte Carlo methods, a detailed analysis of the Monte Carlo and the Hemi-cube methods (Chapter 2) for a few different test cases, with known analytical solutions, such as well known parallel plates, hinged plates and two parallel discs along same normal was made. The relationship between numerical schemes, accuracy and CPU time is included in the analysis. A comparison between the Monte Carlo method and the Hemi-cube method was also made.

Also, a new approach called Multiple Reflection of View Factors (MRV) method which takes reflectivity into account is proposed in this chapter.

To validate the finite element code an original simple experimental rig was designed. Experimental data is presented in Chapter 3. This includes temperature measurements of emitters (a disc, a cylinder and a square plate) and receivers (square plates composed of different materials with different thickness) for different distance ratios between them, as well as different angles between them. All measurements presented in this chapter were carried out using thermocouples in combination with a thermal image camera.

In Chapter 4 a theoretical background of the finite element method used in heat transfer calculations is given. After finite element discretization a system of matrix equations is obtained. This system of equations can be solved using several methods (direct and iterative). Special attention was given to iterative solvers. A theoretical explanation with a historical overview of the conjugate gradient method, with other methods as its modifications, is given in Appendix B. A Fortran 90 program which was written to solve transient heat conduction using Preconditioned Bi-conjugate Gradient method is given in Appendix C.

Heat conduction analysis, including both transient and steady state with comparisons between different time stepping methods, different numerical schemes and different iterative solvers, is presented in Chapter 5. All results presented in this chapter are obtained from a Fortran 90 code which was not included in **Pharo**.

Experimental data presented earlier (Chapter 3) was later used to test the finite element code, including all heat transfer mechanisms and this is analyzed in Chapter 6. A few different test cases from the simplest one such as two parallel plates case to the most complicated one such as a jet engine were analyzed in this chapter. Also presented is a sensitivity analysis which includes emissivity, numerical schemes and the number of rays used in view factor calculations. All results presented in this chapter were obtained under

following assumptions:
1. the temperature of each element is uniform;
2. the surface properties are uniform;
3. emissivity, absorptivity and reflectivity are independent of wavelength and direction;
4. all energy is emitted and reflected diffusely; and
5. the incident and hence reflected energy flux is uniform over each element.

Microstructure of the sample composed of brass with different magnifications and measured roughness of the plates composed of steel, brass and aluminium with thickness of 5 [mm] are given in Appendix D.

Finally, this thesis is concluded with a chapter which includes the general conclusions of all work that has been made during my PhD research.

Chapter 2

View Factor Calculation

2.1 Thermal radiation

The nature of radiation, which has puzzled scientists across centuries, can be considered from two viewpoints: classical electromagnetic wave theory and quantum mechanics. These two theories, with few exceptions, give similar results. The difference between them is how they approach some of the very important effects, such as the spectral distribution of the energy emitted from a body and the behavior of the radiative properties of gases.

Maxwell (1831-1879), as the pioneer of classical electromagnetic wave theory, proposed that energy of radiation travels as a vibratory electric and magnetic disturbance through space in a direction normal to those disturbances (1865).

So, the electric oscillation (red) lying in the xy plane, the magnetic (blue) lying in the xz plane are perpendicular to each other (Figure 2.1).

The electric component of the wave can be written

$$E = E_0 e^{[i(k \cdot r - \nu t)]} \tag{2.1}$$

where E_0 is a constant, k is the wave-vector which determines the wavelength and direction of propagation of the wave, and ν is the frequency. As can be seen in Figure 2.1 the wave is travelling in the x direction (perpendicular to the coupled electric and magnetic fields) with a constant speed (the speed of propagation for electromagnetic radiation in vacuum is the same as for light which is $c_0 = 2.9979 \cdot 10^8 \ [m/s]$). This means that $k \cdot E_0 = 0$.

The speed (c) in any other medium is less than (c_0). The relationship between them is commonly given in the following equation:

$$n = \frac{c_0}{c} \tag{2.2}$$

where n is index of refraction greater than 1 (sometimes, such as for gases, it is very close to 1).

In order to understand and also to classify electromagnetic radiation it is necessary to mention the following terms:

a) frequency of oscillation (ν);

b) wave length (λ); and

c) wave number.

Frequency of oscillation of thermal radiation does not change when a wave is passing through materials with a different refractive index, which gives a great advantage for some calculations. The unit for frequency is [Hz].

The wavelength (λ) can be described as the distance between successive 'peaks' of the wave. Common units for wavelength are micrometer [μm], where 1 [μm] $= 10^{-6}$ [m] and $\overset{\circ}{A} = 10^{-10}$ [m].

The electromagnetic spectrum covers an enormous range of wavelengths, from very short waves (such as cosmic or gamma rays) to very long broadcasting ones. It is very interesting to mention that our eyes are only sensitive to identify the 'visible' range (Figure 2.2). Our eyes have a peak sensitivity of about 5000 [$\overset{\circ}{A}$], meaning the wavelength of light we can see most clearly is 5000 [$\overset{\circ}{A}$].

The Sun gives off the largest percentage of its light at about 5300 [$\overset{\circ}{A}$]. This means that our eyes are perfectly evolved to see the light that Sun gives off. However, radiant energy is not only provided by the Sun, it is also produced by every object whose temperature is greater than 0 [K]. **Maxwell's** theory was revolutionary in the 19th century and many scientists tried to explain thermal radiation mechanism using this theory. As an example the Wien, and Rayleigh - Jeans Laws will be analyzed. **Wilhelm Wien** (1864-1928) made a theory that predicted the overall form of the curve by treating the radiation as gas molecules. He suggested the concrete form

$$e(\nu, T) = a\nu^3 e^{(-b\nu/T)} \tag{2.3}$$

which is well known as **Wien Radiation Formula** (1896).

However, at long wavelengths his theory disagreed with experimental data. At the same time Rayleigh and Jeans wrote a formula by considering the radiation within a blackbody cavity to be made up of a series of standing waves. According to the Maxwell theory they thought that electromagnetic radiation was emitted by oscillating atoms in the walls of the blackbody and that this radiation set up a standing wave between the walls. Their formula, which expresses the intensity of radiation emitted by a blackbody at a specific wavelength, can be written

$$e_{\lambda,T}(\lambda, T) = \frac{2\pi ckT}{\lambda^4} \tag{2.4}$$

where $k = 1.380658 \; [J/K]$ is Boltzmann constant and c is the speed of light. A comparison between equation 2.4 and experimental data, as can be seen in Figure 2.3, shows that Rayleigh-Jeans Law can be used for large wavelengths. Unfortunately, it does not give correct results at short wavelengths. According to equation 2.4, a decrease of wavelength λ causes an increase of intensity of radiation. At the point where λ is approaching 0 the intensity of radiation will near infinity. This absurd prediction is known as the *ultra-violet catastrophe*. However, it is known that each temperature has its own peak wavelength (2.5), and the energy emitted either side of this peak dropped. As can be seen in Figure 2.4 the Rayleigh-Jeans Law does not predict the peak wavelength.

Max Karl Ernst Ludwig Planck (1858-1947), a former Kirchoff student and one of the the greatest German scientists, knew the results of experimental work which had already been carried out and also the Rayleigh's problem to fit an analytical curve with experimental data. He solved this problem successfully by describing that the energy of the oscillators must be quantized, where each quantum has an energy of:

$$E = h\nu \tag{2.5}$$

He gave the primary law governing blackbody radiation, known as **Planck Radiation Law** (announced to the Berlin Physical Society on October 19, 1900) Kangro (1976), which governs the intensity of radiation emitted by unit surface area into a fixed direction (solid angle) from a blackbody as a function of wavelength for a fixed temperature. The following equation describes Planck's Law:

$$e_{\lambda,T}(\lambda, T) = \frac{2hc^2}{\lambda^5} \frac{1}{e^{hc/\lambda kT} - 1} \tag{2.6}$$

where $h = 6.6260755 \cdot 10^{-34} \; [Js]$ is Planck constant. Equation (2.6) determines emission into vacuum, for emission into a medium the index of refraction has to be involved. In this case equation (2.6) becomes:

$$e_{\lambda,T}(\lambda, T) = \frac{2hc^2}{n^2 \lambda_m^5} \frac{1}{e^{hc/\lambda_m kT} - 1} \tag{2.7}$$

Here λ_m is wavelength *inside* the medium.

A graphical explanation of equation (2.6) is illustrated in Figure 2.5 shown below. It can be seen, and it was mentioned earlier, that every line (Planck curve) has its own peak. At this peak the wavelength λ reaches the value, which is defined by **Wien's Displacement Law** (1893):

$$\lambda_{max} = \frac{2897.8[\mu m K]}{T[K]} \tag{2.8}$$

Equation (2.8) is valid for emission into vacuum, and it becomes for emission into a medium:

$$\lambda_{max} = \frac{2897.8\ [\mu m K]}{nT\ [K]} \tag{2.9}$$

The curves in the diagram show that a temperature increase causes an increase in the total radiant energy. At the same time the wavelength is decreasing.

While, equations (2.6) and (2.7) give results for a single wavelength, one new law, which can be derived from Planck Law, becomes very useful. It is the **Stefan-Boltzmann Law**. Deduced by Slovenian (Austrian) physicist Josef Stefan (1835-1893) in 1879 and theoretically explained by his former student Ludwig Boltzmann (1844-1906) in 1884, it was the first law to give the relationship between temperature and total radiant energy being emitted at all wavelengths by the blackbody. This law can be expressed as:

$$e_b = \pi i_b' = \int_0^\infty e_{\lambda b}(\lambda)d\lambda = \pi \int_0^\infty i_{\lambda b}'(\lambda)d\lambda = \sigma T^4 \tag{2.10}$$

All these laws, in the first approach, describe the radiation in the case where the emitting body is a so-called 'blackbody'. A blackbody does not exist in nature, and is defined as an ideal body that absorbs all the incident radiation that falls on its surface. A blackbody, as a perfect emitter and also a perfect absorber, can be used for comparison with a real body emitting radiation.

In nature, there are only a few materials with the same ability as a blackbody to absorb radiant energy. There are carbon black, platinum black, gold black and some specially formulated black paints.

However, there are more materials which have the ability to absorb radiant energy as blackbody, but only in a narrow wavelength region.

In the case when the radiating body is not a blackbody it is necessary to introduce a new term - *emissivity* $\varepsilon(\lambda, T)$. Emissivity or *emission coefficient* is defined as the ratio of the radiation emitted from any body and the radiation that would be emitted if that body was blackbody. Emissivity of a blackbody is equal to 1, while any other body has an emissivity from zero to one. Emissivity usually depends on many factors, such as body temperature, wavelength of emitted energy and angle of emission (see Figure 2.6).

Objects that show a wavelength-independent and a temperature-independent emissivity are called greybodies. The name greybody does not have a physical explanation, and it is only used as an expression for bodies which are not

blackbodies. Stefan-Boltzmann Law, involving the emissivity of a greybody, becomes:

$$e_b = \varepsilon \sigma T^4 \tag{2.11}$$

Between two surfaces A_1 and A_2, when surface A_1, acting as a greybody as an emitter and acting as a blackbody as a receiver, while surface A_2 acting as a blackbody as a receiver and acting as a greybody as an emitter, the net heat exchange between them is therefore:

$$Q_{1 \rightleftharpoons 2} = \sigma(\varepsilon_1 T_1^4 - \varepsilon_2 T_2^4)A_1 F_{1-2} = \sigma(\varepsilon_1 T_1^4 - \varepsilon_2 T_2^4)A_2 F_{2-1} \tag{2.12}$$

ε_1 is emissivity of the surface 1, ε_2 is emissivity of the surface 2, and F_{1-2} is the view (configuration) factor. This is one of the variations of the Stefan-Boltzmann Law which is used in analysis presented in Chapter 6.

From equation (2.12) it can be seen that energy transferred between two bodies depends on the difference between their absolute temperatures, which is raised to the fourth power. In a case when the heat transfer between two bodies has to be calculated, and one of them is very hot (above few hundreds $°C$), thermal radiation becomes the most important heat transfer mechanism.

2.1.1   Lambert's Cosine Law

Before Lambert, **Pierre Bouguer** (1698-1758) discovered the law which expresses the relationship between the absorption of radiant energy and the absorbing medium. This law is well-known as **Bouguer's Law** (1729).

Knowing about work which had been carried out earlier by Bouguer, **Johann Henrich Lambert** (1728-1777) carried out his own experiments with a few primitive instruments, and his conclusions resulted in laws that bear his name.

Equation (2.13) is the well-known **Lambert's Cosine Law** which states that the brightness of a diffusely radiating plane surface is proportional to the cosine of the angle formed by the line of sight and the normal to the surface (1760).

Intensity is a term that defines the radiation emitted in any direction. The radiation in an interval $d\lambda$ around a single wavelength is defined as *spectral* intensity (for a blackbody it is written as $i_{\lambda b}(\lambda)$, while *total* intensity ($i_b = \int_{\lambda=0}^{\infty} i_{\lambda b}(\lambda)d\lambda$) includes all wavelengths. Intensity is defined on the basis of projected area. It is often very useful to know the energy that is emitted by a black surface per unit time in very narrow wavelength interval, around the wavelength λ, per unit elemental surface area, which can be written as

$e_{\lambda b}(\lambda, \theta, \varphi)$. The relationship between $e_{\lambda b}(\lambda, \theta, \varphi)$ and $i_{\lambda b}(\lambda)$ is:

$$e_{\lambda b}(\lambda, \theta, \varphi) = i_{\lambda b}(\lambda) \cos \theta = e_{\lambda b}(\lambda, \theta) \tag{2.13}$$

2.2 Numerical Methods for the View Factor Calculation

A simple explanation of what is meant by 'view factor' is shown in Figure 2.7. Generally speaking the view factor indicates how a surface 'sees' other surfaces, i.e. the geometrical view. The finite areas A_1 and A_2 are at temperatures T_1 and T_2, and are oriented so that their normals build angles θ_1 and θ_2 with the line that links them.

From Figure 2.7 and the definitions of the view factor for a radiating point source dA_1, and an intercepting area dA_2, the total energy per unit time living dA_1 and incident on dA_2 is:

$$d^2 Q'_{d1-d2} = i'_1 dA_1 cos\theta_1 d\omega_1 \tag{2.14}$$

where i'_1 is the total intensity leaving dA_1, $d\omega_1$ is the solid angle subtended by dA_2 when viewed from dA_1. The solid angle is related to the projected area of dA_2 and the distance between differential elements by following expression:

$$d\omega_1 = \frac{dA_2 cos\theta}{r^2} \tag{2.15}$$

Substituting this expression (2.15) into equation (2.14) gives the following equation:

$$d^2 Q'_{d1-d2} = \frac{i'_1 dA_1 cos\theta_1 dA_2 cos\theta_2}{r^2} \tag{2.16}$$

At the same time the radiation leaving dA_2 and arrives at dA_1 can be written as:

$$d^2 Q'_{d2-d1} = \frac{i'_2 dA_2 cos\theta_2 dA_1 cos\theta_1}{r^2} \tag{2.17}$$

The view factor defined as the fraction of energy leaving diffuse surface element dA_1 that arrives at diffuse surface element dA_2 can be written as:

$$dF_{d1-d2} = \frac{d^2 Q'_{d1-d2}}{\pi i'_1 dA_1} = \frac{i'_1 cos\theta_1 cos\theta_2 dA_1 dA_2}{\pi i'_1 dA_1} = \frac{cos\theta_1 cos\theta_2 dA_2}{\pi r^2} \tag{2.18}$$

where $\pi i'_1 dA_1$ is the total diffuse energy leaving dA_1 within the entire hemispherical solid angle over dA_1.

Similarly integration of (2.18) over A_1 gives F_{12} from A_1 to A_2:

$$A_1 F_{1-2} = \int_{A_2} F_{dA_1 - dA_2} dA_1 = \int_{A_1} \int_{A_2} \frac{\cos\theta_1 \cos\theta_2}{\pi r^2} dA_2 dA_1 \qquad (2.19)$$

In the Stefan-Boltzmann equation, as seen earlier, the view (configuration) factor plays a very important role. From equation (2.19) it can be seen that view (configuration, form) factor depends on the shape and orientation of the surfaces as well as the distance between them. Obviously, the presence of obstacles (shadowing) between surfaces is not included here. An analytical solution of equation (2.19) is possible for simple geometrical configurations, while for more complex geometrical configurations it cannot be used.

Since the 1960s many methods for calculating view factors have been developed with varying degrees of success. However, this thesis does not include an analysis of all these methods, but instead will focus on the following methods: the Monte Carlo, the Hemi-cube and the Integration methods.

2.2.1 The Monte Carlo Method

The Monte Carlo method as one of the methods of stochastic techniques, is widely used in many disciplines such as physics, mathematics, chemistry and as well as radiative heat transfer. These techniques are based on the use of random numbers and probability statistics to investigate problems in many areas. Generally, to call something a 'Monte Carlo' method, all we need to do is use random numbers to examine our problem. The basic characteristic of the Monte Carlo method, as applied here, is that energy emitted by a finite area is substituted with a total number of N rays, where each ray carries the same amount of energy (Ballance (1973), Pattanaik (1993), Parthasarathy (1995), etc.). For example Ballance (1973) calculated view factor using the Monte Carlo method to within approximately 5 percent. Randomly chosen sample points represent the origin of the rays. The coordinates of a random point included in a triangle element are defined by following equations:

$$\begin{aligned}
x &= x_1 + s(x_2 - x_1) + t(x_3 - x_1) \\
y &= y_1 + s(y_2 - y_1) + t(y_3 - y_1) \\
z &= z_1 + s(z_2 - z_1) + t(z_3 - z_1)
\end{aligned} \qquad (2.20)$$

according that s and t are defined as:

$$\begin{aligned}
s &= 1 - \sqrt{1 - random[0]} \\
t &= (1 - s) random[0]
\end{aligned} \qquad (2.21)$$

where $random[0]$ is a uniformly distributed random number in the interval $[0,1]$.

For a planar rectangular surface the location of emission is in principle defined by:

$$
\begin{aligned}
x &= x_{min} + (x_{max} - x_{min})random[0] \\
y &= y_{min} + (y_{max} - y_{min})random[0] \\
z &= z_{min} + (z_{max} - z_{min})random[0]
\end{aligned}
\tag{2.22}
$$

The subscripts max and min denote, respectively, the maximum and minimum values of the appropriate coordinate on the surface element.

Other than the random sample point, the centre of the finite element face can be chosen to be an origin of emanating rays. For a triangular element it is defined by following equations:

$$
\begin{aligned}
x &= (x_1 + x_2 + x_3)/3 \\
y &= (y_1 + y_2 + y_3)/3 \\
z &= (z_1 + z_2 + z_3)/3
\end{aligned}
\tag{2.23}
$$

while for a rectangular element the centre is defined as:

$$
\begin{aligned}
x &= x_{min} + (x_{max} - x_{min})/2 \\
y &= y_{min} + (y_{max} - y_{min})/2 \\
z &= z_{min} + (z_{max} - z_{min})/2
\end{aligned}
\tag{2.24}
$$

Assuming the distribution of the rays sent by an emitter is governed by the *cosine* distribution as it is in Baranoski (2001), the final expression for the angles, which present the angular displacements, without any formal mathematical procedure, is given as:

$$
\begin{aligned}
\alpha &= \arccos(\sqrt{1 - random[0]}) \\
\beta &= 2\pi random[0]
\end{aligned}
\tag{2.25}
$$

Some of the N rays will hit another surface (m rays), while others will miss. The view factor, which links finite elements i and j can be simply represented by

$$
F_{ij} = \frac{m}{N}
\tag{2.26}
$$

View factor calculation using the Monte Carlo method can be found in many existing computer programs such as MONTE, NEVADA, MuSES, or RadTherm as well as many other less famous examples, Siegel (2002). In

this thesis, the calculation considers both simple and more complex surfaces divided into n finite elements, where rays are shot randomly from two origins: the first origin is a randomly chosen point of a triangle element, while the second origin is the centre of a triangular element.

For this calculation an original computer program has been written, and has been tested using published analytical solutions. Calculations considered several different geometries such as the well-known parallel plate, hinged plates, parallel circular discs along the same normal and a cylinder and square plate cases. A few different numerical schemes as well as a comparison of the results obtained are presented.

Example 1: Two parallel square plates

Consider two parallel plates each divided into a different number of finite elements (Figure 2.8). The width (a) and the length (b) of the plates are the same ($a = b$). The distance ratio between them is denoted as ($c = distance/a$), and it is increased from 0 to 4. Results for view factors using different numerical schemes and different numbers of rays will be presented in the text that follows.

The analytical solution for this case is given by:

$$F_{12} = \frac{2}{\pi XY} \left\{ \ln \left[\frac{(1+X^2)(1+Y^2)}{1+X^2+Y^2} \right]^{1/2} + Y\sqrt{(1+X^2)} \right.$$

$$\tan^{-1}\left(\frac{Y}{(1+X^2)}\right) + X\sqrt{1+Y^2}\tan^{-1}\left(\frac{X}{(1+Y^2)}\right)$$

$$\left. -Y\tan^{-1}Y - X\tan^{-1}X \right\} \qquad (2.27)$$

where, $X = a/c$ and $Y = b/c$.

All results are presented according to the numerical scheme and number of rays used in calculations.

The difference between the two sets of solutions was calculated as:

$$\frac{F_{12(MonteCarlo)} - F_{12(analytical)}}{F_{12(analytical)}} \cdot 100 = \delta[\%] \qquad (2.28)$$

a) mesh 10x10

The emitter and the receiver are divided into 100 surface elements each. Results obtained are presented in Table 2.1 using 100, 1000 and 10000 rays.

From Table 2.1 it can be seen that an increase of number of rays gives better results. Also, an increase of distance ratios causes a decrease in the accuracy of results obtained. However, the Monte Carlo method is a stochastic method and requires that many experiments have to be run. Therefore, these conclusions are general and cannot be taken as conclusive as they are the result of a few calculations.

b) mesh 25x25

Following the same order as in the previous section, results are presented using the same number of rays as for the 25x25 mesh (Table 2.2). A comparison of results presented in Tables 2.1 and 2.2) shows that an increase of mesh resolution gives a better accuracy of results obtained. But, this conclusion can be drawn for the whole plate only. A disagreement between the accuracy of results obtained for a overall plate and a single element is discuss later in the text.

c) mesh 40x40

Differences between the analytical solutions and the model for the mesh 40x40 are presented in Table 2.3. As mentioned earlier, an increase of mesh resolution causes an increase of distance ratios and a decrease of view factor values between surfaces. The analysis of the relationship between numerical sensitivity and the Monte Carlo method presented in Vujičić (2005c) shows that an increase of distance ratios between surfaces requires an increase of rays used for view factor calculations.

Example 2: Hinged plates

In this section the relationship between numerical schemes (number of the rays) and view factor for a few different cases is considered. The calculations are made for different angles ($\varphi = 30, 45, 60, 90, 120, 135, 150[°]$) and different geometries ($A = a/c, B = b/c$) of plates (Figure 2.9).

The analytical solution for each angle is different and they involve large equations. As an example the analytical solution for angle $\varphi = 90[°]$ is

written below:

$$F_{12} = \frac{1}{\pi W} \left(W \tan^{-1} \frac{1}{W} + H \tan^{-1} \frac{1}{H} - \sqrt{H^2 + W^2} \tan^{-1} \frac{1}{\sqrt{H^2 + W^2}} \right.$$

$$+ \frac{1}{4} \ln \left\{ \frac{(1+W^2)(1+H^2)}{1+W^2+H^2} \left[\frac{W^2(1+W^2+H^2)}{(1+W^2)(W^2+H^2)} \right]^{W^2} \right.$$

$$\left. \left. \left[\frac{H^2(1+W^2+H^2)}{(1+H^2)(W^2+H^2)} \right]^{H^2} \right\} \right) \tag{2.29}$$

where $H = b/a$, $W = c/a$

a) A=1, B=1

Plates, with a 90 degree angle between them, used in this case were divided into 400, 2500 and 6400 elements. The results obtained are presented in Table 2.4. For view factor calculations 10, 100, 1000 and 10000 rays per element were used, depending on what mesh was chosen. Generally speaking for this example as for previous ones, an increase of number of rays gives a better accuracy of results obtained.

b) A=1.5, B=1

Differences between analytical solutions and model for different mesh resolutions and different number of rays used for the view factor calculation are presented in Figure 2.5.

c) A=2, B=1

Obtained results are presented in Table 2.6. In Table 2.6 can be seen that an increase of mesh resolution causes a decrease of accuracy of results obtained. The reasons for this behaviour are explained in the text earlier.

A real engineering problem has far more complex geometry than those above which are just special cases. Consequently, a further test of the program was performed which includes two more examples.

Example 2-1: Two hinged plates including an angle between them φ

For this calculation one plate was divided into 4 triangular finite elements, while the second was divided into 4,8,12,16 triangular finite elements (depending on the chosen geometry).

a) A=1, B=1

Results obtained for this case are presented in Table 2.7. From Table 2.7 can be seen that an increase of the angle between plates causes a decrease of view factor values.

b) A=2, B=1

Results obtained are presented in Table 2.8.

c) A=4, B=1

Results obtained are presented in Table 2.9.

Example 2-2: Two hinged plates including an angle and a distance between them φ

a) This example includes the following geometrical relationship: $A = 1; B = 1$, for the same angles as in example 2-1 (Figure 2.10). Results obtained are presented in Table 2.10.

b) The same geometrical relationship, as in the previous example, was considered in this analysis. The difference between these two examples is the direction of the separation distance, which is given as in Figure 2.11 for this case. Results obtained are presented in Table 2.11.

Example 3: Parallel circular discs along the same normal

One of the experiments described later considers a disc as an emitter and a square plate as a receiver. An analytical solution for this case is not known, which was the reason for using two parallel circular discs along the same normal to test the program.

The analytical solution for this case is given in the following equation

$$F_{12} = \frac{1}{2}\left[X - \sqrt{X^2 - 4\left(\frac{R_2}{R_1}\right)^2} \right] \qquad (2.30)$$

where are $X = 1 + \frac{1+R_2^2}{R_1^2}$, $R_1 = \frac{r_1}{h}$ and $R_2 = \frac{r_2}{h}$ as could be seen in Figure 6.13. Calculations consider discs with the same diameter $r_1 = r_2$.

For the calculations three different divisions of the perimeter, such as 4x10, 4x20 and 4x40 were used. Also, 100, 1000, 2000, 5000, 10000 and 16000 rays, depending on the numerical scheme for the view factor calculations,

were used. A few different distances, $h/r = 0.5, 1, 1.5$ and 2, between discs were used.

Obtained results for different numerical schemes and different number of rays per element are presented in Figures 2.13, 2.14 and 2.15 respectively.

A random point or the centre of the triangle as an origin?

In this section a comparison between view factors obtained using a random point of the triangle or the centre of the triangle as an origin of rays was made. Three simple cases: parallel plates; hinged plates; and parallel discs; along same normal were considered. Results obtained for a random point as origin are presented in tables already included in the subsection Example 1. This means that only results obtained for the centre of the triangle as an origin are presented in Table 2.12.

A comparison between the results presented in Table 2.12 and their counterpart in Tables 2.1, 2.2 and 2.3 for the chosen distance ratio $C/L = 1$ does not give the advantage to either of these approaches. At the same time a comparison between a random point as origin (Table 2.4) and the centre of the triangle (Table 2.13) for hinged plates, shows a slight advantage if the centre of triangle is used as an origin.

Further analysis considers two parallel discs along same normals. From Figure 2.16 it can be seen that neither of these two origins has a great advantage.

One special case presented in Figure 2.17 eliminates the centre of a finite element as origin. As it can be seen from Figure 2.17 there is not any view factor between elements A_{11} and A_{22} while the centre of the triangular element (C_{11}) lies in the section of the triangular element bounded by the projection of the body B_2 (left side of the line $L_1 - L_2$). The other method for the view factor calculation called Hemi-cube method which uses a centre of an element as origin also struggles with this type of problem. Obviously, a view factor between elements A_{11} and A_{22} exists. Random point as an origin deals with this problem without any difficulty.

It should be noted that the program which uses a random point as an origin consumes 2 % more computation time, than one with the centre as an origin.

Accuracy, CPU time and optimization

In this text a simple two parallel case is presented. Plates are divided into 2, 4 and 50 triangular finite elements. The following diagrams (Figure 2.18, 2.19

and 2.20) present the difference between a numerical and an analytical solution.

From these diagrams it can be seen that the difference between a numerical and an analytical solution decreases with an increase of the number of finite elements. However, this is an interim conclusion that will be discussed later. Three numerical schemes used for two parallel plates meshing will be analyzed. The values of view factors presented in Tables 2.1, 2.2 and 2.3 are averaged values of the all view factor values for a single element included in the each plate.

View factors of two single elements which are belonging to the parallel plates each with the distance ratio of $C/L = 0.2$ between them are presented in Table 2.14. The length and the width of plates where same and that is 197 $[mm]$. Using mesh 10x10 the dimension of the each element becomes 19.7 x 19.7 $[mm]$ while for the numerical scheme 25x25 it was 7.88 x 7.88 $[mm]$. Finally, for mesh 40x40, the dimension of the each element becomes 4.925 x 4.925 $[mm]$.

A comparison between the results presented in Table 2.1, Table 2.2 and Table 2.3 with results presented in Table 2.14 shows a huge difference between the accuracy of the averaged view factor values for whole plate and the view factor value for the single element. The explanation of this anomaly could be made in the following sense: an increase of the mesh density causes a decrease of the size of a single element further causing an increase of the distance ratio between single elements. At the same time an increase in the distance between elements means for high accuracy of results an increase of the number of rays used for calculations Vujičić (2005c). However, all of these cause the processing time to rapidly increase (see Table 2.15). From the diagrams presented above great care should be taken concerning the minimum number of rays sent from a surface. The main question to be asked when applying the Monte Carlo method (taking care about accuracy and CPU time) is: How large should N be? Here the exponential *Chebyshev* inequality and normal distribution approximation were applied. In the following text the final equation will be given without any mathematical procedure Baranoski (2001).

The number of sample rays (N) derived from the exponential *Chebyshev* inequality is given by:

$$N = \left\lceil \frac{\ln(2/\delta)}{2\varepsilon^2} \right\rceil \tag{2.31}$$

where δ is the confidence. The choice of confidence is highly dependent on the application. For example, illuminating engineers need radiative transfer solutions accurate from 1 to 10%.

The selection of the value ε depends on how deep in the region of convergence it has to go. The next equation can be very useful:

$$K = \frac{A}{d} \tag{2.32}$$

where A is the area of the receiver, and d is the distance between an emitter and a receiver. The smaller value of the K gives the smaller value of the ε.

At the same time, the number of the rays (N) is obtained by the normal distribution (Hahn (1967)) as an approximation of the binomial distribution as:

$$N = \frac{p(1-p)}{E^2} Z^2 \tag{2.33}$$

The initial estimate p can be estimated by conducting a small experiment in the computer or can be initialized as 0.5 for a conservative sample. The value of Z is chosen according to the error value E. Normally a confidence limit of 98[%] is chosen and corresponding Z is 2.0542.

The optimization, which includes a distance between an emitter and a receiver, considers only element to element or face to face problems. Therefore it cannot be applied in **Pharo**. The main reason for this is that view factor calculations included in **Pharo** involve several different individual distances, rather than one single distance.

Conclusions

The algorithm of the Monte Carlo method is simple and does not depend on the presence of an obstacle, which is one of its advantages. As mentioned earlier, for the view factor calculation, an original program has been written in Fortran 90. The analysis of results shows that the number of rays used for the view factor calculation is crucial. An increase of the number of rays used for the view factor calculation should cause an increase of accuracy of results obtained. However, this statement is general and sometimes better accuracy of results obtained is gained with lower number of rays. The difference between analytical and numerical results for the view factor between two single elements with the distance ratio of 0.5 between them is presented in Figure 2.33. As it can be seen from Figure 2.33 accuracy of results obtained is varying in the strip depending on the number of rays used in simulations. The width of the strip becomes narrower with an increase of the number of rays used in calculations.

During calculations, it was noted that the view factor values obtained using the Monte Carlo method, change from realization to realization, even when the same number of rays were used. This behaviour is caused by the

random number generator, whose working can be explained as follows: If one starts a computer and runs a calculation using a certain number of rays, a view factor value will be obtained. Repeating the same calculation produces a different view factor value. The main reason for this difference is the starting point of the random number generator. However, if one restarts the computer and runs the same calculation again, the same result as the first will be obtained. The main reason for this behaviour is that the random number generator always starts at the same point when the computer restarts.

From the view factor calculation point of the view, an increase of the mesh resolution does not cause increased accuracy between single elements. Unfortunately, it has been shown that it causes the opposite effect - worse accuracy. Also, an increase of the mesh resolution causes an increase in CPU time.

However, the results obtained using the Monte Carlo method suggest that this method can be used for the view factor calculation with high efficiency.

2.2.2 The Hemi-cube Method

The Hemi-cube method, introduced by M. F. Cohen (Cohen (1985)), is based on the well-known **Nusselt's** analogy, where he calculated form-factor using a hemisphere with a unit radius. As can be seen from Figure 2.21 all patches in the environment are projected onto the hemisphere. The view factor is equivalent to the fraction of the circle, which is projected down onto the base of the hemisphere. Cohen's idea is that it is easier to project onto an imaginary unit size hemi-cube, which is constructed around the centre of the patch, than onto a hemisphere. The hemi-cube is later divided into square 'pixels' (see Figure 2.22). The number of pixels depends on the chosen resolution. The calculations here consider parallel plates with several distances between them, applied to two different cases, and to hinged plates.

Delta form-factor

It should be noted that view-factors are computed for each pixel. If the area of a pixel is ΔA, its view factor is:

$$\Delta View\ factor = \frac{\cos \phi_i \cos \phi_j}{\pi \cdot r^2} \Delta A \qquad (2.34)$$

Delta view factors can be computed and stored in a look-up table.

Top of the hemi-cube As it is shown in Figure 2.23, r is defined as:

$$r = \sqrt{x^2 + y^2 + 1} \qquad (2.35)$$

At the same time angles ϕ_i and ϕ_j are the same:

$$\cos\phi_i = \cos\phi_j = \frac{1}{\sqrt{x^2 + y^2 + 1}} \qquad (2.36)$$

Substituting cos angles defined in equation (2.36) into equation (2.34) equation for form-factor becomes:

$$\Delta View\ factor = \frac{1}{\pi(x^2 + y^2 + 1)^2}\Delta A \qquad (2.37)$$

Side of the hemi-cube   For the side of the hemi-cube (Figure 2.24) where the magnitude of the x-coordinate is -1, the angles ϕ_i and ϕ_j are calculated using the following equations written below:

$$\cos\phi_i = \frac{z}{\sqrt{y^2 + z^2 + 1}}$$
$$\cos\phi_j = \frac{1}{\sqrt{y^2 + z^2 + 1}} \qquad (2.38)$$

while delta view factor is obtained by:

$$\Delta View\ factor = \frac{z}{\pi(y^2 + z^2 + 1)^2}\Delta A \qquad (2.39)$$

Results and discussion

As was mentioned above two different cases were analyzed:
a) parallel plates; and
b) hinged plates.

a) parallel plates

Parallel plates case is divided into two cases:
a1) the whole plate is covered by one hemi-cube;
a2) the plate is divided into elements and every element is covered by its own hemi-cube.

a1)   The first diagram (Figure 2.25) presents the results of the calculation where is whole plate covered by one hemi-cube. The results prove that this method does not give good results when the distance between surfaces

is smaller than their size. The second diagram (Figure 2.26) presents the difference (error) between the numerical and the analytical solutions. N represents resolution (total number of pixels is $3 \cdot N^2$). From the diagram presented in Figure 2.26 it can be seen that an increase in the number of pixels causes an increase of accuracy of results obtained. However, an error between numerical and analytical results will exist even if the number of pixels reach an infinite value.

a2) The calculation includes two parallel plates, each of the size $1.0 \times 1.0[m]$, with distance between them varied from 0.1 [m] to 7.0 [m], as can be seen in Figure 2.27. Every plate is divided into 5×5 elements, 10×10 elements and 25×25 elements. In Figure 2.28 it can be seen that the results obtained when the plate is divided into elements give better agreement with analytical solutions than when the plate is not divided. Further division of the plate into an even greater number of elements gives even better results. However, care must be taken of CPU time, because increasing the number of elements also causes an increase in the CPU time. Note, *nex* and *ney* represent the number of divisions in x and y direction.

b) hinged plates

One geometry ($A = B = 1$) with three different numerical schemes (10x10x4, 25x25x4 and 40x40x4) using different numbers of pixels is analyzed in this case.

b1) mesh 10x10

Plates divided into 100 surface elements each are presented in Figure 2.29, while the results obtained are presented in Table 2.16. From Table 2.16 it can be seen that an increase of number of rays used causes a better accuracy of results obtained.

b2) mesh 25x25

Results obtained for the plates divided into 625 surface elements each are presented in Table 2.17.

b3) mesh 40x40

Results obtained for the plates divided into 1600 surface elements each are presented in Table 2.18. From Table 2.18 can be noted that an increase of mesh resolution causes a better accuracy of results obtained for overall plate. An analysis of results obtained for single elements shows a disagreement with the statement drown for overall plate.

The Hemi-cube method in a real environment

One simple test case, such as parallel plates was analyzed in the previous subsection. However, a real environment considers more complex relationships between finite surfaces, therefore the view factor calculation has to be adapted to deal with complex geometries.

The basic idea is presented in ten steps given in the text that follows:
step 1 - formatting a hemi-cube with the centre in the origin $(0,0,0)$,
step 2 - define normal vector $sf = (0,0,1)$,
step 3 - calculate an angle *cosangle* between a vector sf and a normal vector of the surface *kvecti* which is included in enclosure,
step 4 - define parameters ss, cc, tt as:

$$
\begin{aligned}
ss &= \sqrt{1. - (cosangle)^2} \\
cc &= (cosangle) \\
tt &= 1. - (cosangle)
\end{aligned}
\tag{2.40}
$$

step 5 - calculate a unit vector uv of the axis of rotation:

$$
\begin{aligned}
uv(1) &= sf(2) * kvecti(3) - sf(3) * kvecti(2) \\
uv(2) &= sf(3) * kvecti(1) - sf(1) * kvecti(3) \\
uv(3) &= sf(1) * kvecti(2) - sf(2) * kvecti(1)
\end{aligned}
\tag{2.41}
$$

step 6 - set up rotation matrix:

$$\begin{array}{rcl} rot(1,1) & = & uv(1)^2 * tt + cc \\ rot(2,1) & = & uv(1) * uv(2) * tt + uv(3) * ss \\ rot(3,1) & = & uv(1) * uv(3) * tt - uv(2) * ss \\ rot(1,2) & = & uv(2) * uv(1) * tt - uv(3) * ss \\ rot(2,2) & = & uv(2)^2 * tt + cc \\ rot(3,2) & = & uv(2) * uv(3) * tt + uv(1) * ss \\ rot(1,3) & = & uv(3) * uv(1) * tt + uv(2) * ss \\ rot(2,3) & = & uv(3) * uv(2) * tt - uv(1) * ss \\ rot(3,3) & = & uv(3)^2 * tt + cc \end{array} \tag{2.42}$$

step 7 - define vectors with origin in $0,0,0$ with directions through the middle of pixels $(n1(xx_{pix}, yy_{pix}, zz_{pix}))$,
step 8 - rotate previous defined vectors using rotate matrix;
$n1 = matmul(rot, n1)$
step 9 - translate obtained vectors to the centre of the element,
step 10 - check target and calculate view factor.

An advantage of this method is that only one hemi-cube has to be constructed, then later rotated for a calculated angle between normal vector sf and the normal vector of a surface $kvecti$, making this method faster than the Monte Carlo method.

Conclusions

The Hemi-cube method is a well established method for view factor calculation in computer graphics, illumination industry, as well as in radiative heat transfer. The analysis of results for a few simple test cases, where the analytical solutions are known, shows a good agreement of the results obtained when compared with these analytical solutions. It is expected that an increase of the mesh resolution gives better results for the whole plate. However, it is shown that an increase of the mesh resolution (discretization of domain) as well as the hemi-cube resolution (an increase of 'pixel' number) does not produce a better solution. The main reason for this is that view factor obtained by the Hemi-cube method can be overestimated or underestimated, which is connected to the size of pixels. Also, everything said about accuracy, an individual and an overall view factor value for the Monte Carlo method is valid for the Hemi-cube method. This means that with higher mesh resolution a view factor value for whole plate is more accurate. At the same time a view factor value for an individual element is less accurate.

2.2.3 The Integration Methods

The Contour Integration Method

The Contour Integration method was one of the first methods used for view factor calculation. The basic idea was applying **Stokes'(Green)** theorem where multiple integration over a surface may be changed to a single integration around the contour of the surface (Sparrow (1963)). Many papers have been published since the 1960's where different relationships between differential elements, a differential element and a finite element, and finite elements were analyzed. For example Minning (1977) used contour integration to derive closed form factor from planar element to the surface of right frustum of cone when the element is in plane perpendicular to cone axis, while Haller (1963) derives view factor from planar element on longitudinal fin to infinitely long tube, and corrects errors in derivation in some earlier published work. More complex geometries were analyzed in the papers written by Juul (1982) where double integral expression for the view factor between parallel opposed cylinders of finite length and unequal radius was derived, and by Mahbod (1984) where contour integration was used to derive view factors between a differential band on the surface of a sphere and a finite strip on the interior of coaxial cylinder; and between a coaxial annular ring on the cylinder base and a finite strip on the interior of a coaxial cylinder when blocked by a coaxial sphere.

Let the functions P, Q and R be any twice-differentiable function of x, y and z. The three dimensional Stokes' theorem presents the relationship between an integral of P, Q and R around the contour of the area and an integral over the surface A of the same area:

$$\oint_C (P dx + Q dy + R dz) = \int_A \left[\left(\frac{\partial R}{\partial y} - \frac{\partial Q}{\partial z} \right) \cos \alpha + \right.$$

$$\left. + \left(\frac{\partial P}{\partial z} - \frac{\partial R}{\partial x} \right) \cos \gamma + \left(\frac{\partial Q}{\partial x} - \frac{\partial P}{\partial y} \right) \cos \delta \right] dA \qquad (2.43)$$

Now, introduce the angles (ϕ_1, ϕ_2) between the normals of the finite areas and line (S) which joining the areas:

$$\cos \phi_1 = \frac{x_2 - x_1}{S} \cos \alpha_1 + \frac{y_2 - y_1}{S} \cos \gamma_1 + \frac{z_2 - z_1}{S} \cos \delta_1$$

$$\cos \phi_2 = \frac{x_1 - x_2}{S} \cos \alpha_2 + \frac{y_1 - y_2}{S} \cos \gamma_2 + \frac{z_1 - z_2}{S} \cos \delta_2 \qquad (2.44)$$

The following equation presents the view factor between two finite areas:

$$A_1 F_{1-2} = A_2 F_{2-1} = \int_{A_1} F_{d1-2} dA_1 =$$

$$\frac{1}{2\pi} \oint_{C_2} \left[\int_{A_1} \frac{(y_2 - y_1)n_1 - (z_2 - z_1)m_1}{S^2} dA_1 \right] dx_2 +$$

$$\frac{1}{2\pi} \oint_{C_2} \left[\int_{A_1} \frac{(z_2 - z_1)l_1 - (x_2 - x_1)n_1}{S^2} dA_1 \right] dy_2 +$$

$$\frac{1}{2\pi} \oint_{C_2} \left[\int_{A_1} \frac{(x_2 - x_1)m_1 - (y_2 - y_1)l_1}{S^2} dA_1 \right] dz_2 \qquad (2.45)$$

where $l = \cos\alpha, m = \cos\gamma, n = \cos\delta$.

Applying Stokes' theorem equation for view factor calculation becomes:

$$F_{1-2} = \frac{1}{2\pi A_1} \oint_{C_1} \oint_{C_2} (\ln S dx_2 dx_1 + \ln S dy_2 dy_1 + \ln S dz_2 dz_1) \qquad (2.46)$$

Starting with simple geometries such as disc to disc case (Feingold (1978)) this method was later used to calculate view factors for more complex cases (Minning (1977), Chung (1982c)).

The Area Integration Method

The basic idea is that the surfaces A_i and A_j are divided into n finite elements $A_i(i = 1, 2, 3, \cdots, n)$ and $A_j(j = 1, 2, 3, \cdots, n)$, so that equation for the view factor calculation may be approximated by:

$$F_{i,j} = \frac{1}{A_1} \sum_{i=1}^{n} \sum_{j=1}^{n} \frac{\cos\theta_i \cos\theta_j A_i A_j}{\pi r_{ij}^2} \qquad (2.47)$$

There are a few interesting papers written by Chung (1982a) and Shapiro (1983). In the first one the Gaussian quadrature integration was utilized together with finite element geometries using a few different meshes as well as two and six point Gaussian quadrature. In the paper written by Shapiro a computer code named FACET is presented. FACET includes all integration methods, such as Line integration, Area integration and Mitalas-Stephenson methods.

The Mitalas and Stephenson Method

Mitalas (1966) introduce a method where one integral is solved analytically, while other is solved numerically, so the equation for the view factor calculation in case where the surfaces I and J are quadrilaterals, becomes:

$$F_{IJ} = \frac{1}{2\pi A_1} \sum \sum \phi(p,q) \oint [(T\cos\phi\ln T + S\cos\phi\ln S + U\omega - R)dv]_{p,q}$$

$$(2.48)$$

where S, T, U, ϕ, and ω are functions of v and:

$$\phi(p,q) = l_p l_q + m_p m_q + n_p n_q \qquad (2.49)$$

where dv is an element on the contour of A_2, while the other symbols are shown in Figure 2.31.

The calculation was made for two geometrical cases: parallel plates and hinged plates.

Results and discussion

The results obtained are presented in tables for the Line integration method, Area integration method and Mitalas & Stephenson method respectively. Analysis of these results shows that view factors obtained by the Line integration method have the best accuracy to analytical solutions. The Area integration method has a lower level of accuracy, but is still better than the Mitalas-Stephenson method. However, all of them have a problem with shadowing which is crucial (Shapiro (1983), Choi (2002)).

The Line integration method

As explained above two cases were considered: parallel plates and hinged plates, and the obtained results are shown respectively.

During the calculation the boundary line was divided into five segments. The results obtained are compared with analytical solutions and as can be seen in Table 2.19 there is good agreement between them.

a) Parallel plates

Table 2.19 presents the results of calculation for the distance between plates from 0.1 to 7. View factor calculation in this case considers the plates of the same size.

b) Hinged plates

As can be seen in Table 2.20 there are several geometrical relations between plates. The obtained results show good agreement between numerical and analytical solutions.

The Area integration method

a) Parallel plates

This method considers the same size of plates for the view factor calculation between parallel plates as in the previous case. During the calculation the plates were divided into five identical finite elements.

The results obtained do not show as good agreement as the results from the Line integration method, especially for a short distance between the plates (see Table 2.21). However, the results obtained still have a good agreement with analytical solutions.

b) Hinged plates

The calculation considers the same geometrical relations between hinged plates as used during the calculation when the Line integration method was applied.

The results obtained do not show good agreement with analytical solutions for following relations: $L/N = 1/1$, $1/2$ and $1/10$, while for others relations the error is acceptable (see Table 2.22).

The Mitalas-Stephenson method

Two different cases, parallel plates and hinged plates cases, are considered for this examination:

a) Parallel plates

Generally speaking the results obtained show a good agreement with analytical solutions except for the case when the distance between the plates is very short (see Table 2.23).

b) Hinged plates

Obtained result for this case are presented in Table 2.24.

2.2.4 Conclusions

A general comparison of all the methods used for the view factor calculation will be presented in this section, with special attention given to the comparison between the Monte Carlo and the Hemi-cube methods. Two parallel plates cases with different separation ratios, different mesh resolutions and different number of rays per element are taken for examination. Accuracy and CPU time were also taken to be criterions in the analysis.

Results obtained using the Monte Carlo and Hemi-cube methods for plates divided by mesh 10x10 with 100, 1000 and 10000 rays per element are presented in Figure 2.32. It can be seen that the lines presented in this figure do not present the trend of difference. Their role is to help a clearer presentation of results obtained for the same method, the same number of rays and a different distance ratio. A more realistic trend of difference for two parallel elements with the distance ratio of 0.5 between them using the Monte Carlo method with different number of rays per element (from 100 to 10000 with step of 5 rays) is presented in Figure 2.33. From this figure it can be seen that difference between model and analytical solution has a fluctuating decreasing trend. At the same time results obtained using the Hemi-cube method do not give a fluctuating value of difference between the model and the analytical solution, as was observed when applying the Monte Carlo method.

However, in Figure 2.32 it can be seen that the amplitude of difference for the Monte Carlo method is smaller than for the Hemi-cube method, thereby giving an advantage to the Monte Carlo method.

Also, the results presented in Figures 2.34 and 2.35 draw the same conclusion. Namely, that the Monte Carlo method has an advantage over the Hemi-cube method.

A comparison between the Monte Carlo method, the Hemi-cube method and integration methods given in the paper written by Emery (1991) concludes that the Monte Carlo method may be the best choice for the view factor calculation as well as gaining insight into the level of computational effort required to achieve a given accuracy.

The values of calculated view factor used for comparisons in the Figures 2.32, 2.34 and 2.35 are the sum of the view factors of all elements included in the plate. However, if these finite element meshes were to be applied in a radiative heat transfer simulation, then it is the *individual* element view factors between elements that would be used, as was reported in the subsection 2.2.1 for the Monte Carlo method.

The same conclusions can be drawn for the Hemi-cube method. In the text that follows two parallel plates case divided by mesh 10x10 with the

distance ratio $c/L = 0.2$ is presented. It was noticed that the distance ratio between two parallel *individual* elements becomes 2. A comparison between the results presented in Figures 2.32, 2.34 and 2.35 with the results presented in Table 2.25 shows a huge difference between the accuracy of the averaged view factor values and the values at each individual element. However, it can be useful for a comparison between different methods and as well as for a conservation of energy in heat transfer simulations.

CPU Performance of Methods Used for View Factor Calculation

A comparison between the Hemi-cube and the Monte Carlo methods, which considers two parallel square plates divided by three different meshes (10x10; 25x25 and 40x40), is presented in this section.

As can be seen from Figure **??** the Hemi-cube method has a greater advantage over the Monte Carlo method. An average difference in CPU time between the Hemi-cube method and the Monte Carlo method is about 20%.

In applications where accuracy can take values up to 10 % (illumination technique) the Hemi-cube method, which is faster than the Monte Carlo method, has an advantage. However, it is very difficult to write two different programs which have roughly the same level of optimization. Therefore CPU time is sometimes not the best criteria in the process of selection as to which program is the most appropriate to use.

2.3 Reflectivity

When heat transported by radiation reaches a surface one part is absorbed while another is reflected. According to the Kirchoff Law for greybody, absorptivity and emissivity are equal, so reflectivity is defined as:

$$\rho = 1 - \epsilon \tag{2.50}$$

Equation (2.50) is only valid for non transmissive materials. For materials with low emissivity it is obvious that reflectivity plays a crucial role in heat transfer simulation. Also it becomes very important for short distances between bodies or surfaces. A historical overview with existing methods will be given in the following text. Afterwards, the *Multiple reflection of view factors* method will be presented.

2.3.1 Historical Overview

Application of equation (2.12) is one of the ways to calculate the net heat exchanged between two grey surfaces. As it was mentioned earlier during

the derivation of this equation it was assumed that surfaces act as greybody as emitter and as blackbody as receiver. Two more derivations of Stefan-Boltzmann Law are analyzed in the text that follows.

$$Q_{1 \rightleftharpoons 2} = \sigma(\varepsilon_2 T_1^4 - \varepsilon_1 T_2^4)A_1 F_{1-2} \tag{2.51}$$

Equation (2.51) is obtained assuming that an emitter acts as blackbody while a receiver acts as greybody.

$$Q_{1 \rightleftharpoons 2} = \sigma \varepsilon_1 \varepsilon_2 (T_1^4 - T_2^4)A_1 F_{1-2} \tag{2.52}$$

In equation (2.52) both an emitter and a receiver act as greybody.

The results obtained using these equations are presented in Chapter 6.

It can be noticed that in all these equations the reflectivity as a surface property is not considered.

According to Figure 2.38 view factor between elements 1 and 4 is 0, so there is no heat exchanged between them (eq. (2.12) or eq. (2.54)). At the same time, it is obvious that an amount of the heat which leaves surface 1 will arrive on surface 4 through reflection via surfaces 2 and 3. In the beginning Seban, the discussion on the paper written by E. M. Sparrow 1963, suggested that the reflectivity could be expressed as the sum of a diffuse and a specular component (Mahan (2002)). Based on this idea firstly Mahan and Eskin introduced the concept of the *radiation distribution factor*, then later Mahan (Mahan (2002)) defines the *total radiation distribution factor* as the fraction of the total radiation emitted from a surface element i that is absorbed by a surface element j, due both to direct radiation and all possible reflections within the enclosure. This definition includes directional emission and absorption and bi-directional reflection. The method, suggested by Mahan, assumes specular reflection (case **a** in Figure 2.37), so for $\theta_i = \theta_r$ directions of reflected rays could be defined and diffuse reflection (case **b**), so it is possible to write that:

$$\alpha = 1 - \rho = 1 - \rho^d - \rho^s \tag{2.53}$$

where ρ^d presents the diffuse reflectivity and ρ^s presents the specular component.

Radiosity

Radiosity is a general term for a group of algorithms which work under assumption that all considered surfaces are pure diffuse, so all reflections are diffuse. There are many different approaches, depending on what quantity is unknown (Gebhart (1961)), which are basically equivalent.

Applying radiosity method for two surfaces gives the following equation:

$$Q_{i \rightleftharpoons j} = \left[\frac{1 - \varepsilon_i}{\varepsilon_i A_i} + \frac{1}{A_i F_{i-j}} + \frac{1 - \varepsilon_j}{\varepsilon_j A_j} \right]^{-1} \sigma(T_i^4 - T_j^4) \qquad (2.54)$$

Equation (2.54) considers reflection between surfaces A_i and A_j without including other surfaces A_k for $k \neq i, j$ (see Figure 2.38).

A consideration of the whole enclosure can lead to the following summation:

$$\sum_{j=1}^{N} \left(\frac{\delta_{kj}}{\epsilon_j} - F_{k-j} \frac{1 - \epsilon_j}{\epsilon_j} \right) \frac{Q_j}{A_j} = \sum_{j=1}^{N} F_{k-j} \sigma(T_k^4 - T_j^4) \qquad (2.55)$$

written for the k-th surface which can take one of the values from 1 to N. δ_{kj} is the Kronecker delta factor which is zero for $k \neq j$ and 1 for $k = j$.

While another approach is to introduce transfer factors which are defined from view factors yields:

$$\sum_{j=1}^{N} \left(\frac{\delta_{kj}}{\epsilon_j} - F_{k-j} \frac{1 - \epsilon_j}{\epsilon_j} \right) q_j = -F_{kn}$$

$$\sum_{j=1}^{N} \left(\frac{\delta_{kj}}{\epsilon_j} - F_{n-j} \frac{1 - \epsilon_j}{\epsilon_j} \right) q_j = 1 - F_{nn} \qquad (2.56)$$

for $k \neq n$.

A comparison between Radiosity method and the MRV method presented in the text bellow for a simple enclosure is given in Appendix A.

2.3.2 The Multiple Reflection of View Factors (MRV) Method

In this section a new approach, named the Multiple Reflection of View Factors (MRV) method, which I am proposing as part of this work, considers diffuse reflection will be analyzed. The basic idea of the MRV method can be explained using Figure 2.38. As it can be seen Figure 2.38 considers four elements defined with its own total hemispherical emissivity and total hemispherical reflectivity, so view factors F_{12}, F_{13}, F_{23}, F_{24} and F_{34} are corresponding between them. The net heat exchanged between elements is given

in following expressions:

$$
\begin{aligned}
Q_{12} &= f(F_{12}) \\
Q_{13} &= f(F_{13}) \\
Q_{23} &= f(F_{23}) \\
Q_{24} &= f(F_{24}) \\
Q_{34} &= f(F_{34})
\end{aligned}
\tag{2.57}
$$

$\alpha_2 Q_{12} = \alpha_2 f(F_{12})$ is absorbed heat by element 2, while $\rho_2 Q_{12} = \rho_2 f(F_{12})$ is heat reflected in the surrounding enclosure. According to the MRV method $\rho_2 f(F_{12}) F_{23}$ is heat reflected from element 2 that arrives to element 3, while $\rho_2 f(F_{12}) F_{24}$ is heat that arrives to element 4. After reflection the view factor is reassembled. For example the view factor F_{13} between surfaces 1 and 3 is reassembled into $F_{13} = F_{13direct} + F_{13ref.2} + F_{13ref2.ref.4}$. Obviously, all these reflections must stop at some stage. The criterium used in the MRV method is given in the following expression:

$$
\frac{(F_{i-j} F_{j-k} F_{k-l} \rho(j) \rho(k) \cdot 100)}{F_{i-j}} \leq 0.1
\tag{2.58}
$$

An original program has been developed to implement this algorithm. The program will stop all calculations for the current element if the criterion above is satisfied (i.e. if the received heat at element l from the initial element i is less than 0.1 percent of the heat exchanged between element i and element j, where element j is the second element in the chain). New view factor values (reflectivity added to the old value) are applied to the equation (2.54). To satisfy conservation of energy the whole domain is included in a huge environmental box. A view factor between each element and the environmental box is calculated.

As an example the 3 plates (see Figure 2.39) case is chosen. As it can be seen from the figure, view factor calculation does not give any value between face 2 of element 13 (white surface of MAT1) and all faces of the elements from 51 to 75 (upper side of the MAT3). View factor values between the face 1 of the element 13 and faces 2 of the elements from 26 to 50 (lower side of the MAT2) without applying MRV method are presented in Figures 2.40, 2.41 and 2.42. View factors between the face 2 of the element 13 and elements from 51 to 75 are zero.

After first reflection the view factors between the face 2 of the element 13 and faces 2 of the elements from 51 to 75 are presented in 2.43, 2.44 and 2.45. It can be seen that these view factors values are not equal to zero, showing that between face 2 of the element 13 and faces 2 of the elements from 51 to

75 a radiative heat flux is exchanged. This will cause a temperature increase of the faces 2 of the elements from 51 to 75.

Distance	Number of rays	View Factor	Anal. solution	Difference $\delta[\%]$
0.2	100	0.686330	0.690245	-0.567
	1000	0.689433	0.690245	-0.11764
	10000	0.690143	0.690245	-0.0242
0.5	100	0.416246	0.41525	0.2396
	1000	0.414469	0.41525	-0.188
	10000	0.415272	0.41525	0.0053
0.7	100	0.306947	0.304417	0.8311
	1000	0.304947	0.304417	0.174
	10000	0.304215	0.304417	-0.0877
1.0	100	0.199448	0.199825	-0.2
	1000	0.200903	0.199825	0.55
	10000	0.199666	0.199825	-0.08
2.0	100	0.0692471	0.06859	0.96
	1000	0.0691154	0.06859	0.77
	10000	0.0685545	0.06859	0.052
3.0	100	0.0355444	0.032971	7.8
	1000	0.0334736	0.032971	1.5
	10000	0.0330689	0.032971	0.3
4.0	100	0.0235429	0.019107	23.2
	1000	0.0193648	0.019107	1.35
	10000	0.0192793	0.019107	0.9

Table 2.1: View factors compared with analytical solutions for parallel plates (mesh 10x10) using the Monte Carlo method

Distance	Number of rays	View Factor	Anal. solution	Difference $\delta[\%]$
	100	0.690814	0.690245	0.0824
0.2	1000	0.691253	0.690245	0.146035
	10000	0.691041	0.690245	0.11532
	100	0.416382	0.41525	0.272607
0.5	1000	0.416373	0.41525	0.2704
	10000	0.415502	0.41525	0.0607
	100	0.306548	0.304417	0.7
0.7	1000	0.305397	0.304417	0.322
	10000	0.304501	0.304417	0.0276
	100	0.200426	0.199825	0.3
1.0	1000	0.200182	0.199825	0.07
	10000	0.199505	0.199825	-0.3
	10	0.131797	0.06859	92.2
2.0	100	0.0690564	0.06859	0.68
	1000	0.0685673	0.06859	0.033
	10	0.116273	0.032971	252.7
3.0	100	0.04311	0.032971	4.1
	1000	0.0329861	0.032971	0.05
	10	0.110132	0.019107	476.4
4.0	100	0.0222921	0.019107	16.7
	1000	0.0190912	0.019107	0.08

Table 2.2: View factors compared with analytical solutions for parallel plates (mesh 25x25) using the Monte Carlo method

Distance	Number of rays	View Factor	Anal. solution	Difference $\delta[\%]$
	100	0.689182	0.690245	-0.154
0.2	1000	0.685072	0.690245	-0.75
	2000	0.685105	0.690245	-0.775
	100	0.415883	0.41525	0.1524
0.5	1000	0.411744	0.41525	-0.88525
	2000	0.409428	0.41525	-1.4
	100	0.305612	0.304417	0.393
0.7	1000	0.30276	0.304417	-0.544
	2000	0.299985	0.304417	-1.456
	100	0.201058	0.199825	0.69
1.0	1000	0.1999925	0.199825	0.05
	2000	0.198059	0.199825	-0.88
	10	0.136912	0.06859	99.6
2.0	100	0.0697886	0.06859	1.75
	1000	0.068447	0.06859	0.21
	10	0.116968	0.032971	254.8
3.0	100	0.0343382	0.032971	4.15
	1000	0.0330315	0.032971	0.2
	10	0.109278	0.019107	471.9
4.0	100	0.0227706	0.019107	19.2
	1000	0.0191321	0.019107	0.13

Table 2.3: View factors compared with analytical solutions for parallel plates (mesh 40x40) using the Monte Carlo method

Mesh	Number of rays	View factors	Analytical solution	Difference $\delta[\%]$
	10	0.233928	0.20004	16.94
10x10	100	0.200043	0.20004	0.0015
	1000	0.199169	0.20004	-0.44
	10000	0.199578	0.20004	-0.23
	10	0.251972	0.20004	25.96
25x25	100	0.199783	0.20004	-0.13
	1000	0.200235	0.20004	-0.097
	10	0.248415	0.20004	24.2
40x40	100	0.199948	0.20004	-0.05
	1000	0.200432	0.20004	0.2

Table 2.4: Obtained results compared to analytical solution for hinged plates using the Monte Carlo method

Mesh	Number of rays	View factors	Analytical solution	Difference $\delta[\%]$
	10	0.22189	0.14822	49.7
10x10(B)	100	0.151172	0.14822	1.96
10x15(A)	1000	0.148125	0.14822	0.064
	10000	0.148298	0.14822	0.05
	10	0.224951	0.14822	51
25x25(B)	100	0.147558	0.14822	-0.45
25x38(A)	1000	0.148415	0.14822	0.13
	10	0.225143	0.14822	51.9
40x40(B)	100	0.14947	0.14822	0.84
40x60(A)	1000	0.148386	0.14822	0.11

Table 2.5: Obtained results compared to the analytical solution for hinged plates where using the Monte Carlo method

Mesh	Number of rays	View factors	Analytical solution	Difference $\delta[\%]$
10x10(B) 10x15(A)	10	0.21081	0.11643	81
	100	0.120712	0.11643	3.68
	1000	0.116432	0.11643	0.0017
	10000	0.116272	0.11643	-0.136
25x25(B) 25x38(A)	10	0.213945	0.11643	83.75
	100	0.119419	0.11643	2.57
	1000	0.116685	0.11643	0.219
40x40(B) 40x60(A)	10	0.215917	0.11643	85.5
	100	0.120959	0.11643	3.89
	1000	0.116602	0.11643	0.147

Table 2.6: Obtained results compared to the analytical solution

Angle(ϕ)[^{o}]	View factors	Analytical solution	Difference δ[%]
30	0.6173125	0.619028	-0.2764
45	0.4825125	0.483347	-0.17295
60	0.3730625	0.370905	0.57832
90	0.2025375	0.200043776	1.23124
120	0.08765	0.086615	1.1808
135	0.0484	0.04831	0.18595
150	0.021325	0.021346	-0.098476

Table 2.7: Results obtained by the Monte Carlo method and analytical solutions for hinged plates (A=B=1) divided into 4 elements each, including different angles between them

Angle(ϕ)[^{o}]	View factors	Analytical solution	Difference δ[%]
30	0.6999	0.700100	-0.0285803
45	0.555712	0.556138	-0.0076571
60	0.431225	0.429971	0.29079
90	0.2347	0.232853	0.7934
120	0.101313	0.100808	0.497965
135	0.0563625	0.056206	0.277672
150	0.0244375	0.024826	-1.58977

Table 2.8: Results obtained by the Monte Carlo method and analytical solution for hinged plates (A=2, B=1) divided into 8 and 4 elements each, including different angles between them

Angle(ϕ)[^{o}]	View factors	Analytical solution	Difference δ[%]
30	0.709275	0.709846	-0.0805065
45	0.569937	0.570557	-0.108702
60	0.447137	0.445869	0.283688
90	0.246837	0.245223	0.658176
120	0.107413	0.107099	0.291871
135	0.0602625	0.059871	0.649661
150	0.026125	0.026492	-1.40479

Table 2.9: Results obtained by the Monte Carlo method and analytical solutions for hinged plates (A=4, B=1) divided into 16 and 4 elements each, including different angles between them

Angle(ϕ)[^{o}]	View factors
0	0.196525
30	0.135412
45	0.108213
60	0.0816
90	0.0336375
120	0.0035875
135	0.0

Table 2.10: Results obtained by the Monte Carlo method for hinged plates including different angles between them and separation distance in $-y$ direction

Angle(ϕ)[^{o}]	View factors
0	0.0
30	0.0818625
45	0.0719
60	0.0573875
90	0.0314625
120	0.0134625
135	0.007675
150	0.0031875

Table 2.11: Results obtained by Monte Carlo method for hinged plates including different angles between them and separation distance in z direction

Mesh	Distance	Number of rays	Difference $\delta[\%]$
	1	10	11.9
10x10	1	100	-1.41
	1	1000	0.706
	1	10000	-0.04
	1	10	9.7
25x25	1	100	-0.6
	1	100	0.2
	1	10000	-0.23
	1	10	12.98
40x40	1	100	0.49
	1	1000	0.135

Table 2.12: Parallel plates with distance ratio C/A=1 for a centre as an origin using the Monte Carlo method

Mesh	Number of rays	Difference $\delta[\%]$
	10	23.4
10x10	100	1.53
	1000	-1
	10000	0.1
	10	-1.1
25x25	100	-0.128
	100	0.094
	10	23.4
40x40	100	-0.56
	1000	0.097

Table 2.13: Hinged plates for the geometry a=b=c=1 for a centre as an origin using the Monte Carlo method

Mesh	C/A	Number of rays	View factors	Anal. solution	Diff. $\delta[\%]$
10x10	2	100	0.07	0.06859	2.06
	2	1000	0.0655	0.06859	-4.505
	2	10000	0.0702	0.06859	2.35
	2	30000	0.0.0694	0.06859	1.18
25x25	5	100	0.015	0.012404	20.93
	5	1000	0.0135	0.012404	8.84
	5	10000	0.01195	0.012404	-3.66
	5	30000	0.0129667	0.012404	4.54
40x40	8	100	no res.	0.00492246	no res.
	8	1000	0.005	0.00492246	1.575
	8	10000	0.0046	0.00492246	-6.55
	8	30000	0.0053	0.00492246	7.67

Table 2.14: Obtained view factor values for each element compared to analytical solution

Mesh	Number of reys/element	Total number of rays	CPU [s]
10x10	10	2000	0.618
	100	20000	5.198
	1000	200000	50.6
	10000	2000000	506.79
25x25	10	12500	3.806
	100	125000	36.57
	1000	1250000	363.643
40x40	10	32000	11.38
	100	320000	110
	1000	3200000	1114.162

Table 2.15: CPU time using the Monte Carlo method

Number of divisions (N)	View factors	Abs[Difference] $\delta[\%]$
20	0.201066	0.5
40	0.201409	0.68
80	0.201736	0.85
100	0.203064	0.1.5

Table 2.16: Results obtained for hinged plates divided by mesh 10x10 using the Hemi-cube method

Number of divisions (N)	View factors	Abs[Difference] δ[%]
4	0.208786	4.3
10	0.200503	0.2
20	0.199457	0.0.29
40	0.199253	0.39
50	0.202031	0.995

Table 2.17: Results obtained for hinged plates divided by mesh 25x25 using the Hemi-cube method

Number of divisions (N)	View factors	Abs[Difference] δ[%]
1/1	0.2770983	38.51884
1/2	0.2638335	13.30494
1/4	0.2455187	0.1205045
1/6	0.2460569	0.7152548
1/8	0.2447192	1.628074
1/10	0.23986	3.751667

Table 2.18: Results obtained for hinged plates divided by mesh 40x40 using the Hemi-cube method

Distance	View factors	Abs[Difference] $\delta[\%]$
0.1	0.8270047	0.00123
0.15	0.7549195	0.00123
0.2	0.6902522	0.0011
0.3	0.579536	0.00091
0.5	0.4152533	0.000746
1.0	0.1998249	0.000462
1.5	0.1107067	0.000249
2.0	0.0685896	0.000076
2.5	0.0461373	0.00008
3.0	0.0329714	0.000135
3.5	0.0246613	0.00107
4.0	0.0191069	0.001628
4.5	0.0152222	0.00102
5.0	0.0124039	0.001
5.5	0.010297	0.00237
6.0	0.008682	0.0027997
6.5	0.007417	0.003747
7.0	0.006409	0.00284

Table 2.19: Results obtained for parallel plates using the Line integration method

L/N	View factors	Abs[Difference] δ[%]
1/1	0.2000196	0.012067
1/2	0.2328287	0.00123
1/4	0.2451993	0.00977
1/6	0.2478055	0.00965
1/8	0.2487454	0.00964
1/10	0.2491856	0.0096

Table 2.20: Results obtained for hinged plates using the Line integration method

Distance	View factors	Abs[Difference] δ[%]
0.1	1.777738	114.9637
0.15	1.006442	33.31946
0.2	0.7672804	11.16065
0.3	0.5883358	1.519339
0.5	0.4154198	0.040119
1.0	0.1998247	0.000059
1.5	0.1107066	0.0001144
2.0	0.0685895	0.00013035
2.5	0.0461374	0.0000565
3.0	0.0329714	0.000135
3.5	0.0246613	0.00107
4.0	0.0191069	0.001628
4.5	0.0152222	0.00102
5.0	0.0124039	0.001
5.5	0.010297	0.00237
6.0	0.008682	0.0027997
6.5	0.007417	0.003747
7.0	0.006409	0.00284

Table 2.21: Results obtained for parallel plates using the Area integration method

L/N	View factors	Abs[Difference] δ[%]
1/1	0.2770983	38.51884
1/2	0.2638335	13.30494
1/4	0.2455187	0.1205045
1/6	0.2460569	0.7152548
1/8	0.2447192	1.628074
1/10	0.23986	3.751667

Table 2.22: Results obtained for hinged plates using the Area integration method

Distance	View factors	Abs[Difference] δ[%]
0.1	1.50511	81.99754
0.15	0.9280703	22.93786
0.2	0.75235587	8.998847
0.3	0.6006986	3.652589
0.5	0.4244551	2.215969
1.0	0.20022752	1.226262
1.5	0.1115543	0.765561
2.0	0.06893769	0.5074656
2.5	0.04630118	0.3550451
3.0	0.0329714	0.000135
3.5	0.0247099	0.1971687
4.0	0.0191364	0.1544556
4.5	0.01524108	0.12356
5.0	0.0124165	0.10233
5.5	0.0103057	0.084648
6.0	0.008688	0.0713028
6.5	0.00742197	0.0606947
7.0	0.0064126	0.05167862

Table 2.23: Results obtained for parallel plates using the Mitalas-Stephenson method

L/N	View factors	Abs[Difference] $\delta[\%]$
1/1	0.2265479	13.24917
1/2	0.2405327	3.298275
1/4	0.2258306	7.908157
1/6	0.2016398	18.63768
1/8	0.1739476	30.07678
1/10	0.1471824	40.94029

Table 2.24: Results obtained for hinged plates using Mitalas-Stephenson method

Number of rays per element	View factors	Diff. (individual)$\delta[\%]$	Diff. (whole plate)$\delta[\%]$
100	0.126971	85.12	2.5
1000	0.059218	-13.663	0.887
10000	0.0688777	0.42	0.241

Table 2.25: Obtained results compared to the analytical solution for individual element and whole plate using the Hemi-cube method
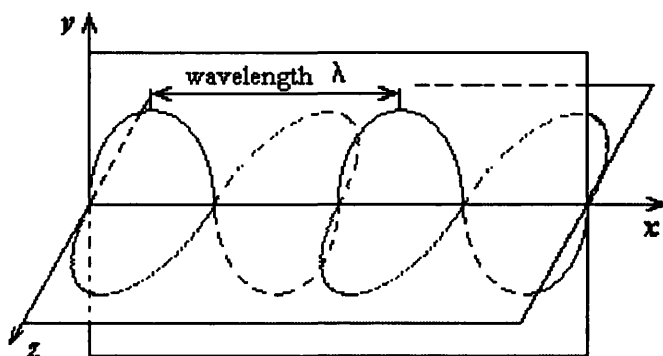
Figure 2.1: Electromagnetic oscillations
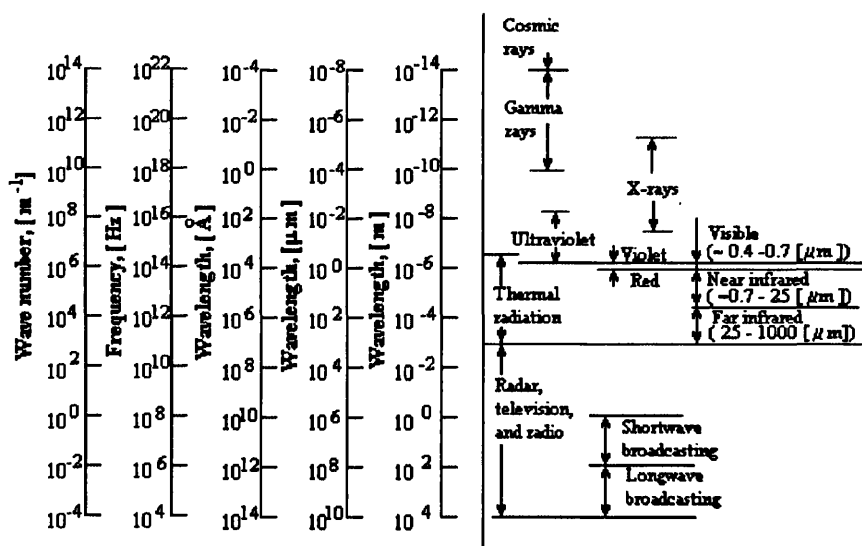
Figure 2.2: Electromagnetic spectrum
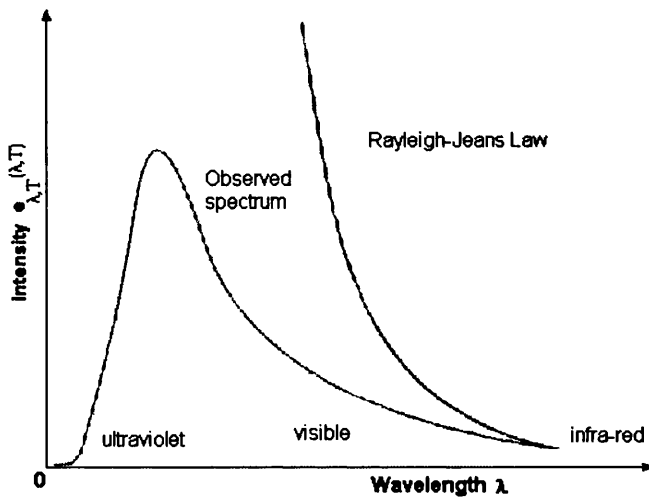
Figure 2.3: Rayleigh-Jeans Law and Experimental Data
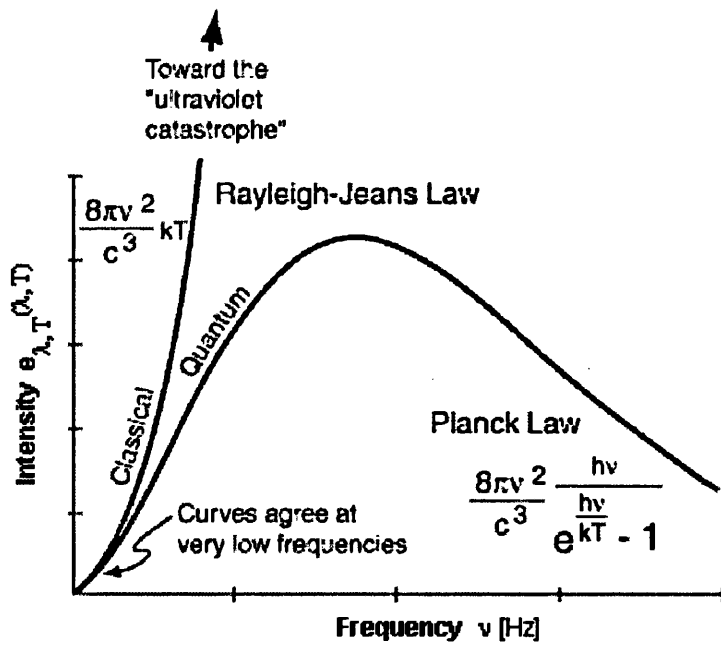
Figure 2.4: Comparison between Plank's Law and Rayleigh-Jeans Law
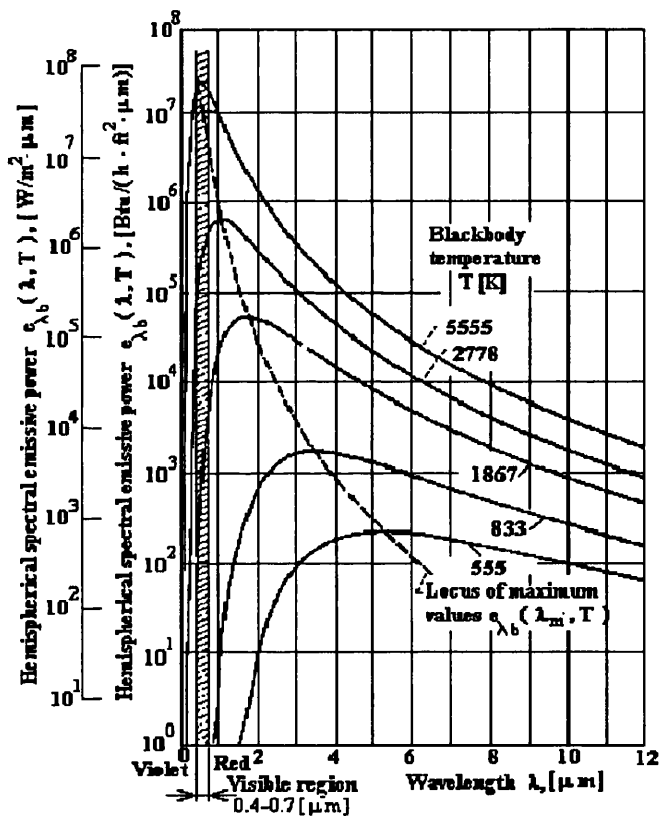
Figure 2.5: Hemispherical spectral emissive power of a blackbody
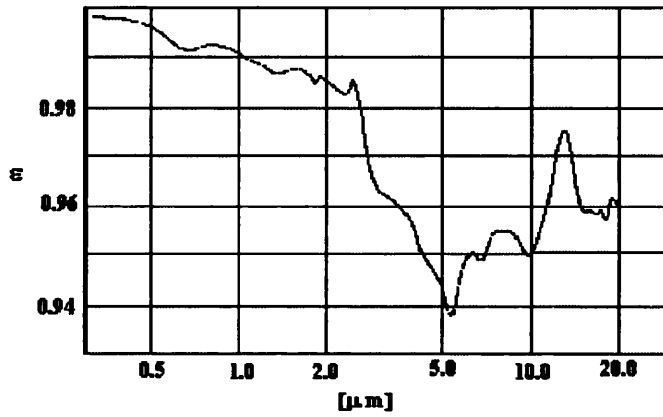
Figure 2.6: Emissivity as a function of wavelength
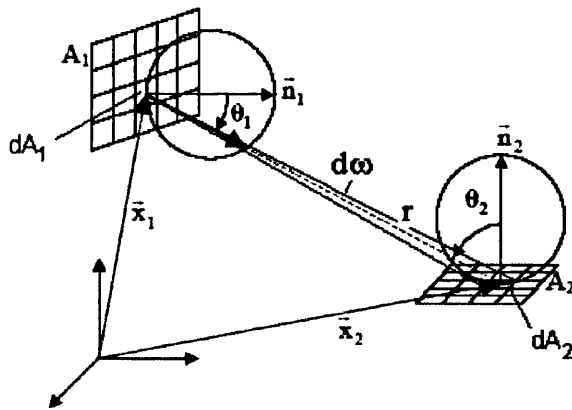
Figure 2.7: Radiant interchange between finite areas
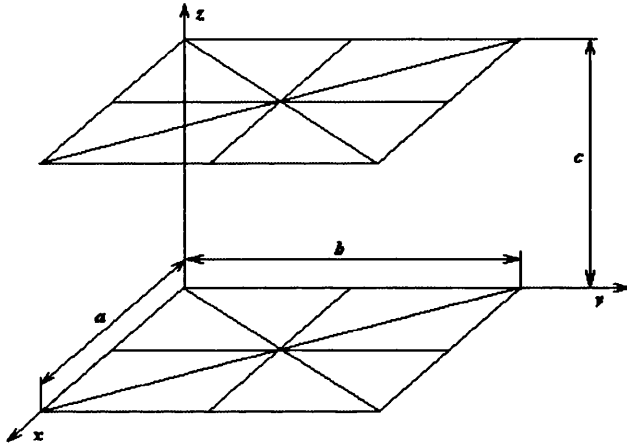
Figure 2.8: Two parallel plates
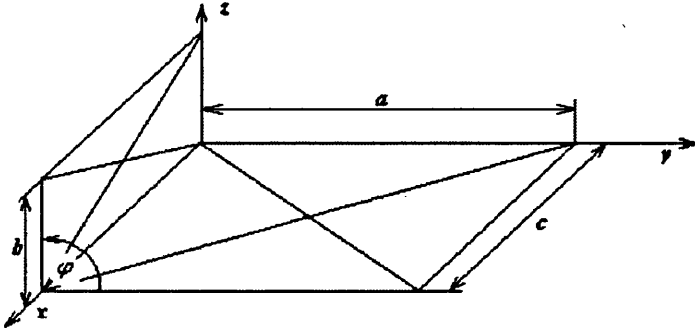
Figure 2.9: Hinged plates
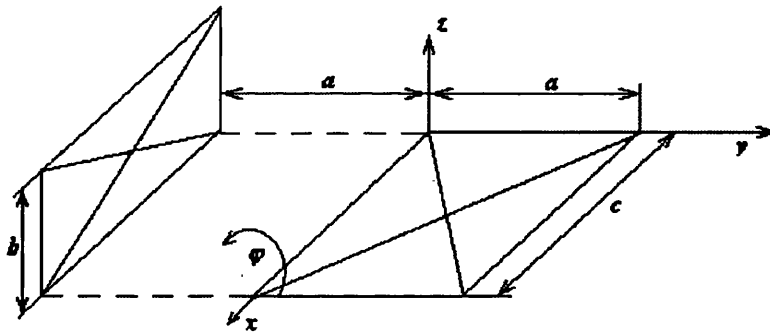
Figure 2.10: Hinged plates including distance (a)
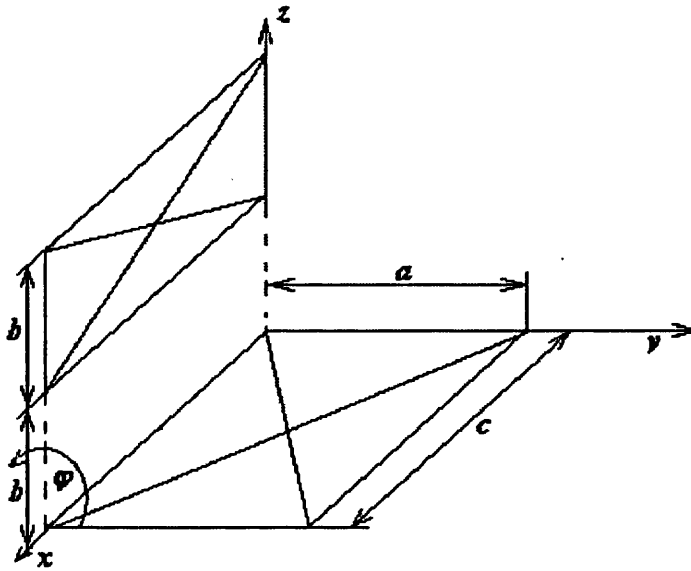
Figure 2.11: Hinged plates including distance (b)
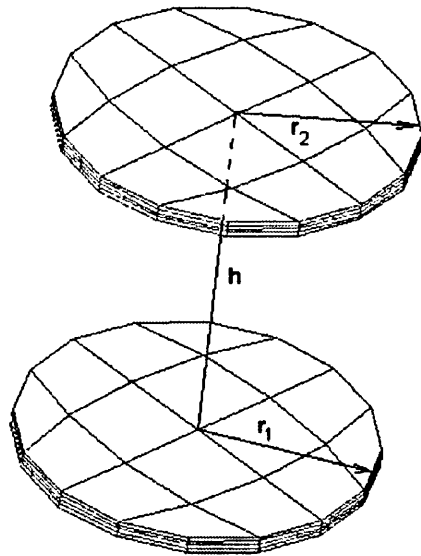
Figure 2.12: Two parallel discs along same normal
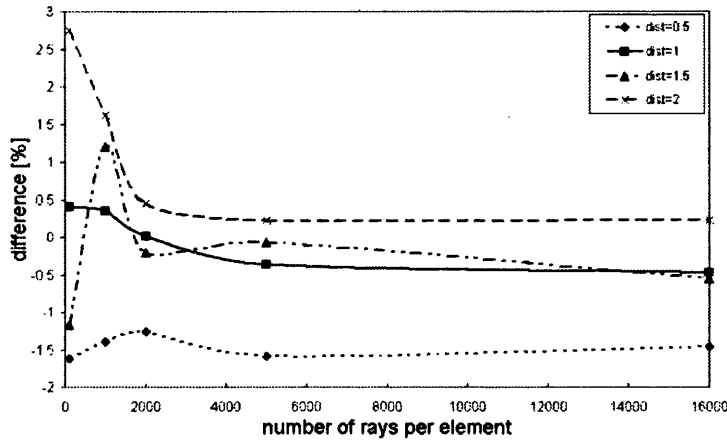
Figure 2.13: Mesh 4x10, difference between model and analytical solution for two parallel discs using the Monte Carlo method
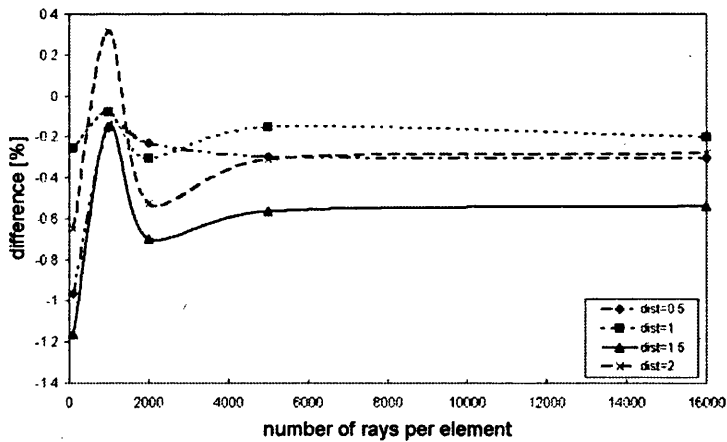
Figure 2.14: Mesh 4x20, difference between model and analytical solution for two parallel discs using the Monte Carlo method
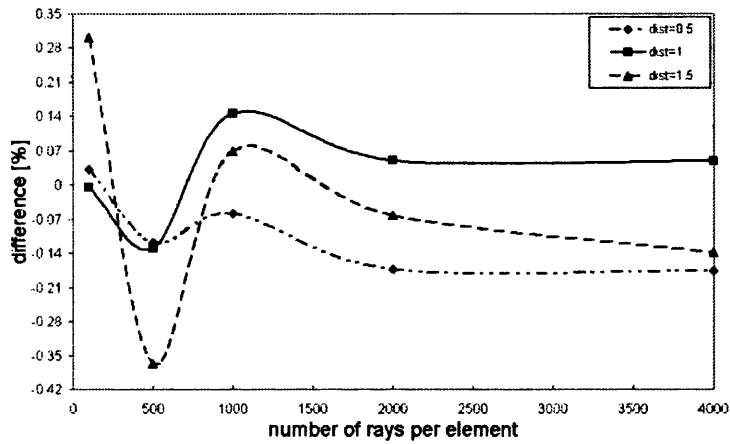
Figure 2.15: Mesh 4x40, difference between model and analytical solution for two parallel discs using the Monte Carlo method
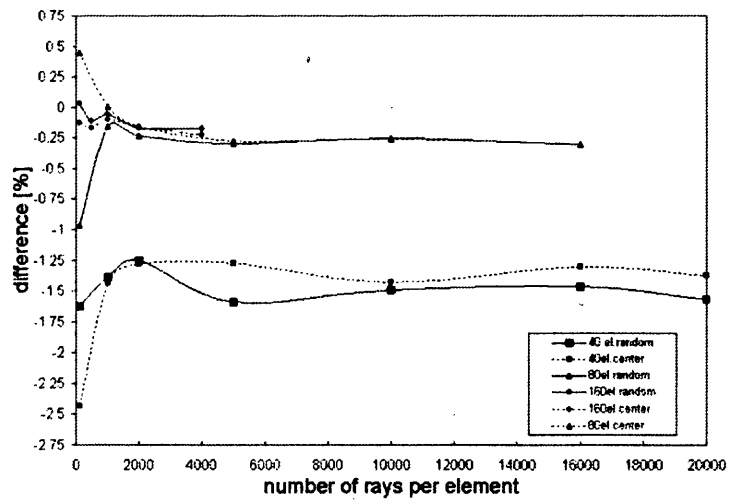
Figure 2.16: A comparison between a random point and a centre of the triangle as an origin for parallel discs
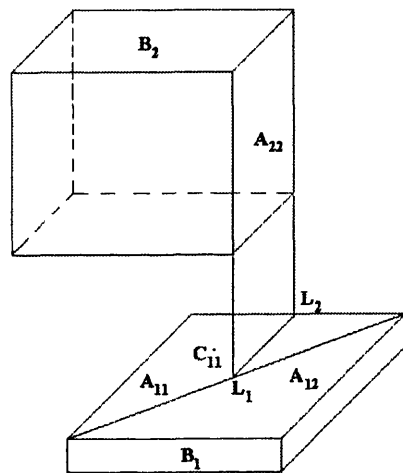
Figure 2.17: A special case with partial shadowing
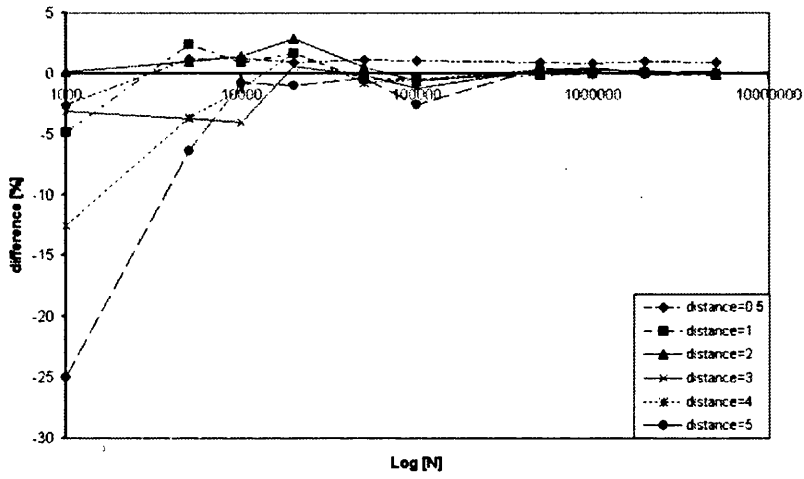
Figure 2.18: The difference between numerical and analytical solution for parallel plates divided into 2 triangles using the Monte Carlo method
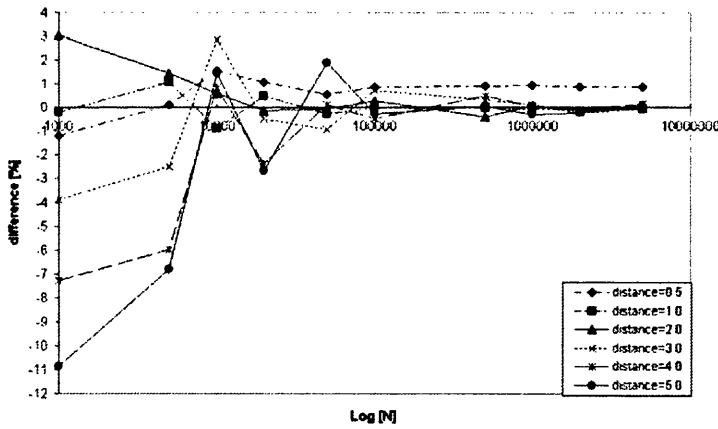
Figure 2.19: The difference between numerical and analytical solution for parallel plates divided into 4 triangles using the Monte Carlo method
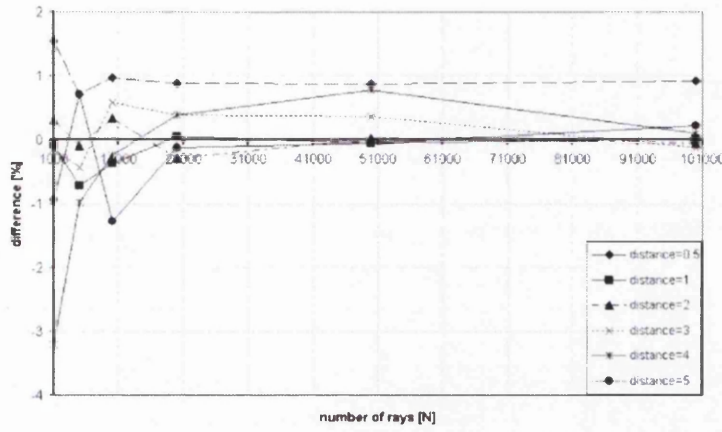
Figure 2.20: The difference between numerical and analytical solution for parallel plates divided into 50 triangles using the Monte Carlo method
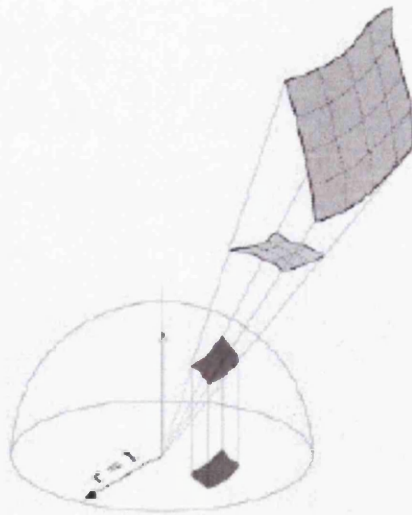
Figure 2.21: Nusselt analogy - hemisphere
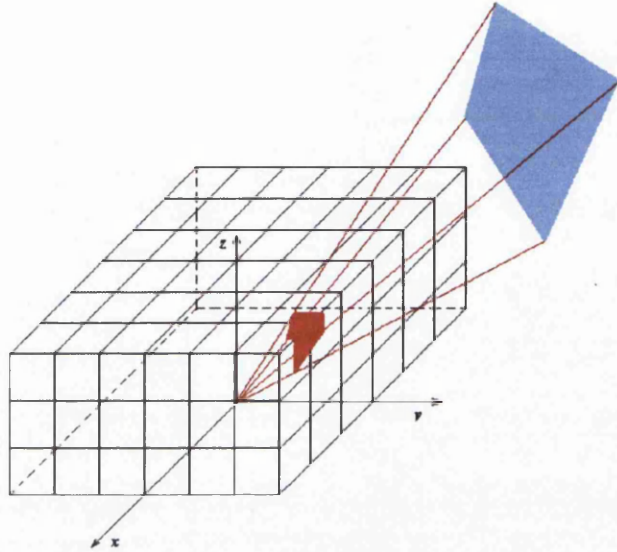
Figure 2.22: Hemi-cube
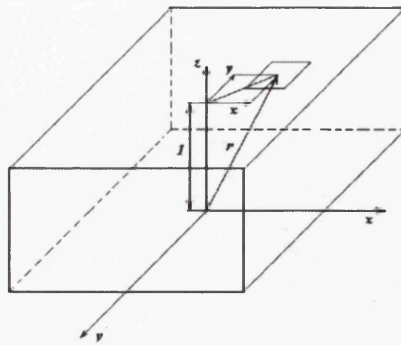
Figure 2.23: Top of hemi-cube
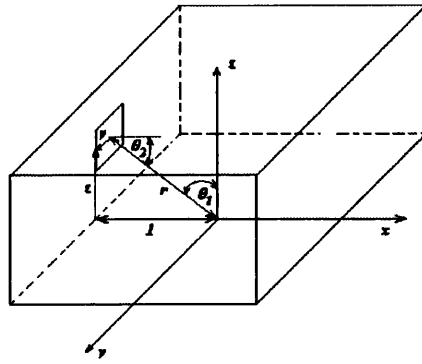
Figure 2.24: Side of hemi-cube
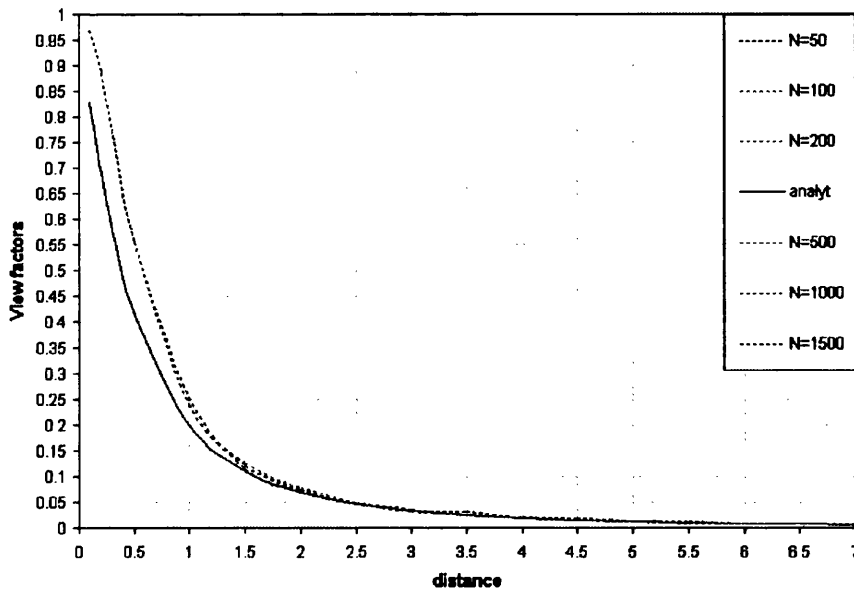
Figure 2.25: View factors for parallel plates using the Hemi-cube method (whole plate which is one element covered by one hemi-cube)
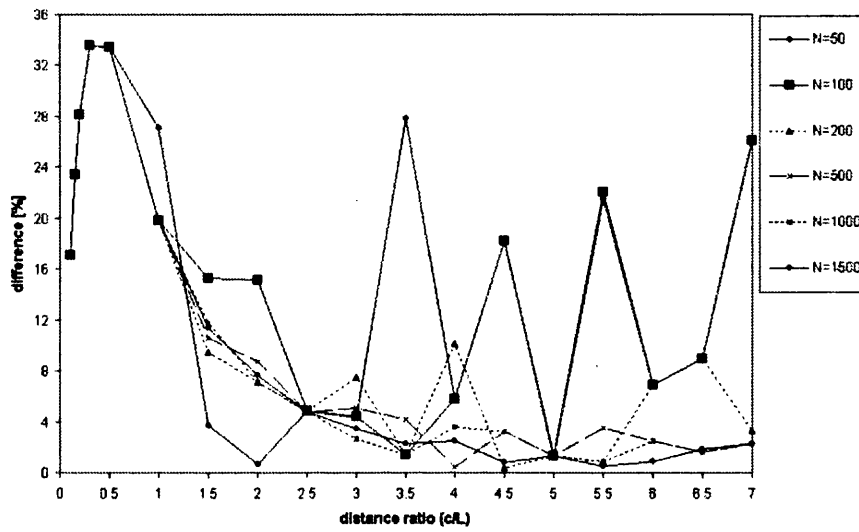
Figure 2.26: Difference between numerical and analytical solutions using the Hemi-cube method (whole plate is one element covered by one hemi-cube)
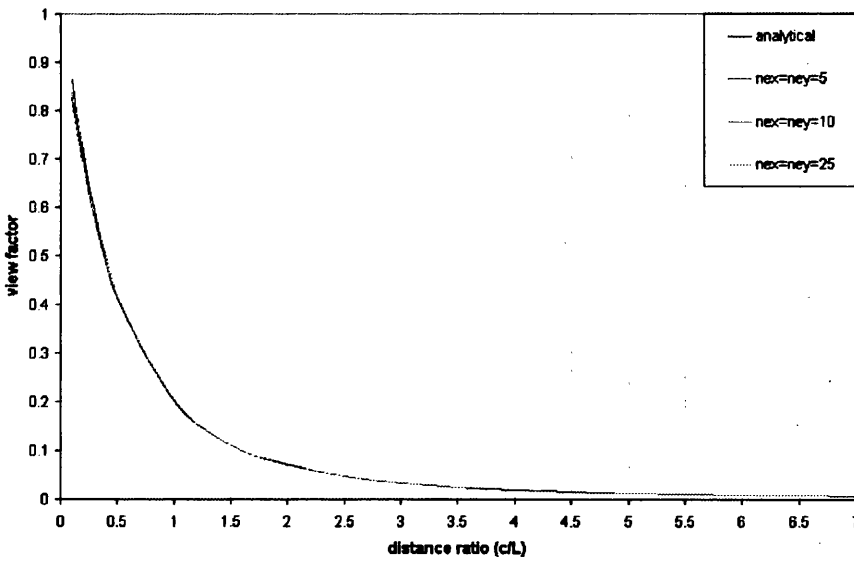
Figure 2.27: View factor for parallel plates using the Hemi-cube method (divided plates by three meshes)
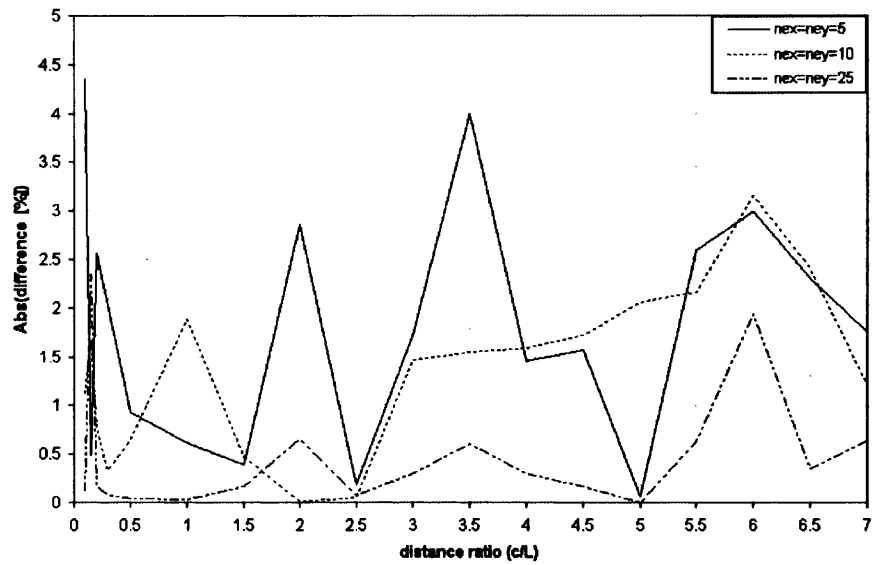
Figure 2.28: Difference between numerical and analytical solutions using the Hemi-cube method (divided plates by three meshes)
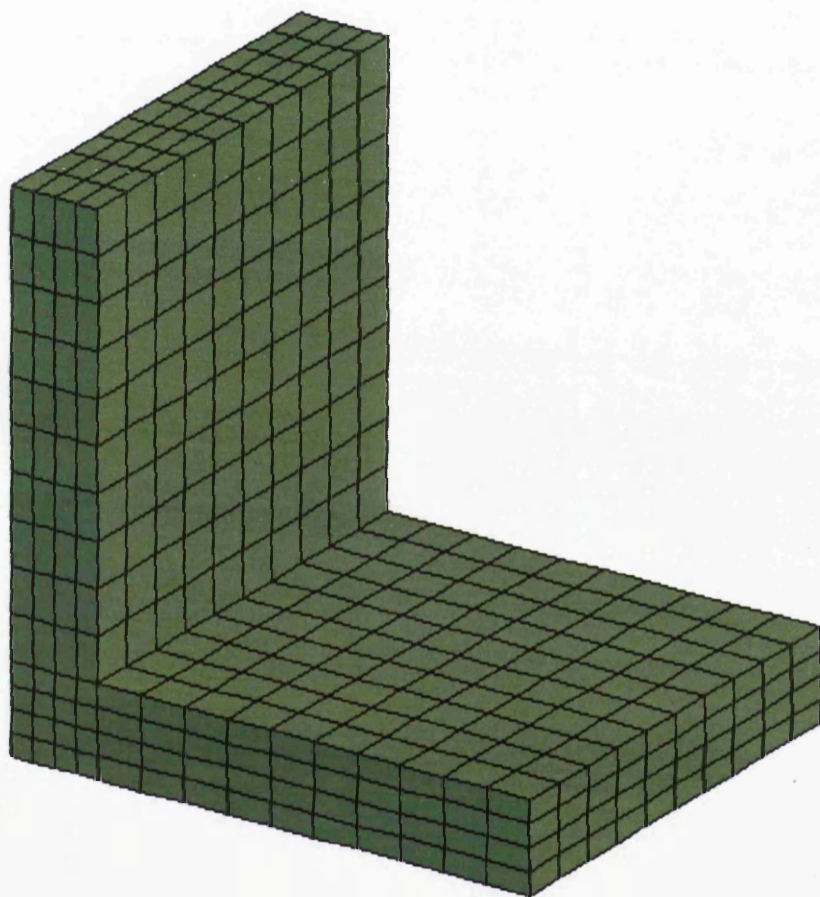
Figure 2.29: Hinged plates divided by mesh 10x10x4
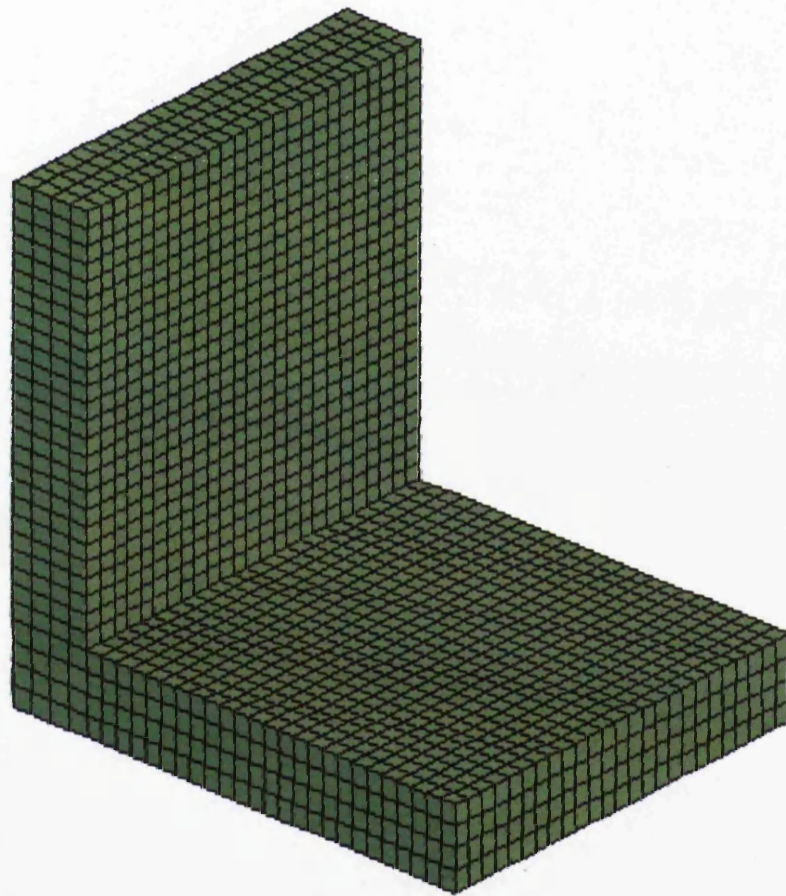
Figure 2.30: Hinged plates divided by mesh 25x25x4
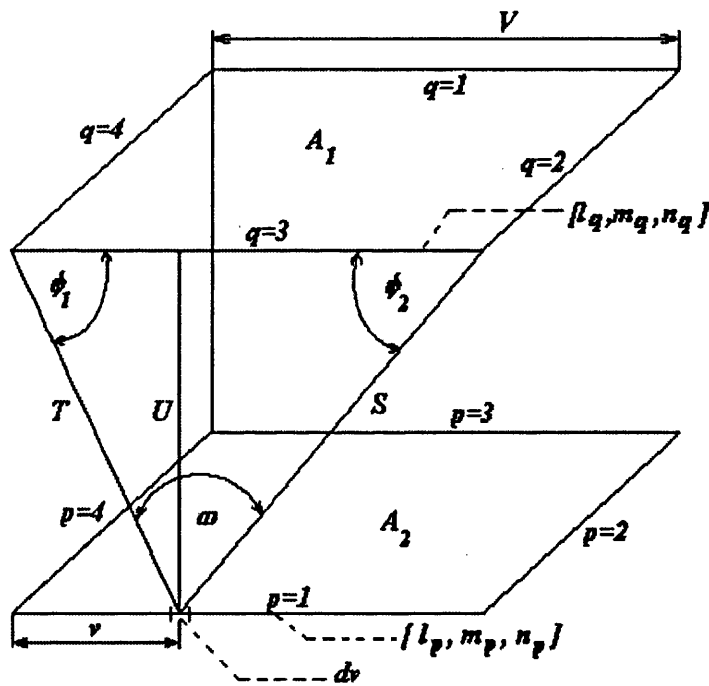
Figure 2.31: Symbols used in contour integration
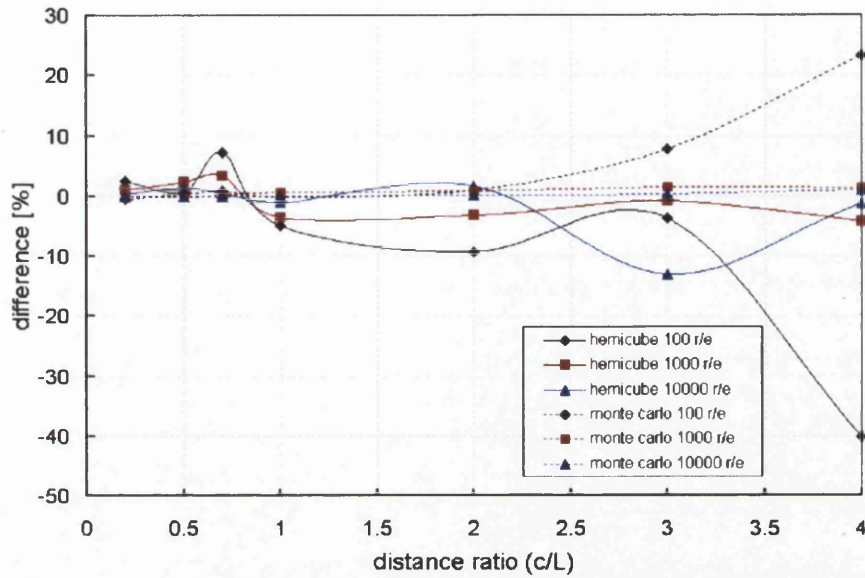
Figure 2.32: Comparison between the Monte Carlo and the Hemi-cube methods (two parallel plates divided by mesh 10x10)
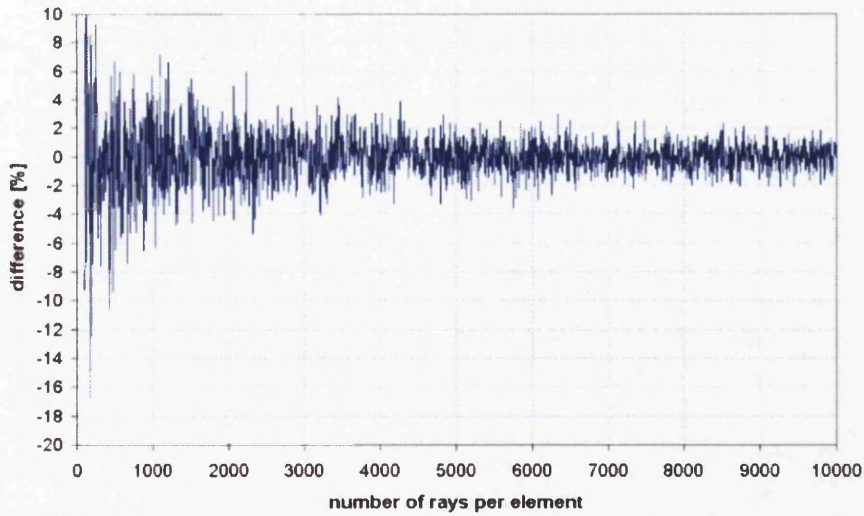
Figure 2.33: Difference between model and analytical solution for two parallel elements with the distance ratio $c/L = 0.5$ between them using the Monte Carlo method
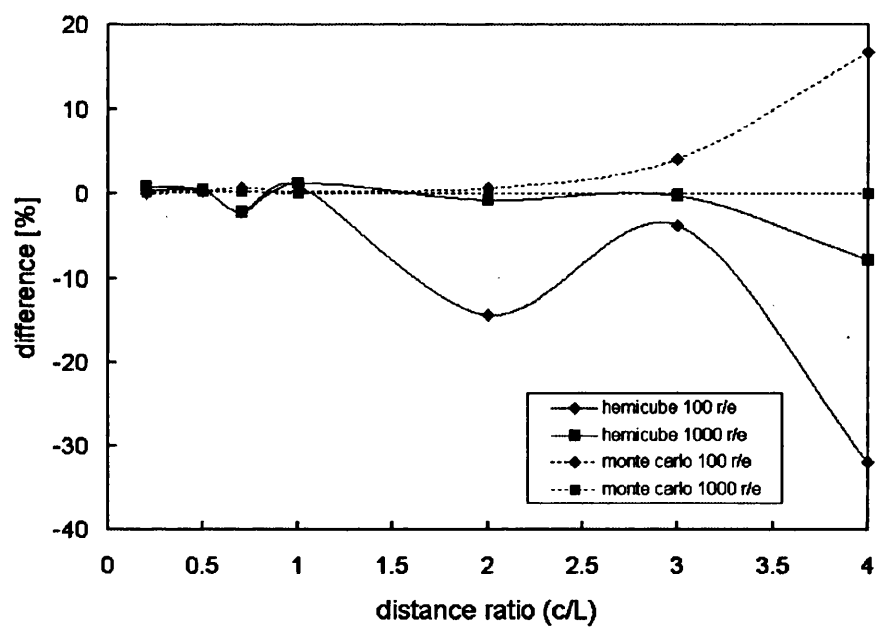
Figure 2.34: Comparison between the Monte Carlo and the Hemi-cube methods for two parallel plates divided by mesh 25x25
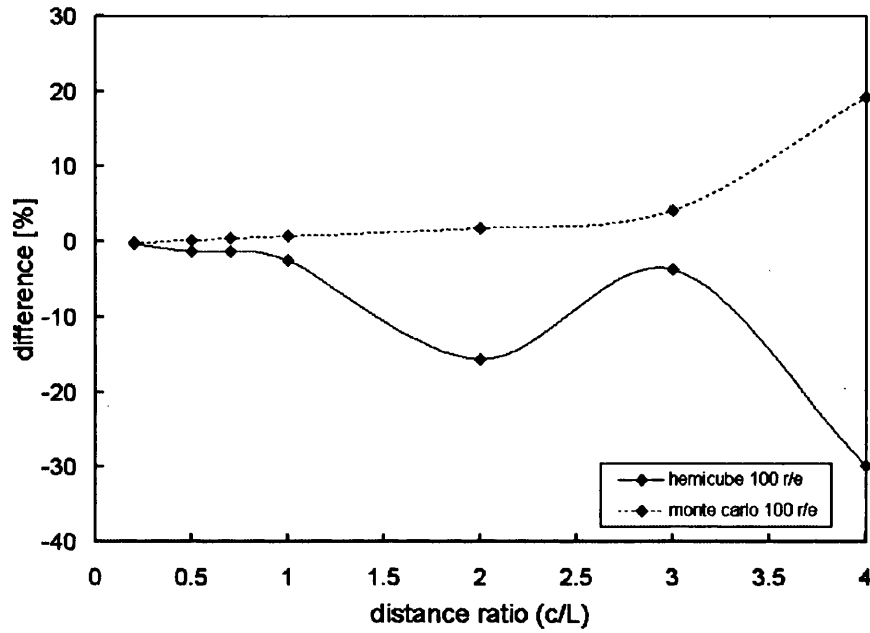
Figure 2.35: Comparison between the Monte Carlo and the Hemi-cube methods for two parallel plates divided by mesh 40x40
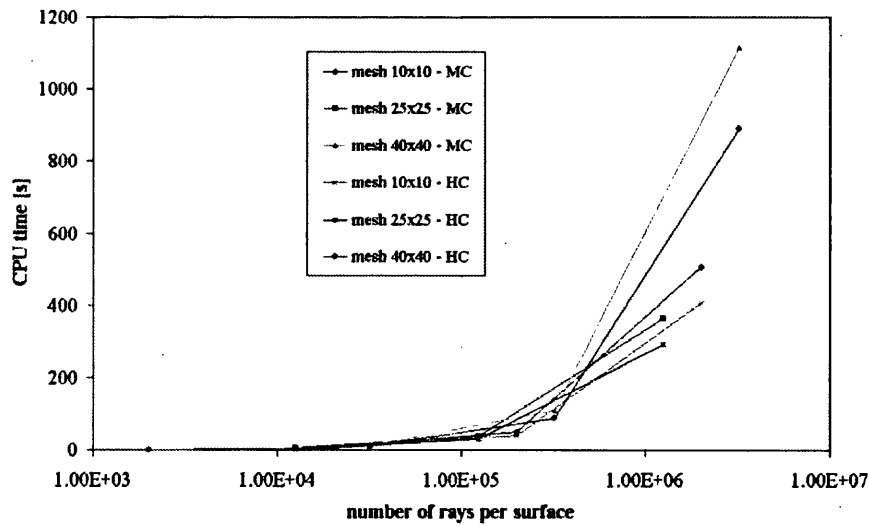
Figure 2.36: CPU performance of the Hemi-cube and the Monte Carlo methods
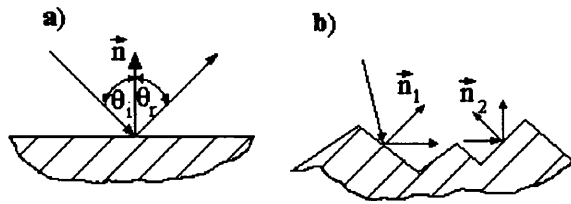
Figure 2.37: A receiving element with a) a smooth specular surface b) a rough diffuse surface
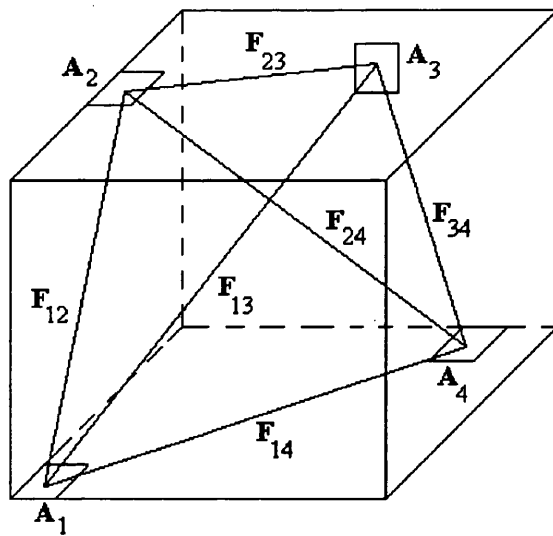
Figure 2.38: A general 3D enclosure

CHAPTER 2. VIEW FACTOR CALCULATION
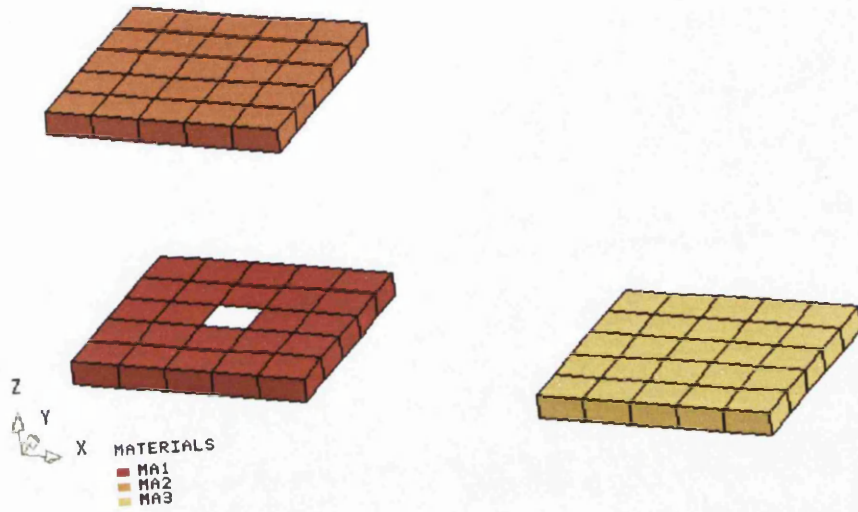
Figure 2.39: 3 plates case
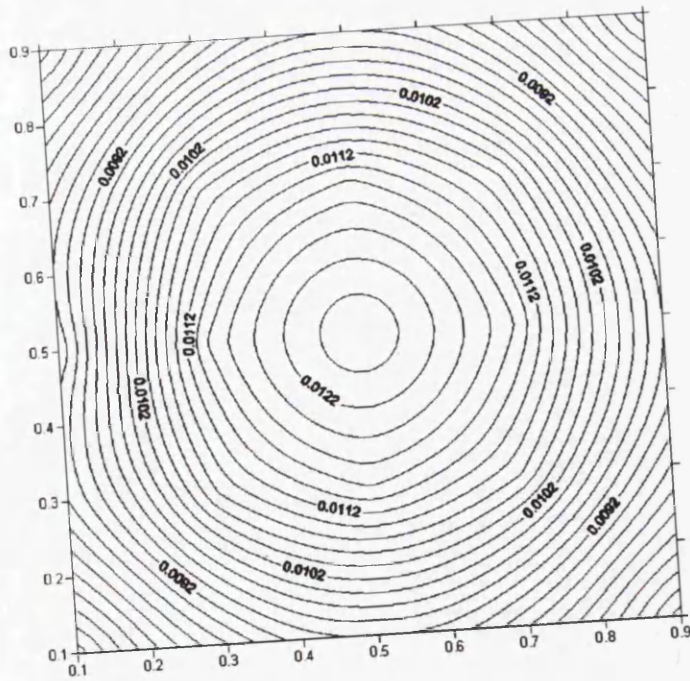
Figure 2.40: Contours of view factors values between face 2 of the element 13 and faces 1 of the elements from 26 to 50
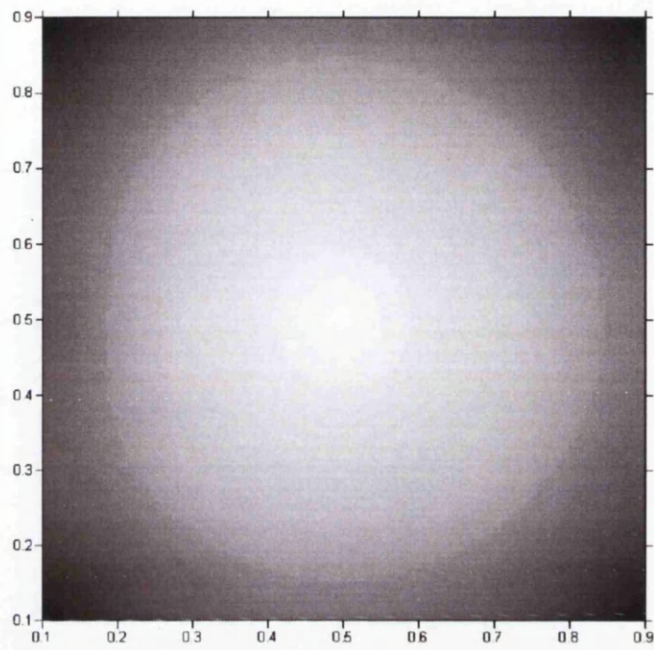
Figure 2.41: Images of view factors values between face 2 of the element 13 and faces 1 of the elements from 26 to 50
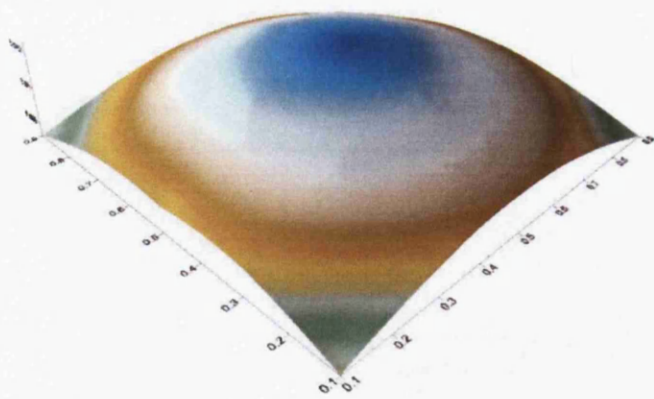
Figure 2.42: Surface of view factors values between face 2 of the element 13 and faces 1 of the elements from 26 to 50
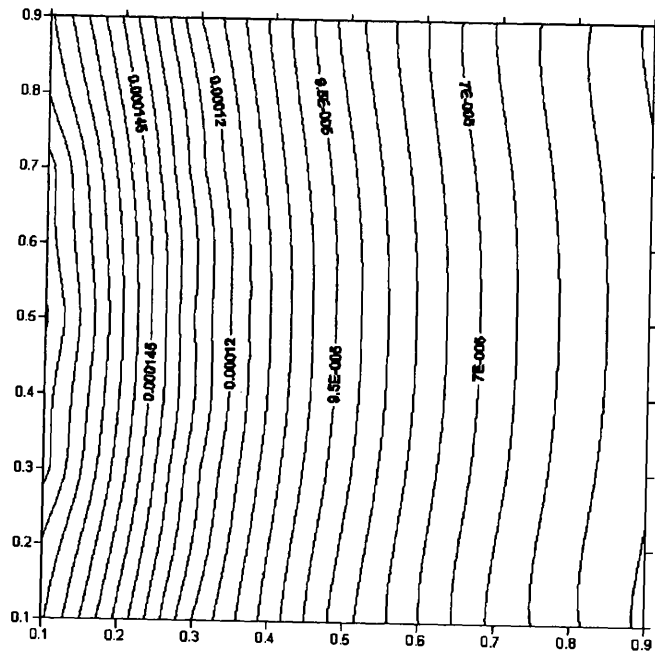
Figure 2.43: Contours of view factors values between face 2 of the element 13 and faces 1 of the elements from 51 to 75
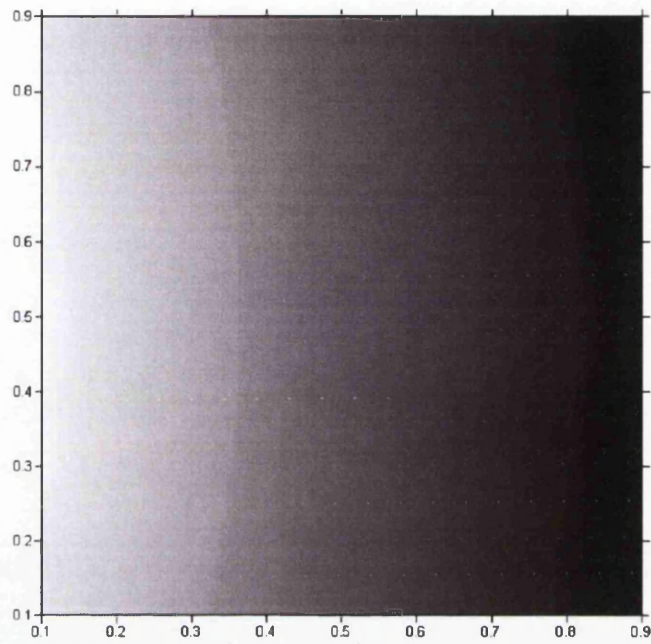
Figure 2.44: Images of view factors values between face 2 of the element 13 and faces 1 of the elements from 51 to 75
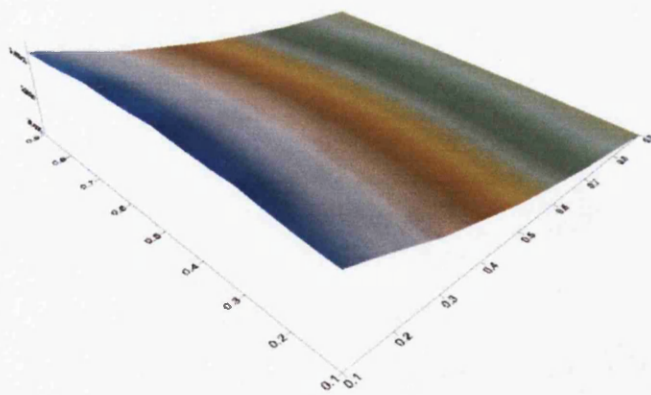
Figure 2.45: Surface of view factors values between face 2 of the element 13 and faces 1 of the elements from 51 to 75

Chapter 3

Experimental Data

The development of commercial high-speed civil, space transportation and as well as military air-force requires highly sophisticated design tools. These aircraft will experience higher in-flight temperatures due to the increased rate of aerodynamic heating associated with high-speed flight. Therefore, the goal of technological development in this area is to provide the next generation of design tools to increase design confidence, and thereby reduce the development cycle time for aircraft. For all these reasons, the consideration of radiative heat transfer, in addition to conduction and convection, becomes very important.

In the previous chapter it was noted that radiative heat transfer prediction including view factor calculation plays a central role in **Pharo**. Also in Chapter 2, the view (geometrical) factor calculation including the Monte Carlo method, the Hemi-cube method and Integration methods was explained. Several test cases, such as the well known parallel plates, hinged plates and parallel circular discs along the same normal cases for known analytical solutions, were chosen to validate view factor routines. Later, view factor values will be used in heat transfer simulations (Chapter 6) where the temperature field of the enclosure was obtained as a final result.

In the Introduction (Chapter 1) several commercial codes which include radiative heat transfer were mentioned. All these codes should pass a process of validation or a comparison with existing experimental data. However, until now there has been little research conducted which combines both view factor information and heat transfer effects simultaneously. There are many reasons why resources of this experimental work are very poor. One of these is its complexity. Knowing that radiative heat transfer has been always combined with convection and conduction during experiments it is very difficult to analyze it separately. Thermal conduction will take a place even if experiments are run in a vacuum. A second reason is that radiative heat transfer

depends on many different factors, such as surface properties (emissivity, reflectivity, roughness etc.). The determination of surface properties of samples used in experiments is a very difficult process and there are few places in the UK where it can be conducted.

Also, experimental rigs used in academia, which already exist on market, are very simple with very poor measurement of temperatures of the participating plates (a single thermocouple per each plate is used very often). Additionally, many rigs have used a light bulb as a source of heat. This was the main reason for us to build a simple experimental rig, but more sophisticated than all these on market, which allowed experiments to be performed that combine view factor effects with measured heat transfer. The results of these experiments given in this chapter are presented as experimental benchmark data for model users and developers.

The rig (see Figure 3.1) was built at the University of Wales, Swansea, according to an original design. It consists of a track (which is contained within a heat resistant low reflectivity painted box), which can hold both an emitter and a receiver of various shapes, sizes and constitutive materials. The experimental analysis includes three emitters: a black painted cylinder (made of brass) with dimension of $\phi 28 \times 197[mm]$, a disc (made of steel) with diameter of $D = 182[mm]$ and a square shaped emitter (made of steel) with dimension of $197 \times 197[mm]$. The receiver has a dimension of $197 \times 197[mm]$ and is composed of steel, brass and aluminium, with thickness ranging from 3 to 15 $[mm]$.

Also, the receivers and emitters can rotate and build an angle from 0 to $360[°]$ between them. The distance between an emitter and a receiver increases from 0 to 4 (dimensionless c/D).

Temperatures of an emitter and a receiver were measured using thermocouples in combination with infra-red thermal imaging camera (**Thermo Tracer TH7102**).

Before any presentation of the experimental results it is necessary to first give some theoretical explanation about emissivity, absorptivity and reflectivity.

3.1 Emissivity, Absorptivity and Reflectivity

3.1.1 Emissivity

As discussed in Section 2.1, emissivity specifies how well a real (grey) body emits energy as compared with a blackbody. Emissivity is often measured experimentally in a direction normal to the surface as a function of wave-

length (Figure 3.2). If an experiment is set up for unit wavelength interval $d\lambda$, the results obtained present directional spectral emissivity $\varepsilon_\lambda(\lambda, \theta\varphi, T_A)$.

Directional spectral emissivity can be calculated by following equation:

$$\varepsilon_\lambda(\lambda, \theta, \varphi, T_A) = \frac{i_\lambda(\lambda, \theta, \varphi, T_A)}{i_{\lambda b}(\lambda, T_A)} \qquad (3.1)$$

Spectral emissivity over the thermal infrared ($3\,[\mu m] - 60\,[\mu m]$) is a key property in determining energy transfer. For military applications emissivity may be as important as temperature in creating the 'signature' of a target for passive infrared systems, while for infrared LIDAR for example, reflectance at the chosen laser wavelength is the key property.

Integrating directional spectral emissivity for all wavelength gives *directional total* emissivity, which is described as:

$$\varepsilon(\theta\varphi, T_A) = \frac{\pi \int_0^\infty \varepsilon_\lambda(\lambda, \theta, \varphi, T_A) \cdot i_{\lambda b}(\lambda, T_A)d\lambda}{\sigma \cdot T_A^4} \qquad (3.2)$$

The spectral radiation emitted by unit surface area into all directions of the hemisphere is called *hemispherical spectral* emissivity and calculated as:

$$\varepsilon_\lambda(\lambda, T_A) = \frac{e_\lambda(\lambda, T_A)}{e_{\lambda b}(\lambda, T_A)} = \frac{1}{\pi} \int_{\varphi=0}^{2\pi} \int_{\theta=0}^{\pi/2} \varepsilon_\lambda(\lambda, \theta, \varphi, T_A) \cos\theta \sin\theta d\theta d\varphi \quad (3.3)$$

Integration over all λ and all directions gives the hemispherical total emissivity as:

$$\varepsilon(T_A) = \frac{\pi \int_0^\infty \varepsilon_\lambda(\lambda, T_A) e_{\lambda b}(\lambda, T_A)d\lambda}{\sigma \cdot T_A^4} \qquad (3.4)$$

All radiation thermometers (RTs), commonly called pyrometers, contain one or more sensors that convert thermal radiation received through some type of optics into an electrical signal. Often, the RT contains one or more optical filters that allow only a selected wavelength (within a narrow band) to reach the sensor. These RTs are calibrated by aiming them at a blackbody and noting the sensors electrical signal output as a function of blackbody temperature. For correct temperature measurement a proper emissivity value has to be defined. This is not always easy. In the text below a partial list of potential problems is given:

1. The actual emitting surface! Often, even very thin coatings on the surface can affect the emissivity value of the surface and (depending on the coating thickness) the correct emissivity value may be that of the coating, not the main substrate.

2. Regardless of what the emitting surface is composed of, the micro-scopic (and macroscopic) roughness of the surface causes differences in emissivity simply because a rougher surface has a larger emitting area. Generally, emissivity of the most opaque emitting surfaces increases as wavelength becomes shorter.

3. The geometric shape of a surface affects the required emissivity set-ting. Convex surfaces, such as cylinder or balls have emissivity values that drop with increased curvature simply because they spread their radiation over a wider angle.

4. Smoke, steam, water droplets or particulate matter may reduce radia-tion.

3.1.2 Absorptivity

The fraction of the energy incident on a body that is absorbed by the body presents the absorptivity. Compared with emissivity, the absorptivity has additional complexities because directional and spectral characteristics of the incident radiation must be included.

Directional spectral absorptivity could be calculated by:

$$\alpha_\lambda(\lambda, \theta, \varphi, T_A) = \frac{d^2 Q_{\lambda,a}(\lambda, \theta, \varphi, T_A) d\lambda}{i_{\lambda,i}(\lambda, \theta, \varphi) dA \cos\theta d\omega d\lambda} \tag{3.5}$$

The directional total absorptivity is the energy including all wavelength that is absorbed from a given direction, divided by the energy incident from that direction and it is described by following equation:

$$\alpha(\theta, \varphi, T_A) = \frac{\int_0^\infty \alpha_\lambda(\lambda, \theta, \varphi, T_A) i_{\lambda,i}(\lambda, \theta, \varphi) d\lambda}{\int_0^\infty i_{\lambda,i}(\lambda, \theta, \varphi) d\lambda} \tag{3.6}$$

The hemispherical spectral absorptivity is the fraction of the spectral energy that is absorbed from the spectral energy that is incident from all directions of a surrounding hemisphere.

$$\alpha_\lambda(\lambda, T_A) = \frac{\int_D \alpha_\lambda(\lambda, \theta, \varphi, T_A) i_{\lambda,i}(\lambda, \theta, \varphi, T_A) \cos\theta d\omega}{\int_D i_{\lambda,i}(\lambda, \theta, \varphi, T_A) \cos\theta d\omega} \tag{3.7}$$

The hemispherical total absorptivity represents the fraction of energy ab-sorbed that is incident from all directions of the enclosing hemisphere and

for all wavelengths and is calculated according to:

$$\alpha(T_A) = \frac{\int_D \left[\int_0^\infty \alpha_\lambda(\lambda, \theta, \varphi, T_A) i_{\lambda,i}(\lambda, \theta, \varphi) \right] \cos\theta d\omega}{\int_D \left[\int_0^\infty i_{\lambda,i}(\lambda, \theta, \varphi) d\lambda \right] \cos\theta d\omega} \tag{3.8}$$

In this thesis one more Law, known as the **Kirchoff** Law will be mentioned. This Law gives the simple relation between emissivity and absorptivity (for spectral quantity) as:

$$\varepsilon_\lambda(\lambda, \theta, \varphi, T_A) = \alpha_\lambda(\lambda, \theta, \varphi, T_A) \tag{3.9}$$

Hence when $\varepsilon_\lambda(\lambda, \theta, \varphi, T_A)$ and $\alpha_\lambda(\lambda, \theta, \varphi, T_A)$ are dependent on wavelength, there is the equality $\varepsilon(\theta, \varphi, T_A) = \alpha(\theta, \varphi, T_A)$ only when the incident radiation meets the restriction $i_{\lambda,i}(\lambda, \theta, \varphi) = C(\theta, \varphi) i_{\lambda,b}(\lambda, T_A)$, where C is independent of wavelength.

3.1.3   Reflectivity

To specify the reflective properties care must be taken regarding the angle at which the incident energy impinges on the surface and also the direction being considered for the reflective energy.

Spectral (as well as total) reflectivity can be divided into:

1. bidirectional;

2. directional-hemispherical;

3. hemispherical-directional; and

4. hemispherical.

1. *Bidirectional spectral* reflectivity is a ratio expressing the contribution that $i_{\lambda,i}(\lambda, \theta, \varphi) \cos\theta d\omega$ makes to the reflected spectral intensity in the (θ_r, φ_r) direction and it is described by following equation:

$$\rho_\lambda(\lambda, \theta_r, \varphi_r, \theta, \varphi) = \frac{i_{\lambda,r}(\lambda, \theta_r, \varphi_r, \theta, \varphi)}{i_{\lambda,i}(\lambda, \theta, \varphi) \cos\theta d\omega} \tag{3.10}$$

Bidirectional total reflectivity gives the relationship between the total energy incident from direction (θ, φ) and reflected total intensity into direction (θ_r, φ_r).

$$\rho(\theta_r, \varphi_r, \theta, \varphi) = \frac{i_r(\theta_r, \varphi_r, \theta, \varphi)}{i_i(\theta, \varphi) \cos\theta d\omega} \tag{3.11}$$

2. *Directional-hemispherical spectral* reflectivity is defined as the energy reflected into all solid angles divided by the energy incident from one direction:

$$\rho_\lambda(\lambda, \theta, \varphi) = \int_D \rho_\lambda(\lambda, \theta_r, \varphi_r, \theta, \varphi) \cos\theta_r d\omega_r \qquad (3.12)$$

The diagram (Figure 3.3) given below is an example of directional-hemispherical spectral reflectivity.

The diagram presents directional-hemispherical reflectivity for silver at $\lambda = 546[nm]$, as a function of angle of incidence.

Directional-hemispherical total reflectivity is defined as the fraction of the total energy incident from a single direction that is reflected into all angular directions.

$$\rho(\theta, \varphi) = \frac{\int_0^\infty \rho_\lambda(\lambda, \theta, \varphi) i_{\lambda,i}(\lambda, \theta, \varphi) d\lambda}{\int_0^\infty i_{\lambda,i}(\lambda, \theta, \varphi) d\lambda} \qquad (3.13)$$

3. *Hemispherical-directional spectral* reflectivity takes place when incident radiation from all directions is reflected into one direction.

$$\rho_\lambda(\lambda, \theta_r, \varphi_r) = \frac{\int_D \rho_\lambda(\lambda, \theta_r, \varphi_r, \theta, \varphi) i_{\lambda,i}(\lambda, \theta, \varphi) \cos\theta d\omega}{\frac{1}{\pi} \int_D i_{\lambda,i}(\lambda, \theta, \varphi) \cos\theta d\omega} \qquad (3.14)$$

Hemispherical-directional total reflectivity is governed by the following equation:

$$\rho(\theta_r, \varphi_r) = \frac{\int_0^\infty \rho_\lambda(\lambda, \theta_r, \varphi_r) i_{\lambda,i}(\lambda) d\lambda}{\int_0^\infty i_{\lambda,i}(\lambda) d\lambda} \qquad (3.15)$$

4. *Hemispherical spectral* reflectivity is reflectivity when incident radiation comes from all directions that is reflected into all angular directions.

$$\rho_\lambda(\lambda) = \frac{\int_D \rho_\lambda(\lambda, \theta, \varphi) i_{\lambda,i}(\lambda, \theta, \varphi) \cos\theta d\omega}{\int_D i_{\lambda,i}(\lambda, \theta, \varphi) \cos\theta d\omega} \qquad (3.16)$$

hemispherical total reflectivity is defined by next equation.

$$\rho = \frac{\int_0^\infty \rho_\lambda(\lambda) dQ_{\lambda,i}(\lambda) d\lambda}{\int_0^\infty dQ_{\lambda,i}(\lambda) d\lambda} \qquad (3.17)$$

3.2 Thermocouple, Measuring and Calibration

For temperature measurement K-type thermocouples were chosen. Unfortunately, during the calibration an error between the real and the read temperature was noticed. The following diagram (Figure 3.4) presents the error

for the thermocouple No. 8. As can be seen from the diagram the error has a linear progression and depends on the temperature. Equation of the line, which gives the best approximation of the error, for the chosen thermocouple (No. 8), is $t_{real} = t_{read} + (0.0692255 \cdot t_{read} - 1.38451)$. In the worst case the difference between the real and the calibration temperature is for temperature about $t_{real} = 380 \ [°C]$, and it is less than 2 $[°C]$ (i.e. less than 0.526 %).

The temperatures of the emitter and the receiver have been measured by ten (10) thermocouples in combination with Thermo Tracer TH7102. At the same time, the temperature of the internal side of the box was measured. The experimental results will be presented as diagrams in the following order: type of the emitter; the material; the thickness; and the angle between the emitter and the receiver.

During the experiments the ambient temperature changed and caused different readings for the same temperatures of the receiver. To eliminate this problem a fixed ambient temperature was chosen ($t_{amb} = 22.3 \ [°C]$).

For distance ratio ($c/D > 2$) the temperature of the top internal side of the box becomes very important. Discussion about this problem, and other issues such as convection, will be given in section 3.5.

3.3 Thermo-Physical Properties

3.3.1 Microstructure and Roughness

As was mentioned earlier samples composed of three different materials (steel, aluminium and brass) were used in the experiments. A detailed analysis of microstructure of brass sample is given only in the text that follows. Microstructure with different magnifications is given in Appendix D.

As it is known, brass is a copper zinc alloy. Depending on the percentage of zinc there are many different brasses. In general, they have good strength and corrosion resistance, although their structure and properties are a function of zinc content. Alloys containing up to approximately 35 % zinc are single phase alloys, consisting of a solid solution of zinc and alpha copper. These brasses have good strength and ductility which increase with increasing zinc content. The alpha alloys can be differentiated by a gradual a gradual change in color, from golden yellow to red, as the zinc content is increased up to 35 % (see Figure D.4). Brasses containing between 32 and 39 % zinc have a two phase structure, composed of alpha and beta phases. Yellow brasses are in this intermediate category of brasses. Brasses containing more than 39 % zinc have a predominantly beta structure. The beta phase is harder

than the alpha phase.

During a process of solidification the first material to solidify is almost pure copper, as the dendrites continue to solidify they become a mixture of copper and zinc. A composition gradient exists across the dendrite, with zero zinc content at the centre and highest zinc content at the outer edge. The composition gradient is called coring, and it typically occurs with alloys that freeze over a wide temperature range. Subsequent working and annealing breaks up the dendritic structure. The resulting microstructure consists of twinned, equiaxed grains of alpha brass. The annealed microstructure is made up of equiaxed, twinned grains of alpha copper, similar to the structure of unalloyed copper. The grains appear in different shades due to their different orientations. The twins are parallel lines that extend across individual grains. The twins result from a fault in the staking sequence of the copper atoms, making it difficult to distinguish the individual grains.

Alpha copper is the primary phase in cast alloys containing up to approximately 40% zinc.

The beta phase (see Figure D.4),which is the high zinc phase, is the minor constituent filling in the areas between the alpha dendrites. The microstructure of brasses containing up to approximately 40 % zinc consists of alpha dendrites with beta surrounding the dendrites. The wrought materials consist of grains of alpha and beta. Cast alloys with greater than 40 % zinc contain primary dendrites of beta phase. If the material is fast-cooled, the structure consists entirely of beta phase. During a slower cool, the alpha precipitates out of solution at the crystal boundaries, forming a structure of beta dendrites surrounded by alpha. This structure is called a Widmanstatten structure, because a geometrical pattern of alpha is formed on the certain crystallographic orientations of the beta lattice. The wrought, two phase material consists of grains of beta and alpha. Hot rolling tends to elongate the grains in the rolling direction.

The sample which is analyzed was not made of high quality, so non metallic inclosures which are surrounded with beta phase can be noted in Figure D.4.

Roughness of all three materials were measured and presented in Figures D.5, D.6 and D.7 respectively.

3.3.2   Thermal Conductivity

"Armfield" is a company which produces engineering teaching and research equipment. One of apparatuses which they have been producing is 'HT11'. This apparatus is used in linear heat conduction analysis to find thermal conductivity of materials. To find thermal conductivities of plates used as a

receiver in experiments three discs with diameter of 25 [*mm*] were cut. Using this apparatus measurements were taken three times for each specimen using different heat flux as result of different voltage (10, 15 and 20 [*V*]). As result, thermal conductivities of samples are given in Table 3.1.

3.3.3 Surface Properties

Surface properties of samples used in experiments presented in the thesis were obtained using SOC-100 Hemispherical Directional Reflectometer.

The SOC-100 Hemispherical Directional Reflectometer provides polarized, angular reflectivity measurements from 10 to 80 incident angles. Coupled to the Nicolet Magna (tm) FTIR, the SOC-100 works in the entire spectral region available for that FTIR. It has the capability to measure the collimated and scattered transmittance of samples, and by using a specular beam blocker, the diffuse and specular partition of the scattered energy. From the direct measurements other values can be calculated directional and near normal emissivity, directional angular emissivity, total hemispherical emissivity, solar absorptivity, and optical constants.

Hemispherical emissivity (HE) of samples used for experiments for wavelength in region from 2 [*μm*] to 25 [*μm*] is presented in Figure 3.5. According to Figure 2.2 this wavelength region is included in thermal radiation - near infrared. From Figure 3.5 it can be seen that the front side of the black painted steel sample has the highest hemispherical emissivity (noted as JG0065 Black1) of 0.923394. At the same time hemispherical emissivity reached its minimum at 0.761761. The average value of hemispherical emissivity of the front side of the black painted steel sample in the analyzed wavelength region was found to be 0.855878. Hemispherical emissivity of the back side of the black painted steel sample (noted as JG0066 Black2) reached its maximum at 0.921352 ($\lambda = 8.6$ [*μm*]), while its minimum was at 0.72073 ($\lambda = 4.99$ [*μm*]). The average value for the analyzed region was found to be 0.830166. It can be seen that except at short wavelengths, the difference between hemispherical emissivity trends on the front and back sides of the black painted steel sample is almost negligible.

Also, from Figure 3.5 it can be seen that the front side of the sample composed of brass (JG0061 Brass1) reached its maximum at 0.268266, while the minimum value was 0.037448. The average value of hemispherical emissivity of the front side was found to be 0.173137. At the same time hemispherical emissivity of the back side (JG0062 Brass2) of the same sample reached its maximum at 0.266984, while its minimum value was 0.068045. The average value for the analyzed wavelength region was found to be 0.186851.

Hemispherical emissivity on the front side (JG0063 Aluminium1) of the

sample composed of aluminium reached its maximum at 0.361794, while the minimum value was 0.130755. The average value for the analyzed region was found to be 0.286888. At the same time hemispherical emissivity of the back side (JG0064 Aluminium2) of the same sample reached its maximum at 0.18492, while its minimum value was 0.038331. The average value for the analyzed region was found to be 0.112422.

Directional hemispherical reflectivity (DHR) for the angle of 8 [^{o}] for wavelength region from 0.3 [μm] to 2.5 [μm] is presented in Figure 3.6. According to Figure 2.2 this wavelength region is included in thermal radiation - far infrared.

As was expected the back side of the black painted steel sample has the lowest directional hemispherical reflectivity, which reached its maximum at 13.205 %. The minimum value of the same sample was 3.6779 %. The average value of the analyzed region was found to be 8.277 %. At the same time the directional hemispherical reflectivity of the front side of the black painted sample composed of steel reached its maximum at 12.926 %. The minimum value was 3.9158 % while the average value was found to be 7.5666 %. A difference between average values of the front and the back sides of the sample is very small. Therefore, taking an average value of these values will not cause a large error to be made in the calculations.

Directional hemispherical reflectivity of the front side of the brass reached its maximum at 75.532135 %, while the minimum value was 7.4861326 %. At the same time the average value was found to be 56.705 %. At the same time directional hemispherical reflectivity of the back side of the sample composed of brass reached its maximum at 74.7742 %, while its minimum was 5.856 %. At the same time the average value was found to be 56.677 %. The difference between average values of the front and the back sides of the sample is very small and can be considered as negligible for calculations.

Directional hemispherical reflectivity of the front side of the aluminium reached its maximum at 68.687 %, while the minimum value was 34.4315 %. At the same time the average value was found to be 57.9376 %. At the same time directional hemispherical reflectivity of the back side of the sample composed of aluminium reached its maximum at 82.5907 %, while its minimum was 21.64324 %. At the same time the average value was found to be 63.1424 %. The difference between average values of the front and the back sides of the sample is the largest of all samples (about 0.5205 %) and has to be considered for the calculations.

The **Pharo** program works with bodies which have the same surface properties for the entire body. The results shown from the previous analysis of directional hemispherical reflectivity, outline the importance of attaching surface properties to each element of the domain. Therefore, even where the

difference between the front and back sides is negligible, more accurate results are obtained when this is considered, and as has been shown the difference can be large and thereby have a considerable impact on the results.

Aspect variations of average polarization for hemispherical directional reflectivity (HDR), diffuse directional reflectivity (DDR) and specular directional reflectivity (SDR) for three samples analyzed are presented in the text that follows. Wavelength region from 2 $[\mu m]$ to 15 $[\mu m]$, which is included in thermal radiation-near infrared, was chosen for the measurements. Eight different angles of incident 8, 20, 40, 50, 60, 70, 75 and 80 ^{o} were analyzed.

Sample composed of brass

Aspect angle variations of average polarization for HDR of the front side of the sample are presented in Figure 3.7. At the same time an aspect angle variation of average polarization for DDR is presented in Figure 3.8, while an aspect angle variation of average polarization for SDR is presented in Figure 3.9.

From these figures it can be seen that with an increase in wavelength the average polarization increased for HDR and SDR while a decreasing trend for DDR was noted. Also, an increase in the angle of incident gave a higher average reflectivity for HDR and SDR. At the same time a decreasing trend of average reflectance for DDR was found.

Aspect angle variations of average, perpendicular and parallel polarization for wavelength from 3 $[\mu m]$ to 5 $[\mu m]$ are presented in Figure 3.10. At the same time aspect angle variations of average, perpendicular and parallel polarization for wavelength from 8 $[\mu m]$ to 12 $[\mu m]$ are presented in Figure 3.11.

From Figures 3.10 and 3.11 it can be seen that reflectance of average and perpendicular polarizations for HDR and SDR have greater values than for DDR, while reflectivity of parallel polarization for DDR has greater values than for HDR and SDR.

Sample composed of aluminium

An aspect angle variation of average polarization for HDR of the front side of sample is presented in Figure 3.12. At the same time an aspect angle variation of the average polarization for DDR is presented in Figure 3.13, while an aspect angle variation of the average polarization for SDR is presented in Figure 3.14. From Figures 3.12, 3.13 and 3.14 the same conclusions can be drawn as in the previous case.

Aspect angle variations of average, perpendicular and parallel polarization for wavelength from 3 [μm] to 5 [μm] are presented in Figure 3.15. At the same time aspect angle variations of average, perpendicular and parallel polarization for wavelength from 8 [μm] to 12 [μm] are presented in Figure 3.16.

The difference between this and previous case is the smaller reflectance of average, parallel and perpendicular for SDR than for DDR (lower angles of incident).

Sample composed of black painted steel-front side

An aspect angle variation of average polarization for HDR of the front side of sample is presented in Figure 3.17. At the same time aspect angle variations of average polarization for DDR are presented in Figure 3.18, while aspect angle variations of average polarization for SDR are presented in Figure 3.19. An increase in the angle of incident caused higher reflectivity for HDR, SDR and DDR.

Aspect angle variations of average, perpendicular and parallel polarization for wavelength from 3 [μm] to 5 [μm] are presented in Figure 3.20. At the same time aspect angle variations of average, perpendicular and parallel polarization for wavelength from 8 [μm] to 12 [μm] are presented in Figure 3.21.

Sample composed of black painted steel-back side

Aspect angle variations of average polarization for HDR of the back side of the sample are presented in Figure 3.22. At the same time aspect angle variations of average polarization for DDR is presented in Figure 3.23, while aspect angle variations of average polarization for SDR are presented in Figure 3.24.

Aspect angle variations of average, perpendicular and parallel polarization for wavelength from 3 [μm] to 5 [μm] are presented in Figure 3.25. At the same time aspect angle variations of average, perpendicular and parallel polarization for wavelength from 8 [μm] to 12 [μm] are presented in Figure 3.26.

3.4 Results

3.4.1 The Square Plate as an Emitter

A square plate composed of steel with dimension of $\neq$3x197x197 completely insulated, except its front side, was used as an emitter, while an identical

square plate with thickness of $\neq 10$ was used as a receiver (see Figure 3.27).

Three different cases will be presented in this section:

a) parallel plates without shadowing;

b) hinged plates; and

c) parallel plates with shadowing.

a) parallel plates

The first case considers two parallel plates with different distance ratios between them. Two sets of experiments were made for two different power levels of the heating elements used to heat up the receiver.

The temperature (four measuring points) of the emitter and the receiver (six measuring points) were measured simultaneously. The temperatures of the back side of the receiver for different distance ratios and different power ratios of the emitter are presented in Figure 3.28. These temperatures will be used later for an examination of the heat transfer code which has been written.

Thermocouples tc1r(20%), tc2r(20%), tc3r(20%), tc4r(20%) and tc5r(20%) represent temperatures of the receiver according to Figure 3.29 while tc1r(40%), tc2r(40%), tc3r(40%) and tc4r(40%) represent temperatures of the receiver according to Figure 3.30.

Temperatures of the receiver presented in Figure 3.28 have a logical trend, so higher temperatures were measured for higher power of the emitter. A temperature drop is also noted with an increase of distance ratios between the emitter and the receiver. For distance ratios larger than 4 temperatures of the receiver almost dropped to the ambient temperature.

b) hinged plates

In Figure 3.31 the position of the hinged plates is shown, while the positions of the measuring points were chosen according to Figure 3.29.

Temperatures of the emitter and the receiver are presented in Table 3.2. In Table 3.2 it can be noticed very low temperature of the emitter (about 246 $[°C]$). The main reason is that this experiment was run with 20 % of power. However, a temperature difference as result of different position of thermocouple can be seen (receiver has got higher temperatures in areas closer to receiver).

3.4.2 The Disc Plate as an Emitter

All diagrams presented in the following text show a similar decreasing trend. The receiver with high emissivity (Figure 3.33) has a temperature of about 270 [$°C$] for distance ratio $c/D = 0.1$, while the receiver with low emissivity (Figure 3.40) for the same distance ratio was at a temperature of about 95 [$°C$].

The emitter used in these experiments is composed of steel and painted with a black heat resistant low reflectivity paint.

The steel plate as a receiver ($\neq 5 \times 197 \times 197$ [mm])

In order to give a useful presentation not all the measured data will be presented. Therefore only one diagram with both emitters temperatures and receivers temperatures will be presented (Figure 3.32). In Figure 3.32 it can be seen that experiments were run until both emitter and receiver reached steady state (more than 6000 [s]). Also, in Figure 3.32 Tc1e, Tc2e, Tc3e and Tc4e represent temperatures of the emitter while Tc1r, Tc2r, Tc3r and Tc4r represent temperatures of the receiver at measuring points.

Figure 3.33 presents temperatures of the receiver composed of steel with thickness of 5 [mm]($\neq$ is symbol for thickness) for different distance ratios ($0.1 \leq c/D \leq 4$). As can be seen in Figure 3.33 two new measuring points were added to the receiver and their positions are drawn in Figure 3.30.

Temperatures presented in Figure 3.33 decrease with an increase of distance ratios (from 265 [$°C$] to 31 [$°C$]). A temperature difference between the temperatures of the receiver when there is a smaller distance ratio is noted. The main reason for this temperature difference is the position of the thermocouples (see Figure 3.30). With an increase of distance ratios this temperature difference decreased. This is the caused by a decrease in the heat flux received. The ambient temperature is also presented in Figure 3.33.

The steel plate as a receiver ($\neq 10 \times 197 \times 197$ [mm])

A decreasing trend of temperatures of the receiver for different distance ratios is presented in Figure 3.34.

Thermocouple positions are given in the following Figure 3.35. These positions are only valid for these experiments.

A comparison between temperatures presented in 3.33 and Figure 3.34 shows that temperatures measured for the steel plate as a receiver with thickness of 10 [mm] lie in the region between maximum and minimum temperature measured for the steel plate as a receiver with thickness of 5 [mm]. The

difference in the temperatures was caused by the different positions of the thermocouples. According that both plates are coated with black paint, the same emissivity (absorptivity) can be expected for them both.

As mentioned earlier an infra-red thermal imaging camera (Thermo Tracer TH7102) was used for temperature measurement. In order to make a simple and compact presentation of the investigation, only three thermal images will be given. These are:
a) the back of the receiver;
b) the front of the receiver; and
c) the front of the emitter.

The back of the receiver is shown in Figure 3.36, the front of the receiver in Figure 3.37 and the front of the emitter in Figure 3.38.

The brass plate as a receiver ($\neq 5 \times 197 \times 197$ [mm])

The temperatures of the receiver composed of brass with thickness of 5 [mm] are presented in Figure 3.39. The distance ratio between emitter and receiver was increased from $c/D = 0.1$ to $c/D = 4$. In Figure 3.39 it can be seen that temperatures (maximum temperature was measured for the distance ratio $c/D = 0.1$) decreased with an increase of distance ratios. For distance ratio $c/D = 0.1$ different temperatures of the receiver were measured depending on the position of the thermocouple (157 [$°C$] to 135 [$°C$]). Minimum temperatures were measured for the distance ratio $c/D = 4$ and it was just above ambient temperature.

The brass plate as a receiver ($\neq 7 \times 197 \times 197$ [mm])

This set of experiments started with the distance ratio $c/D = 0.2$ with thermocouple positions as presented in Figure 3.35. At this distance ratio a maximum temperature of 98 [$°C$] was measured. A decreasing trend of temperatures of the receiver composed of brass with thickness of 7 [mm] is presented in Figure 3.40.

A comparison between temperatures presented in Figure 3.40 and Figure 3.39 shows a temperature difference for the same distance ratio. This difference is caused by both the different positions of thermocouples and the different surface properties of the material (roughness, absorptivity, reflectivity).

While receivers composed of steel were painted with black paint of high absorptivity to gain uniform and same surface property, receivers composed of brass and aluminium were used without any treatment.

The aluminium plate as a receiver ($\neq 5 \times 197 \times 197$ [mm])

Temperature data obtained for the aluminium plate with thickness of 5 [mm] is presented in Figure 3.41. The positions of thermocouples used in experiments were according to Figure 3.33. The starting distance ratio in these experiments was $c/D = 0.1$, and in this case a maximum temperature of 248 [$^\circ C$] was measured. As it was noted earlier an increase of distance ratio caused the temperature of the receiver to fall.

The aluminium plate as a receiver ($\neq 7 \times 197 \times 197$ [mm])

Temperatures of the aluminium plate with thickness of 7 [mm] are presented in Figure 3.42. The positions of thermocouples used in experiments were according to Figure 3.35. Temperatures of the receiver have a decreasing trend, as it was noted in the presentation of earlier results. The starting distance ratio for this set of experiments was $c/D = 0.2$ and for this distance ratio a maximum temperature of 145 [$^\circ C$] was measured. With an increase in distance ratios, the temperature of the receiver dropped to just above ambient temperature.

The brass plate with different emissivity as a receiver ($\neq 7 \times 197 \times 197$ [mm])

The purpose of this experiment was to analyze temperature changes of the receiver changing its emissivity (absorptivity) keeping the distance between the emitter (a disc) and the receiver constant (135 [mm]).

At the start, all surfaces of the receiver were untreated and had a high reflectivity. Later, when temperatures of the receiver reached a steady state the back side of the receiver was painted with black paint (high emissivity) which caused a fall in its temperature. This was to be expected because under these new conditions the receiver emitted more heat while receiving the same amount of heat from the emitter. After a while, when the temperature of the receiver was stabilized, the front side of the receiver was also painted with same black paint. Therefore, the surface absorptivity increased causing a temperature increase. In Figure 3.43 the temperature trend as result of different emissivity (absorptivity) can be seen. All these temperature changes of the receiver were subsequently reflected to the temperature of the emitter, causing it to fall.

3.4.3 Hinged Plates

In this section three experimental cases which include the angle of 25, 50, and 90 degrees between plates were considered. Also, in case 1 and 2 the distance ratio c/D was changed from 0.2 to 4. In these cases the black painted receiver composed of steel with dimension of $\neq 15 \times 197 \times 197$ [mm] was used. Positions of measuring points according to Figure 3.35 were chosen.

a) $\alpha = 25$ [^{o}]

Hinged plates including the angle of 25 degree between them and different distance ratios are considered in this case. Experimental data is given in Figure 3.44. As it can be seen from Figure 3.44 temperatures for the shortest distance ratio ($c/D = 0.2$) were in the region from 138 [$^\circ C$] to 155 [$^\circ C$]. This gave a difference of 17 [$^\circ C$] between the highest and the lowest temperature of the receiver. The reasons for this difference are the geometries of emitter and receiver, as well as the temperature non-uniformity of the emitter. An increase of the distance ratio caused a decrease in the temperatures of the receiver.

b) $\alpha = 50$ [^{o}]

Experimental data for hinged plates including the angle of 50 degrees and different distance ratios between them is presented in Figure 3.45. In Figure 3.45 it can be noted that the temperatures of the receiver for the distance ratio $c/D = 0.2$ were in region between 92 [$^\circ C$] to 97 [$^\circ C$]. A comparison between temperatures obtained in this case with ones obtained in the previous case, shows a difference of about 50 [$^\circ C$]. This difference was expected and is caused by the greater angle between the emitter and the receiver (projection of the receiver onto a plane which is parallel to the emitter is smaller than in the previous case).

c) $\alpha = 90$ [^{o}]

Finally, hinged plates with the angle of 90 degrees between them was considered. The experimental data for this case is presented in Figure 3.46. Figure 3.46 includes the thermal image with four temperature line profiles. In this figure it can be seen that one end of temperature line profiles is at the hottest point of the receiver front surface (137 [$^\circ C$]). From this point temperature decreases gradually to about 97 [$^\circ C$] which was measured near to the edge of the receiver.

3.4.4 Shadowing

One experimental case, which includes shadowing, will be presented in the following text. The distance ratio (c/D) between the emitter and the receiver was equal to one, and an obstacle was placed exactly halfway between them, in the left lower corner looking from the emitter. The obstacle was composed of steel with the dimensions of $\neq$2x100x100 and its back side was insulated. The results measured are presented in Figure 3.47.

From Figure 3.47 it can be seen that presence of the obstacle causes a significant drop in the temperatures of the receiver (from 53 [$°C$] to 40 [$°C$]). It can also be seen that presence of the obstacle causes a temperature drop of whole receiver for about $8 - 9$ [$°C$].

3.4.5 The Cylinder as an Emitter

The rig which considers a cylinder as an emitter and a squared plate as receiver is presented in Figure 3.48. The geometry of both the emitter and the receiver was: ϕ28x197 [mm] of the emitter and $\neq$10x197x197 [mm] of the receiver. While the emitter is composed of brass, the receiver is composed of steel. Surfaces both of them were painted with black paint.

Measurements were taken for a few different distance ratios c/d where c is the distance, d is the diameter of the emitter. Transient temperatures of the emitter and the receiver for the distance ratio $c/d = 1.9$ are presented in Figure 3.49. The temperature of the surface of the cylinder is shown as $Tc2e$, while the temperature of the internal point of the cylinder as $Tc1e$. This temperature difference was used for the calculation of heat flux through cylinder. The measuring points of the receiver are presented in Figure 3.29.

Experimental data for different distance ratios (from $c/d = 1.9$ to $c/d = 9$) is presented in Figure 3.50. From Figure 3.50 it can be seen that temperatures have a decreasing trend which is not as steep as was noted during previous experiments.

3.4.6 Reflectivity

Reflectivity plays a very important role in radiative transfer simulations, especially when the distance between surfaces or bodies is small, and the reflectivity of the surfaces included in the calculations is very high.

During experiments it was noticed that temperatures of the emitter changed depending on the distance between the emitter and the receiver. The following diagram (Figure 3.51), which is given as an example, presents the temperature of the centre of the disc which was used as an emitter while the

receiver was composed of brass. This diagram is valid only for the presented case. For different receivers, with different reflectivity, the temperatures of the emitter will be different. From Figure 3.51 it can be seen that the temperature of the emitter has a decreasing trend, which is a result of an increase in the separation distance between an emitter and a receiver.

Further work considers four experiments designed specially for reflectivity analysis. These experiments consider a disc plate as an emitter, and a brass plate and an aluminium plate as receivers (receiver 1 and receiver 2 respectively). The positions of the emitter and receiver 2 were fixed, while the position of receiver 1 was changed: 1- the emitter and receiver 1 are parallel to each other and the distance between them was 135 [mm]; and 2- the emitter and receiver 1 build the angle of $\alpha = 25[^o]$ between them (Figure 3.52). The distance between the centre of the emitter and the middle of receiver 2 was fixed at 294.5 [mm].

Additionally, two different front surfaces of receiver 2 were included in these experiments. In the first case the front surface of receiver 2 was clean, while in the second the surface was painted with black paint.

In total four cases were considered in this analysis:

case 1 - the emitter and receiver 1 are parallel to each other, while receiver 2 is not painted;

case 2 - the emitter and receiver 1 are parallel to each other, while receiver 2 is painted;

case 3 - the emitter and receiver 1 build the angle of 25 [^{o}] between them, while receiver 2 is not painted;

case 4 - the emitter and receiver 1 build the angle of 25 [^{o}] between them, while receiver 2 is painted.

Experimental data for all these cases is presented in Table 3.3. From Table 3.3 it can be seen that the lowest temperatures of receiver 2 were obtained during the second case (about 24 [$^\circ C$]). Considering that the front surface of the receiver 2 was untreated, with a high reflectivity, these temperatures were expected. Rotating receiver 1 so that it created an angle of 25 [^{o}] with the emitter caused an increase in the temperatures of receiver 2. Instead of being parallel, as it was in the first case, here receiver 1 and receiver 2 can better "see" each other. A further increase was caused by painting receiver 2 with black paint.

Two thermal images presented in Figures 3.53 and 3.54 show the temperature distribution within the box, mainly as a result of reflection from receiver 1. In Figure 3.53 a hot spot can be clearly seen on the side of the box, which has shape of a ring, as a result of the reflection from receiver 1. The emitter was an obstacle placed between receiver 1 and the side of the box.

Also, receiver 2 was warmed up by the reflection from receiver 1. To give a more detailed presentation three line profiles are shown in Figure 3.53.

At the same time the longer side of the box, which is perpendicular to the emitter and receivers, was warmed up by both direct radiation and reflection. The hot spot presented in Figure 3.54 was caused by this, and ten random points were chosen to obtain a clear picture of temperature distribution within it. It can be noted that maximum temperature was about 38 [$°C$].

3.5 Conclusions

Experimental data of the temperatures of the receivers shows a logical trend. A comparison between temperatures measured for the same thickness of plates as receivers composed of different materials (steel, brass and aluminium) for the same distance ratio (for example $c/D = 0.1$) shows a huge difference between them. As was expected the temperatures obtained for the black painted receiver composed of steel were the highest (approx. 270 [$°C$]), while temperatures of the receiver composed of brass were the lowest (approx. 158 [$°C$]). This temperature difference was purely a result of the high absorptivity difference between the black painted surface and that of the untreated brass surface.

During the experiments there were a few elements which had to be taken into consideration, such as the location of the equipment in the laboratory, natural convection, and reflectivity. The effects of natural convection are cooling to both emitter and receiver, and heating of the internal side of the box. The temperature of the hottest point of the box was measured and is presented in the following diagram (Figure 3.55).

As was mentioned earlier these effects become very important when the distance ratio (c/D) between an emitter and a receiver is smaller than two. Figure 3.56 presents the region heated by natural convection and considers the distance ratio (c/D) was equal to 0.75. The difference between temperatures presented in Figure 3.55 and the highest temperature of the region presented in Figure 3.56 is caused by different power ratio used in experiments. The first experiment was run with 60 [%] of power, while the second one ran with 50 [%] of power.

In the section 3.4.6 experimental data which presents reflectivity effect is given. From Table 3.3 an expected value of temperatures of the emitter and receivers can be seen. For example a comparison between case 1 and case 2 shows that a black painted receiver 2 will reflect less heat to receiver 1 causing a temperature drop of receiver 1. Further, a temperature drop of

receiver 1 will caused a temperature drop of the emitter. The same effect was gained by rotating receiver 1 so that it created an angle with the emitter. In this case view factor between the emitter and receiver 1 decreased, causing a temperature decrease of receiver 1. At the same time view factor between receiver 1 and receiver 2 increased causing a temperature increase of receiver 2. Use of black paint with high absorptivity also causes a further increase of the temperature of receiver 2.

material	dimension [mm]	thermal conductivity [W/mK]
brass	ϕ25.03x$\neq$4.83	124.55
steel	ϕ25.06x$\neq$5.02	18.9
aluminium	ϕ25x$\neq$4.99	232.7

Table 3.1: Thermal conductivity of brass, steel and aluminium specimens

position	temperature [^oC]
tc1e	246.2
tc1r	48
tc2r	53.1
tc3r	49.2
tc4r	53.2
tc5r	49
tc6r	48
tc7r	47
tc8r	52

Table 3.2: Temperatures of the emitter and the receiver for the hinged plates case

temp. $[^oC]$	case 1	case 2	case 3	case 4
t_{brass_1}	50.68	42.77	41.27	39.134
t_{brass_2}	50.78	42.87	42.34	40.307
t_{brass_3}	51.21	43.52	42.23	39.99
t_{brass_4}	52	44	43	41
t_{al_1}	24.06	23.96	26.3	29.2
t_{al_2}	24.06	23.96	26.3	29.5
t_{al_3}	23.53	23.42	25.77	28.98
t_{al_4}	24.4	23.21	25.77	28.77
t_{e_1}	444.16	434.75	429.94	430.26
t_{e_2}	457	450	447	445
$t_{amb.}$	19.8	18	18.5	16.8

Table 3.3: Temperatures of the emitter, receivers and ambient for different test cases
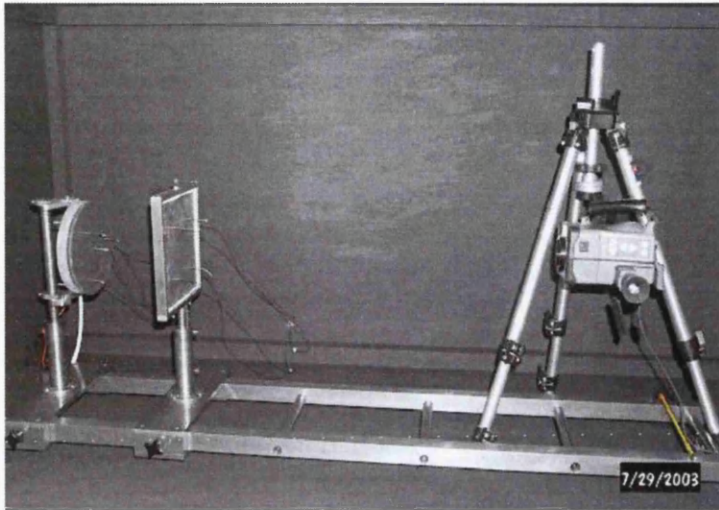
Figure 3.1: The experimental rig
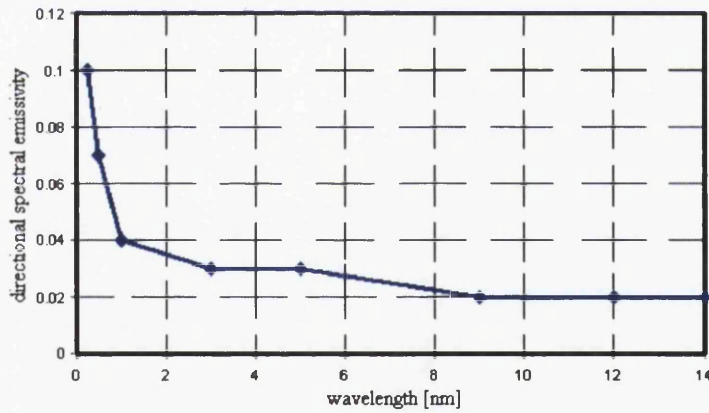
Figure 3.2: Directional spectral emissivity as a function of wavelength for a specimen composed of silver at $295[K]$
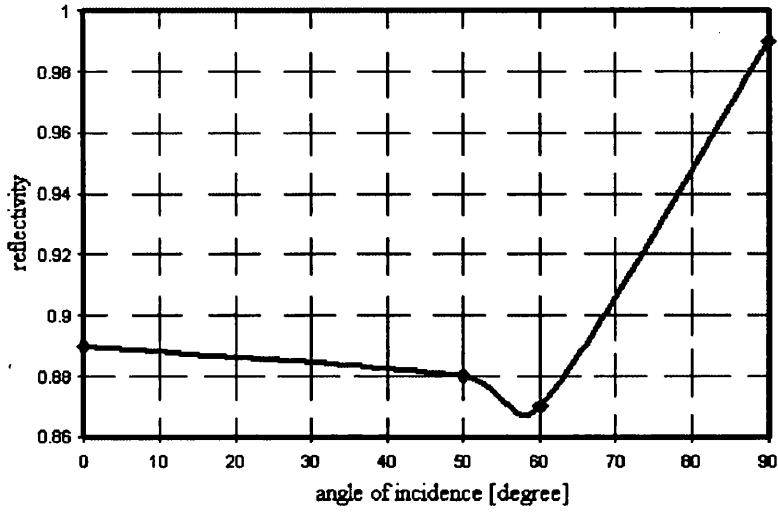
Figure 3.3: Directional-hemispherical reflectivity
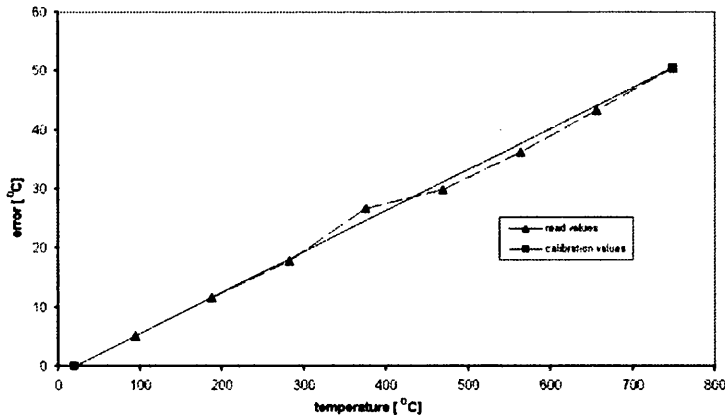
Figure 3.4: Real and calibration temperature values for the thermocouple No. 8
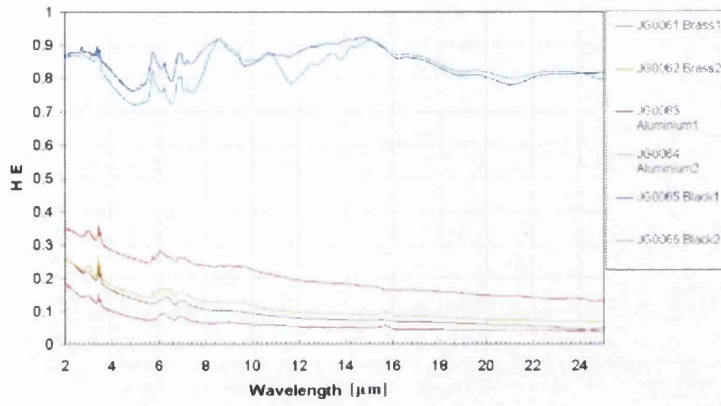
Figure 3.5: Hemispherical emissivity of samples
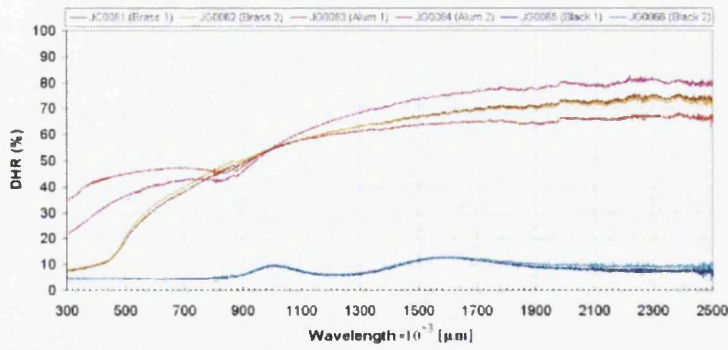
Figure 3.6: Directional hemispherical reflectivity of samples
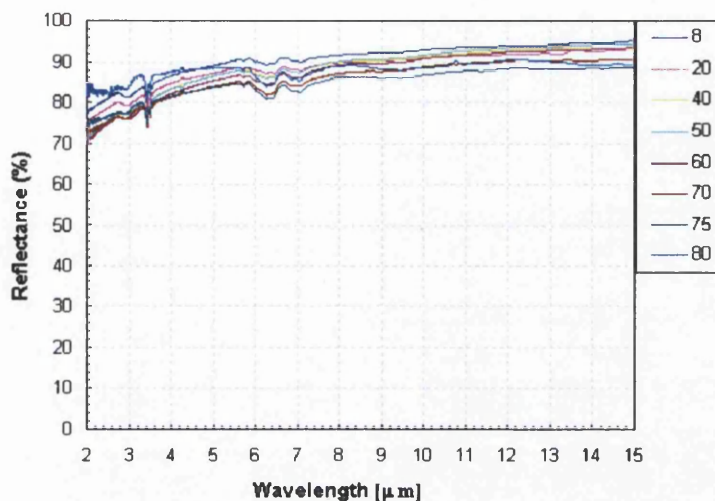
Figure 3.7: Hemispherical directional reflectivity of the sample composed of brass
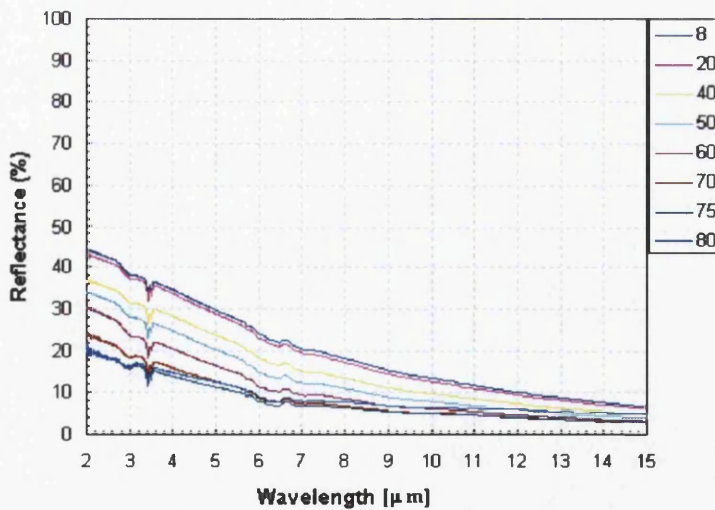
Figure 3.8: Diffuse directional reflectivity of the sample composed of brass
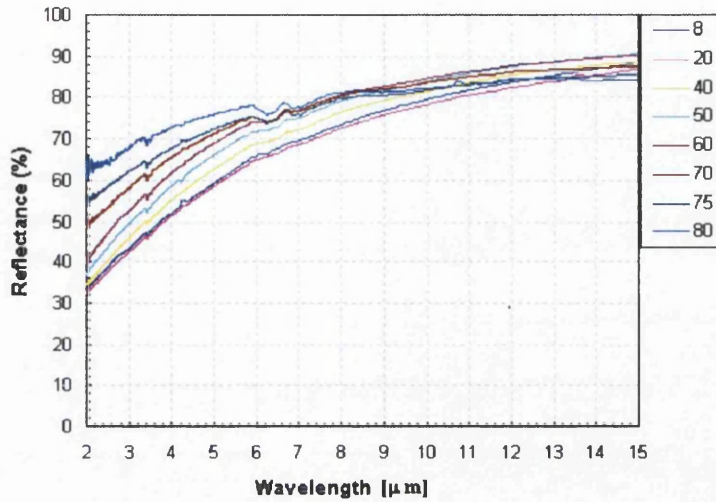
Figure 3.9: Specular directional reflectivity of the sample composed of brass
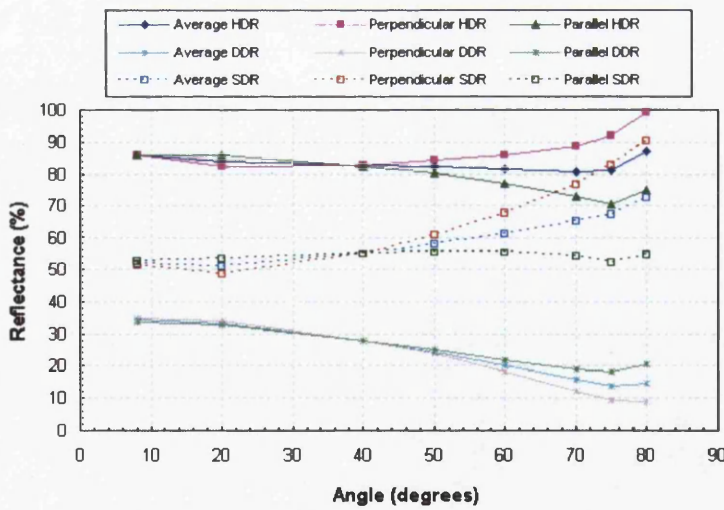
Figure 3.10: An aspect variation for $3 - 5$ $[\mu m]$ of the sample composed of brass
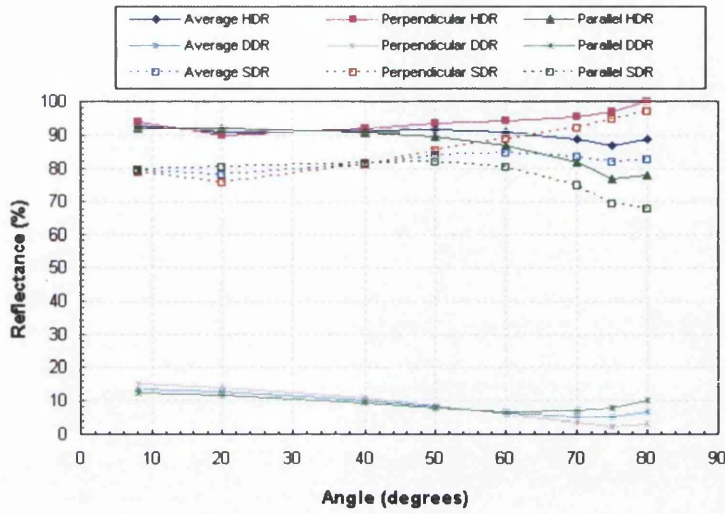
Figure 3.11: An aspect variation for $8 - 12$ $[\mu m]$ of the sample composed of brass
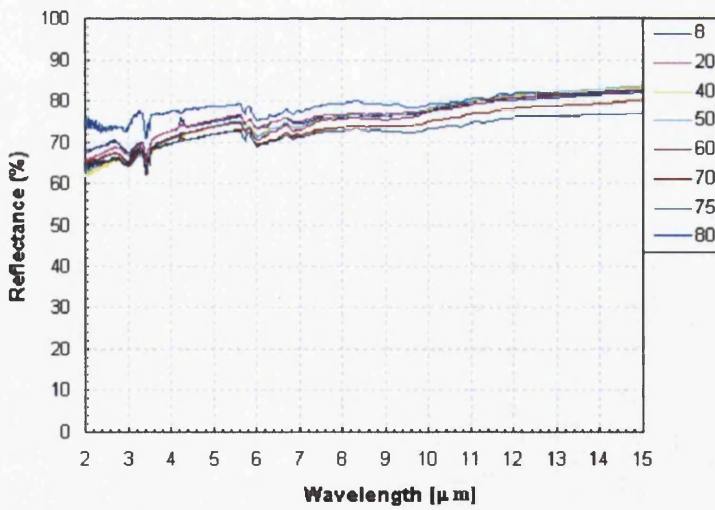
Figure 3.12: Hemispherical directional reflectance of the sample composed of aluminium
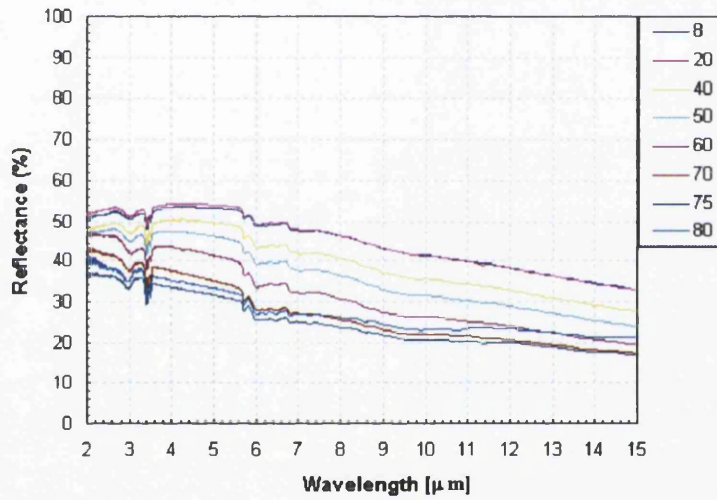
Figure 3.13: Diffuse directional reflectivity of the sample composed of aluminium
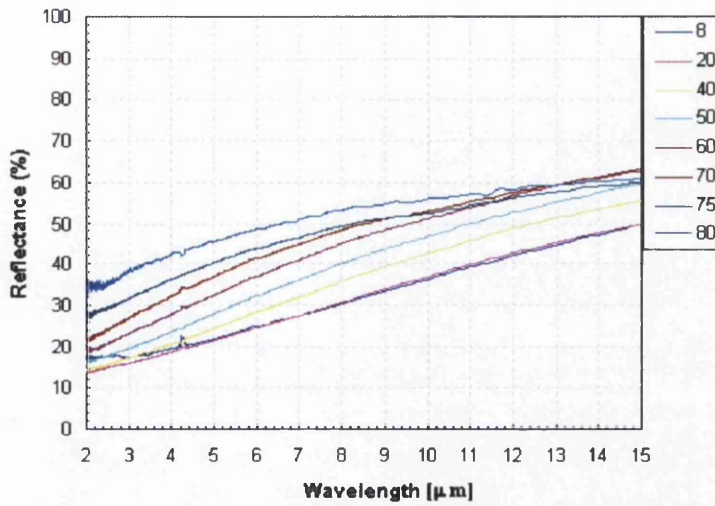
Figure 3.14: Specular directional reflectivity of the sample composed of aluminium
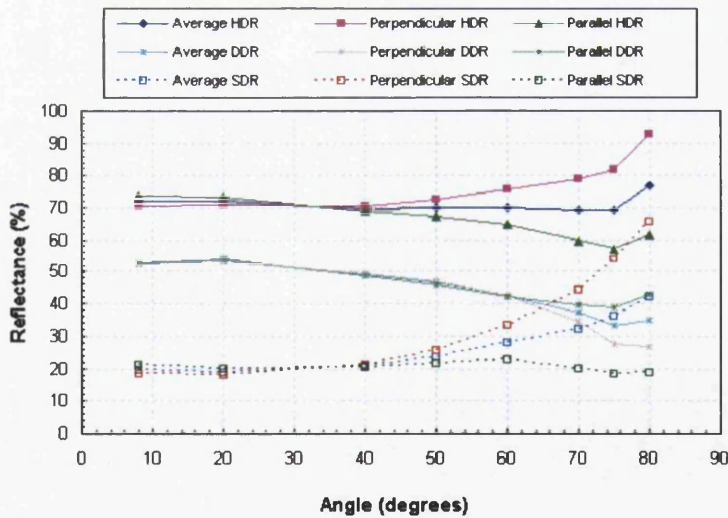
Figure 3.15: An aspect variation for $3 - 5$ $[\mu m]$ of the sample composed of aluminium
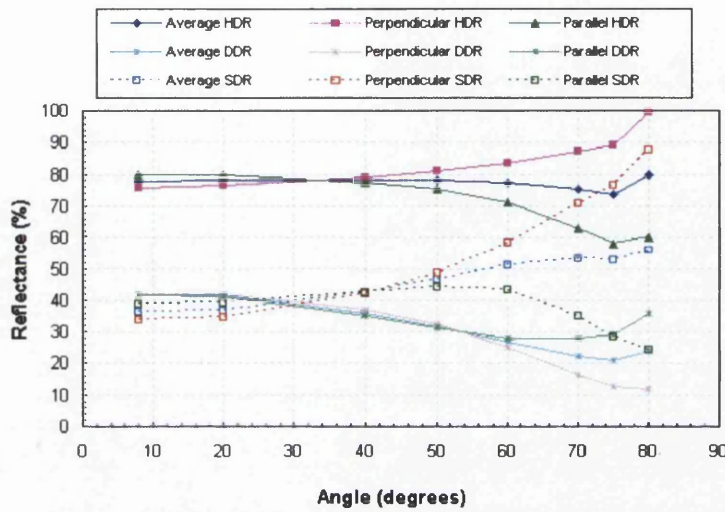
Figure 3.16: An aspect variation for $8 - 12$ $[\mu m]$ of the sample composed of aluminium
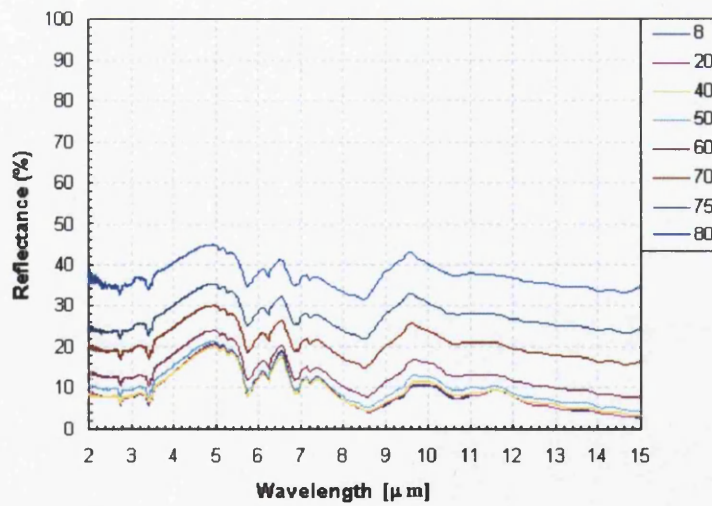
Figure 3.17: Hemispherical directional reflectivity of the front side of the sample composed of steel
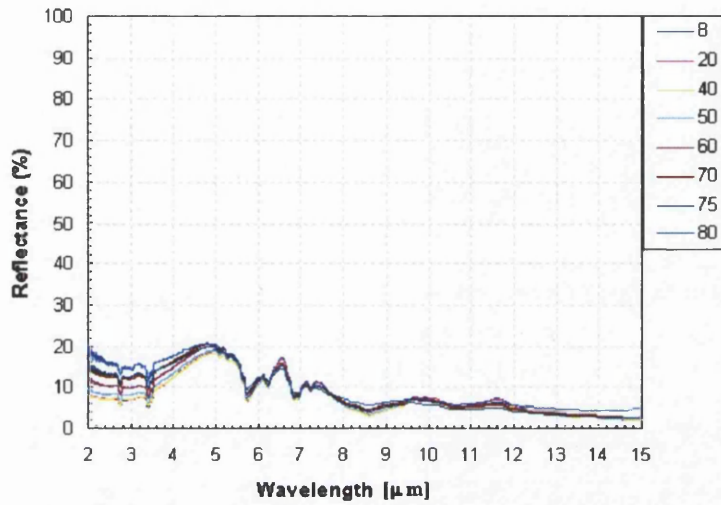
Figure 3.18: Diffuse directional reflectivity of the front side of the sample composed of steel
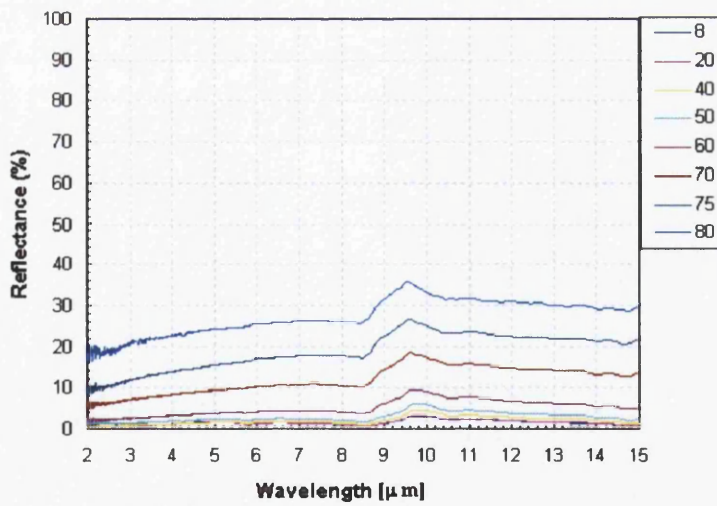
Figure 3.19: Specular directional reflectivity of the front side of the sample composed of steel
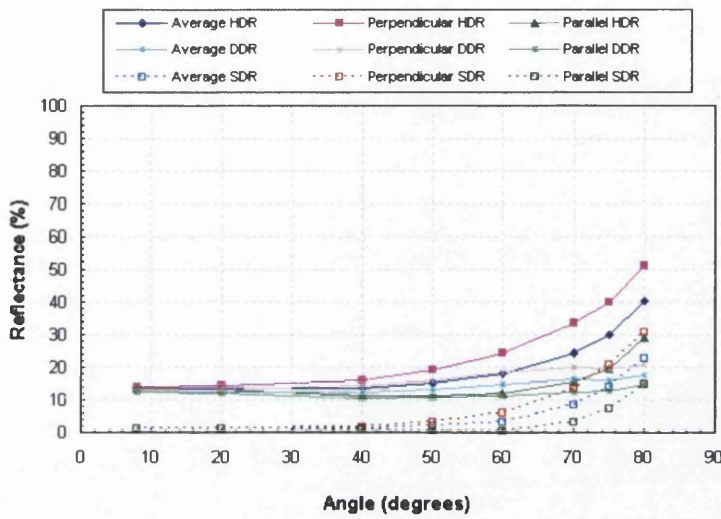
Figure 3.20: An aspect variation for $3-5$ $[\mu m]$ of the front side of the sample composed of steel
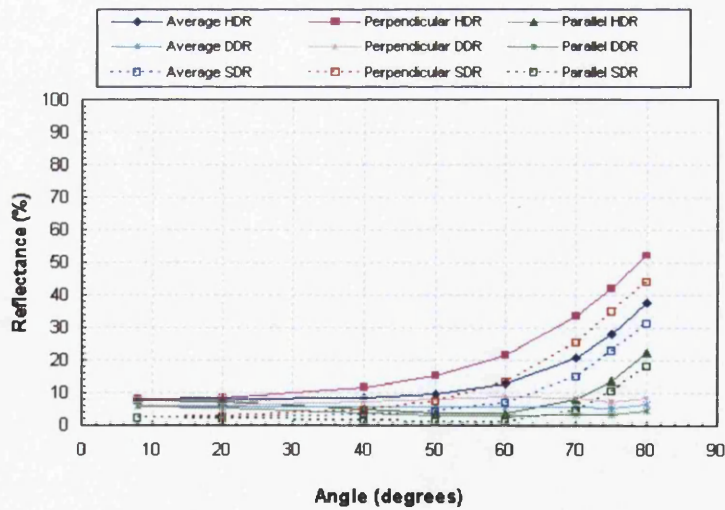
Figure 3.21: An aspect variation for $8-12$ $[\mu m]$ of the front side of the sample composed of steel
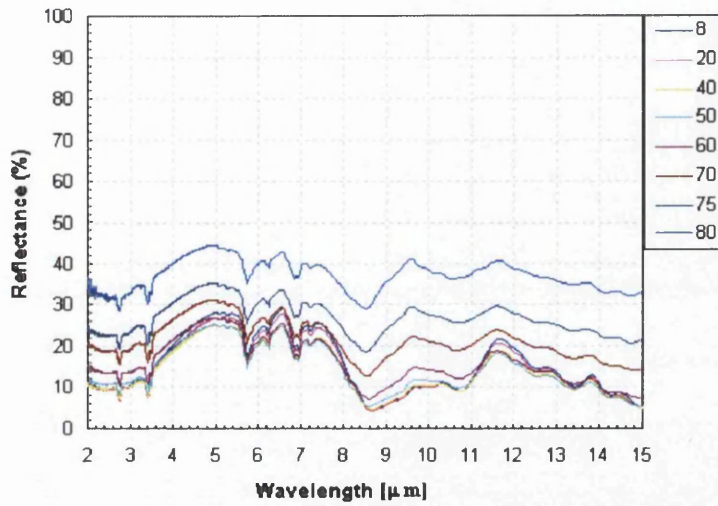
Figure 3.22: Hemispherical directional reflectivity of the back side of the sample composed of steel
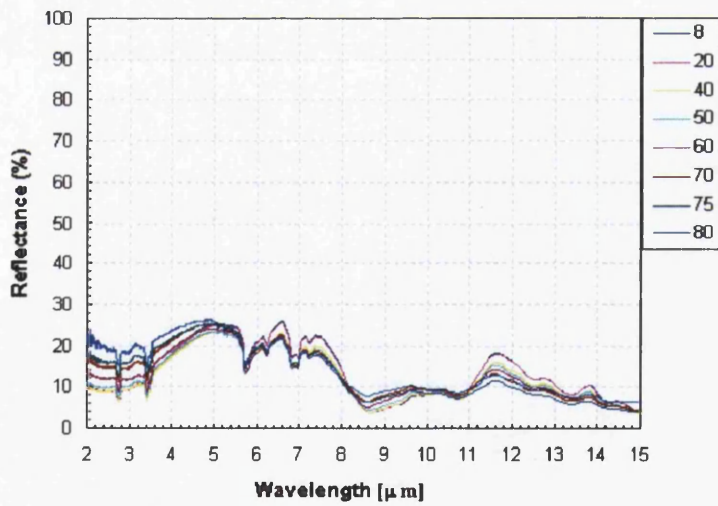
Figure 3.23: Diffuse directional reflectivity of the back side of the sample composed of steel
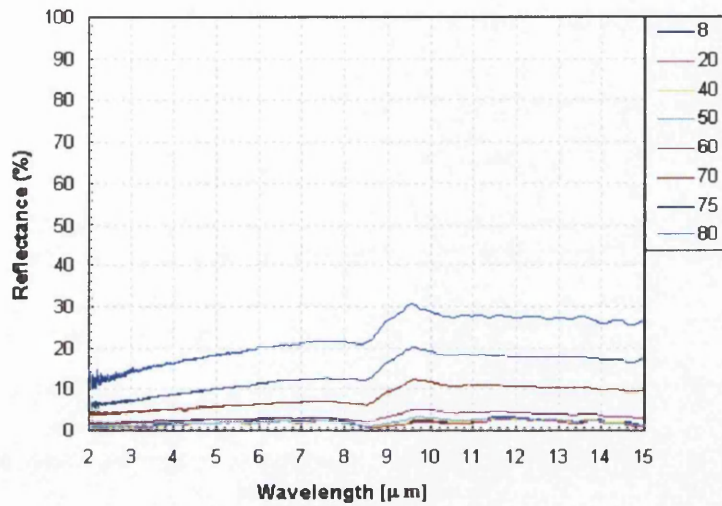
Figure 3.24: Specular directional reflectivity of the back side of the sample composed of steel
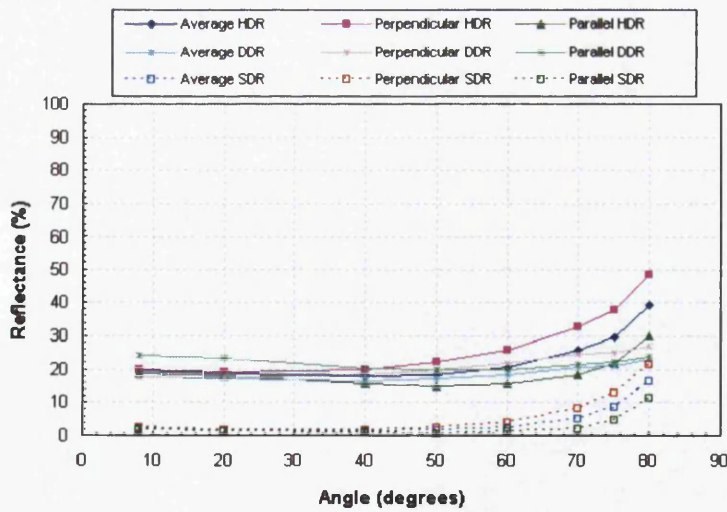
Figure 3.25: An aspect variation for $3-5$ $[\mu m]$ of the back side of the sample composed of steel
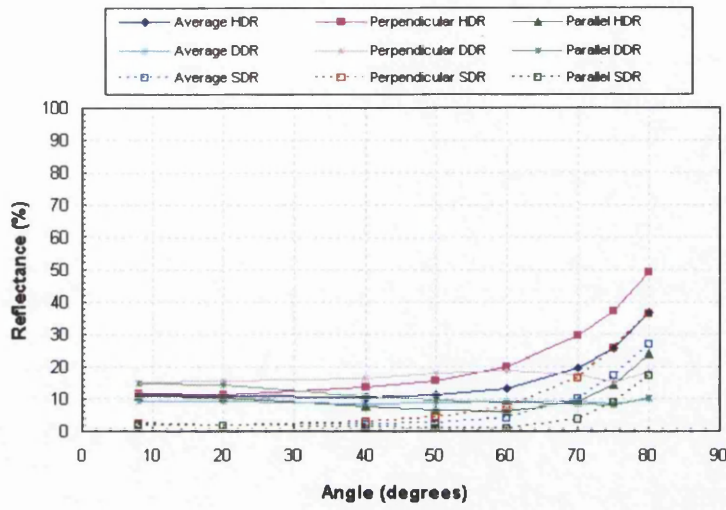
Figure 3.26: An aspect variation for $8-12$ $[\mu m]$ of the back side of the sample composed of steel
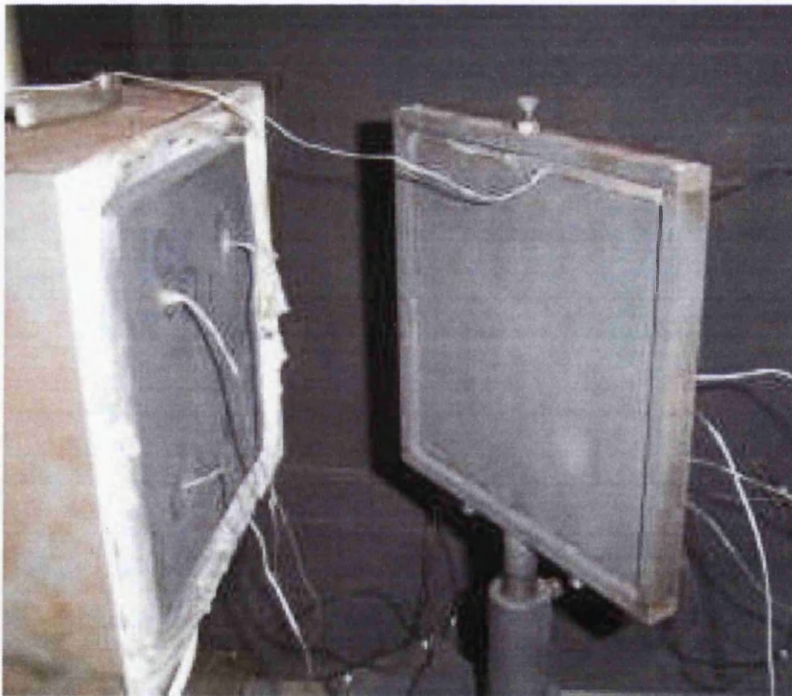
Figure 3.27: Experimental rig with a squared plate as an emitter
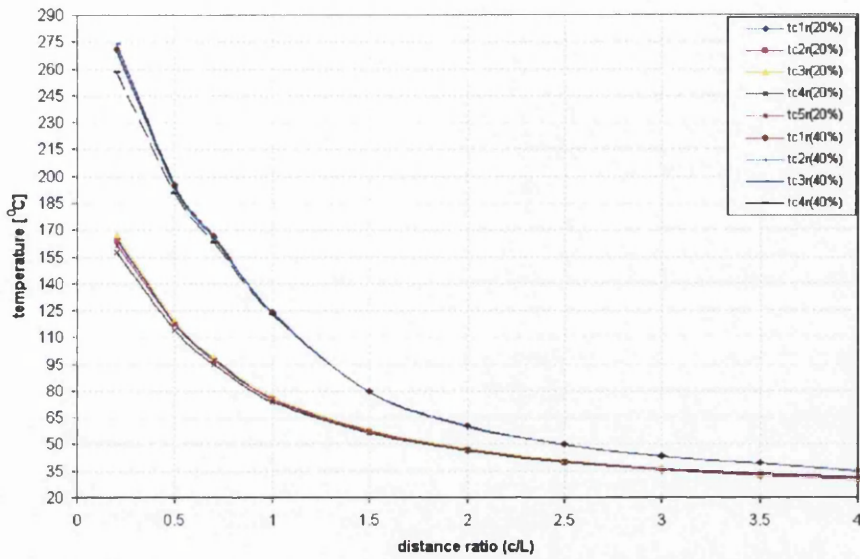
Figure 3.28: Temperatures of the receiver ($\neq$3x197x197 [mm]) composed of steel with dimension of (a square plate as an emitter)
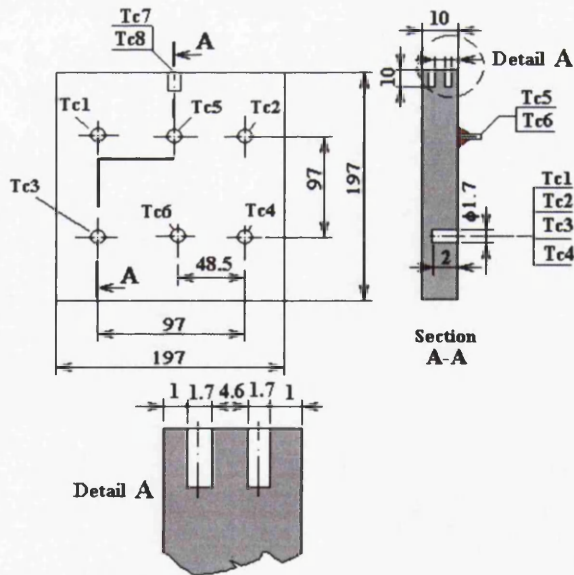
Figure 3.29: The receiver with measuring points (20% of power) with a square plate as an emitter
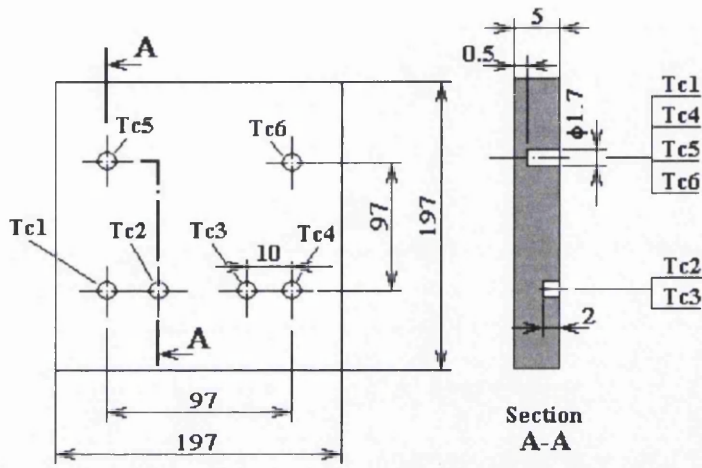
Figure 3.30: The receiver with measuring points (40% of power) with a square plate as an emitter
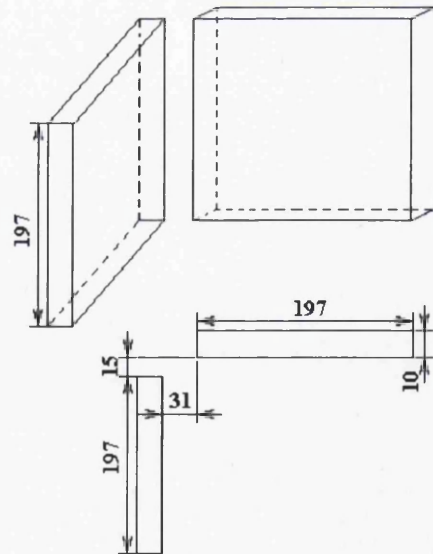
Figure 3.31: Hinged plates with a square plate as an emitter
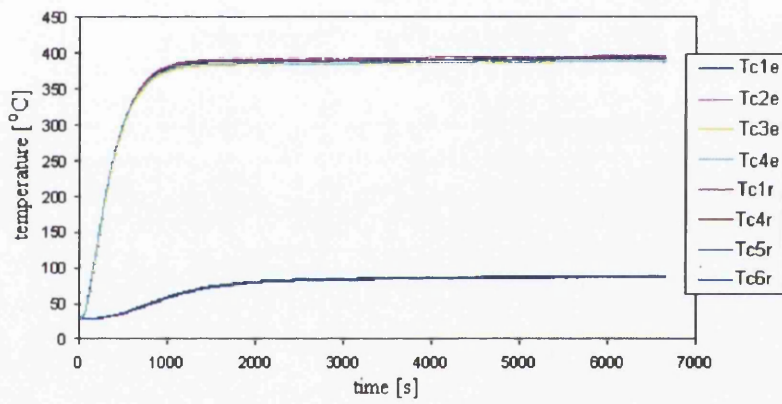
Figure 3.32: Temperatures of the emitter and the receiver for the distance $c/D = 1.0$ with a disc as an emitter and the steel plate ($\neq$5x197x197 $[mm]$) as a receiver
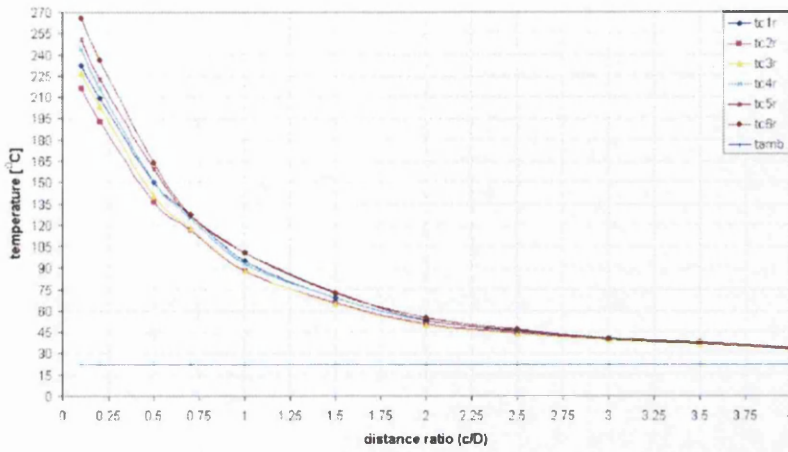
Figure 3.33: Temperatures of the receiver composed of steel ($\neq$5x197x197 [mm]) with a disc as an emitter
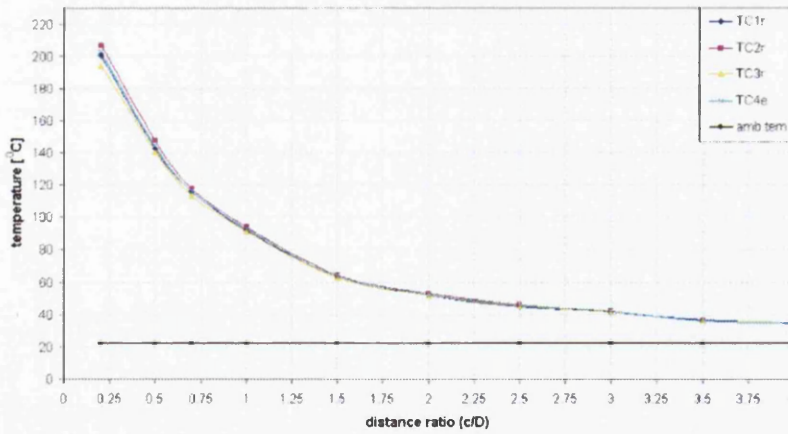
Figure 3.34: Temperatures of the receiver ($\neq$10x197x197 [mm]) composed of steel with a disc as an emitter
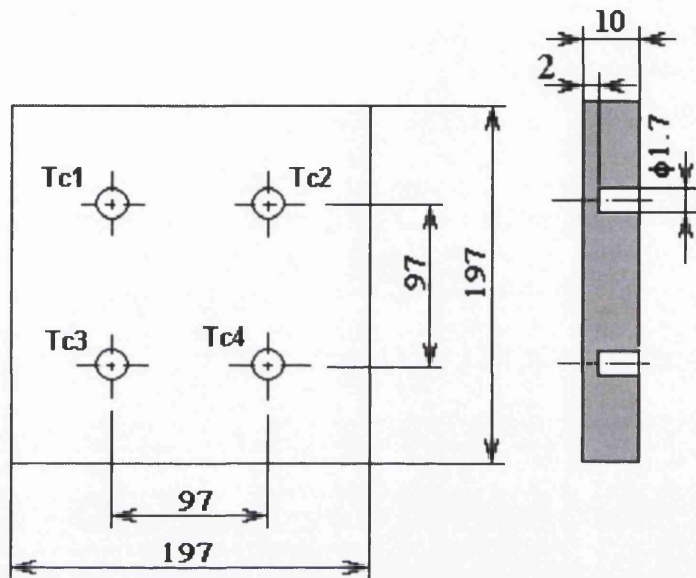
Figure 3.35: Measuring points of the receiver

Figure 3.36: Thermal image of the back side of the receiver
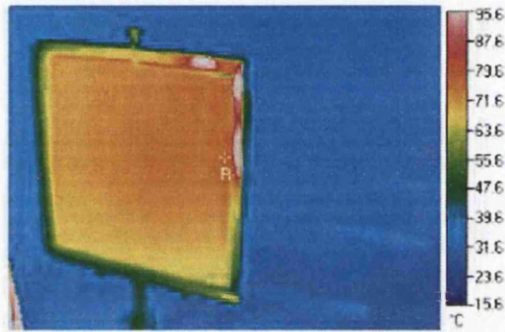
Figure 3.37: Thermal image of the front side of the receiver
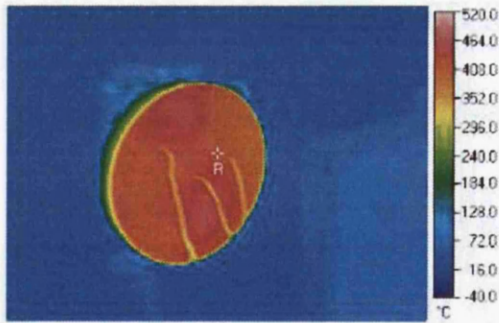
Figure 3.38: Thermal image of the front side of the emitter
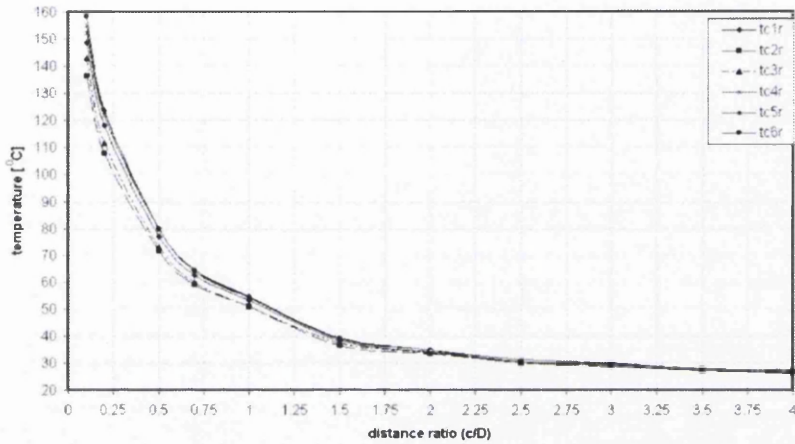
Figure 3.39: Temperatures of the receiver ($\neq$5x197x197 [mm]) composed of brass with a disc as an emitter
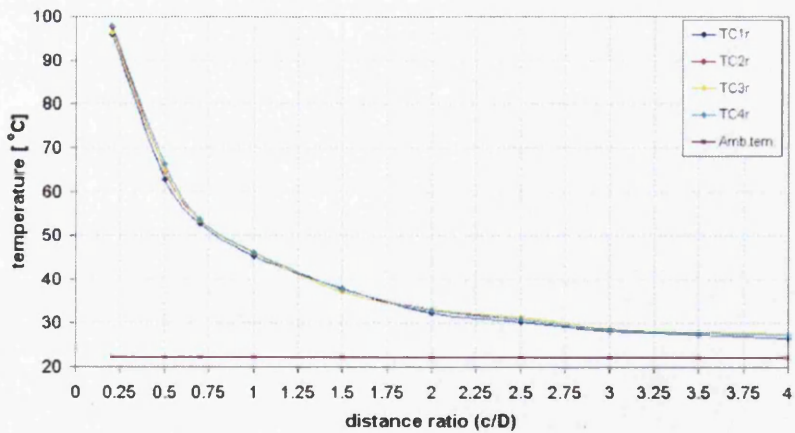
Figure 3.40: Temperatures of the receiver ($\neq$7x197x197 [mm]) composed of brass with a disc as an emitter
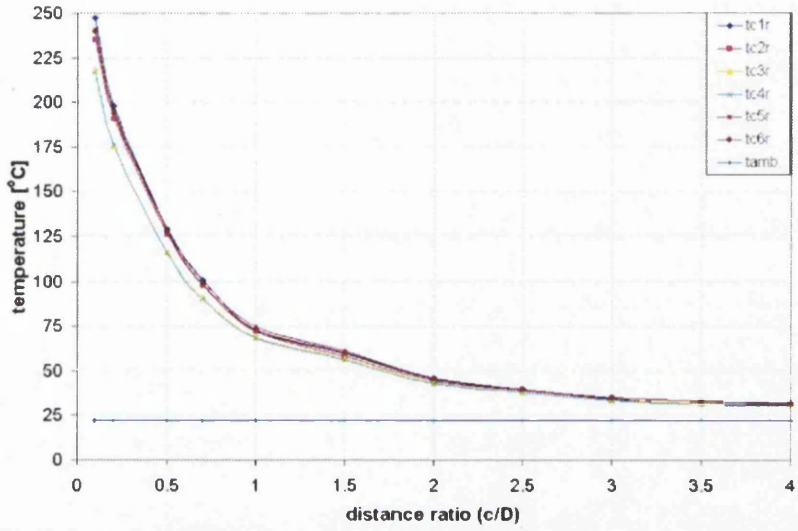
Figure 3.41: Temperatures of the receiver ($\neq$5x197x197 [mm]) composed of aluminium with a disc as an emitter
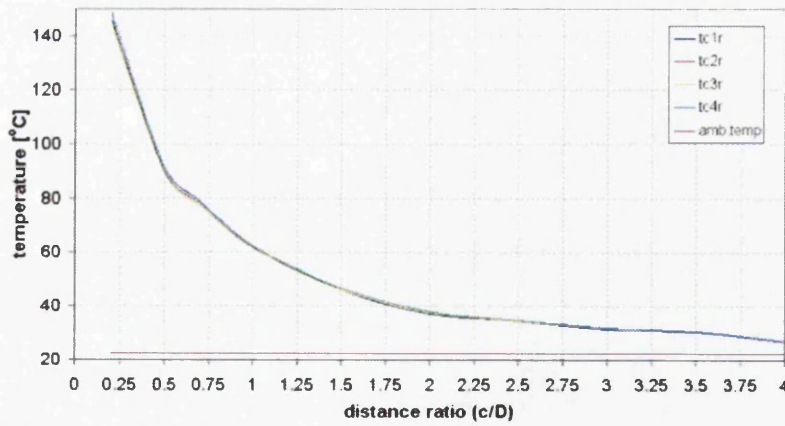
Figure 3.42: Temperatures of the receiver ($\neq$7x197x197 [mm]) composed of aluminium with a disc as an emitter
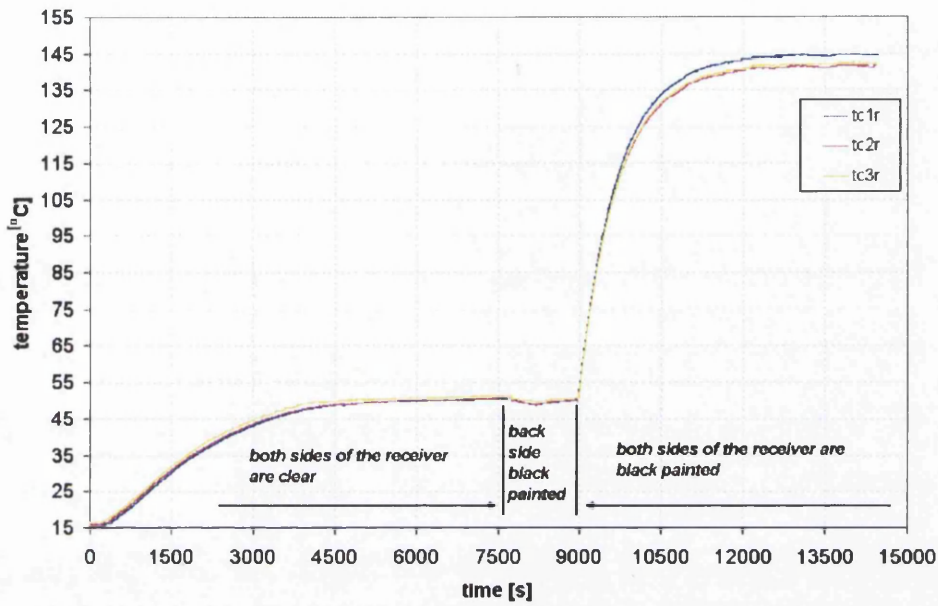
Figure 3.43: Temperatures of the receiver composed of brass with different emissivity with a disc as an emitter
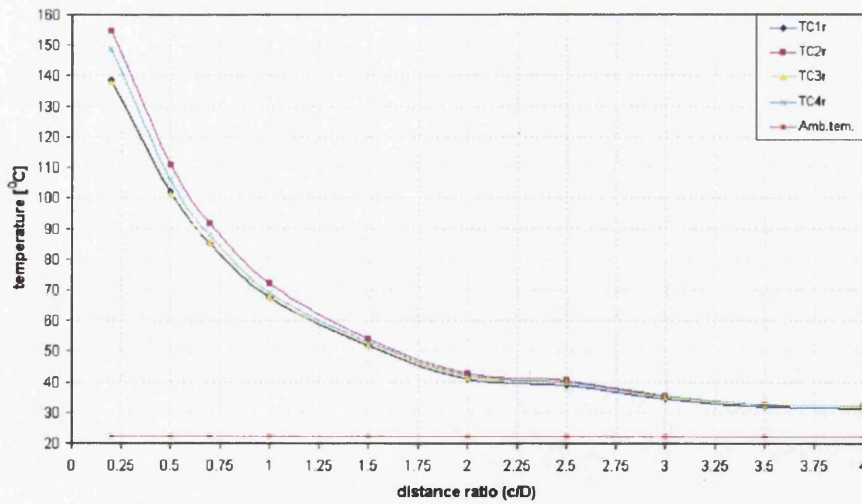
Figure 3.44: Temperatures of the receiver ($\neq$15x197x197 [mm]) composed of steel. The angle between the emitter (a disc) and the receiver was 25 degrees
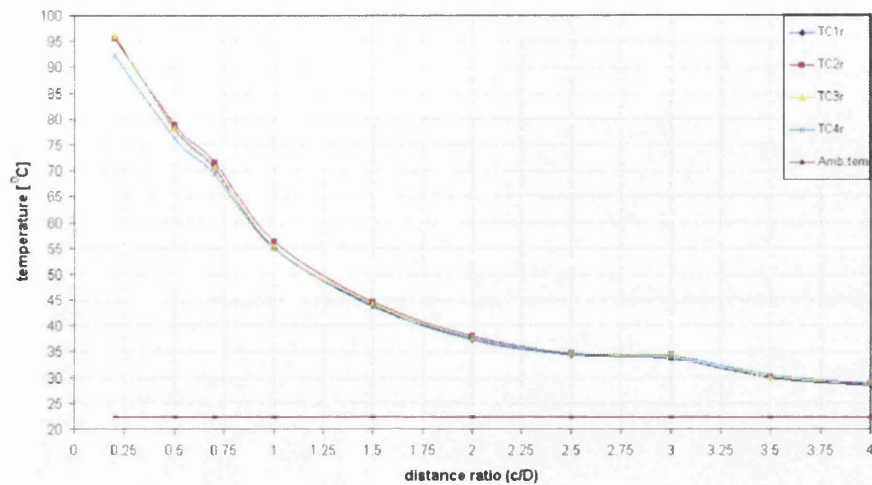
Figure 3.45: Temperatures of the receiver ($\neq$15x197x197 [mm]) composed of steel. The angle between the emitter (a disc) and the receiver was 50 degrees
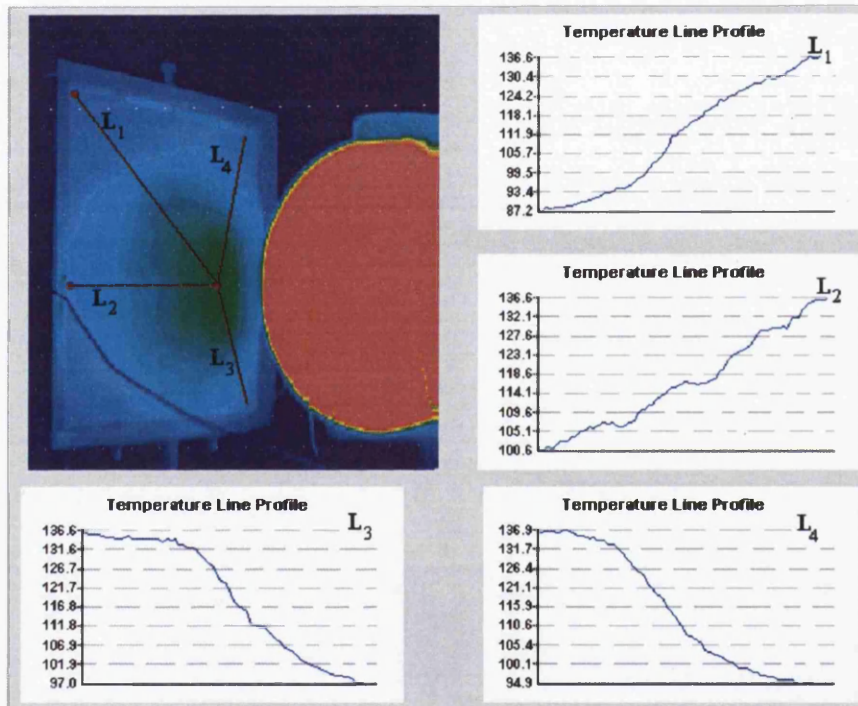
Figure 3.46: Thermal image of the front side of the receiver with temperature line profiles - Temperature scale in $[^oC]$
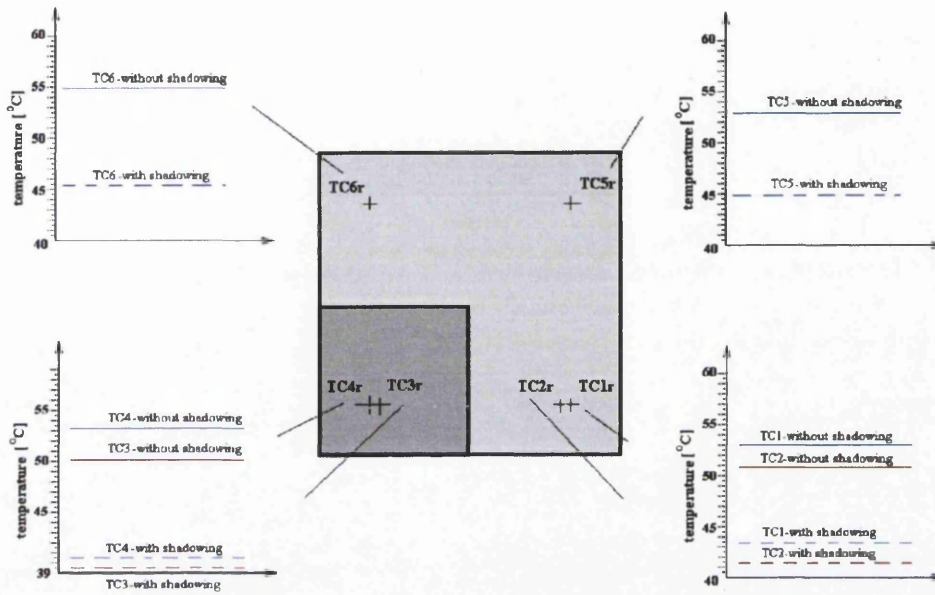
Figure 3.47: Temperatures of the receiver with and without shadowing
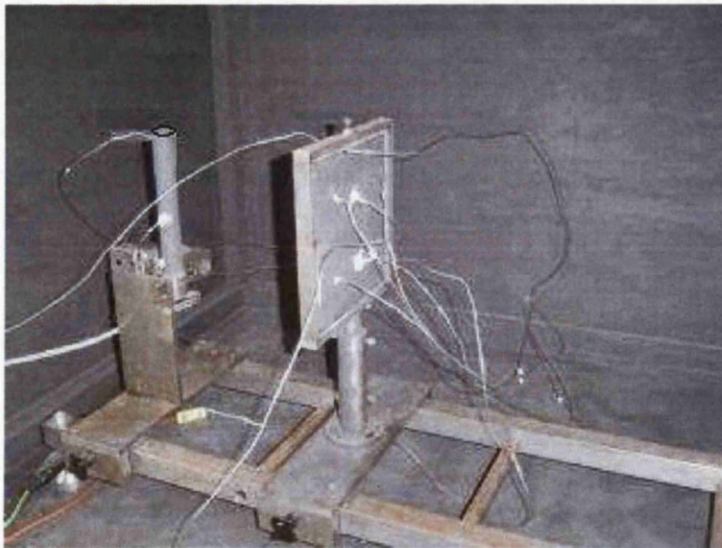
Figure 3.48: Experimental rig with a cylinder as an emitter and a receiver composed of steel
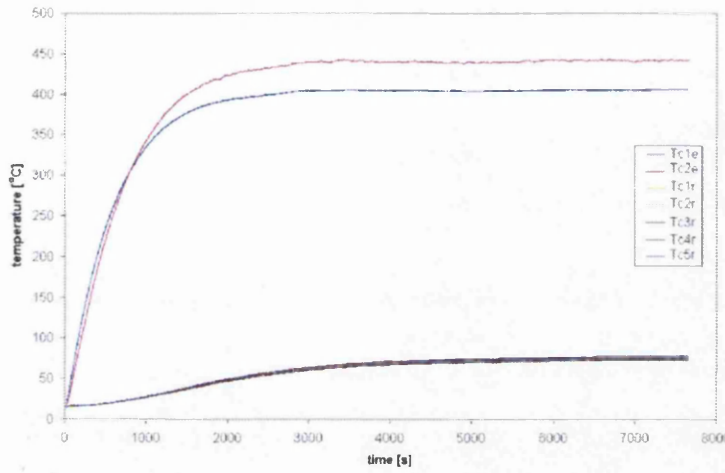
Figure 3.49: Transient temperatures of the emitter and the receiver composed of steel ($\neq$10x197x197 [mm])
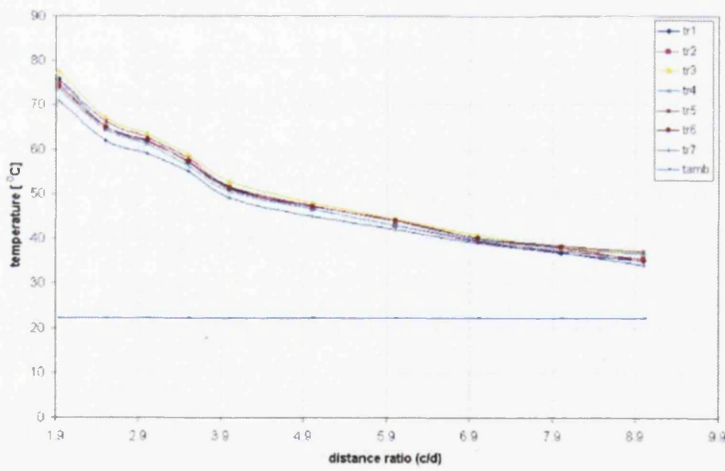
Figure 3.50: Temperatures of the receiver ($\neq$10x197x197 [mm]) composed of steel for different distance ratios with a cylinder as an emitter
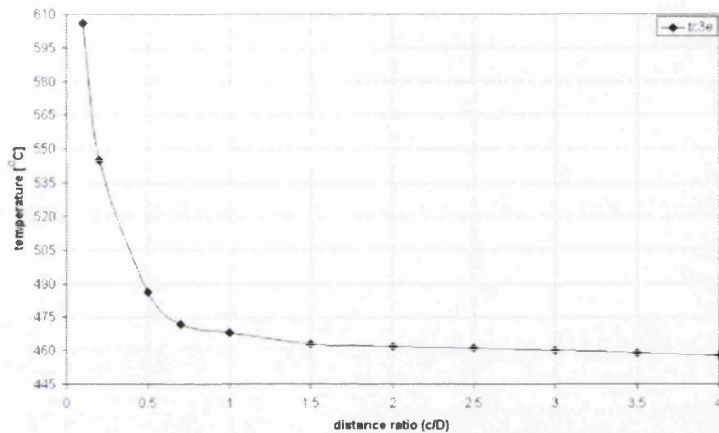
Figure 3.51: Temperatures of the center of the emitter (a disc) when the receiver is composed of brass
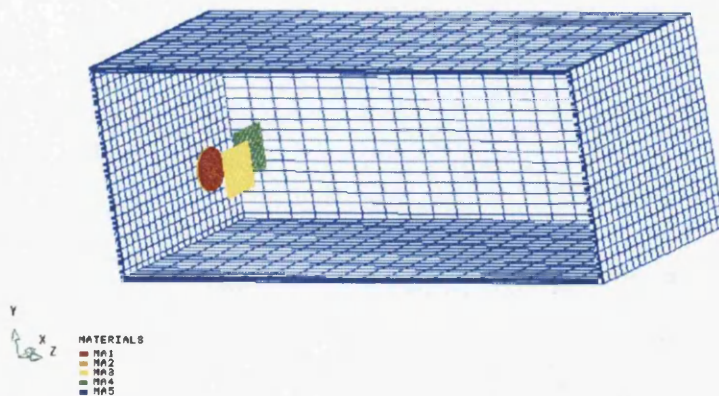
Figure 3.52: Positions of the emitter and receivers in more complex environment
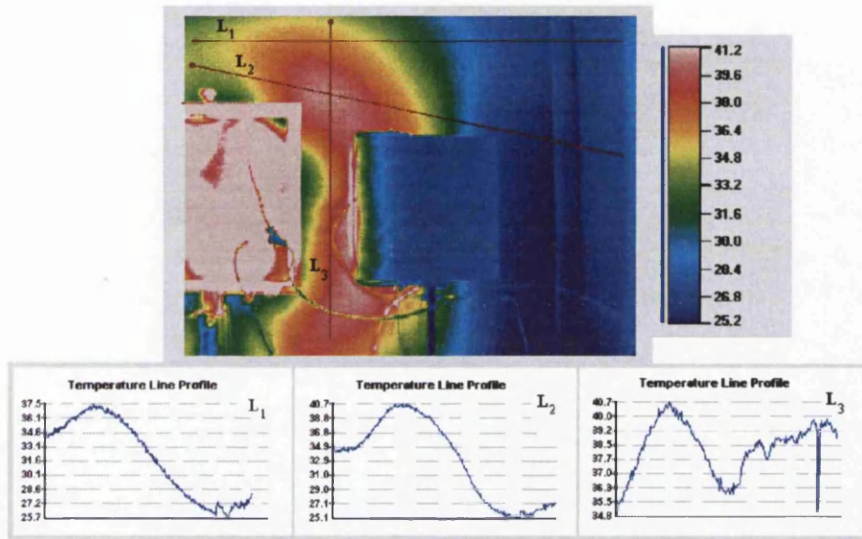
Figure 3.53: Temperature distribution of the box behind the emitter - Temperature scale in [^oC]

	Ref.	Point 2	Point 3	Point 4	Point 5	Point 6	Point 7	Point 8	Point 9	Point 10
Emissivity	1	1	1	1	1	1	1	1	1	1
Avg Temp °C										
Min Temp °C										
Max Temp °C	38.3	34.4	31.0	27.3	24.4	31.5	28.1	25.8	22.4	30.5
Delta Ref. °C		-3.9	-7.3	-11.0	-13.9	-6.8	-10.2	-12.5	-15.9	-7.8
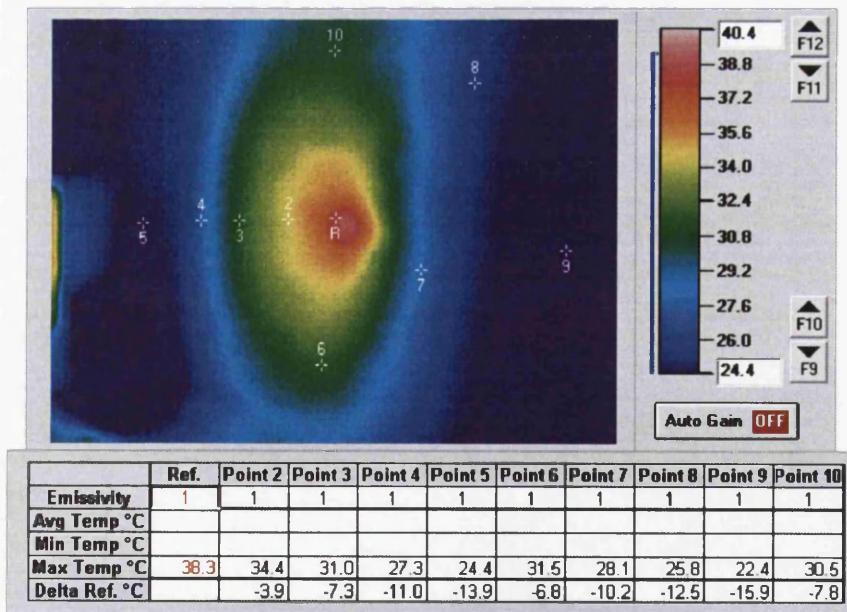
Figure 3.54: Temperature distribution of the box exposed to reflection of the receiver 1 and receiver 2 - Temperature scale in [^oC]
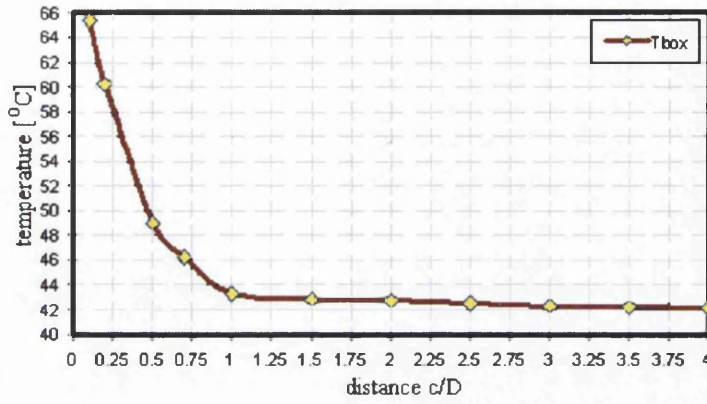
Figure 3.55: Internal temperature of the hottest point of the box for different distance ratios

	Ref.	Point 2	Point 3	Point 4	Point 5	Point 6	Point 7	Point 8	Point 9	Point 10
Emissivity	1	1	1	1	1	1	1	1	1	1
Avg Temp °C										
Min Temp °C										
Max Temp °C	34.6	35.8	36.3	35.4	34.3	33.1	32.4	25.7	30.1	37.8
Delta Ref. °C		1.2	1.7	0.8	-0.3	-1.5	-2.2	-8.9	-4.5	3.2
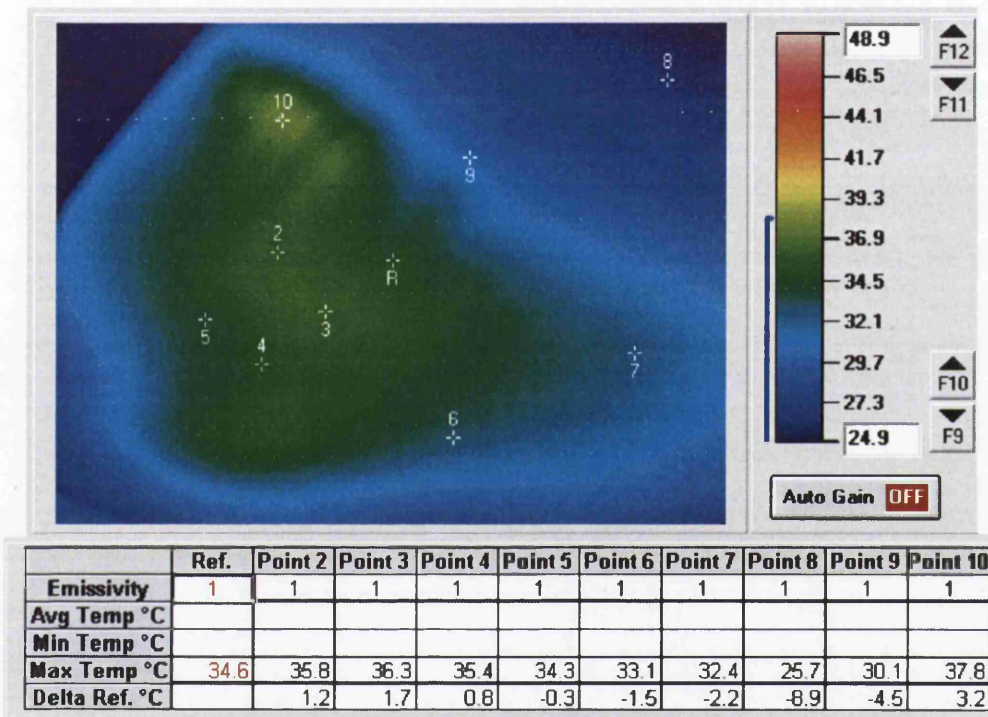
Figure 3.56: Temperature distribution of the top of the box (thermal image) - Temperature scale in [°C]

Chapter 4

The Finite Element Method

4.1   Introduction

During view factor calculations enclosure is discretized using the finite element technique. Later, thermal conduction (transient) which took place in heat transfer simulations is solved applying the Finite Element method . This is the main reason for giving a gentle introduction of Finite element method.

As it is known, the finite element method has been developed in parallel with the introduction of powerful and fast computers over the last forty years. It started from the field of structural analysis for stress calculation mainly between 1940 and 1960. Later, the concept, based on dividing a structure into small substructures of various shapes and re-assembling it after each substructure was analyzed, became a very useful tool for heat transfer calculation, solving fluid mechanics problems, electro magnetic calculation etc.

An introduction to the mathematical formulation of the finite element method can be found in Strang and Fix (1973). At same time an excellent engineering treatment of finite element methods is given by Zienkiewicz (1977) or Fletcher (1991).

4.2   Space Discretization

In the finite element method the space is broken into a set of discrete volumes (3D problems) or finite elements (2D problems) that are generally unstructured. Triangles and quadrilaterals are the most used elements in 2D analysis, while tetrahedra and hexahedra are most common in 3D analysis.

131

The finite element technique uses global (x, y, z) and local (ξ, η, ζ) coordinate systems. Governing equations analyzed later in the text will be given in terms of the global coordinates. In the text that follows the relationship between global and local coordinate systems will be explained. As an example the quadrilateral element is taken. The variables are approximated by linear combinations of known *basis* functions (also well-known as *shape, interpolation* functions). For a four-noded quadrilateral element with corner nodes the shape functions take the simple form:

$$
\begin{aligned}
N_1(\xi, \eta) &= \frac{1}{4}(1 - \xi)(1 - \eta) \\
N_2(\xi, \eta) &= \frac{1}{4}(1 - \xi)(1 + \eta) \\
N_3(\xi, \eta) &= \frac{1}{4}(1 + \xi)(1 + \eta) \\
N_4(\xi, \eta) &= \frac{1}{4}(1 + \xi)(1 - \eta)
\end{aligned}
\tag{4.1}
$$

The calculation made for this presentation considers an eight-noded quadrilateral element, eight-noded and twenty-noded hexahedron elements. The shape functions for these elements are given below. The shape functions of four-noded quadrilateral and eight-noded hexahedron elements are linear *Lagrangian* while the shape functions of eight-noded quadrilateral and twenty-noded hexahedron elements are quadratic *Lagrangian*.

eight-noded quadrilateral element:

$$
\begin{aligned}
N_1(\xi, \eta) &= \frac{1}{4}(\xi^2 - \xi)(\eta^2 - \eta) \\
N_2(\xi, \eta) &= \frac{1}{2}(\xi^2 + \xi)(\eta^2 - \eta) \\
N_3(\xi, \eta) &= \frac{1}{4}(\xi^2 + \xi)(\eta^2 - \eta) \\
N_4(\xi, \eta) &= \frac{1}{2}(\xi^2 + \xi)(1 - \eta^2) \\
N_5(\xi, \eta) &= \frac{1}{2}(\xi^2 + \xi)(\eta^2 + \eta) \\
N_6(\xi, \eta) &= \frac{1}{2}(1 - \xi^2)(\eta^2 + \eta) \\
N_7(\xi, \eta) &= \frac{1}{4}(\xi^2 - \xi)(\eta^2 + \eta) \\
N_8(\xi, \eta) &= \frac{1}{2}(\xi^2 - \xi)(1 - \eta^2)
\end{aligned}
\tag{4.2}
$$

In Figure 4.1 four different finite elements which are used in heat transfer

and fluid flow calculations are presented.

eight-noded hexahedron element:

$$\xi_i = (-1, -1, 1, 0, -1, -1, 1, 0)$$
$$\eta_i = (-1, -1, -1, -1, 1, 1, 1, 1)$$
$$\zeta_i = (-1, 1, 0, -1, -1, 1, 0, -1)$$
$$do \ k = 1, 8$$
$$\xi_p = \xi * \xi_i(k); \eta_p = \eta * \eta_i(k); \zeta_p = \zeta * \zeta_i(k)$$
$$if \ (k == 1.or.k == 2.or.k == 5.or.k == 6) \ then$$
$$N_{(k)}(\xi, \eta, \zeta) = \frac{1}{8}(1 + \xi_p)(1 + \eta_p)(1 + \zeta_p)(\xi_p + \eta_p + \zeta_p - 2)$$
$$if \ (k == 4.or.k == 8) \ then$$
$$N_{(k)}(\xi, \eta, \zeta) = \frac{1}{4}(1 - \xi^2)(1 + \eta_p)(1 + \zeta_p)$$
$$if \ (k == 3.or.k == 7) \ then$$
$$N_{(k)}(\xi, \eta, \zeta) = \frac{1}{4}(1 + \xi_p)(1 + \eta_p)(1 - \zeta^2) \qquad (4.3)$$

twenty-noded hexahedron element:

$$\xi_i = (-1, -1, -1, 0, 1, 1, 1, 0, -1, -1,$$
$$1, 1, -1, -1, -1, 0, 1, 1, 1, 0)$$
$$\eta_i = (-1, -1, -1, -1, -1, -1, -1, -1,$$
$$0, 0, 0, 0, 1, 1, 1, 1, 1, 1, 1, 1)$$
$$\zeta_i = (-1, 0, 1, 1, 1, 0, -1, -1, -1, 1,$$
$$1, -1, -1, 0, 1, 1, 1, 0, -1, -1)$$
$$do \ k = 1, 20$$
$$\xi_p = \xi \cdot \xi_i(k); \eta_p = \eta \cdot \eta_i(k); \zeta_p = \zeta \cdot \zeta_i(k)$$
$$if \ (k == 4.or.k == 8.or.k == 16.or.k == 20) \ then$$
$$N_{(k)}(\xi, \eta, \zeta) = \frac{1}{4}(1 - \xi^2)(1 + \eta_p)(1 + \zeta_p)$$
$$if \ (k >= 9.and.k <= 12) \ then$$
$$N_{(k)}(\xi, \eta, \zeta) = \frac{1}{4}(1 + \xi_p)(1 - \eta^2)(1 + \zeta_p)$$
$$if \ (k == 2.or.k == 6.or.k == 14.or.k == 18) \ then$$
$$N_{(k)}(\xi, \eta, \zeta) = \frac{1}{4}(1 + \xi_p)(1 + \eta_p)(1 - \zeta^2)$$
$$if \ (k == 1.or.k == 3.or.k == 5.or.k == 7.or.$$
$$k == 13.or.k == 15.or.k == 17.or.k == 19) \ then$$

$$N_{(k)}(\xi, \eta, \zeta) = \frac{1}{8}(1 + \xi_p)(1 + \eta_p)(1 + \zeta_p)(\xi_p + \eta_p + \zeta_p - 2) \tag{4.4}$$

For four-noded quadrilateral element, as mentioned earlier, we have that

$$x = N_1 x_1 + N_2 x_2 + N_3 x_3 + N_4 x_4 = \mathbf{N}\mathbf{x}$$
$$y = N_1 y_1 + N_2 y_2 + N_3 y_3 + N_4 y_4 = \mathbf{N}\mathbf{y} \tag{4.5}$$

Derivatives of the shape functions can be easily converted from one coordinate system to the other by applying the chain rule of partial differentiation. The expression in matrix form is given below.

$$\begin{bmatrix} \frac{\partial}{\partial \xi} \\ \frac{\partial}{\partial \eta} \end{bmatrix} = \begin{bmatrix} \frac{\partial x}{\partial \xi} & \frac{\partial y}{\partial \xi} \\ \frac{\partial x}{\partial \eta} & \frac{\partial y}{\partial \eta} \end{bmatrix} \begin{bmatrix} \frac{\partial}{\partial x} \\ \frac{\partial}{\partial y} \end{bmatrix} = \mathbf{J} \begin{bmatrix} \frac{\partial}{\partial x} \\ \frac{\partial}{\partial y} \end{bmatrix} \tag{4.6}$$

or

$$\begin{bmatrix} \frac{\partial}{\partial x} \\ \frac{\partial}{\partial y} \end{bmatrix} = \mathbf{J}^{-1} \begin{bmatrix} \frac{\partial}{\partial \xi} \\ \frac{\partial}{\partial \eta} \end{bmatrix} \tag{4.7}$$

where **J** is the *Jacobian* matrix. Following integrals transformation

$$\int\int dxdy = \int_{-1}^{1}\int_{-1}^{1} det|\mathbf{J}|d\xi d\eta \tag{4.8}$$

$det|\mathbf{J}|$ needs to be calculated.

4.3 Numerical Integration

In the cases that the integration function is not given in the explicit form, as well as tablature values of the integration function in the integration domain, the integral presented in equation (4.8) is evaluated numerically, using **Gauss-Legendre** integration formula.

The main characteristic of this method is that the integration function is approximated by Lagrange polynomial. In 2D case it is:

$$\int_{-1}^{1}\int_{-1}^{1} f(\xi,\eta)d\xi d\eta \simeq \sum_{i=1}^{n}\sum_{j=1}^{n} w_i w_j f(\xi_i \eta_j)$$

$$\simeq \sum_{i=1}^{nip} W_i f(\xi,\eta)_i \tag{4.9}$$

where $nip = n^2$ is the total number of integration points, w_i and w_j or W_i are weighting coefficients and ξ_i, η_j are coordinate positions within the element. Values of weighting coefficient can be found in almost every finite element book.

The accuracy of the numerical integration depends on the number of chosen integration points. At the same time the number of integration points depends on the chosen polynomial that approximated the integration function.
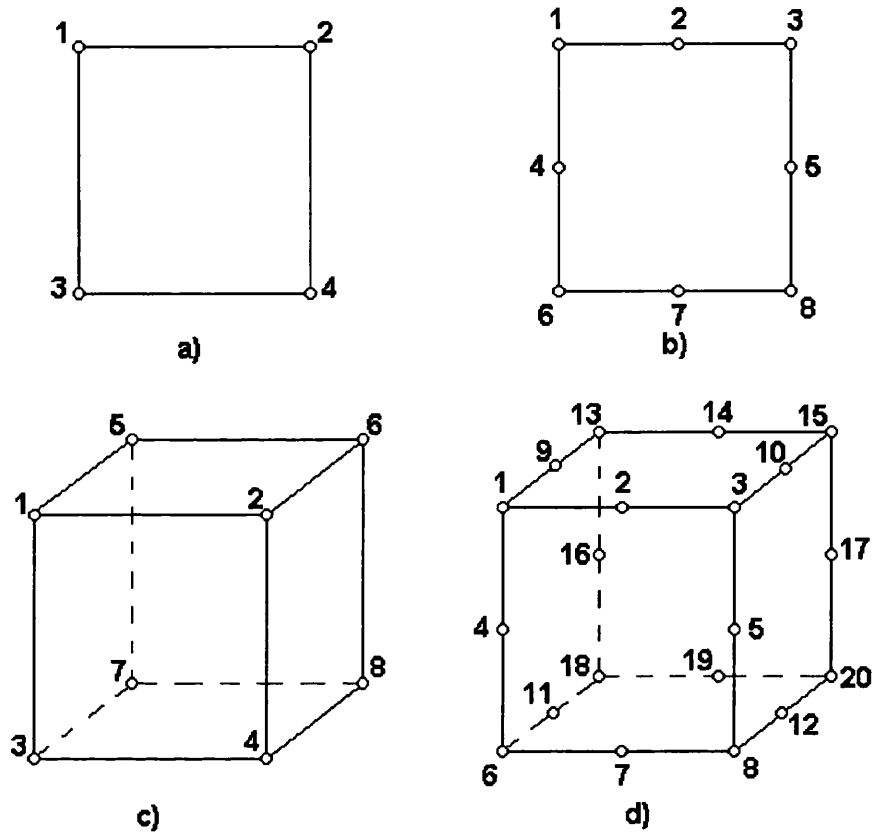
Figure 4.1: a) four noded and b) eight noded quadrilateral elements, c) eight noded and d) twenty noded hexahedron elements

Chapter 5

Heat Conduction

5.1 Basic Equations

The principle of conservation of heat energy over a fixed volume, V, of a medium bounded by a closed surface S, can be used to derive the equation governing heat conduction. The conservation statement is expressed in rate form (Lewis (1996)), so:

rate of increase of heat in V = *rate of heat conduction into V across S*

+ *rate of heat generation within V* (5.1)

The first term in equation (5.1) is defined as:

$$\text{rate of increase of heat in } V = \int_V \rho \frac{\partial u}{\partial t} dV \qquad (5.2)$$

where u is the specific internal energy of the medium. Using $\frac{\partial u}{\partial t} = \frac{\partial u}{\partial T} \cdot \frac{\partial T}{\partial t}$, and introducing the specific heat, c, of the medium defined by $c = \frac{du}{dT}$, yields the following equation:

$$\text{rate of increase of heat in } V = \int_V \rho c \frac{\partial T}{\partial t} dV \qquad (5.3)$$

The second term of equation (5.1) is defined by **Fourier's** Law of conduction, and it is:

$$q = -k(gradT) \cdot \mathbf{n} = -k \frac{\partial T}{\partial n} \qquad (5.4)$$

where k is the thermal conductivity. Finally, the second term could be written as:

$$\text{rate of heat conduction into } V \text{ across } S = \int_S -q dS$$

$$= \int_S k(gradT)\mathbf{n}dS = \int_V div(k \ grad \ T)dV \qquad (5.5)$$

In the third term of equation (5.1), it is assumed that the heat generation is taken as a rate Q per unit volume and it is:

$$rate\ of\ heat\ generation\ within\ V = \int_V QdV \qquad (5.6)$$

Using the final expressions of the terms equation (5.1) produces the conservation statement:

$$\int_V \left(\rho c \frac{\partial T}{\partial t} - div(k\ grad\ T) - Q\right)dV = 0 \qquad (5.7)$$

If the medium is anisotropic, then the thermal conductivity depends upon direction, and is a tensor. Hence, the heat transfer equation is modified to:

$$\int_V \left(\rho c \frac{\partial T}{\partial t} - div(\mathbf{K}grad\ T) - Q\right)dV = 0 \qquad (5.8)$$

where

$$\mathbf{K} = \begin{bmatrix} k_{xx} & k_{xy} & k_{xz} \\ k_{yx} & k_{yy} & k_{yz} \\ k_{zx} & k_{zy} & k_{zz} \end{bmatrix} \qquad (5.9)$$

Steady-state heat conduction is a special case where it is $\frac{\partial T}{\partial t} = 0$, so equation (5.8) becomes:

$$\int_V \left(div(kgradT) + Q\right)dV = 0 \qquad (5.10)$$

Usually, the heat transfer problem is treated in a domain Ω bounded by a closed surface Γ. The classical statement of this problem can be written as:

$$div(k\ gradT) + Q = 0\ in\ \Omega \qquad (5.11)$$

$$T = f(x)\ for\ x\ on\ \Gamma_1 \qquad (5.12)$$

$$q(x) = -(k\ gradT) \cdot \mathbf{n} = -k\frac{\partial T}{\partial n}\ for\ x\ on \Gamma_2 \qquad (5.13)$$

However, the majority of engineering problems to be solved are transient. First-order time dependent heat conduction in non conservative form is given below as:

$$\frac{\partial T}{\partial t} = \frac{k}{\rho \cdot c_p}\left(\frac{\partial^2 T}{\partial x^2} + \frac{\partial^2 T}{\partial y^2} + \frac{\partial^2 T}{\partial z^2}\right) \qquad (5.14)$$

5.2   Finite Element Method and Heat Conduction

In Chapter 4 a theoretical explanation of the finite element method was given. In this section the analysis which treats the finite element method application in heat conduction is presented. At the beginning equation (5.14) is considered in the form:

$$\frac{\partial}{\partial x}\left(k\frac{\partial}{\partial x}T\right) + \frac{\partial}{\partial y}\left(k\frac{\partial}{\partial y}T\right) = q \qquad (5.15)$$

written as $F(T) = q$, where F represents the differential operator. Assuming that $\widetilde{T}$ is an approximation to the solution T, the quantity R, called *residual*,

$$R(\widetilde{T}) = F(\widetilde{T}) - q = \vec{\nabla} \cdot (k\vec{\nabla}\widetilde{T}) - q \qquad (5.16)$$

is different from zero. Hence the residual appears as a measure of the accuracy of the approximation $\widetilde{T}$. Since this error cannot be made to vanish simultaneously in all the points of the discretized domain, a very good solution can be extracted by requiring that some weighted average of the residuals over the domain should be identically zero. If $W(\vec{x})$ is a weight function with appropriate smoothness properties, the *method of weighted residual*, or weak formulation, requires

$$\int_{\Omega} W F(\widetilde{T}) d\Omega = 0 \qquad (5.17)$$

Applying the last equation into equation (5.16) it becomes:

$$\int_{\Omega} W\vec{\nabla} \cdot (k\vec{\nabla}\widetilde{T}) d\Omega = \int_{\Omega} qW d\Omega \qquad (5.18)$$

According to **Green's** (some authors call it **Gauss**) theorem an integration by parts of the second-order derivative terms right-hand side of equation (5.18) becomes:

$$\int_{\Omega} W\vec{\nabla} \cdot (k\vec{\nabla}\widetilde{T}) d\Omega = -\int_{\Omega} k\vec{\nabla}\widetilde{T} \cdot \vec{\nabla}W d\Omega + \oint_{\Gamma} k\frac{\partial\widetilde{T}}{\partial n}W d\Gamma \qquad (5.19)$$

where the normal derivative along the boundary Γ of the domain appears on the right-hand side. Hence, equation (5.18) becomes

$$-\int_{\Omega} k\vec{\nabla}\widetilde{T} \cdot \vec{\nabla}W d\Omega + \oint_{\Gamma} k\frac{\partial\widetilde{T}}{\partial n}W d\Gamma = \int_{\Omega} qW d\Omega \qquad (5.20)$$

There are several different methods according to the choice of the weighting functions.

5.2.1 The Galerkin Method

The Galerkin method is the most widely used method, in which the weighting functions are taken equal to the shape functions (eq.(4.1), (4.2), (4.3) and (4.4)). There is,

$$\mathbf{W} = \mathbf{N}_j \tag{5.21}$$

The heat conduction equation (steady or transient) has one unknown variable (temperature) which means that it has only one degree of freedom per node.

Assuming that $\widetilde{T} = \mathbf{N}_i \mathbf{T}_i$ and the choice $W = \mathbf{N}_j$ equation (5.20) becomes

$$-\sum_i T_i \int_{\Omega_j} k \vec{\nabla} \mathbf{N}_i \cdot \vec{\nabla} \mathbf{N}_j d\Omega + \oint_\Gamma k \frac{\partial \widetilde{T}}{\partial n} \mathbf{N}_j d\Gamma = \int_{\Omega_j} q \mathbf{N}_j d\Omega \tag{5.22}$$

where Ω_j is the subdomain of all elements containing node j and the summation over i covers all the nodes of Ω_j. The first term of the right-hand side of equation (5.22) includes a matrix called the stiffness matrix. The stiffness matrix can be written as:

$$\mathbf{K}_{ij} = \int_{\Omega_j} k \vec{\nabla} \mathbf{N}_i \cdot \vec{\nabla} \mathbf{N}_j d\Omega \equiv (k \vec{\nabla} \mathbf{N}_i, \vec{\nabla} \mathbf{N}_j) \tag{5.23}$$

5.3 Time Dependent Heat Conduction

5.3.1 Introduction

During a calculation of unsteady problems, time as a fourth coordinate direction has to be considered, and together with the space coordinates, must be discretized.

The transient heat conduction is governed by following equation

$$\rho c \frac{\partial T}{\partial t} = div(k \ grad \ T) + Q \tag{5.24}$$

After the finite element discretization equation (5.24) transforms into the matrix equation system

$$\mathbf{M\dot{T}} + \mathbf{KT} = \mathbf{f} \tag{5.25}$$

where $\mathbf{M}$ is the capacitance (mass) matrix, $\mathbf{K}$ is the conductance (coefficient stiffness) matrix, $\mathbf{f}$ is right hand side, and $\mathbf{\dot{T}}$ is the temperature differentiated with respect to time.

Many solution methods for time dependent problems have a step-by-step strategy and they are very similar to ones applied to initial value problems for ordinary differential equations (ODEs) Ferziger (1998). An ordinary differential equation with an initial condition is given below:

$$\frac{d\phi(t)}{dt} = f\big(t, \phi(t)\big); \ \ \phi(t_0) = \phi^0 \tag{5.26}$$

The basic problem is to find the solution ϕ a short time Δt after the initial point. The solution $(\phi^1, t_1 = t_0 + \Delta t)$ is used as a new initial condition for next step $t_2 = t_1 + \Delta t, \ldots, t_n = t_{n-1} + \Delta t$.

An integration of equation (5.26) from t_n to t_{n-1} gives:

$$\int_{t_n}^{t_{n+1}} \frac{d\phi}{dt}dt = \phi^{n+1} - \phi^n = \int_{t_n}^{t_{n+1}} f\big(t, \phi(t)\big)dt \tag{5.27}$$

where $\phi^{n+1} = \phi(t_{n+1})$. This equation is exact. The right-hand side of this equation cannot be evaluated without knowing the solution so some approximation is necessary.

5.3.2 Explicit(Forward Euler) Method

The right-hand side of equation (5.27) is solved in the following way:

$$\phi^{n+1} = \phi^n + f(t_n, \phi^n)\Delta t \tag{5.28}$$

This is the simplest method in which all fluxes and sources are evaluated using known values at t_n. Equation (5.28) can be derived from a **Taylor's** series expansion, which is:

$$\phi(t + \Delta t) = \phi(t) + \Delta t \frac{\partial \phi}{\partial t} + \frac{\Delta t^2}{2!}\frac{\partial^2 \phi}{\partial t^2} + \ldots + \frac{\Delta t^i}{i!}\frac{\partial^i \phi}{\partial t^i} \tag{5.29}$$

A comparison between equations (5.28) and (5.29) shows that the time step length Δt (the error involved in the approximation is proportional to the time step length) taken in (5.28) is first-order, so the explicit method is a first-order method. Applying this method to the transient heat conduction matrix equation system (5.25) yields (Lewis (1996)):

$$\mathbf{M} \cdot \mathbf{T}^{n+1} = (\mathbf{M} - \Delta t\mathbf{K})\mathbf{T}^n + \Delta t f^n \tag{5.30}$$

5.3.3 Implicit(Backward Euler) Method

If, instead, the final point in estimating the integral is used then this yields:

$$\phi^{n+1} = \phi^n + f(t_{n+1}, \phi^{n+1})\Delta t \qquad (5.31)$$

If stability is a prime requirement, the implicit method is highly recommended. In this method, all fluxes and source terms are evaluated in terms of the unknown variable values at the new time level. This method requires much more memory storage than the explicit method. On the other hand the advantage is the possibility of using a large time step, which may result in a more efficient procedure. Applying this method to the transient heat conduction matrix equation system (5.25) yields:

$$(\mathbf{M} + \Delta t\mathbf{K})\mathbf{T}^{n+1} = \mathbf{M}\mathbf{T}^n + \Delta t\mathbf{f}^n \qquad (5.32)$$

5.3.4 θ (Crank-Nicolson) Method

Using straight line interpolation between the initial and final points to construct the approximation gives the following equation:

$$\phi^{n+1} = \phi^n + \frac{1}{2}[f(t_n, \phi^n) + f(t_{n+1}, \phi^{n+1})]\Delta t \qquad (5.33)$$

which is called the *trapezoid rule* and is the basis for the Crank-Nicolson method. The Crank-Nicolson method is an implicit method with second order accuracy and it is the special case of the θ method.

Applying this method to the transient heat conduction matrix equation system (5.25) yields:

$$(\mathbf{M} + \theta\Delta t\mathbf{K})\mathbf{T}^{n+1} = (\mathbf{M} - (1-\theta)\Delta t\mathbf{K})\mathbf{T}^n + \Delta t\mathbf{f}^n \qquad (5.34)$$

5.3.5 Predictor-Corrector Method

The Predictor-Corrector method is a method that tries to include good characteristics of the explicit and the implicit methods. It is known that the explicit method uses little computer memory (little computation time per step) but it is a very unstable method for large time steps, while the implicit method uses more computer memory, but it is a more stable method then the explicit one.

The basic idea is that the solution at the new time step is *predicted* using the explicit method, then the solution is *corrected* applying the trapezoid

rule.

$$\phi^*_{n+1} = \phi^n + f(t_n, \phi^n)\Delta t \tag{5.35}$$

$$\phi_{n+1} = \phi^n + \frac{1}{2}\Big[f(t_n, \phi^n) + f(t_{n+1}, \phi^*_{n+1})\Big]\Delta t \tag{5.36}$$

5.3.6 Runge-Kutta Methods

There are a few different Runge-Kutta methods which are graded from the first to the fourth order.

The fourth order Runge-Kutta method is the most popular Runge-Kutta method. The first two steps of this method use an explicit Euler predictor and an implicit Euler corrector at $t_{n+\frac{1}{2}}$. This is followed by a midpoint rule predictor for the full step and a Simpson's rule final corrector that gives the method its fourth order. The method is:

$$\phi^*_{n+\frac{1}{2}} = \phi^n + \frac{\Delta}{2}f(t_n, \phi^n) \tag{5.37}$$

$$\phi^{**}_{n+\frac{1}{2}} = \phi^n + \frac{\Delta}{2}f(t_{n+\frac{1}{2}}, \phi^*_{n+\frac{1}{2}}) \tag{5.38}$$

$$\phi^*_{n+1} = \phi^n + \Delta f(t_{n+\frac{1}{2}}, \phi^{**}_{n+\frac{1}{2}}) \tag{5.39}$$

$$\phi^{n+1} = \phi^n + \frac{\Delta}{6}\Big[f(t_n, \phi^n) + 2f(t_{n+\frac{1}{2}}, \phi^*_{n+\frac{1}{2}}) +$$

$$+ 2f(t_{n+\frac{1}{2}}, \phi^{**}_{n+\frac{1}{2}}) + f(t_{n+1}, \phi^*_{n+1})\Big] \tag{5.40}$$

The advantages of this method are:
1) the algorithm is self-starting and stable (more than multipoint methods of the same order);
2) it is easy to change the time step at any stage of the calculation;
3) high accuracy; and
4) the procedure is very efficiently programmed for a computer.

The disadvantages are:
1) it is very expensive; and
2) the error term is very complicated and cannot be used for estimation of the truncation error very easily.

All these methods mentioned above are derivations of finite difference algorithms approximating the derivatives in time by using the finite difference method.

In the text that follows a short explanation of **Finite Element Time Stepping** is given.

5.3.7 Finite Element Time Stepping

Finite element time stepping is a method which uses same technique for time discretization as well as that which was used for the discretization of a domain Lewis (1996). Therefore, it is:

$$\mathbf{T} = \sum N_i(t)\mathbf{T}^i \tag{5.41}$$

The shape function is given by:

$$N_n = 1 - \xi \quad N_{n+1} = \xi \tag{5.42}$$

where ξ is a local variable that takes value between 0 and 1. It is described by the following expression:

$$\xi = \frac{t}{\Delta t} \tag{5.43}$$

All these relations assumed that the nodal temperature value is changed from T^n to T^{n+1} over a time step Δt. At the same time the temporal derivatives of the shape function are:

$$\dot{N}_n = -\frac{1}{\Delta t} \quad \dot{N}_{n+1} = \frac{1}{\Delta t} \tag{5.44}$$

The finite element time stepping has been developed in two different ways:
a) the weighted residual method; and
b) the least squared method.

Weighted Residual Method

Applying this method for time discretization of matrix equation system (5.25) gives:

$$\mathbf{M}(\mathbf{T}^n N_n + \mathbf{T}^{n+1} N_{n+1}) + \mathbf{K}(\mathbf{T}^n N_n + \mathbf{T}^{n+1} N_{n+1}) = \mathbf{f} \tag{5.45}$$

Using the weighted residual method in (5.45) gives

$$\left(\frac{\mathbf{M}}{\Delta t} + \mathbf{K}\theta\right)\mathbf{T}^{n+1} = \left(\frac{\mathbf{M}}{\Delta t} - \mathbf{K}(1-\theta)\right)\mathbf{T}^n + \hat{\mathbf{f}} \tag{5.46}$$

where

$$\theta = \frac{\int_0^1 W_j \xi d\xi}{\int_0^1 W_j d\xi} \ and \ \hat{\mathbf{f}} = \frac{\int_0^1 W_j \mathbf{f} d\xi}{\int_0^1 W_j d\xi}$$

If the same spatial interpolation is used for both $\mathbf{f}$ and $\mathbf{T}$, then $\hat{\mathbf{f}}$ is given by

$$\hat{\mathbf{f}} = \theta\mathbf{f} + (1 - \theta)\mathbf{f}^{n+1} \tag{5.47}$$

The difference between the finite element and finite difference approach is that θ in the finite difference algorithm takes the value between 0 and 1, while in the finite element algorithm it depends on the weighting function W_j. This means that explicit, implicit and Crank-Nicolson method are just special cases of the weighted residual method.

Least Squares Method

The main idea of this method is that the error with respect to $\mathbf{T}^{n+1}$ can be minimized to produce a least squares algorithm. That means that across each time step, for example between n and n+1, the functional has to be minimized:

$$\pi = \int_0^1 \left[\mathbf{M}\left(\mathbf{T}^n\dot{N}_n + \mathbf{T}^{n+1}\dot{N}_{n+1}\right) + \mathbf{K}\left(\mathbf{T}^n N_n + \mathbf{T}^{n+1}N_{n+1}\right) - \mathbf{f}\right]^2 d\xi \tag{5.48}$$

The following equation describes the least squares scheme as:

$$\left[\frac{\mathbf{M}^T\mathbf{M}}{\Delta t} + \frac{\left(\mathbf{K}^T\mathbf{M} + \mathbf{M}^T\mathbf{K}\right)}{2} + \mathbf{K}^T\mathbf{K}\frac{\Delta t}{3}\right]\mathbf{T}^{n+1}$$

$$= \left[\frac{\mathbf{M}^T\mathbf{M}}{\Delta t} + \frac{\left(\mathbf{K}^T\mathbf{M} - \mathbf{M}^T\mathbf{K}\right)}{2} - \mathbf{K}^T\mathbf{K}\frac{\Delta t}{6}\right]\mathbf{T}^n$$

$$- \mathbf{K}^T\int_0^1 \mathbf{f}\xi\frac{d\xi}{\Delta t^2} - \mathbf{M}^T\int_0^1 \mathbf{f}\frac{d\xi}{\Delta t} \tag{5.49}$$

According to this result, accuracy is not an advantage of this method. That is the reason why this method is almost forgotten for solving transient heat conduction problems. The advantage of this method is that it can deal with nonsymmetric matrix.

5.4 Sensitivity analysis for heat conduction using different time/space discretization and different solution methods

5.4.1 Geometry and Boundary Conditions

The analysis considers a brick (Figure 5.1) which is divided by eight noded or twenty noded hexahedron finite elements. Dirichlet boundary conditions have been used. The back of the cube was kept at 0 [^oC] while the initial temperature was 100 [^oC].

In this section a sensitivity analysis of transient heat conduction, time steppings, iterative and direct solvers is presented.

In the end, considering limited memory space and CPU time, an element-by-element technique which has greater advantage over formatting global stiffness matrix, was used during calculations.

5.4.2 A Comparison Between Time Steppings

Below follows a presentation of the results for transient heat conduction using finite different time stepping, such as: explicit, implicit and theta method and as well as the finite element scheme which includes the least squares method. In this case the brick (composed of the material with thermal permeability of 1 [m^2/s]) was divided into one thousand eight noded elements and for comparison twenty noded hexahedron elements. The brick is composed of homogeneous and isotropic material with a constant thermal permeability in all three directions ($perm_x = perm_y = perm_z$). For all calculations one time step $\Delta t = 0.01$ was used.

In Figure 5.2 temperatures of the edge of the box looking from its front side to the back side are presented. In Figure 5.3 temperature variation at the point 1 which is positioned in the front upper left corner of the cube during its cooling is presented. The last, Figure 5.4, as an addition to Figure 5.2, presents the comparison between eight noded and twenty noded hexahedron elements.

5.4.3 Numerical Scheme and Accuracy

In this subsection an analysis of obtained results and their dependence on different numerical schemes is presented. For this presentation the cube was divided into:
a) 1000 elements;

b) 8000 elements;

c) 13824 elements;

d) 27000 elements;

e) 64000 elements; and

f) 125000 elements.

In Figure 5.5, given below, temperatures of the point 1 during its cooling effect for different numerical schemes are presented.

5.4.4 Residual, Iterations, CPU Time

In the following Figures 5.6, 5.7, 5.8, 5.9 and 5.10 residuals of the chosen iterative solvers for the following time steps: t=0.01, t=0.1, t=0.5, t=1.0 and t=1.5 are presented. At the same time residuals of the last iteration for all time steps are presented in Figure 5.11.

The number of inner iterations is taken to be one of the criteria for the comparison (Figure 5.12).

Computational time is a very important parameter in the process of choosing which iterative solver is the best for the particular problem. In Table 5.1 computational times for chosen iterative solvers, where mesh 10x10x10 was used, are presented.

At the same time in Table 5.2 CPU times which present a comparison between PCG (slow version) and Gauss methods for different meshes are given.

5.4.5 Conclusions

Characteristics of iterative solvers which qualify or disqualify an iterative solver, such as: the residual trend, the number of inner iterations and CPU time, are discussed respectively in the text that follows.

From Figures 5.6, 5.7, 5.8, 5.9, and 5.10 it can be seen that residual trends of the LSCG method are decreasing the slowest which is a disadvantage for this method. But, at the same time from the same figures it can be seen that residual trends of the LSCG method are decreasing steadily while, for example, the residual trends of the BCGSTAB method which are decreasing much faster have oscillations. Residual trends are affecting the number of inner iterations. Taking the number of inner iterations as a criteria parameter shows that the least squares conjugate gradient method requires the most iterations while the preconditioned conjugate method requires the least iterations. This recommends the PCG method as the best method for solving this type of problem (symmetric positive definite system of equations).

Sometimes, taking the number of inner iterations as a main parameter, can lead to the wrong conclusions. For example, computational time (CPU) that has to be spent to solve the problem (transient heat conduction) using bi-conjugate gradient method is twice that for the conjugate gradient method with same number of inner iterations for both of them (Table 5.1).

In the analysis above the most time-consuming operation is MATMUL. During calculations it is necessary to run this operation at least twice. The results presented in the previous table are obtained using by MATMUL operation as matrix-vector product. MATMUL operation can be organized in a different way and that is given in Appendix C. The reason for doing this is the acceleration of calculations by almost three times. For example, CPU time for PCG method is 1.09157 $[s]$ and for PBCG method is 3.75 $[s]$.

Iterative solvers have great advantages over direct solvers when one has to solve industrial problems with possibly hundreds of thousands elements or more. CPU time presented in Table 5.2 prove this statement. Also, when solving symmetric positive definite matrix system, the PCG appears to be the fastest. Unfortunately, not all industrially relevant partial differential equations are Laplace or Poisson equations. In the case that non symmetric matrix system has to be solved BCG, PBCG, LSCG, CGS, PCGS, BCGSTAB or PBCGSTAB method appear very useful tools. All these methods have been used to solve different types of matrix equations for more than ten years. As an example, Lavery (1996) used these methods to solve turbulent flow (Navier-Stokes equation) of incompressible fluid using $k - l$ method.

There are possibilities that these methods can be used in solving radiative heat transfer problem when it includes reflectivity of materials in so-called **Radiosity** approach (see Chapter 2 subsection Reflectivity). However, it can be one of goals for the future work.

5.5 Steady Heat Conduction

5.5.1 Introduction

In this section the three dimensional steady-state heat conduction for the same brick that was used in the previous section is analyzed. Two opposite sides of the brick were kept at fixed temperatures (100 and 30 [^oC]) as boundary conditions. In this case heat transfer equation without any sink or source of the heat energy becomes:

$$div(k \cdot gradT) = 0 \qquad (5.50)$$

5.5.2 Results

To solve this problem three different methods were applied. These are conjugate gradient method, preconditioned conjugate gradient method and one variation of the Gaussian elimination where elements of stiffness matrix were stored using a 'skyline' method (Smith (1998)).

Temperature distribution for the brick divided into 1000 hexahedron elements with Dirichlet boundary condition is presented in Figure 5.13.

solver	CPU [s]
CG	11.40640
PCG	3.264694
LSCG	55.61998
CGS	15.87282
PCGS	6.409216
BCG	26.48809
PBCG	14.30056
BCGSTAB	34.90018
PBCGSTAB	6.970022
Gauss	6.569446

Table 5.1: CPU time for chosen solvers

mesh	solver	CPU [s]
8000 el.	PCG	62.44
	Gauss	177.92
27000 el.	PCG	303.81
	Gauss	1998.08
64000 el.	PCG	927.02
	Gauss	no point
125000 el.	PCG	2159.42
	Gauss	no point

Table 5.2: CPU time for PCG and Gauss methods
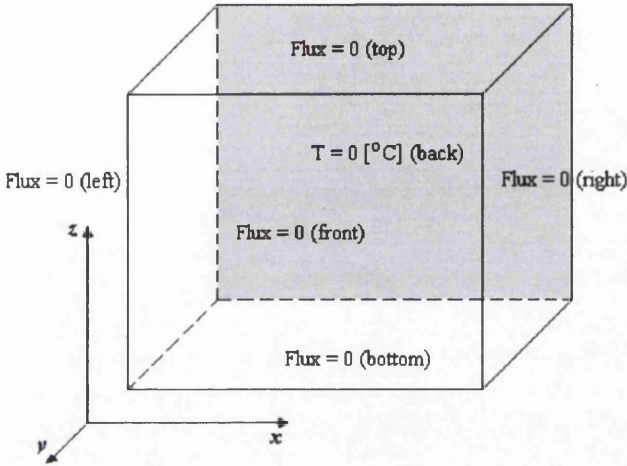
Figure 5.1: Geometry of the homogeneous cube with boundary conditions
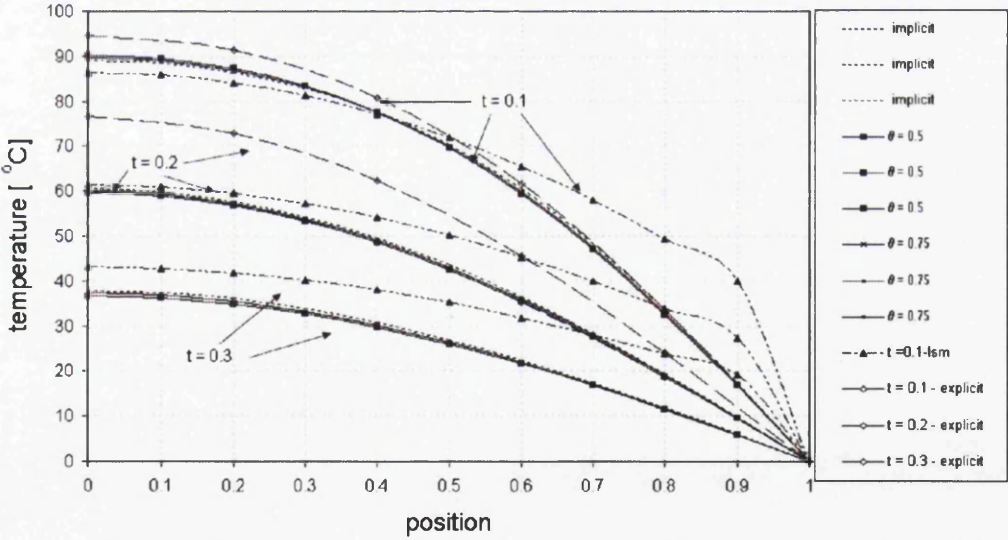
Figure 5.2: Transient temperatures through the brick
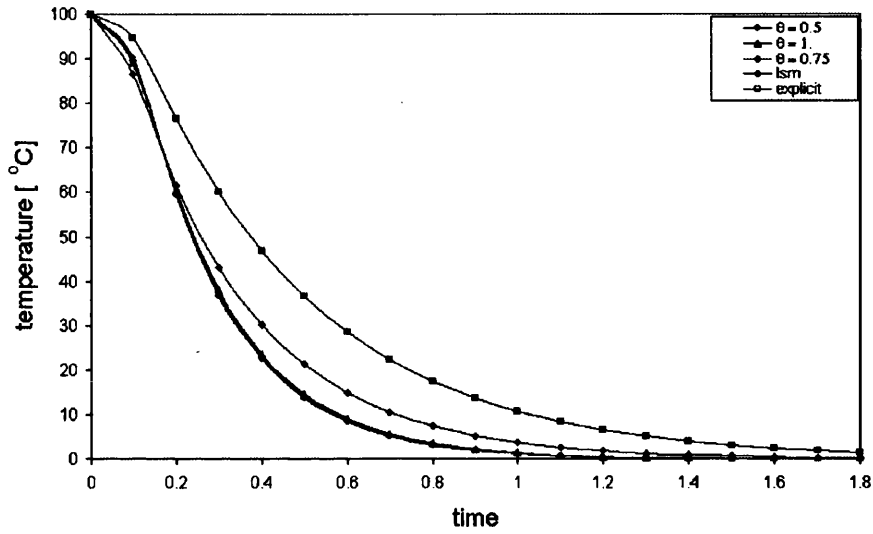
Figure 5.3: Transient temperature at node 1 for mesh 10x10x10
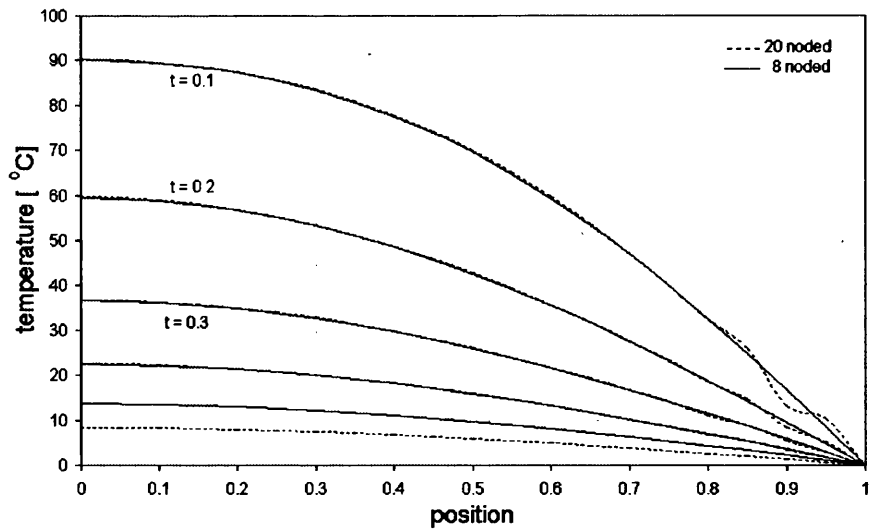
Figure 5.4: Transient temperature for 8-noded and 20-noded elements
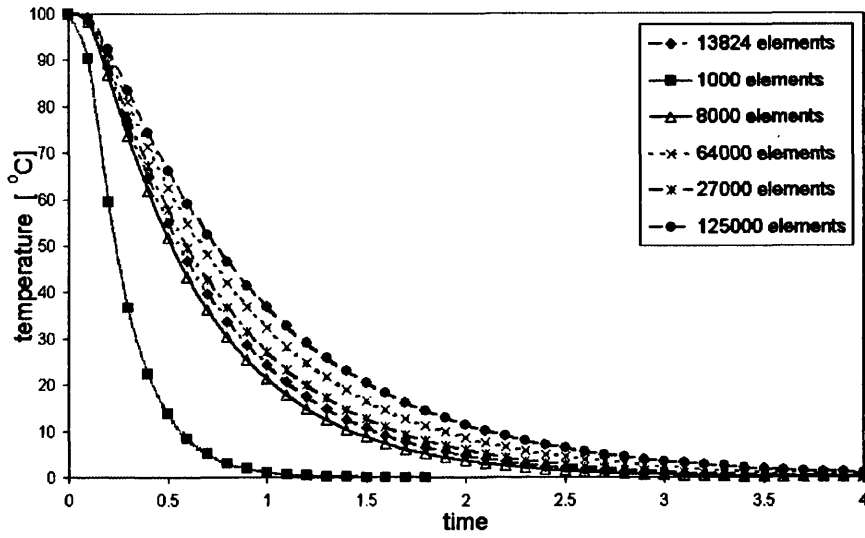
Figure 5.5: Transient temperature at node 1 for different numerical schemes
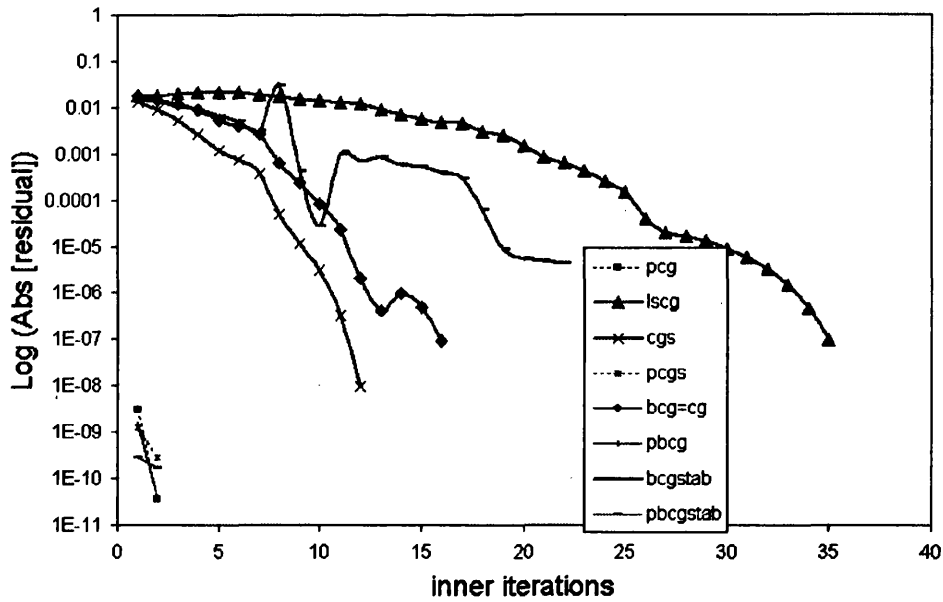
Figure 5.6: Residuals at time $t = 0.01$ for node 1
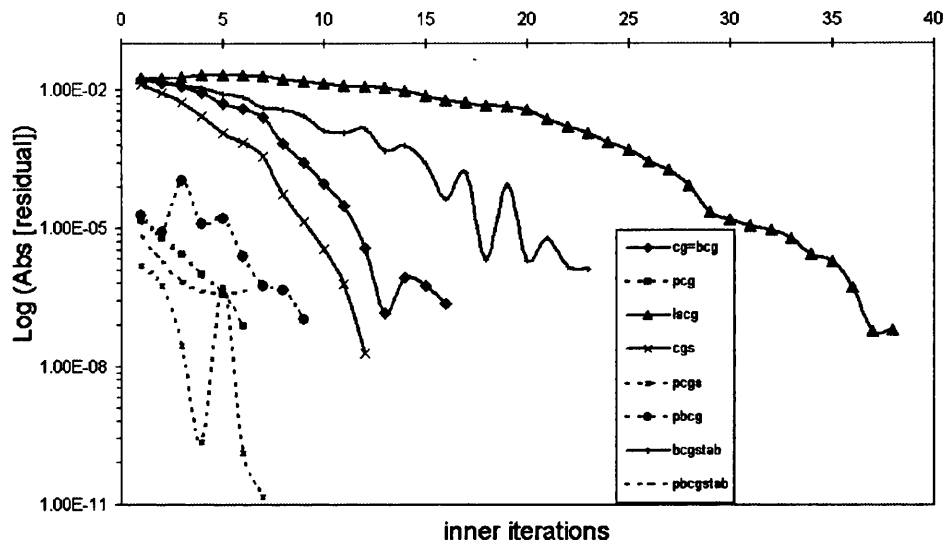
Figure 5.7: Residuals at time $t = 0.1$ for node 1
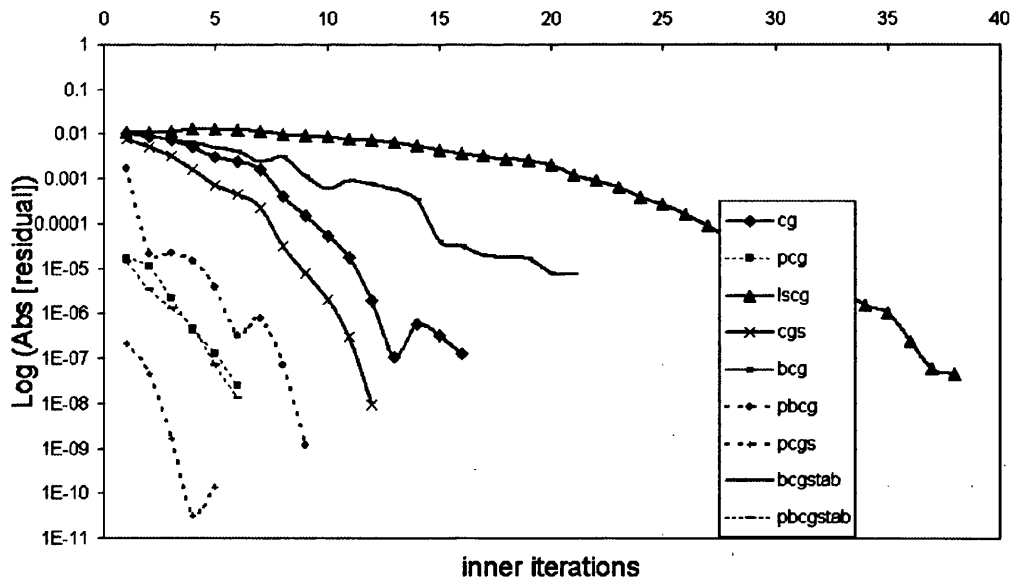
Figure 5.8: Residuals at time $t = 0.5$ for node 1
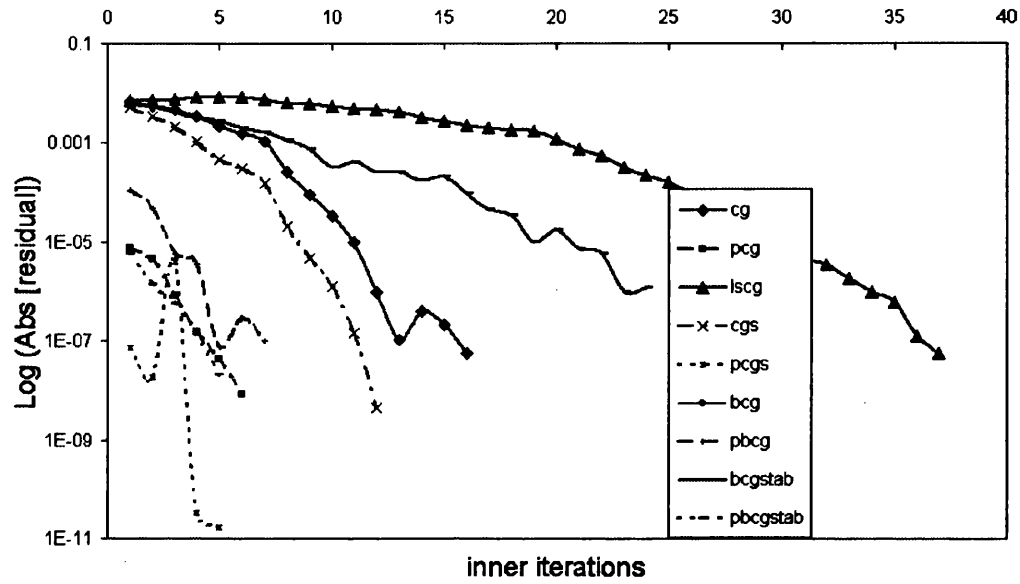
Figure 5.9: Residuals at time $t = 1.0$ for node 1
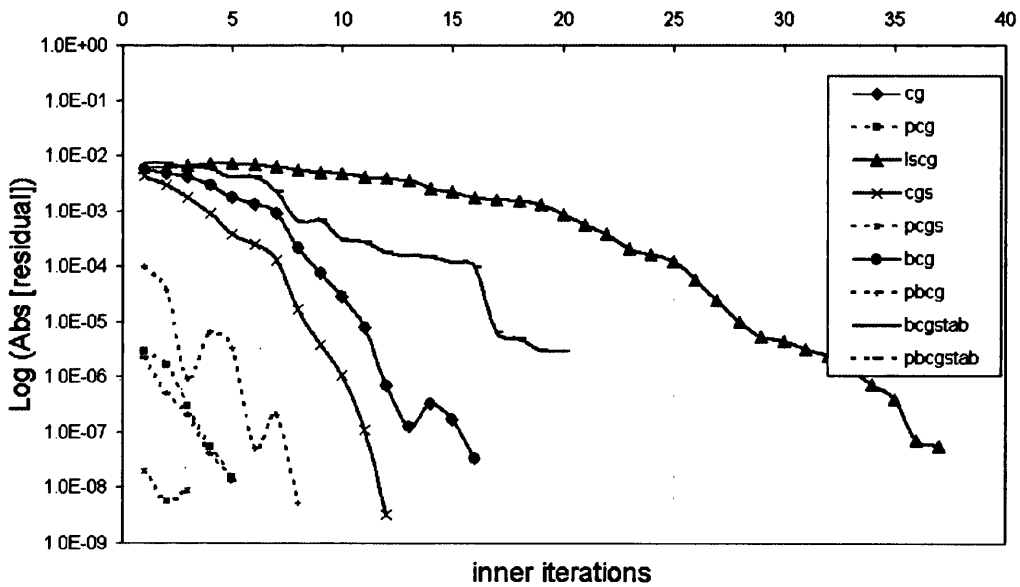
Figure 5.10: Residuals at time $t = 1.5$ for node 1
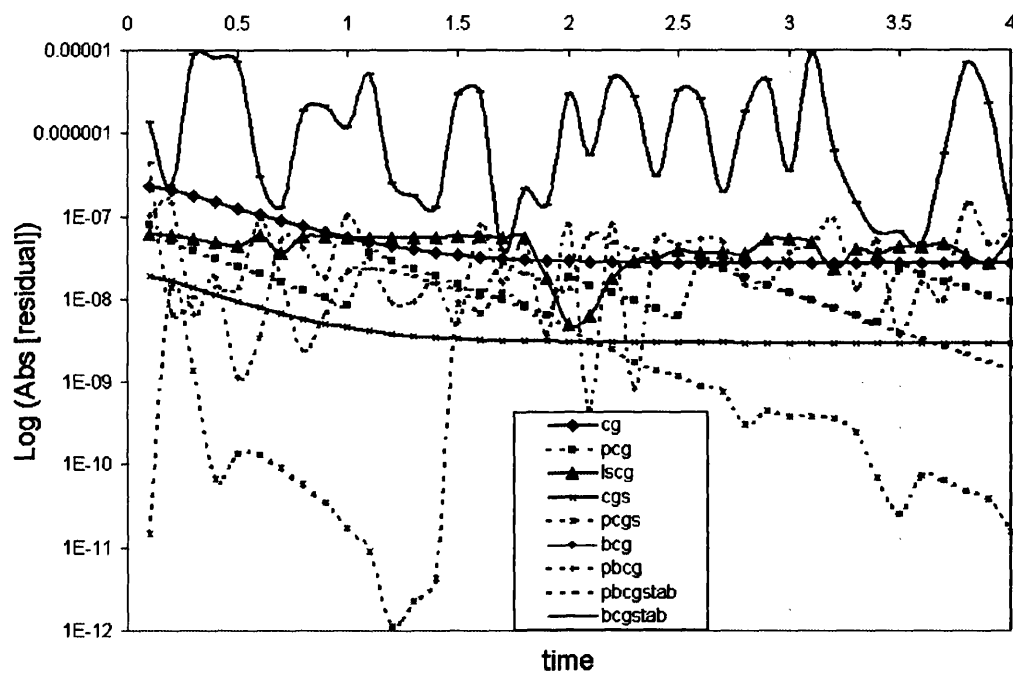
Figure 5.11: Residuals of the last iteration for all time steps
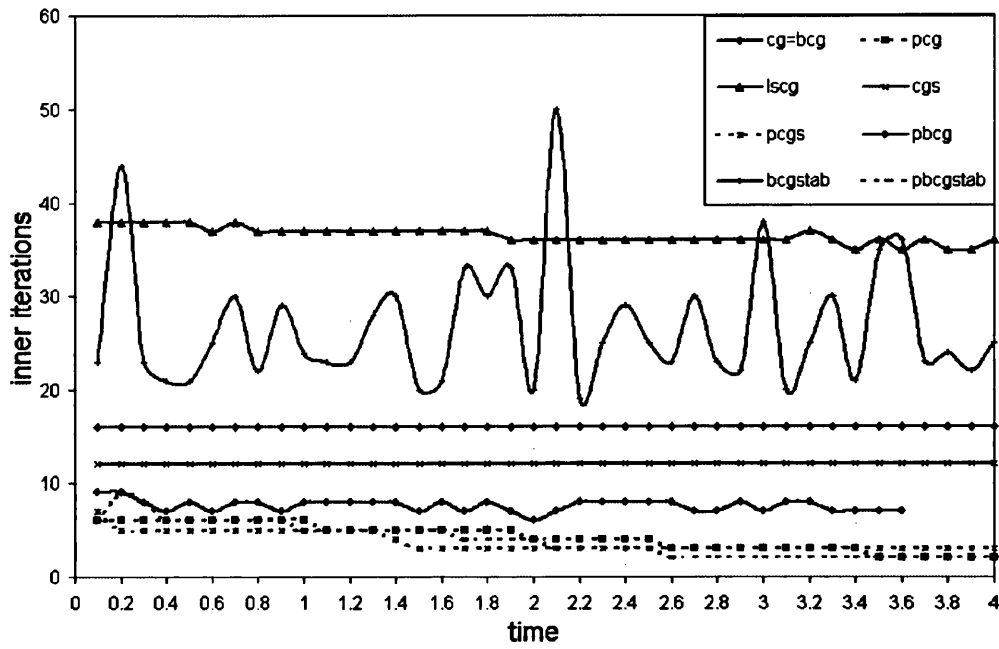
Figure 5.12: Numbers of inner iterations in time
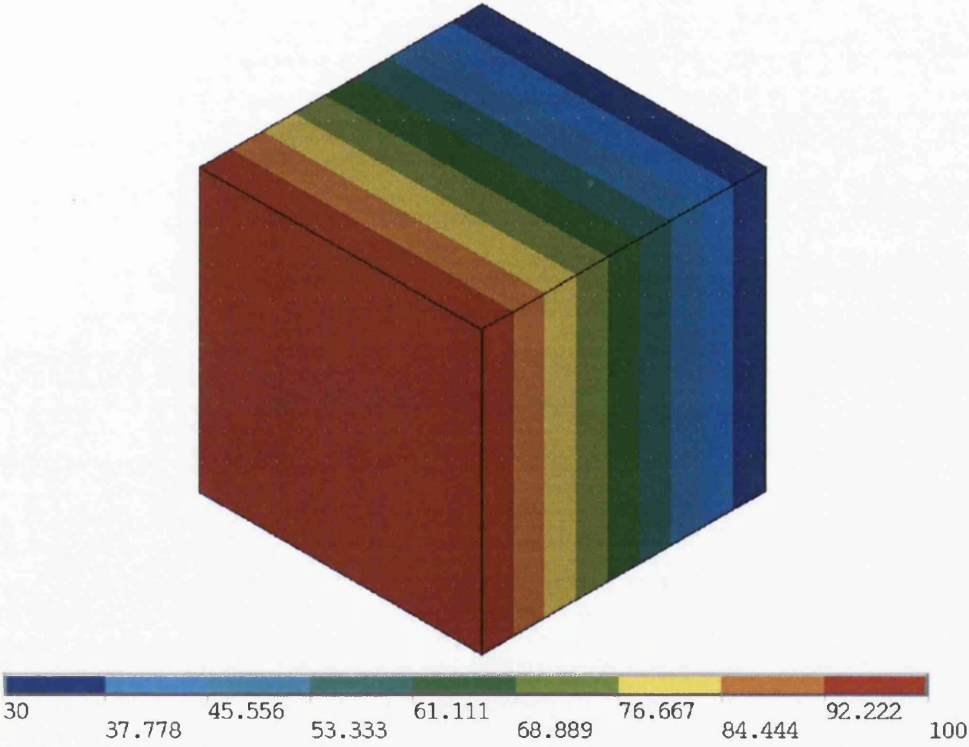
Figure 5.13: Temperature distribution of the brick in steady state - Temperature scale in $[^oC]$

Chapter 6

Heat Transfer Simulation

In this chapter a sensitivity analysis is presented. This is used to examine the relationship between the accuracy of results obtained, mesh division, the number of rays used in the view factor calculations, as well as thermo-physical properties of materials such as thermal conductivity and emissivity, and their effect on the heat exchanged between surfaces. Temperatures of surfaces included in the enclosure and net radiative heat flux exchanged between surfaces are chosen to be relevant parameters in the analysis. Later, obtained surface temperatures will be compared with experimental data (Chapter 3).

6.1 Finite Element Formulation

A theoretical background and governing equations were already given in previous Chapters 2, 5 and Appendix B, so they are not presented again here. However, an application of the Galerkin variational procedure leads to the matrix differential equations system:

$$[\mathbf{M}]\left\{\frac{dT}{dt}\right\} + \left[[\mathbf{K}_c] + [\mathbf{K}_h]\right]T = \mathbf{R}_Q + \mathbf{R}_q + \mathbf{R}_h + \mathbf{R}_r \qquad (6.1)$$

where

$$\mathbf{M} = \int_{\Omega^{(e)}} \rho c_p N[N] d\Omega$$

$$\mathbf{K}_c = \int_{\Omega^{(e)}} [B]^T [\mathbf{k}][B] d\Omega$$

$$\mathbf{K}_h = \int_{\partial\Omega^{(e)} \cap S_2} \rho c_p N[N] d\Omega$$

$$\mathbf{R}_Q = \int_{\Omega^{(e)}} \rho Q N d\Omega$$

$$\mathbf{R}_q = \int_{\partial\Omega^{(e)} \cap S_1} \rho q_s N d\Gamma$$

$$\mathbf{R}_h = \int_{\partial\Omega^{(e)} \cap S_2} h T_f N d\Gamma$$

$$\mathbf{R}_r = - \int_{\partial\Omega^{(e)} \cap S_3} q_r N d\Gamma \tag{6.2}$$

and

$$[\mathbf{B}] = \begin{bmatrix} \frac{\partial N_1}{\partial x} & \frac{\partial N_2}{\partial x} & \cdots & \frac{\partial N_r}{\partial x} \\ \frac{\partial N_1}{\partial y} & \frac{\partial N_2}{\partial y} & \cdots & \frac{\partial N_r}{\partial y} \\ \frac{\partial N_1}{\partial z} & \frac{\partial N_2}{\partial z} & \cdots & \frac{\partial N_r}{\partial z} \end{bmatrix} \tag{6.3}$$

with r, c_p, and $\mathbf{k}$ being the material density, specific heat, and thermal conductivity, respectively. Specific heat flux q_s on surface S_1, convection on surface S_2 with a convection coefficient h and a fluid temperature T_f, and net radiation heat flux q_r on surface S_3 are included as boundary conditions in the definitions given above. Q represents any heat source or sink in the material.

In the present work, radiation heat flux q_r on surface S_3 which is included as boundary condition, is determined using equations (2.12), (2.51) and (2.52) as derivations of Stefan-Boltzmann Law, radiosity face-to-face equation (2.54) and MRV method.

While the first part of this Chapter includes simple cases, such as two parallel plates, disc-plate and a cylinder-plate case, the second part includes more complex enclosures:

a) a disc as an emitter and two receivers within a boundary box;

b) a jet pipe.

6.2 Two Parallel Square Plates

Two parallel plates, used in the examination, with dimension of $\neq 2x197x197$ [mm] for the emitter and $\neq 5x197x197$ [mm] for the receiver are both composed of steel. In the calculation three different numerical schemes are used:

a) emitter

1) 10x10x4
2) 25x25x4
3) 40x40x4

b) receiver

1) 10x10x10
2) 25x25x10
3) 40x40x10

For the view factor calculations the Monte Carlo method was used where 100, 1000, 5000, 10000, 20000 and 50000 rays were used depending on the numerical scheme (Table 6.1).

The following text shows the results obtained for one chosen distance (distance ratio defined as $c = distance/length = 0.7$) between the emitter and the receiver, and for one numerical scheme (10x10). All results of calculations presented in this section were obtained for the same thermo-physical properties of the emitter and the receiver:

a) Thermal conductivity $k_x = k_y = k_z = 16.27$ [W/mK],
b) Emissivity $\epsilon_1 = \epsilon_2 = 0.81$,
c) Absorptivity $\alpha_1 = \alpha_2 = 0.066$,
d) Specific heat capacity $c_p = 503$ [J/kgK] and
e) Density $\rho_1 = \rho_2 = 8030$ [kg/m^3].

Two boundary conditions were used in these calculations: Dirichlet boundary condition and heat transfer coefficient (convection). The back side of the emitter was kept at a fixed temperature. The temperatures (Table 6.2) were taken from the experimental data. Three heat transfer coefficients: the front side of the emitter h_{S_1}; the front side of the receiver h_{S_2}; and the back side of the receiver h_{S_3}, were calculated for both laminar and turbulent fluid flow.

6.2.1 Mesh 10x10

Temperatures of the front side (Figures 6.1, 6.2 and 6.3) and the back side of the receiver (Figures 6.4 and 6.5) as well as radiative flux of the emitter (Figures 6.6 and 6.7) and the receiver obtained for the different number of rays used for the view factor calculations are considered in this presentation. The unit for temperature is $[K]$ while for radiative flux is $[W/m^2]$.

From Figures 6.1, 6.2 and 6.3 it can be seen that where a different number of rays were used for the view factor calculation it produced different values of view factors. Different view factor values during heat transfer simulations caused different temperatures obtained for the receiver (the difference between maximum temperatures of receiver was approx. 60 $[K]$). To ensure that there is a small error in the results obtained an adequate number of rays have to be shot from the emitter. From the figures mentioned above it should be noted that a significant increase in the number of rays from those used does not give any improvement in the results obtained. For example, while the results did improve when increasing the number of rays from 500 to 10000, a further increase from 10000 to 20000 does not show a corresponding improvement.

Similar results can be seen in Figures 6.6 and 6.7, where better radiative heat flux distribution was obtained using a higher number of rays, although again there is no significant improvement in the results when the number of rays is dramatically increased.

6.3 Hinged Plates

Experimental data, including temperatures of the receiver, is presented in subsection 3.4.1, while the heat transfer simulation will be presented in this section. For the presentation the emitter was divided into 1600 hexahedral elements (mesh $20 \times 20 \times 4$) while the receiver was divided into 4000 hexahedral elements (mesh $20 \times 20 \times 10$)(Figure 6.8).

For the view factor calculation 10000 rays were used. The emitter and the receiver are composed of the materials with thermo-physical properties as in the previous case. Heat transfer coefficients of the front side of the emitter, the front side of the receiver and the back side of the receiver are given in Table 6.3.

Temperature distributions on the front and back side of the receiver are presented in Figure 6.9, while the thermal image of the front side of the receiver is presented in Figure 6.10. A comparison between Figures 6.9 and 6.10 shows a high level of the agreement between the numerical results and

experiments. One reason for any difference which existed between the experimental data and the numerical results, was that the heat transfer coefficient used during simulations as a boundary condition had a constant value across the whole surface of the plate. During experiments it has been shown that the receiver does not have a constant value and this assumption used in simulations is an approximation.

6.4 A Disc and a Square Plate

A disc with dimension of $\neq 2 \times \phi 182$, where 182 [mm] is the diameter of the disc, is used as an emitter while a plate, with dimension of $\neq 5 \times 197 \times 197$ [mm], is used as a receiver. Because the emitter is a curved surface, the accuracy of its discretization with finite elements depends on the chosen mesh. This is the reason for giving greater attention to this case.

6.4.1 Mesh 4x10

The title of this (and the following) subsection refers to the perimeter of the disc, which in this case is divided into 40 divisions. This analysis involves the following numerical schemes:
- emitter - 4x10x4
- receiver - 10x10x10
For the view factor calculations 100, 1000, 10000, 20000 and 50000 rays were used. The results obtained are presented in the following order. Firstly, temperature distributions on the front side of the receiver (Figures 6.12, 6.13 and 6.14) with numerical scheme and temperature distributions on the back side of the receiver (Figures 6.15, 6.16 and 6.17) are presented. Later, a radiative flux that is emitted from the emitter (Figures 6.18, 6.19 and 6.20) as well as radiative flux which is received by the receiver (Figure 6.21, 6.22 and 6.23) are presented.

Figures 6.12, 6.13 and 6.14 present the temperature distributions on the front side of the receiver. These show that an increase in the number of rays used for the view factor calculation gives better and more realistic results. The difference between maximum temperatures when 100 and 50000 rays per element were used was 33 [K] which is almost 10 %. The same conclusion can be drawn from Figures 6.15, 6.16 and 6.17.

6.4.2 Mesh 4x20

This analysis involves the following numerical schemes:
- emitter - 4x20x4
- receiver - 20x20x10

For the view factor calculations 100, 1000, 5000, 10000, 20000 and 50000 rays were used. The results obtained, such as temperatures of the front side (Figures 6.24, 6.25 and 6.26) and the back side of the receiver (Figure 6.27, 6.28 and 6.29) are presented in the following order. Radiative flux emitted from the emitter in relationship with the number of rays used for the view factor calculation is presented in Figures 6.30, 6.31 and 6.32, while radiative flux absorbed by the receiver is presented in Figures 6.33, 6.34 and 6.35.

An analysis of Figures 6.24, 6.25 and 6.26 shows the crucial role of the number of rays used for the view factor calculation when applying the Monte Carlo method. It can be noted that using 100 rays per element gives very poor temperature distribution on the front side of the receiver. An analysis of the temperature distributions of the back side of the receiver draws same conclusions. At same time a use of 20000 rays per element gives better results, which can also be noted visually. From Figures 6.30, 6.31 and 6.32 the same conclusions can be drawn.

6.4.3 Mesh 4x40

In this case the perimeter of the emitter is divided into 160 divisions. For the view factor calculations 100, 500, 1000, 2000 and 5000 rays were used. Temperature distributions of the front side (Figures 6.36, 6.37 and 6.38) and the back side (Figures 6.39 and 6.40) of the receiver and radiative flux that is emitted from the emitter (Figures 6.41, 6.42 and 6.43) as well as radiative flux absorbed by the receiver (Figures 6.44, 6.45 and 6.46) are presented in figures at the end of this Chapter.

From Figures 6.36, 6.37 and 6.38 the same conclusions as in previous sections (lower mesh resolutions) can be drawn. A low number of rays (100) per element gives very poor results. Better results can be expected for a higher number of rays (2000) per element.

A comparison between the results obtained for three different mesh resolutions shows that a higher mesh resolution gives better results. At same time it requires more rays per element for the view factor calculation, causing a further increase in CPU time.

An analysis of mesh resolutions and the number of rays when results reach steady state was made. It was noted that different mesh resolutions give similar results with a different number of rays used for view factor calculations.

Introducing CPU time as one of the very important criteria, suggests that during radiative heat transfer simulations the lowest possible mesh resolution and the highest possible number of rays per element are most appropriate to use. Also, it is necessary to be aware of the temperature distribution within a single element.

6.5 A Cylinder and a Square Plate

The final experimental case involves a cylinder, with dimension of $\phi 28 \times 197$ $[mm]$, as an emitter and a plate, with dimension of $\neq 10 \times 197 \times 197$ $[mm]$, divided by the same numerical schemes which was used in the previous cases as a receiver. For this analysis four numerical schemes of the emitter were used: $4 \times 3 \times 10; 4 \times 3 \times 20; 4 \times 3 \times 40;$ and $4 \times 7 \times 40$. For the presentation one distance ratio of $c/D = 1.929$ was selected.

6.5.1 Mesh 4x3x10

The temperature distribution of the front side (Figures 6.47 and 6.48) and the back side (Figures 6.49 and 6.50) of the receiver and as well as radiative flux (Figures 6.51 and 6.52) for different number of rays used for the view factor calculation are presented in this subsection.

Figures 6.47 and 6.48 show an increase in the temperatures of the front side of the receiver when there is an increase of the number of rays used for view factor calculation (the temperature difference between numerical results when 100 and 10000 rays per element were used was approx.25 $[K]$).

6.5.2 Mesh 4x3x20

The temperature distribution of the front side (Figures 6.53, 6.54 and 6.55) and the back side (Figures 6.56 and 6.57) of the receiver and as well as radiative flux (Figures 6.58 and 6.59) for different number of rays used for the view factor calculation are presented in this subsection.

An increase in the mesh resolution causes an increase in both the number of elements and the distance ratios between elements. To obtain more accurate results all these require more rays per element for view factor calculations.

6.6 Numerical Scheme (Mesh), Number of Rays and Temperature

The relationship between the temperature of the receiver and radiative flux exchanged between surfaces depend on the mesh resolution and number of rays used for view factor calculation was analyzed and the results obtained are presented in figures in sections 6.2, 6.4 and 6.5. Different meshes and different number of rays caused different temperatures of the receivers. An average temperature and a minimum temperature of the receiver were chosen to indicate these differences, and this is shown in the results obtained.

6.6.1 Conclusions

In the section 2.2.1 it can be seen that an increase in the number of rays used for the view factor calculation causes higher accuracy in the results. On the other hand in Table 2.15 it can be seen that an increase in the number of rays causes an increase in CPU time. Also, in the section 2.2.1 it was shown that from the view factor calculation point of view increasing mesh resolution does not always give better results. It is necessary to also be aware that a minimum number of rays must be used. At the same time, it is known that mesh resolution is very important in finite element thermal and fluid flow analysis. However, the heat transfer simulation presented in previous section includes all of them, so there has to be a compromise between CPU time and accuracy.

From Tables 6.4, 6.5 and 6.6 it can be seen that an increase in the number of rays causes an increase of the average and the minimum temperature of the receiver. For example, Table 6.4 shows a difference of 48.18 $[K]$ (9.45 %) between average temperatures of the receiver when 100 rays per element and 50000 rays per element were used for the view factor calculation and when the distance ratio between the emitter and the receiver was 0.5. Also, it can be seen when the number of rays used for the view factor calculation reach a certain number, the temperatures of the receiver become stable. Further increases in the number of rays will not cause any change in temperature of the receiver.

6.7 Temperature and Emissivity

A relationship that exists between radiative heat flux (presented through temperatures of the receiver) exchanged between an emitter and a receiver and emissivity of their surfaces is analyzed in this section. It includes a few

different test cases such as:

a) $\epsilon_E = 0.81(steel), 0.3 \leq \epsilon_R(steel) = \leq 0.95$

b) $0.3 \leq \epsilon_E(steel) = \epsilon_R(steel) \leq 0.95$

c) $\epsilon_E = 0.81(steel), 0.05 \leq \epsilon_R(aluminium) = \leq 0.31$

d) $\epsilon_E = 0.81(steel), 0.1 \leq \epsilon_R(brass) = \leq 0.6$

A minimum and an average temperature of the receiver, chosen as parameters, are presented in figures given in the text that follows. For this presentation parallel plates with distance ratio $c/L = 0.7$ were chosen, and for the view factor calculation 10000 rays per element were used.

a) The emitter and the receiver are both composed of steel with thermo-physical properties presented in Table 6.7.

While emissivity of the emitter was kept at a fixed value, the emissivity of the receiver was increased from 0.3 (galvanized surface) to 0.95 (rough plane surface)(Figure 6.60).

b) In the second test case it was assumed that the emitter and the receiver, both composed of steel, have same emissivity which were gradually increased from 0.3 to 0.95 (Figure 6.61).

c) The third case in the analysis considers a receiver composed of aluminium, while the emitter was composed of steel. The emissivity of the emitter was fixed, while emissivity of the receiver was changed slightly from 0.05 (polished surface) to 0.31 (strongly oxidized surface).

The thermo-physical properties of materials are given in Table 6.8 while results obtained are shown in Figure 6.62.

d) The receiver composed of brass and the emitter composed of steel were used in this analysis. Emissivity of the receiver was changed gradually from 0.1 (polished surface) to 0.6 (oxidized surface at 600 [K]), while emissivity of the emitter was fixed at 0.81. The thermo-physical properties of materials are given in Table 6.9 while the results of heat transfer simulation are presented in Figure 6.63.

6.7.1 Conclusions

According to the Stefan-Boltzmann equation an increase of emissivity of the receiver for a constant emissivity of the emitter will cause a temperature drop

of the receiver. From Figure 6.60 it can be seen that the average temperature of the receiver decreases (from 477.64 $[K]$ to 456.2 $[K]$ which is 4.4%) with an increase of emissivity (from 0.3 to 0.95) of the receiver when emissivity of the emitter was fixed at 0.81.

At the same time in Figure 6.61 it can be seen that an increase of emissivity (from 0.3 to 0.95) causes an increase of the average temperature of the receiver from 397.2 $[K]$ to 481.2 $[K]$ (17.5%). This increasing trend was expected because more heat is coming to than is leaving the receiver.

In the third and fourth cases receivers composed of aluminium and brass were analyzed. From Figures 6.62 and 6.63 it can be seen that the temperature trend decreases for an increase of emissivity of the receiver.

6.8 Temperature and Thermal Conductivity

In this section temperature distributions of the receiver and their relationship with different thermal conductivity were analyzed. A receiver composed of steel with thermal conductivities from 20 $[W/mK]$ to 50 $[W/mK]$ was chosen for this examination. Two parallel plates, divided by the same mesh $25x25x10$ with distance ratio (*distance/length*) equal to 0.7 between them, and where 20000 rays were used for the view factor calculation, was chosen for examination. Emissivity of the receiver was $\epsilon = 0.81$. An average temperature and the temperature at node 3543 (the position of this node was $\Delta x = 50$ $[mm]$ and $\Delta y = 50$ $[mm]$ from the left lower corner of the front side) of the receiver were chosen to represent temperature distribution of the receiver in function of thermal conductivity.

6.8.1 Conclusions

The results presented in Figure 6.64 show that thermal conductivity changes do not cause any temperature change in the receiver when heat transfer reaches a steady state. An analysis of the Fourier equation for the heat conduction shows that these results should be expected.

6.9 Heat Transfer Simulation in a Complex Enclosure

As it was mentioned earlier two different cases are studied in this section:
a) a disc as an emitter and two receivers with boundary box;

b) jet pipe.

a) The geometry and the measurement data of the case which is taken for examination are given in Chapter 3. There it can be seen that the enclosure considers a disc (composed of two layers: the first composed of steel with dimension of $\neq$ 3 × 182 × 182 [mm], while the second layer is an insulation with dimension of $\neq$ 20 × 182 × 182 [mm]) as an emitter, a receiver (receiver 1) which is composed of brass with dimension of $\neq$ 7 × 197 × 197 [mm]) and which is parallel to the emitter with the distance of 135 [mm] between them and a receiver (receiver 2) which is composed of aluminium with dimension of $\neq$ 7 × 197 × 197 [mm] positioned in the same plane with the emitter with a distance of 106 [mm] between them within a black painted boundary box. All three equations, already mentioned in Chapter 2, as variations of Stefan-Boltzmann Law are used together with the radiosity face to face equation in the heat transfer simulations. For this presentation following mesh resolution were used:

a) emitter

steel layer 30x30x2=1800 elements

insulation layer 30x30x10=9000 elements

b) receiver 1 30x30x4=3600 elements

c) receiver 2 30x30x4=3600 elements

d) boundary box 29800 elements in total

b) A GNOME Rolls Royce jet pipe will be analyzed in this section (see Figure 6.65). The geometry of the engine is presented in Figure 6.67. The jet pipe was divided into 29232 hexahedron finite elements. The thermo-physical properties of materials are given in Table 6.8. Convection heat transfer coefficients were obtained using commercial CFD code **Phoenics** (see Figure 6.66) and were then imported into **Pharo**.

6.9.1 Radiosity Face to Face Method

a) For the view factor calculation the Hemi-cube method with different resolutions (number of 'pixels') was used. The results obtained for 100, 1000 and 10000 pixels per Hemi-cube are presented in the text that follows (Vujičić (2005b)).

The temperature distribution of the internal side of the boundary box, where 1000 and 10000 pixels were used for the view factor calculation, are

presented in Figures 6.68 and 6.69 respectively. Both figures show hot spots which were noticed earlier during the experiments (see Chapter 3). A comparison between Figure 6.68 and Figure 3.53 with Figure 6.75 shows that there is an acceptable agreement between the results of calculation and experimental data (thermal image camera).

Radiative heat flux exchanged between bodies in enclosure is presented in Figures 6.70 and 6.71. While Figure 6.70 presents results obtained using 100 pixels per element, Figure 6.71 presents results obtained using 1000 pixels per element.

Figures 6.70 and 6.71 show that the distribution of radiative heat flux exchanged between bodies is similar as the distribution of temperatures in the enclosure. Knowing that temperatures of bodies depend upon the heat exchanged between them and the enclosure this can be expected. Area in the enclosure where there is a higher rate of radiative heat flux exchanged can easily be seen.

b) In this case, both the Hemi-cube and the Monte Carlo methods with the same number of rays per element (1000 rays) were used for view factor calculations.

The temperature distribution of a GNOME jet pipe using the Hemi-cube method is presented in Figure 6.72. From this figure it can be seen that the maximum temperature was about 692 $[K]$, while the minimum temperature was 289 $[K]$.

Radiative flux exchanged within a GNOME jet pipe is presented in Figure 6.73.

6.9.2 The MRV Method

The first case which includes one emitter, two receivers and boundary box was analyzed using the MRV method. The analysis of the results obtained using the MRV method starts with the temperature distribution of the internal side of the boundary box. As it can be seen from Figure 6.74 there is an excellent agreement between results obtained using the MRV method and experimental data presented in Figure 3.53. The more detailed comparison can be seen in Figure 6.75, where an excellent agreement between results obtained using the MRV method and experimental data exist.

The average transient temperatures of the emitter and receivers obtained using the MRV method are presented in Figure 6.76. Further analysis which includes a comparison between the average temperatures of receiver 2 (nu-

merical end experimental), presented in Figure 6.77, shows the advantage of the MRV method over the others.

The temperature at the centre of the emitter, and the average temperatures of the receivers and boundary box with experimental data using all three variations of the Stefan-Boltzmann Law, face to face radiosity and MRV method are given in Table 6.11.

In Table 6.11 can be seen that the MRV method gives the most accurate results. Obviously, the accuracy of the results obtained highly depends on the accuracy of the view factor values (Vujičić (2005c)). This is the main reason for using 30000 rays per element. The difference between numerical results and experimental data is within 0.013% (using Celsius temperature scale the difference is 0.08 %) for the emitter and receiver 1. The difference between the average temperature of the receiver 2 obtained using MRV method and measured one was about 0.11% (using Celsius temperature scale the difference is 1.4 %). The difference between the average temperatures obtained using face to face radiosity method and experimental data was from 0.6% (0.49 %) to 1.03% (12.7 %). All three standard variations of the Stefan-Boltzmann Law have been found to be the least accurate.

6.9.3 Stefan-Boltzmann Law (SB)

a) The same enclosure with the same geometry, and the same discretization was used to obtain results presented in this subsection. Equation (2.12) as one of the variations of SB Law was used in heat transfer simulations. The temperature distribution of the internal side of the boundary box is presented in Figure 6.78. In this case 100 pixels per element were used for the view factor calculation. An analysis of the results do not show a good agreement with the experiments. The temperature spots explained in the text above and presented in Chapter 3 cannot be found in Figure 6.78. The low number of rays used for view factor calculation is not the main reason for the higher level of inaccuracy of the results obtained. The main reason for this failure is that reflectivity has not been included in simulations. In the previous section, it has been shown that even simple face to face radiosity method, which includes the effect of reflectivity, gives very accurate results.

Radiative heat flux exchanged between bodies in the enclosure is presented in Figures 6.79 and 6.80.

The results obtained using three variations of SB Law, the simple face to face radiosity method and MRV method are presented in Table 6.11. Average temperatures of bodies in the enclosure were chosen to be parameters for the comparison.

b) Figure 6.81 shows the temperature distribution of a GNOME jet pipe using the Hemi-cube method with 1000 rays per element for the view factor calculation, where equation (2.12) was used for heat transfer simulations. The maximum and the minimum temperatures obtained were 684 [K] and 362 [K] respectively.

At the same time the temperature distribution of a jet pipe using equation (2.51) is presented in Figure 6.82. The maximum and the minimum temperatures obtained were 695 [K] and 338 [K] respectively.

The results obtained using equation (2.52) are presented in Figure 6.83. The maximum and the minimum temperatures obtained were 696 [K] and 339 [K] respectively.

6.10   Conclusions

Table 6.11 shows that the MRV method gives the most accurate results of all equations used for the examination. Reassembled view factor values as the result of multiple reflection cause that the MRV method is the most CPU time consuming method. This is the main disadvantage of the MRV method. This problem can be solved with an application of parallel techniques. The MRV method and as well as methods for the view factor calculation such as the Monte Carlo and Hemi-cube methods are suitable for parallelization, and there are several different parallel approaches that can be used to obtained an approximately linear speed up in radiative heat transfer applications.

At the same time equations (2.51) and (2.52) give worse results than equation (2.12).

Using equation (2.12), net radiative heat flux was calculated without any consideration of reflection. It was also assumed that the receiving element, acting as a blackbody, absorbed all heat that reached it. In this case receiving elements received more heat than when using equations (2.51) and (2.52), causing an increase of its temperatures.

At the same time using equation (2.51) it was assumed that the receiving element acts as a greybody, only absorbing a certain amount of the heat flux. This caused the temperature of the receiving elements to be lower. At the same time, assuming that the emitting elements act as blackbodies, the temperatures of the emitting elements were higher than the temperatures of the emitting elements using equation (2.12).

In the third equation (2.52) it was assumed that both emitting and receiving elements act as greybodies. Temperatures of emitting elements were the highest in both cases.

For all these three equations, when the same surface properties of emitting

and receiving elements exist, it can be noted that the same heat flux is exchanged between them.

During experimental analysis it was noted that an increase in emissivity of receiver 1 caused an increase in the receivers temperature (from 324 [K] to 408 [K]) and a drop in the emitters temperature (approx. 10 degrees). In section 6.7 (where results were obtained using equation (2.12)) it was shown that an increase in receiver emissivity causes a drop in temperatures of the receiver, which is the opposite than what occurred in experiments. At the same time the temperature of the emitter was almost constant. Equations (2.51) and (2.52) give results with an error, but they followed the experimental data. Using these equations a temperature increase of the receiver and a temperature decrease of the emitter are obtained.

6.10.1 CPU Performance of Radiation Methods

A comparison between the radiation methods applied considers a boundary box and three plates. The CPU time needed for calculations using radiation methods applied under the same conditions (the number of rays used for view factor calculation - the Hemi-cube method with 30000 rays per element, time step $\Delta = 2[s]$, time stepping -implicit, iterative solver - preconditioned conjugate gradient, time interval of 6000 [s] when calculations reached steady state, properties of materials etc.) is presented in Table 6.12. From Table 6.12 it can be seen that Stefan-Boltzmann Law required the least computational time. At the same time simple face to face radiosity method required about 11% more CPU time than Stefan-Boltzmann Law, while the MRV method requires the greatest amount of CPU time (125 times more than the Stefan-Boltzmann Law). The main reason that the MRV method requires this additional amount of CPU time is that reflectivity considerations requires extra time for calculation. Also, this is an early stage in the development of the MRV method and future work should consider an acceleration of this method.

Mesh	Number of rays
10x10x10	100
	1000
	10000
	20000
25x25x10	100
	1000
	5000
	10000
	20000
40x40x10	100
	500
	1000
	2000
	5000

Table 6.1: Numerical scheme and number of rays used for the view factor calculation (the Monte Carlo method)

Distance ratio c/L	Temp. of the emitter [K]	HTC [$W/m^2 K$]
0.2	760.65	$h_{S_1}=23$
		$h_{S_2}=21$
		$h_{S_3}=19$
0.5	733.15	$h_{S_1}=22$
		$h_{S_2}=20$
		$h_{S_3}=18$
0.7	725.15	$h_{S_1}=22$
		$h_{S_2}=20$
		$h_{S_3}=18$
1.0	725.15	$h_{S_1}=22$
		$h_{S_2}=20$
		$h_{S_3}=18$

Table 6.2: Boundary conditions for the parallel plates

Temp. of the emitter [K]	HTC [W/m^2K]
	$h_{S_1}=22$
519.4	$h_{S_2}=10$
	$h_{S_3}=8$

Table 6.3: Boundary conditions for the hinged plates

Mesh	Distance ratio c/L	Number of rays	Aver. temp. [K]	Min. temp. [K]
10x10	0.2	100	591.24	562
		1000	605.17	576
		10000	607.09	579
		20000	607.16	579
		50000	607.22	579
	0.5	100	461.95	442
		1000	506.07	483
		10000	510	489
		20000	509.96	489
		50000	510.13	489
	0.7	100	411.23	399
		1000	456.33	440
		10000	461.01	447
		20000	461.34	447
		50000	461.5	447
	1	100	368.08	360
		1000	404.48	396
		10000	413.01	405
		20000	413.12	405
		50000	413.2	405

Table 6.4: Temperatures of the receiver for different number of rays used for the view factor calculation (the Monte Carlo method)

Mesh	Distance ratio c/L	Number of rays	Aver. temp. [K]	Min. temp. [K]
25x25	0.2	100	553.51	525
		1000	598.24	567
		5000	606.23	543
		10000	607.42	576
		20000	608.16	577
	0.5	100	433.52	417
		1000	476.08	455
		5000	506.08	483
		10000	509.67	486
	0.7	100	393.81	384
		1000	420.04	407
		5000	454.37	438
		10000	460.26	444
		20000	461.09	447
	1	100	360.99	355
		1000	373.98	368
		5000	400.73	392
		10000	410.06	401

Table 6.5: Temperatures of the receiver for different number of rays used for the view factor calculation (the Monte carlo method)

Mesh	Distance ratio c/L	Number of rays	Aver. temp. [K]	Min. temp. [K]
40x40	0.2	100	533.94	507
		500	571.39	543
		1000	586.65	557
		2000	596.44	566
	0.5	100	427.47	412
		500	440.89	424
		1000	452.87	434
		2000	469.83	449
	0.7	100	390.68	381
		500	397.31	383
		1000	404.21	393
		2000	415.03	403
		5000	435.81	421
	1	100	359.68	354
		500	362.46	357
		1000	365.7	360
		2000	371.42	365

Table 6.6: Temperatures of the receiver for different number of rays used for the view factor calculation (the Monte Carlo method)

Thermo-physical property	Emitter &Receiver
density $[kg/m^3]$	8030
thermal conductivity $[W/mK]$	16.27
specific heat capacity $[J/kgK]$	503
absorptivity	0.066

Table 6.7: Thermo-physical properties of emitter and receiver composed of steel

Thermo-physical property	Emitter	Receiver
density $[kg/m^3]$	8030	2770
thermal conductivity $[W/mK]$	16.27	119.04
specific heat capacity $[J/kgK]$	503	963
absorptivity	0.066	0.039

Table 6.8: Thermo-physical properties of emitter and receiver composed of steel and aluminium respectively

Thermo-physical property	Emitter	Receiver
density [kg/m^3]	8030	8714
thermal conductivity [W/mK]	16.27	61
specific heat capacity [J/kgK]	503	385
absorptivity	0.066	0.028

Table 6.9: Thermo-physical properties of emitter and receiver composed of steel and brass respectively

Thermo-physical property	Emitter	R 1	R 2	Boundary box
density [kg/m^3]	8030	8714	2700	1600
thermal conductivity [W/mK]	18.9	124.55	232.7	5.69
specific heat capacity [J/kgK]	503	385	753	840
emissivity	0.84	0.177	0.4	0.9

Table 6.10: Thermo-physical properties of emitter, receivers and boundary box respectively

Temp. [K]	exp.	eq.(2.12)	eq.(2.51)	eq.(2.52)	eq.(2.54)	MRV method
emitter	718.16	731	747	762	724.2	719.1
receiver1	324.8	332.18	296	301.4	328.7	324.63
receiver2	299.4	294.6	293	293.5	301.83	298.6
box		293.06	293.08	293.07	298.08	297.04
ambient	292.9					

Table 6.11: Average temperatures of bodies in enclosure using different radiative heat transfer approaches

Stefan-Boltzmann Law	Radiosity face to face	the MRV method
1200	1350	150000

Table 6.12: CPU performance of radiative methods used for simulations - CPU time scale in [s]

Figure 6.1: Mesh 10x10, temperature distribution of the front side of the receiver obtained using the Monte Carlo method with 100 rays/el. for the view factor calculation and equation (2.12) for radiative heat transfer simulation - Temperature scale in [K]

Figure 6.2: Mesh 10x10, temperature distribution of the front side of the receiver obtained using the Monte Carlo method with 1000 and 10000 rays/el. for the view factor calculation and equation (2.12) for radiative heat transfer simulation - Temperature scale in [K]

Figure 6.3: Mesh 10x10, temperature distribution of the front side of the receiver obtained using the Monte Carlo method with 20000 rays/el. for the view factor calculation and equation (2.12) for radiative heat transfer simulation - Temperature scale in [K]

Figure 6.4: Mesh 10x10, temperature distribution of the back side of the receiver obtained using the Monte Carlo method with 100 and 1000 rays/el. for the view factor calculation and equation (2.12) for radiative heat transfer simulation - Temperature scale in [K]

Figure 6.5: Mesh 10x10, temperature distribution of the back side of the receiver obtained using the Monte Carlo method with 10000 and 20000 rays/el. for the view factor calculation and equation (2.12) for radiative heat transfer simulation - Temperature scale in [K]

Figure 6.6: Mesh 10x10, radiative flux of the emitter obtained using the Monte Carlo method with 100 and 1000 rays/el. for the view factor calculation and equation (2.12) for radiative heat transfer simulation - scale in [W/el.]

Figure 6.7: Mesh 10x10, radiative flux of the emitter obtained using using the Monte Carlo method with 10000 and 20000 rays/el. for the view factor calculation and equation (2.12) for radiative heat transfer simulation - scale in [W/el.]

Figure 6.8: Emitter was divided by 20x20x4 mesh while the receiver was divided by 20x20x10 mesh, hinged plates

Figure 6.9: Temperature distributions of a) front side; b) back side of the receiver obtained using the Monte Carlo method with 10000 rays/el. for the view factor calculation - Temperature scale in [K]
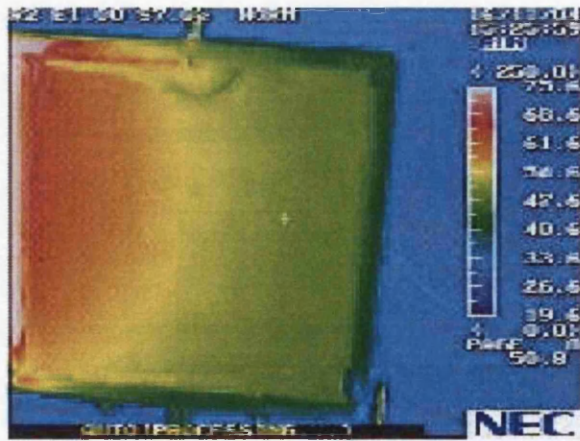
Figure 6.10: Thermal image of the receiver for hinged plates case - Temperature scale in $°C$
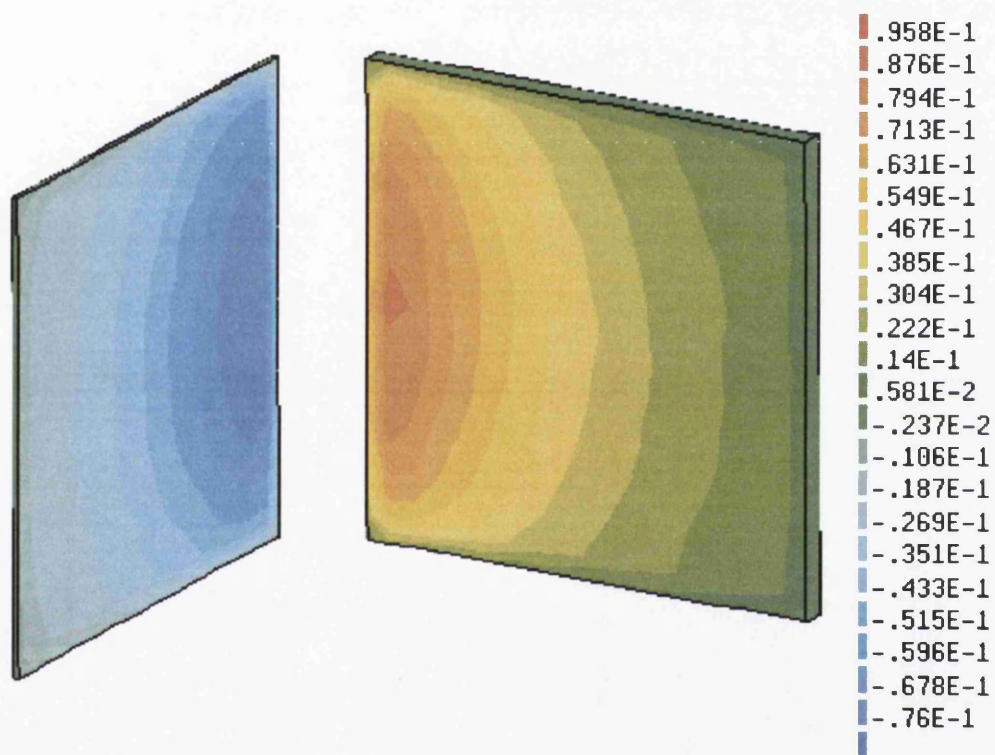
Figure 6.11: Radiative flux exchanged between hinged plates obtained using the Monte Carlo method with 10000 rays/el. for the view factor calculation - Scale in [W/el.]

mesh 10x10x10 - receiver
4x9x4 - emitter

334
333
332
331
331
330
329

100 rays/el.

Figure 6.12: Mesh and temperature distribution of the front side of the receiver obtained using the Monte Carlo method with 100 rays/el. for the view factor calculation and equation (2.12) for the radiative heat transfer simulation - Temperature scale in [K]
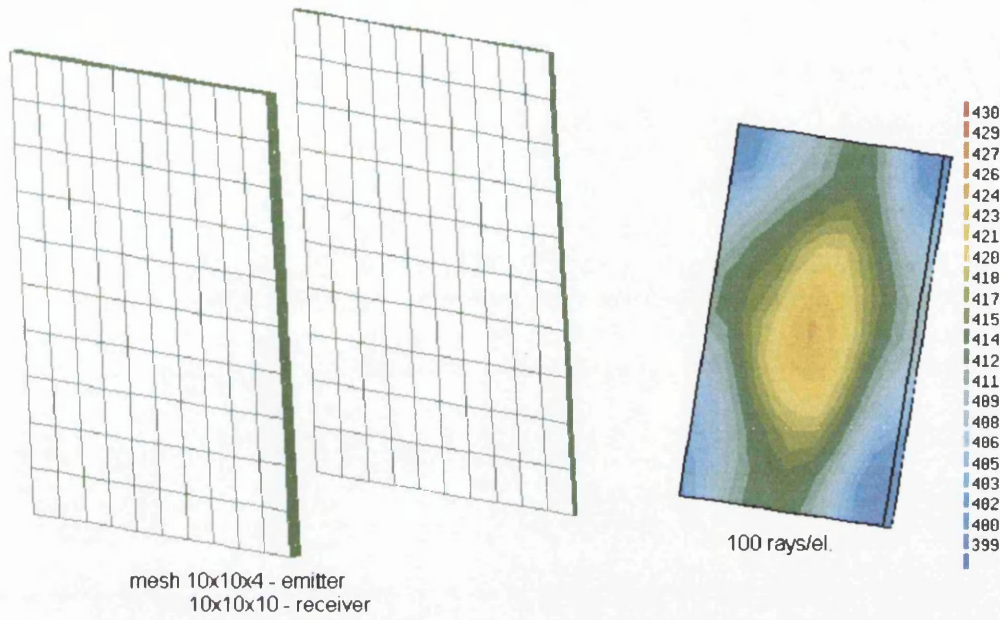
Figure 6.13: Temperature distribution of the front side of the receiver obtained using the Monte Carlo method with 1000 and 10000 rays/el. for the view factor calculation and equation (2.12) for the radiative heat transfer simulation - Temperature scale in [K]

Figure 6.14: Temperature distribution of the front side of the receiver obtained using the Monte Carlo method with 20000 and 50000 rays/el. for the view factor calculation and equation (2.12) for the radiative heat transfer simulation - Temperature scale in [K]
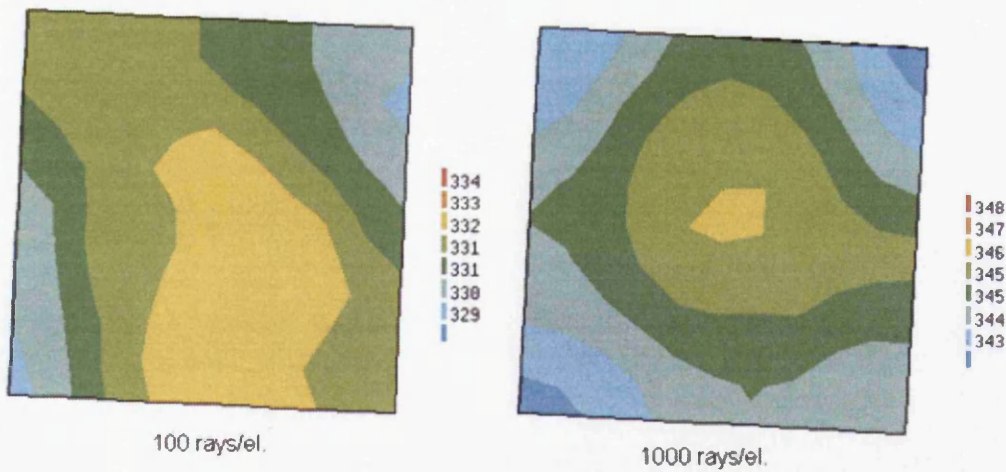
Figure 6.15: Temperature distribution of the back side of the receiver obtained using the Monte Carlo method with 100 and 1000 rays/el. for the view factor calculation and equation (2.12) for the radiative heat transfer simulation - Temperature scale in [K]

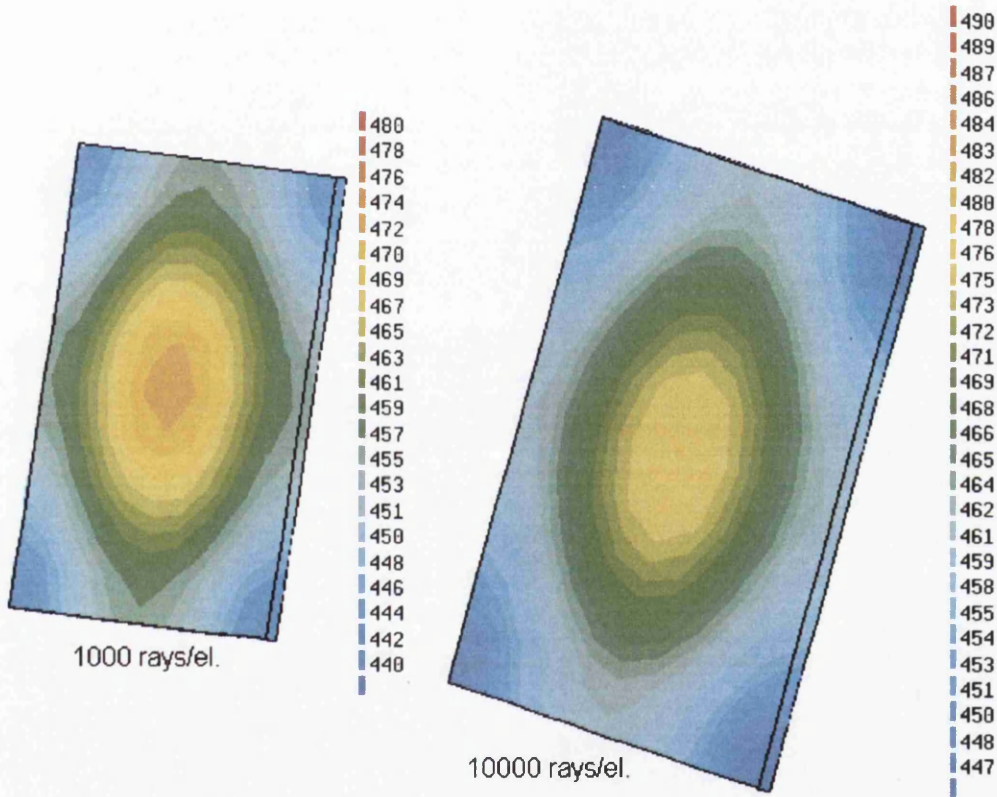Figure 6.16: Temperature distribution of the back side of the receiver obtained using the Monte Carlo method with 10000 and 20000 rays/el. for the view factor calculation and equation (2.12) for the radiative heat transfer simulation - Temperature scale in [K]
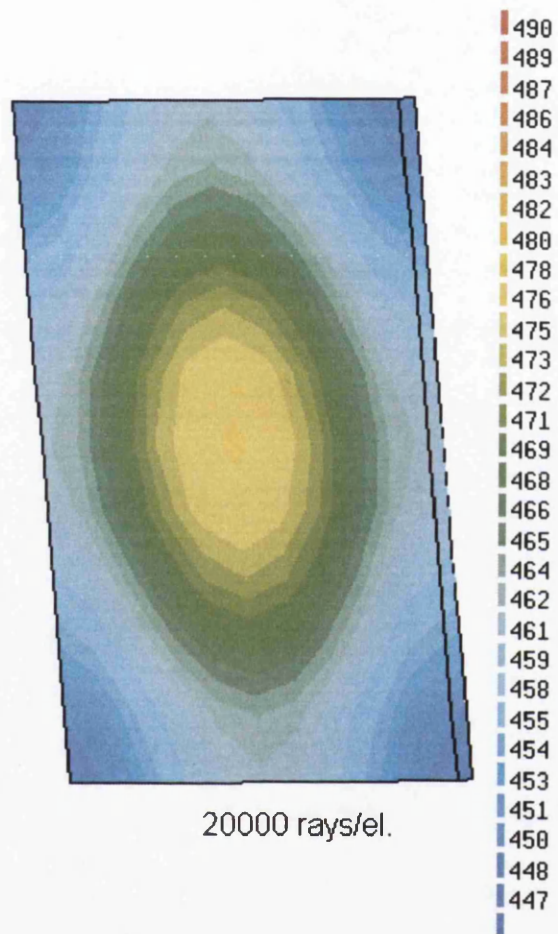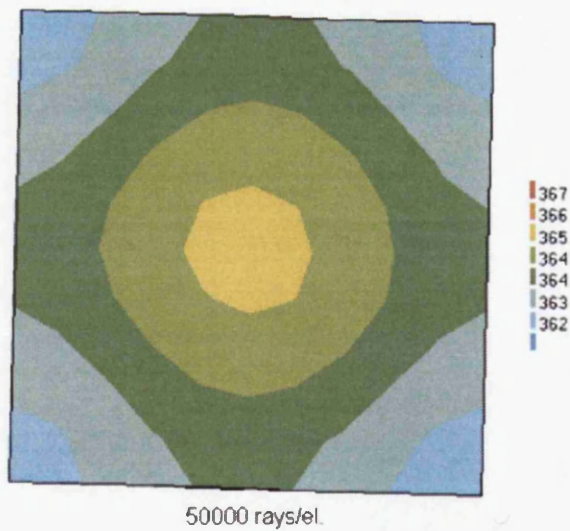

Figure 6.17: Temperature distribution of the back side of the receiver obtained using the Monte Carlo method with 50000 rays/el. for the view factor calculation and equation (2.12) for the radiative heat transfer simulation - Temperature scale in [K]
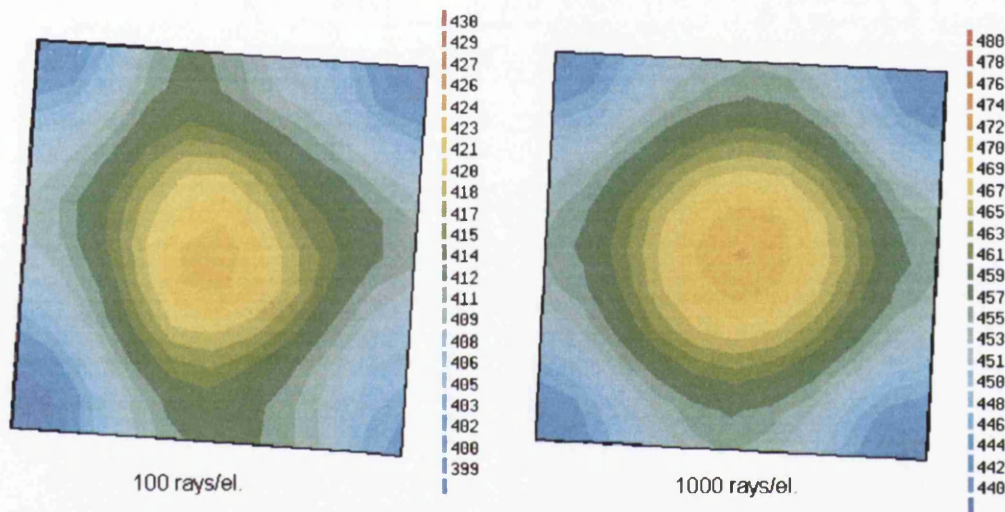
Figure 6.18: Radiative flux of the emitter obtained using the Monte Carlo method with 100 and 1000 rays/el. for the view factor calculation and equation (2.12) for the radiative heat transfer simulation - Scale in [W/el.]

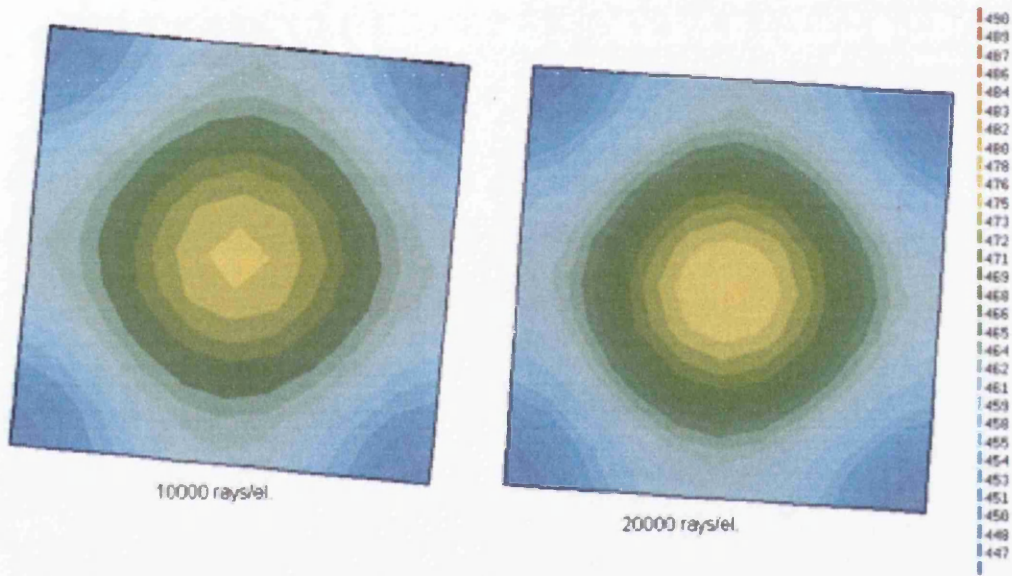Figure 6.19: Radiative flux of the emitter obtained using the Monte Carlo method with 10000 and 20000 rays/el. for the view factor calculation and equation (2.12) for the radiative heat transfer simulation - Scale in [W/el.]

Figure 6.20: Radiative flux of the emitter obtained using the Monte Carlo method with 50000 rays/el. for the view factor calculation and equation (2.12) for the radiative heat transfer simulation - Scale in [W/el.]
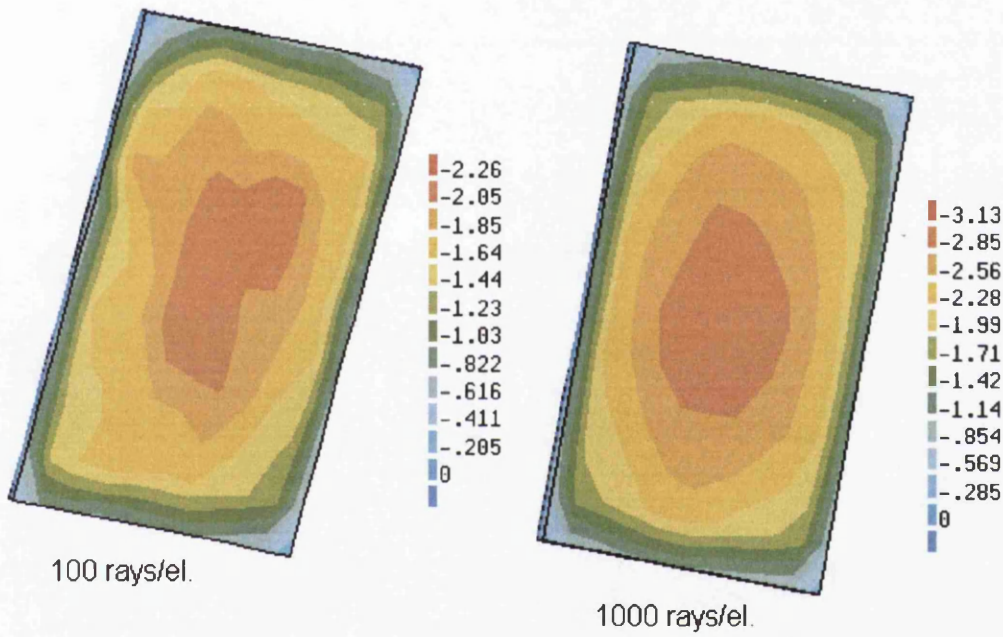

Figure 6.21: Radiative flux of the receiver obtained using the Monte Carlo method with 100 and 1000 rays/el. for the view factor calculation and equation (2.12) for the radiative heat transfer simulation - Scale in [W/el.]

Figure 6.22: Radiative flux of the receiver obtained using the Monte Carlo method with 10000 and 20000 rays/el. for the view factor calculation and equation (2.12) for the radiative heat transfer simulation - Scale in [W/el.]
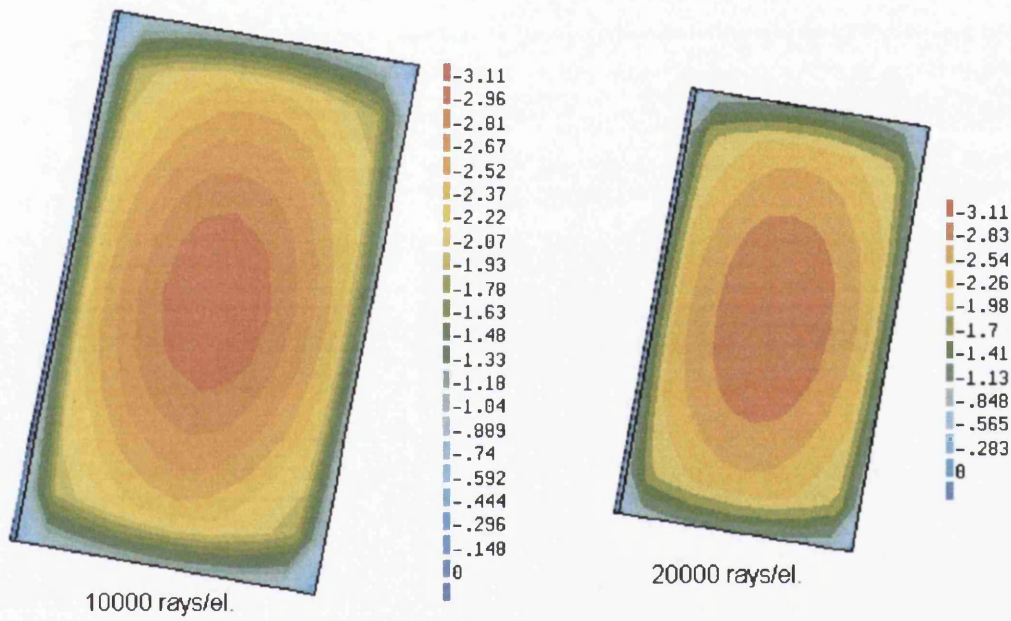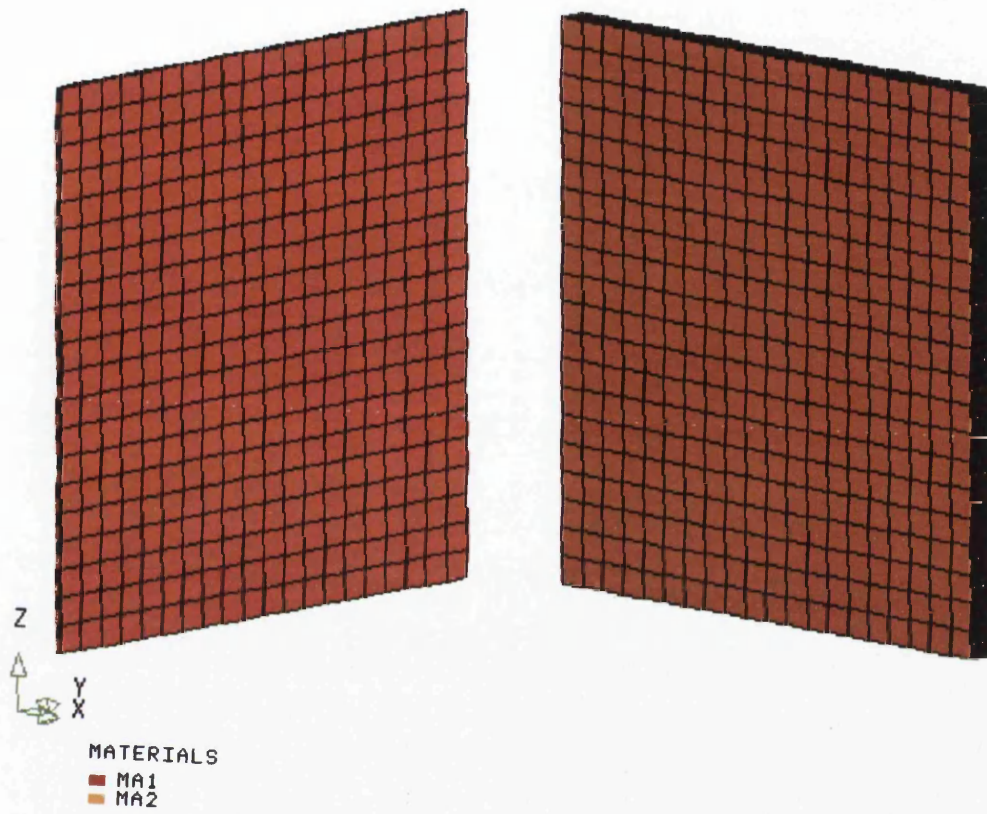

Figure 6.23: Radiative flux of the receiver obtained using the Monte Carlo method with 50000 rays/el. for the view factor calculation and equation (2.12) for the radiative heat transfer simulation - Scale in [W/el.]

mesh 20x20x10 - receiver
4x19x4 - emitter

100 rays/el.

335
334
334
333
333
332
332
331
331
330
330
329

Figure 6.24: Mesh and temperature distribution of the front side of the receiver obtained using the Monte Carlo method with 100 rays/el. for the view factor calculation and equation (2.12) for the radiative heat transfer simulation - Temperature scale in [K]
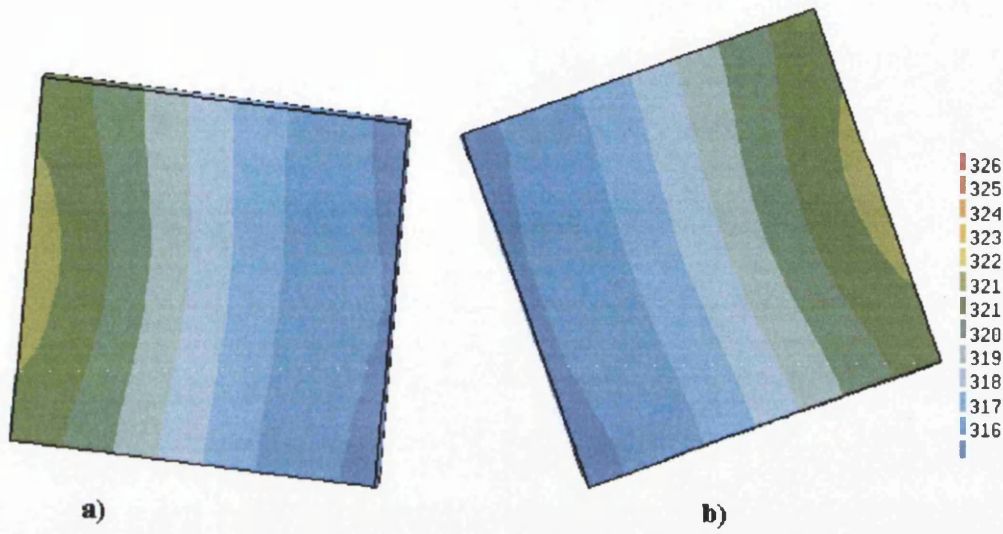
Figure 6.25: Temperature distribution of the front side of the receiver obtained using the Monte Carlo method with 1000 and 5000 rays/el. for the view factor calculation and equation (2.12) for the radiative heat transfer simulation - Temperature scale in [K]

Figure 6.26: Temperature distribution of the front side of the receiver obtained using the Monte Carlo method with 10000 and 20000 rays/el. for the view factor calculation and equation (2.12) for the radiative heat transfer simulation - Temperature scale in [K]

100 rays/el.

1000 rays/el.

Figure 6.27: Temperature distribution of the front side of the receiver obtained using the Monte Carlo method with 100 and 1000 rays/el. for the view factor calculation and equation (2.12) for the radiative heat transfer simulation - Temperature scale in [K]

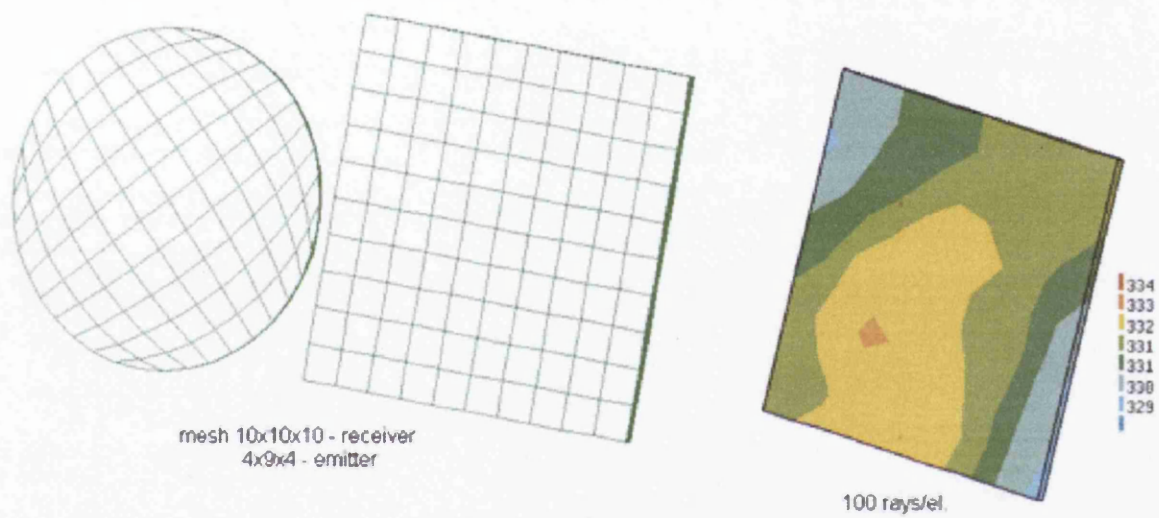5000 rays/el.

10000 rays/el.

Figure 6.28: Temperature distribution of the front side of the receiver obtained using the Monte Carlo method with 5000 and 10000 rays/el. for the view factor calculation and equation (2.12) for the radiative heat transfer simulation - Temperature scale in [K]
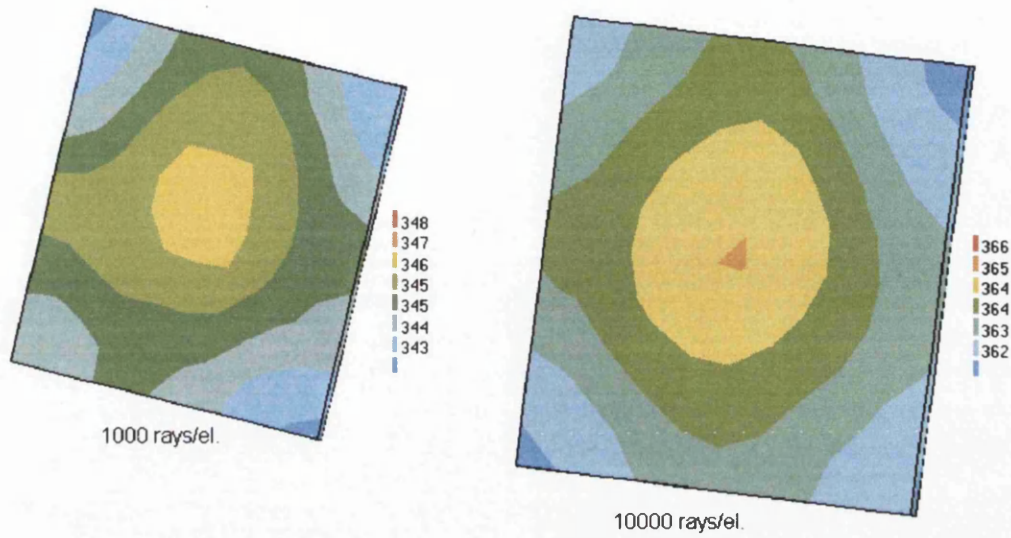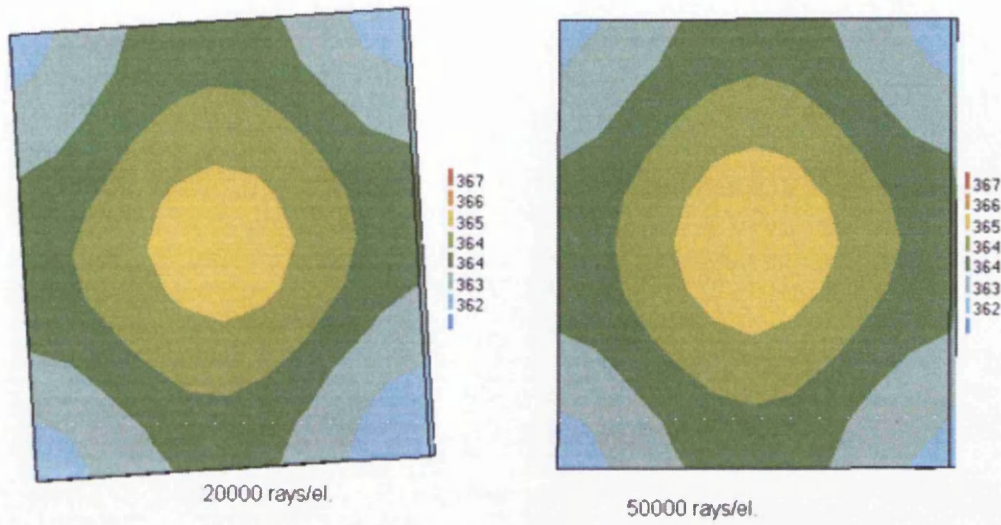
Figure 6.29: Temperature distribution of the front side of the receiver obtained using the Monte Carlo method with 20000 and 50000 rays/el. for the view factor calculation and equation (2.12) for the radiative heat transfer simulation - Temperature scale in [K]


Figure 6.30: Radiative flux of the emitter for 100 and 1000 rays/el.

Figure 6.31: Radiative flux of the emitter obtained using the Monte Carlo method with 5000 and 10000 rays/el. for the view factor calculation and equation (2.12) for the radiative heat transfer simulation - Scale in [W/el.]
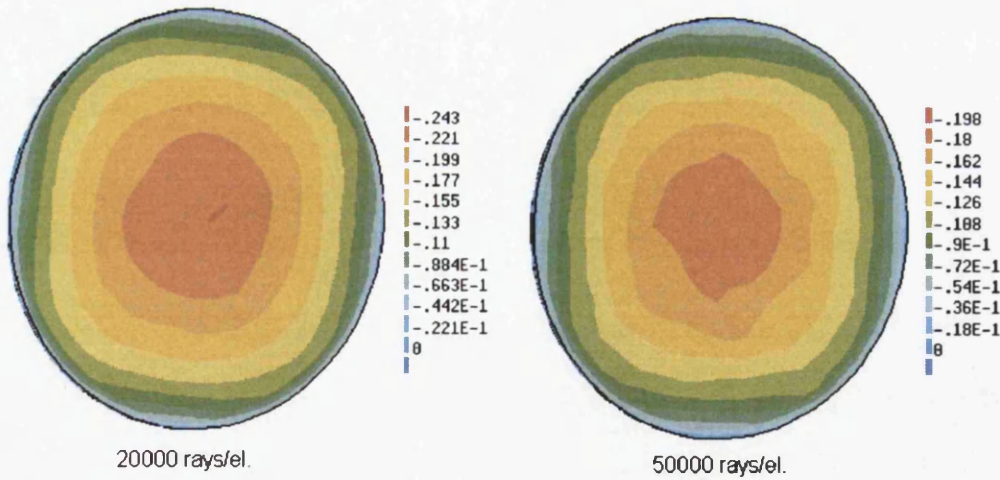
Figure 6.32: Radiative flux of the emitter obtained using the Monte Carlo method with 20000 and 50000 rays/el. for the view factor calculation and equation (2.12) for the radiative heat transfer simulation - Scale in [W/el.]

Figure 6.33: Radiative flux of the receiver obtained using the Monte Carlo method with 100 and 1000 rays/el. for the view factor calculation and equation (2.12) for the radiative heat transfer simulation - Scale in [W/el.]

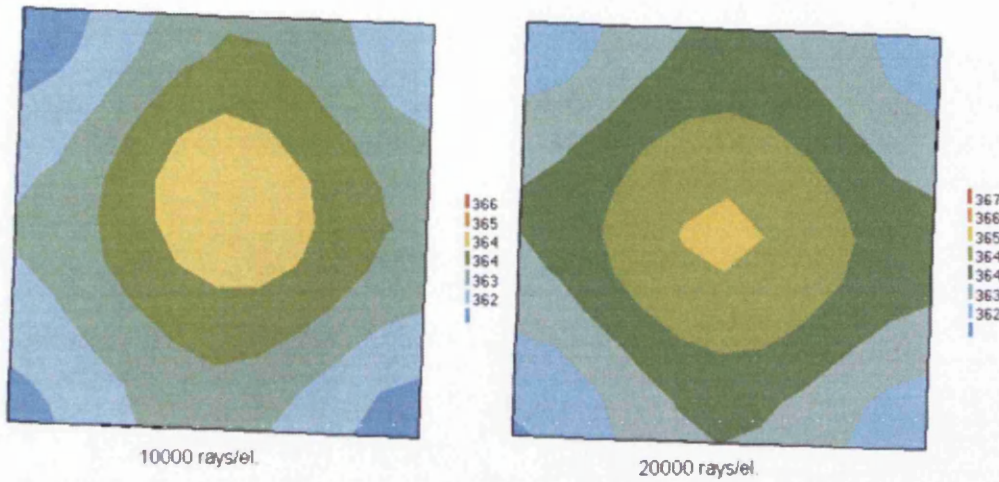Figure 6.34: Radiative flux of the receiver obtained using the Monte Carlo method with 5000 and 10000 rays/el. for the view factor calculation and equation (2.12) for the radiative heat transfer simulation - Scale in [W/el.]

Figure 6.35: Radiative flux of the receiver obtained using the Monte Carlo method with 20000 and 50000 rays/el. for the view factor calculation and equation (2.12) for the radiative heat transfer simulation - Scale in [W/el.]

mesh 40x40x10 - receiver
4x39x4 - emitter

100 rays/el.

333
332
331
331
330
329

Figure 6.36: Mesh and temperature distribution of the front side of the receiver obtained using the Monte Carlo method with 100 rays/el. for the view factor calculation and equation (2.12) for the radiative heat transfer simulation - Temperature scale in [K]
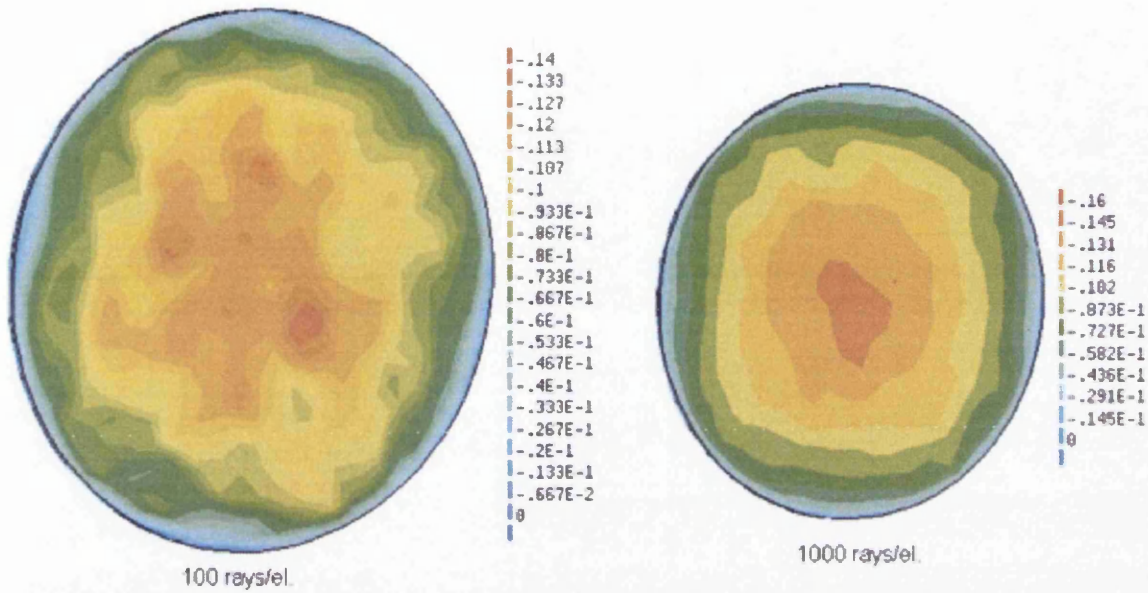
500 rays/el.	1000 rays/el.
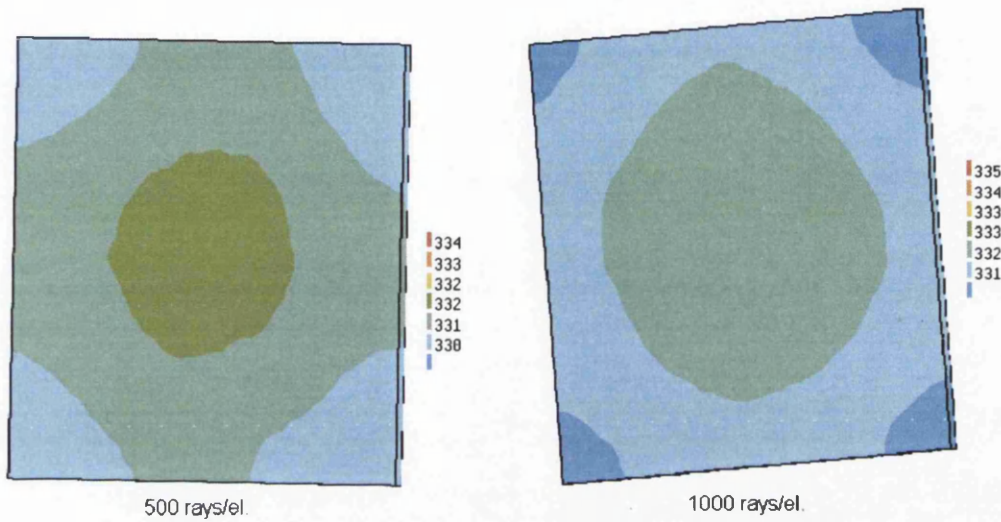
Figure 6.37: Temperature distribution of the front side of the receiver obtained using the Monte Carlo method with 500 and 1000 rays/el. for the view factor calculation and equation (2.12) for the radiative heat transfer simulation - Temperature scale in [K]
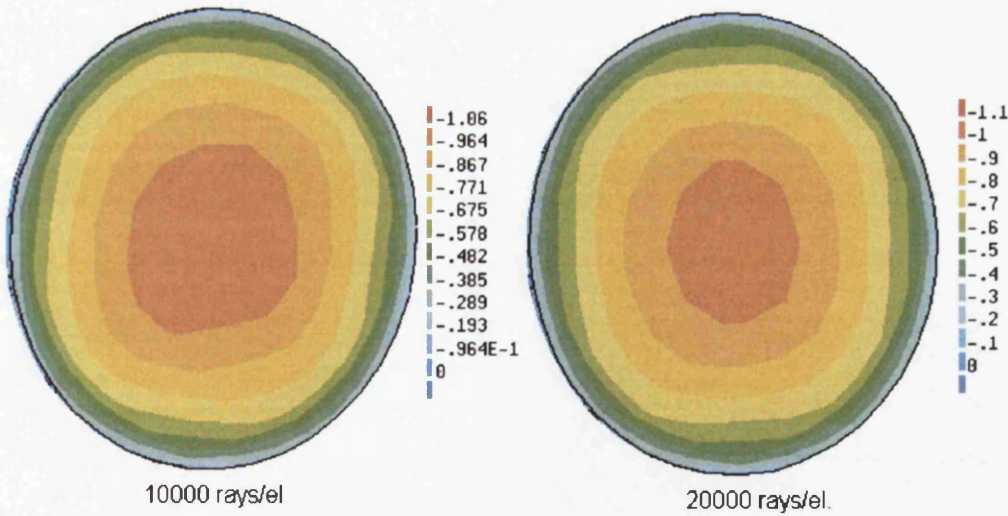

2000 rays/el.	5000 rays/el.
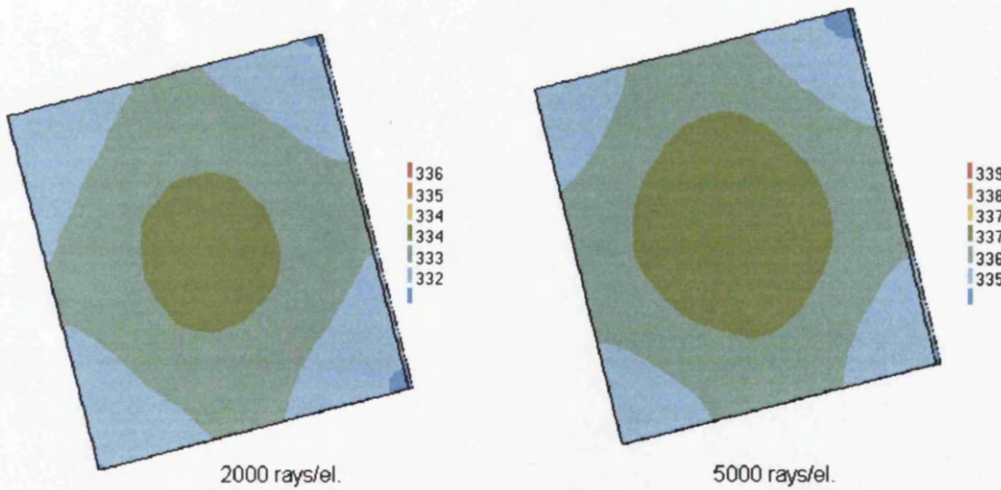
Figure 6.38: Temperature distribution of the front side of the receiver obtained using the Monte Carlo method with 2000 and 5000 rays/el. for the view factor calculation and equation (2.12) for the radiative heat transfer simulation - Temperature scale in [K]

1000 rays/el.
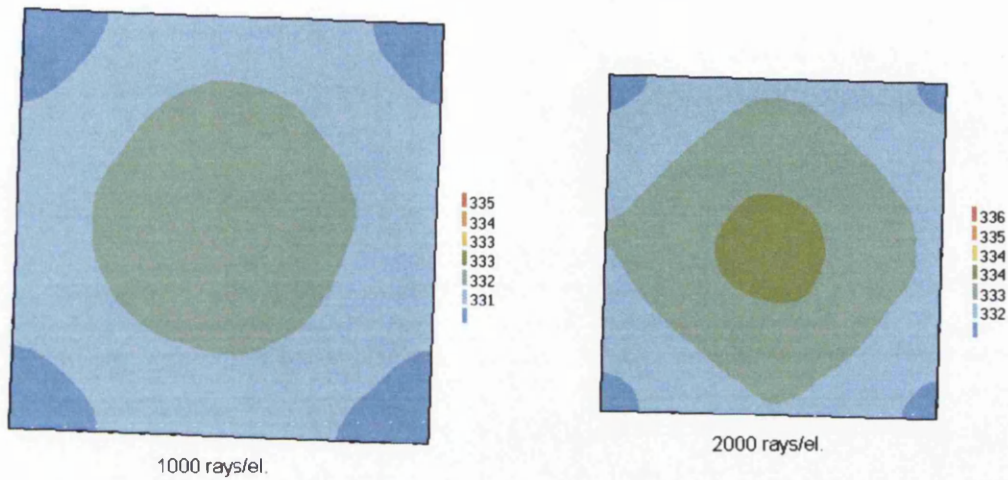
2000 rays/el.

Figure 6.39: Temperature distribution of the back side of the receiver obtained using the Monte Carlo method with 1000 and 2000 rays/el. for the view factor calculation and equation (2.12) for the radiative heat transfer simulation - Temperature scale in [K]
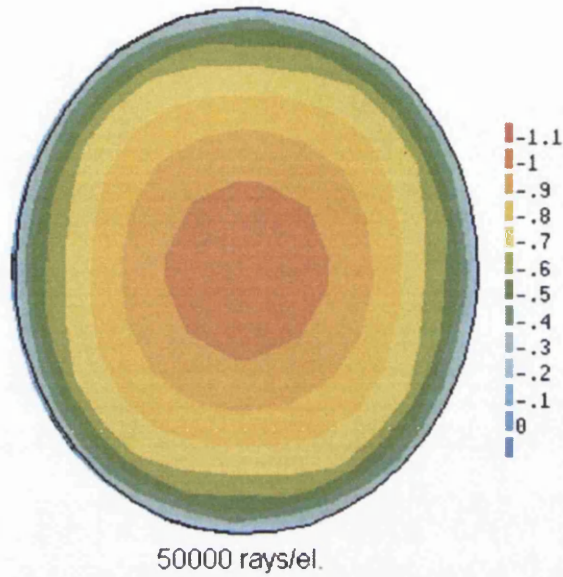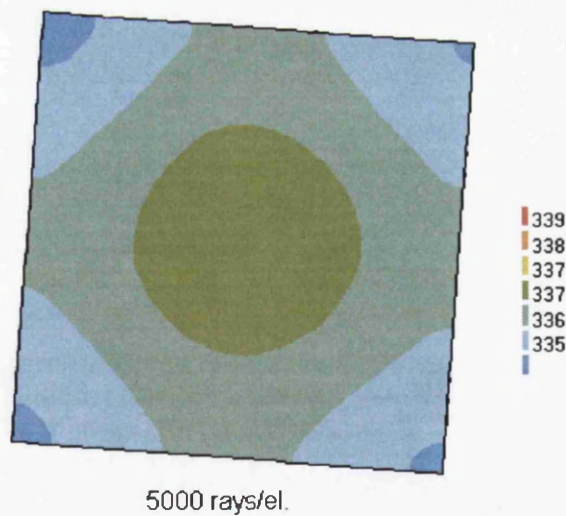

5000 rays/el.

Figure 6.40: Temperature distribution of the back side of the receiver obtained using the Monte Carlo method with 5000 rays/el. for the view factor calculation and equation (2.12) for the radiative heat transfer simulation - Temperature scale in [K]
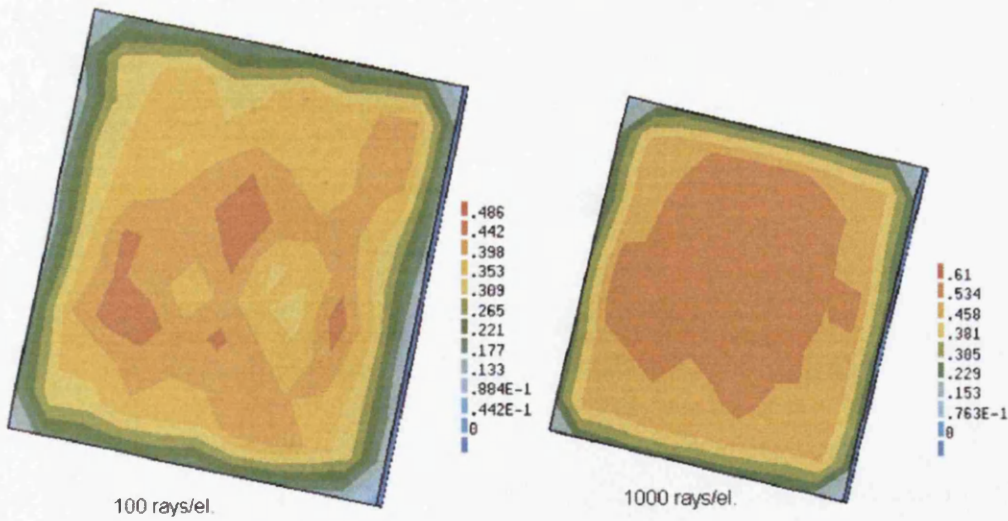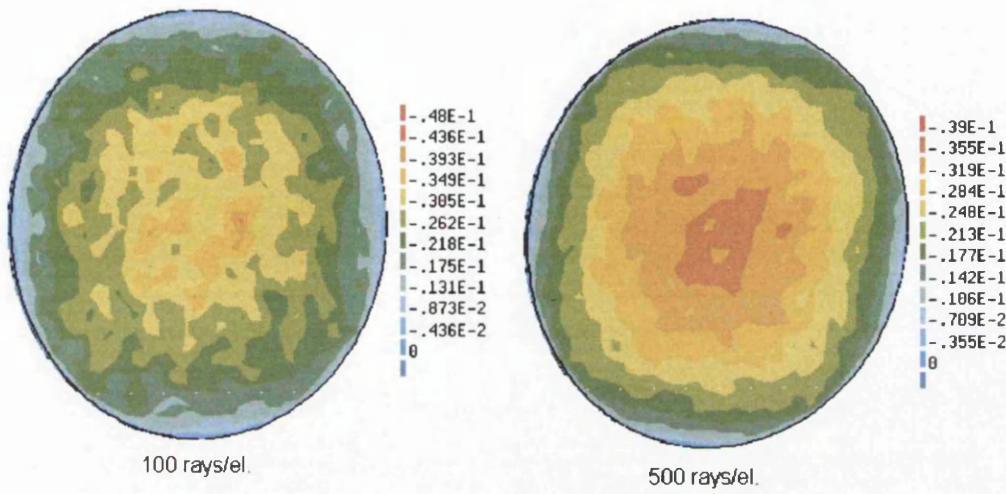
Figure 6.41: Radiative flux of the emitter obtained using the Monte Carlo method with 100 and 500 rays/el. for the view factor calculation and equation (2.12) for the radiative heat transfer simulation - Scale in [W/el.]
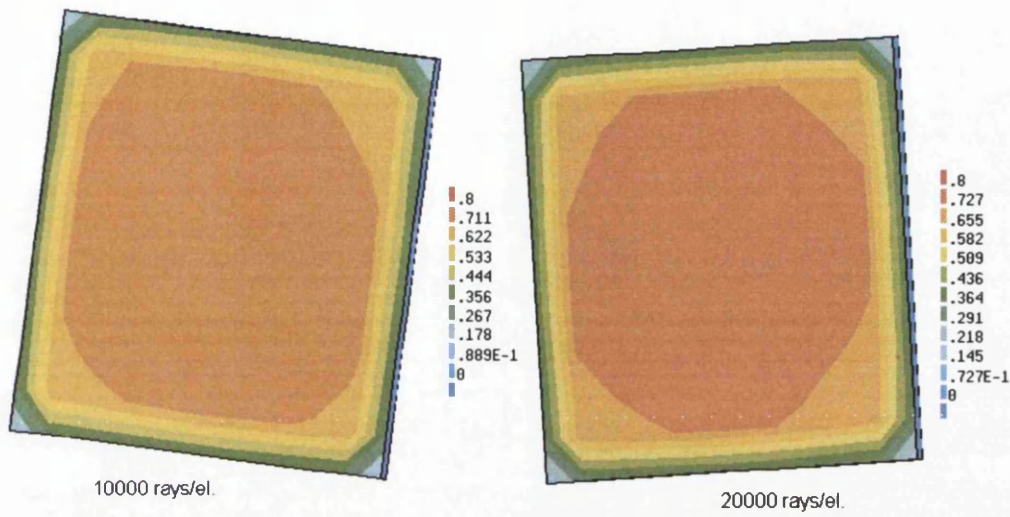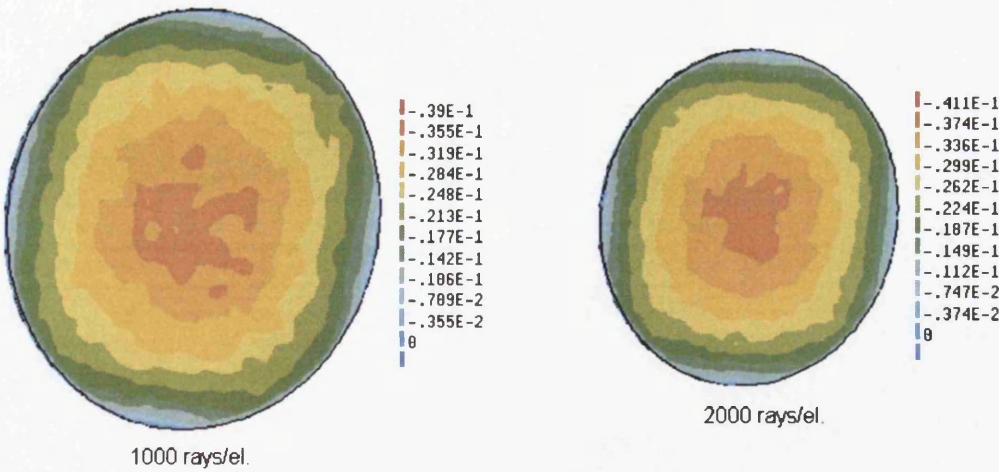

Figure 6.42: Radiative flux of the emitter obtained using the Monte Carlo method with 1000 and 2000 rays/el. for the view factor calculation and equation (2.12) for the radiative heat transfer simulation - Scale in [W/el.]
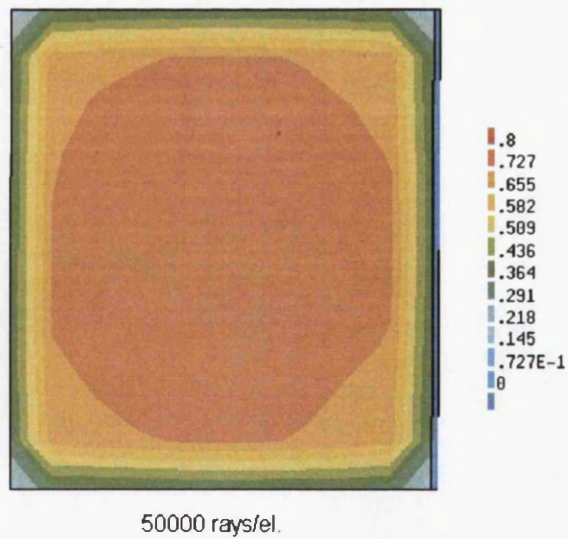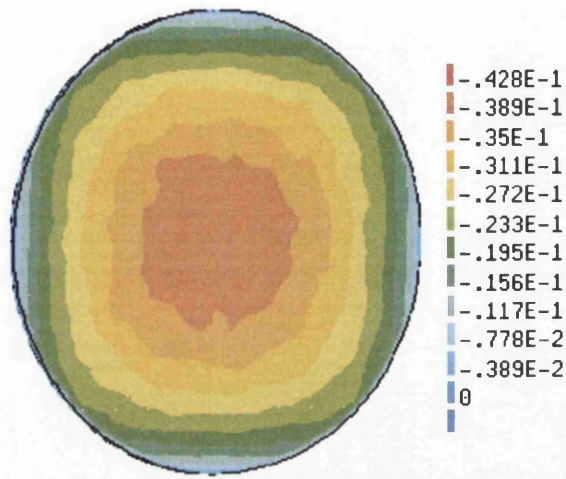
5000 rays/el.

Figure 6.43: Radiative flux of the emitter obtained using the Monte Carlo method with 5000 rays/el. for the view factor calculation and equation (2.12) for the radiative heat transfer simulation - Scale in [W/el.]
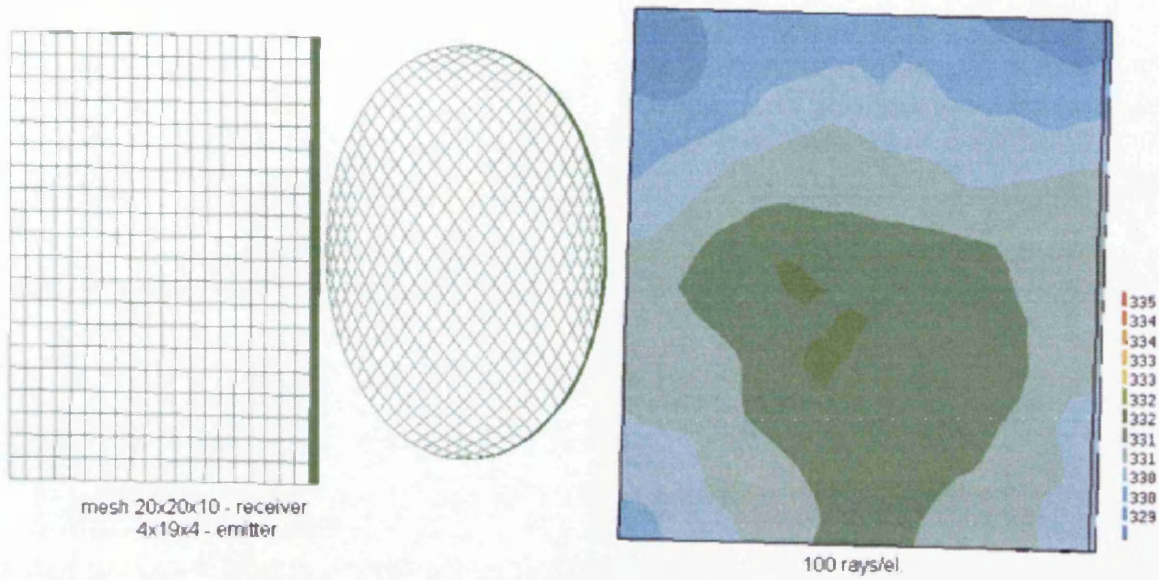

100 rays/el.   500 rays/el.
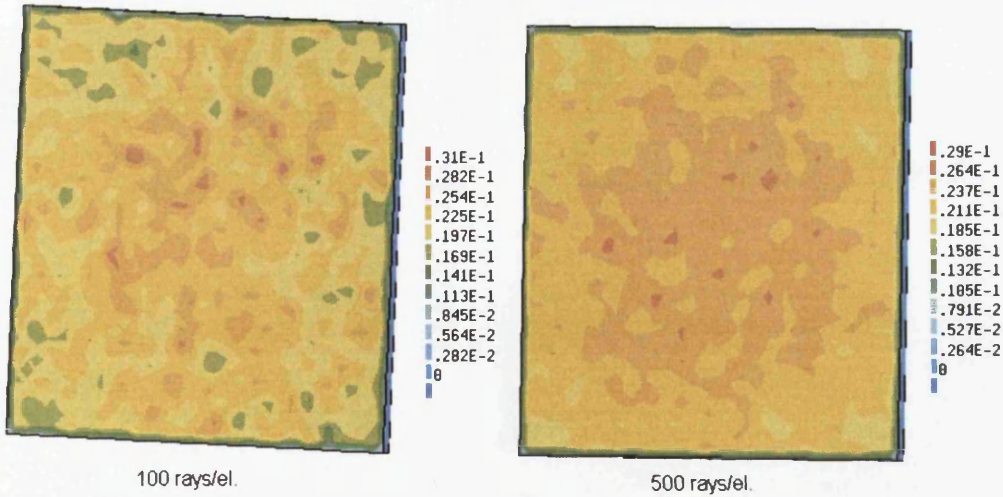
Figure 6.44: Radiative flux of the receiver obtained using the Monte Carlo method with 100 and 500 rays/el. for the view factor calculation and equation (2.12) for the radiative heat transfer simulation - Scale in [W/el.]
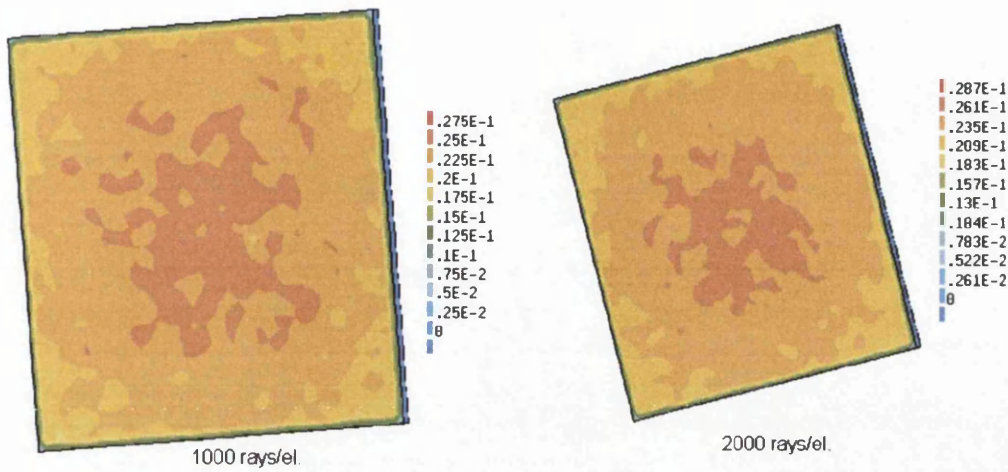
Figure 6.45: Radiative flux of the receiver obtained using the Monte Carlo method with 1000 and 2000 rays/el. for the view factor calculation and equation (2.12) for the radiative heat transfer simulation - Scale in [W/el.]
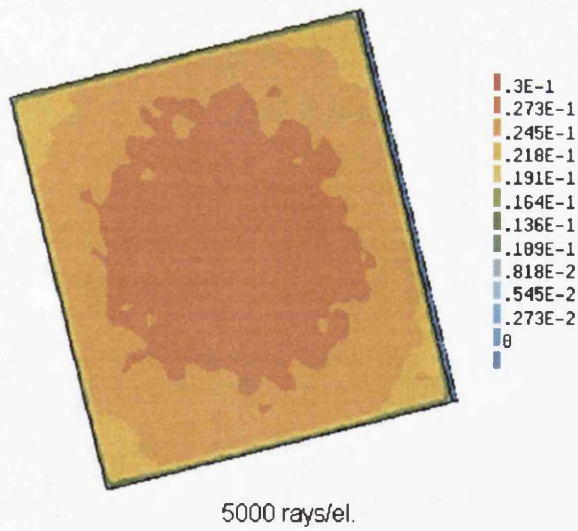
Figure 6.46: Radiative flux of the receiver obtained using the Monte Carlo method with 5000 rays/el. for the view factor calculation and equation (2.12) for the radiative heat transfer simulation - Scale in [W/el.]

mesh 10x10x10 - receiver
4x4x10 - emitter

100 rays/el.

390
389
387
386
385
384
382
381
379
377
376
375
374
372
371
370
369
367
366
365
364
362
361
359
357
356
355
354
352
351
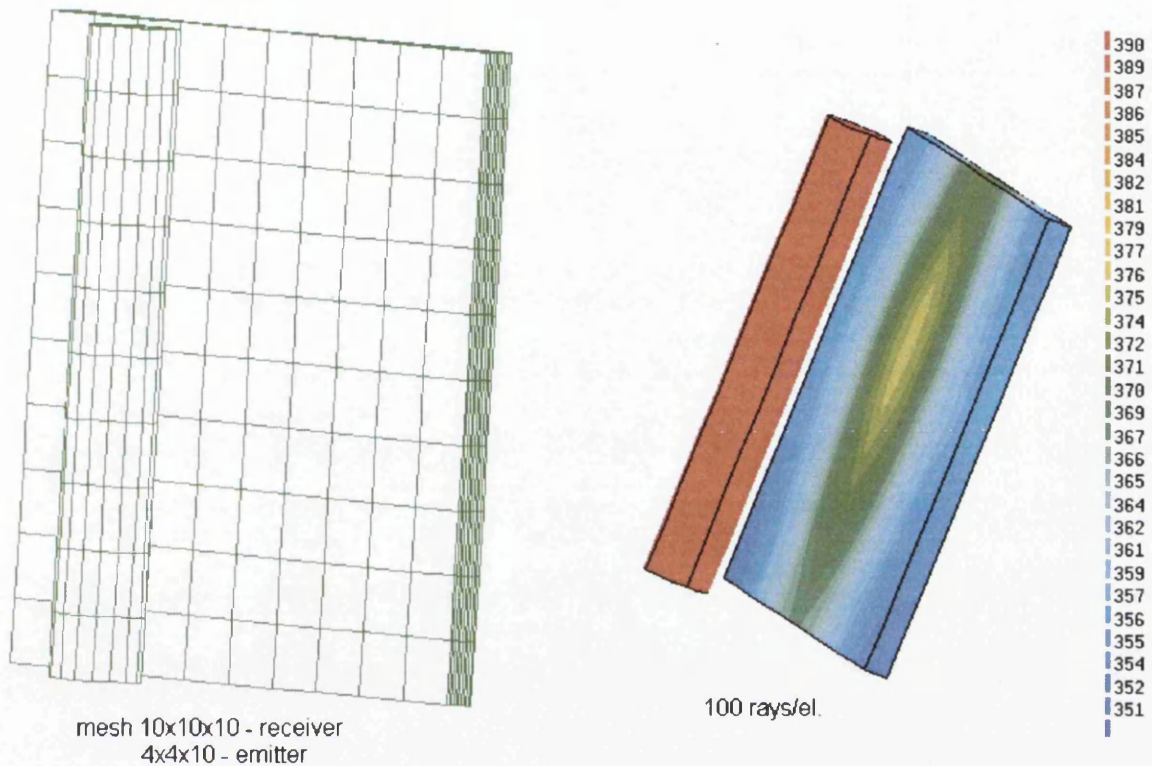
Figure 6.47: Mesh and temperature distribution of the front side of the receiver obtained using the Monte Carlo method with 100 rays/el. for the view factor calculation and equation (2.12) for the radiative heat transfer simulation - Temperature scale in [K]
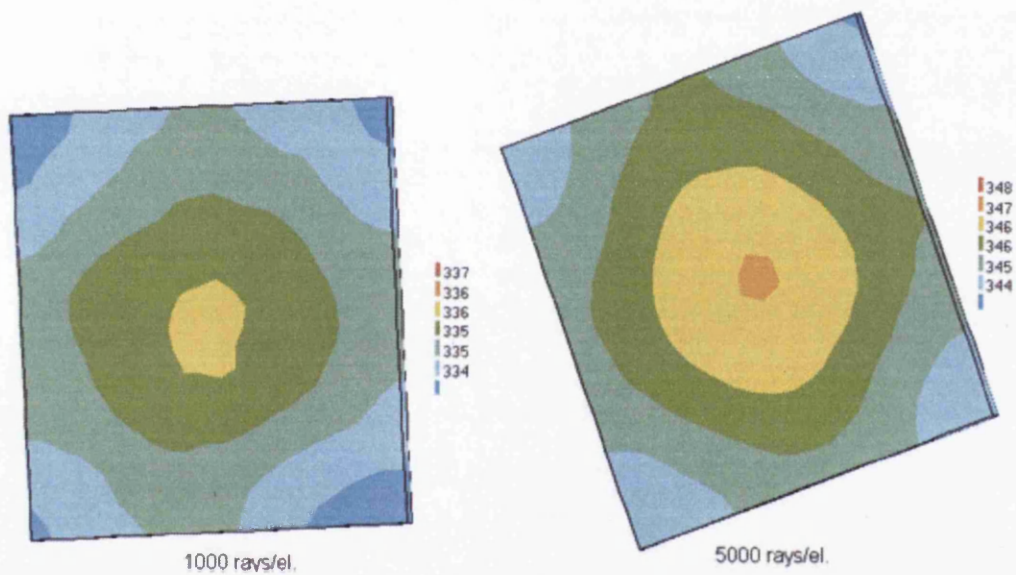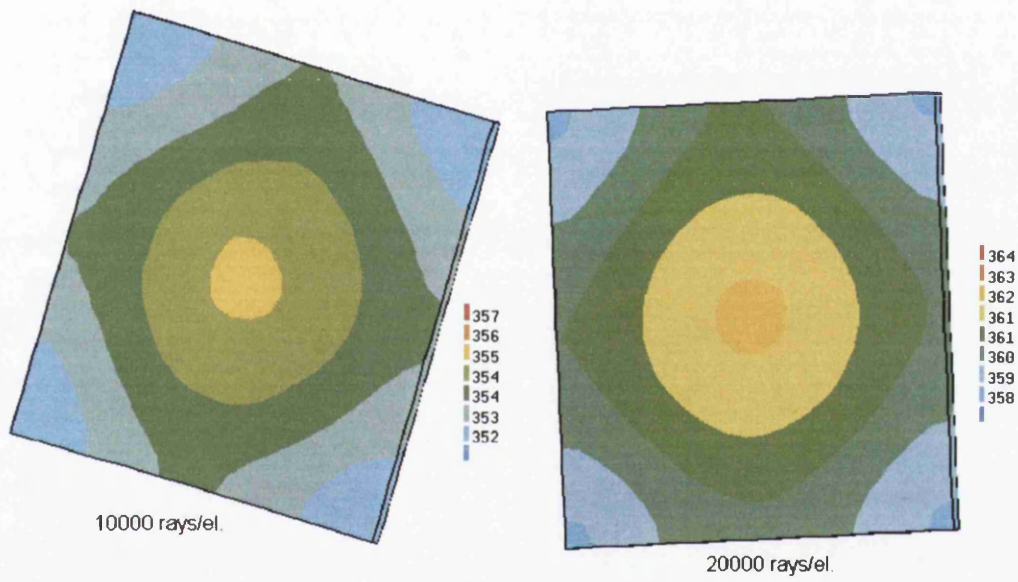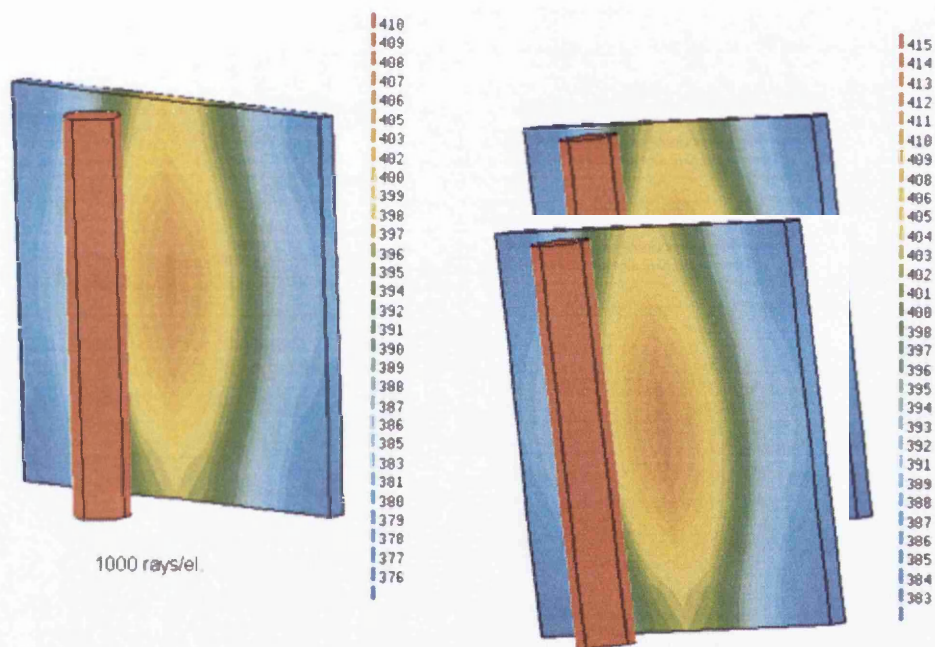
Figure 6.48: Temperature distribution of the front side of the receiver obtained using the Monte Carlo method with 1000 and 10000 rays/el. for the view factor calculation and equation (2.12) for the radiative heat transfer simulation - Temperature scale in [K]
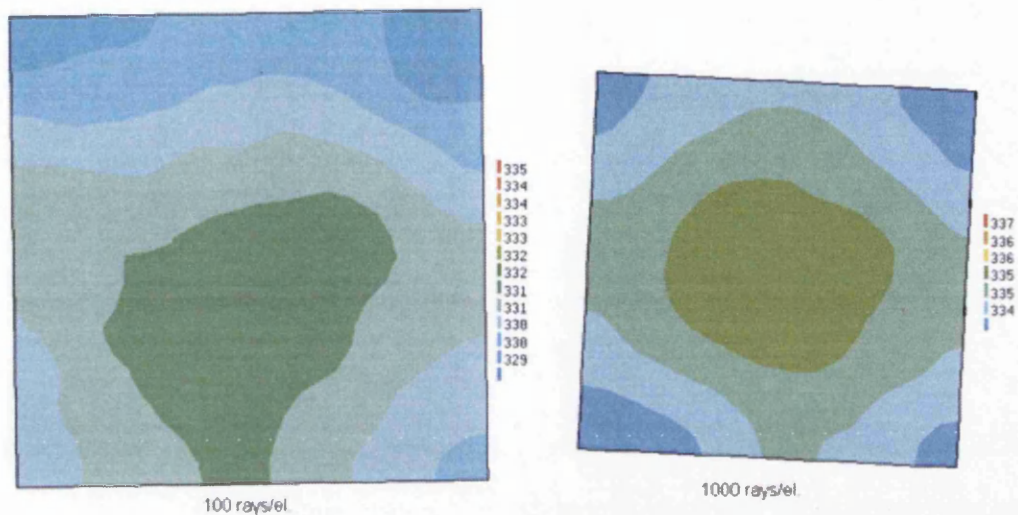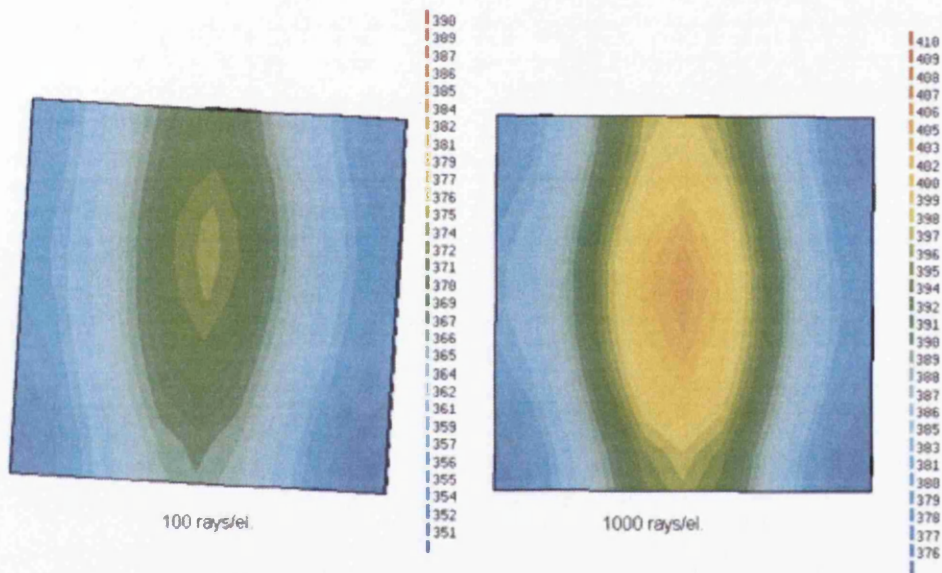
Figure 6.49: Temperature distribution of the back side of the receiver obtained using the Monte Carlo method with 100 and 1000 rays/el. for the view factor calculation and equation (2.12) for the radiative heat transfer simulation - Temperature scale in [K]
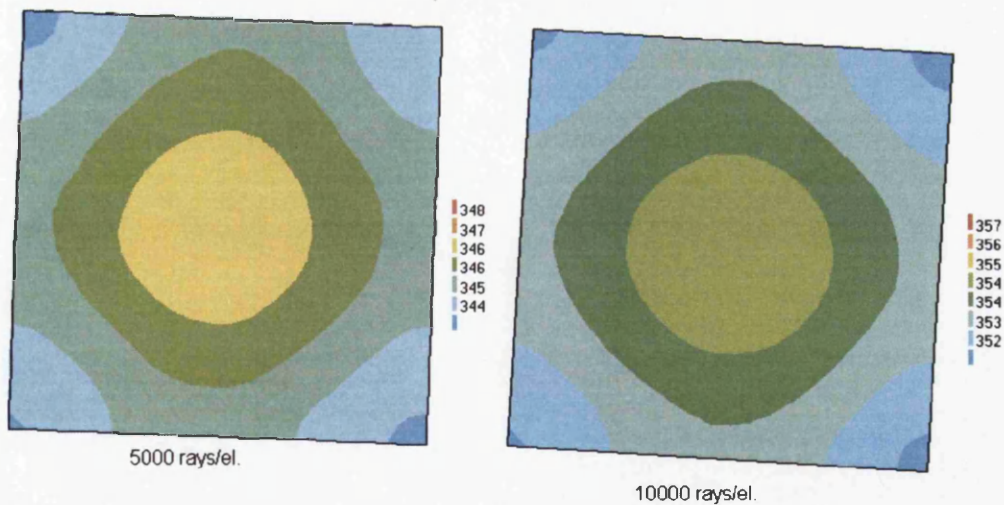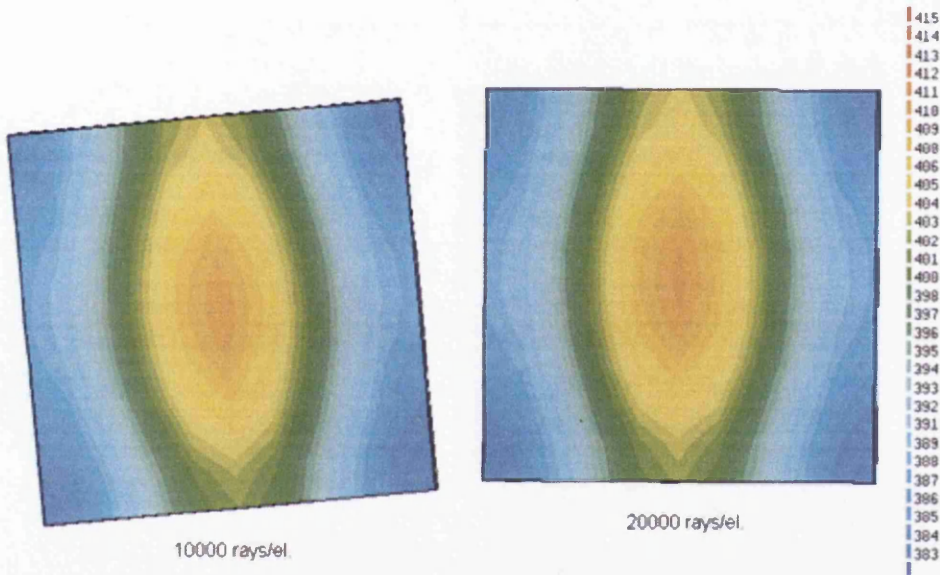
Figure 6.50: Temperature distribution of the back side of the receiver obtained using the Monte Carlo method with 10000 and 20000 rays/el. for the view factor calculation and equation (2.12) for the radiative heat transfer simulation - Temperature scale in [K]
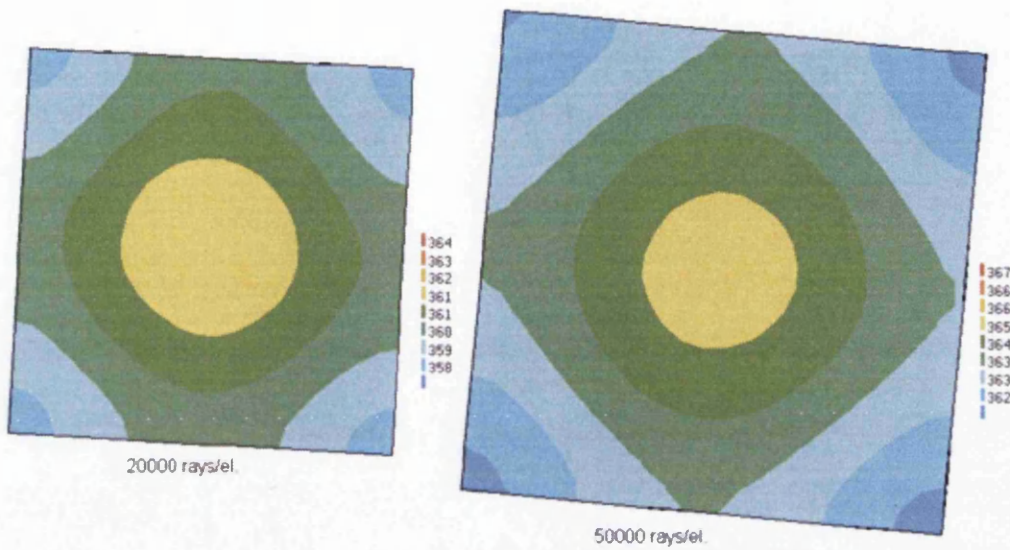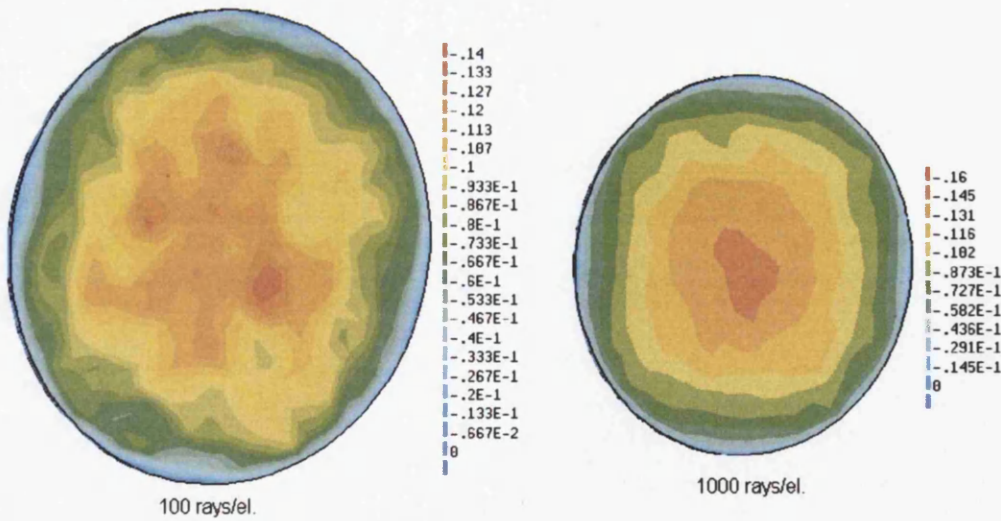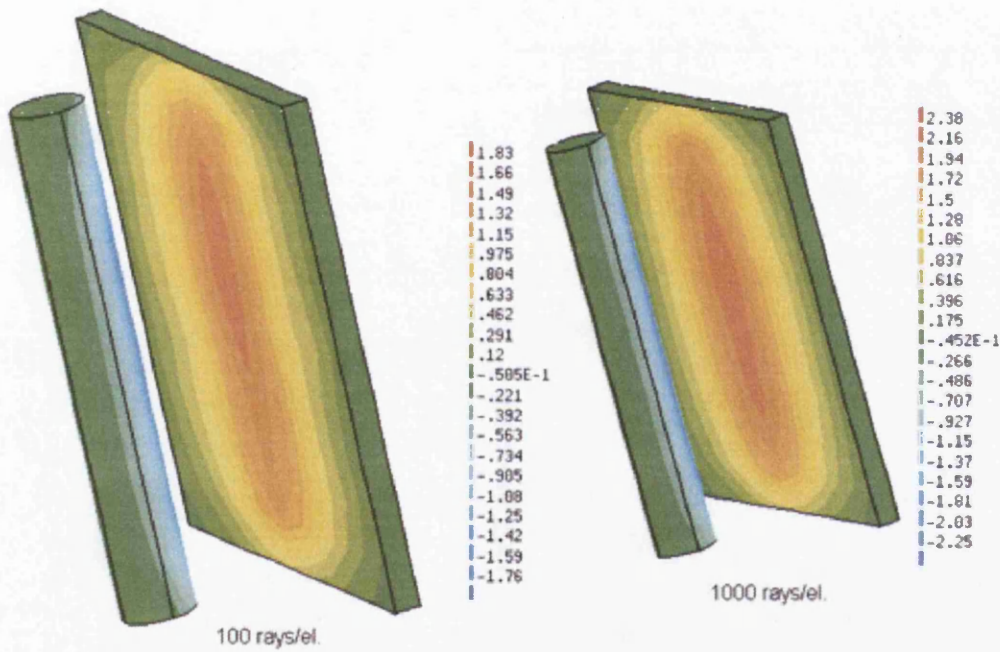
Figure 6.51: Net radiative flux exchanged between the emitter and the receiver obtained using the Monte Carlo method with 100 and 1000 rays/el. for the view factor calculation and equation (2.12) for the radiative heat transfer simulation - Scale in [W/el.]
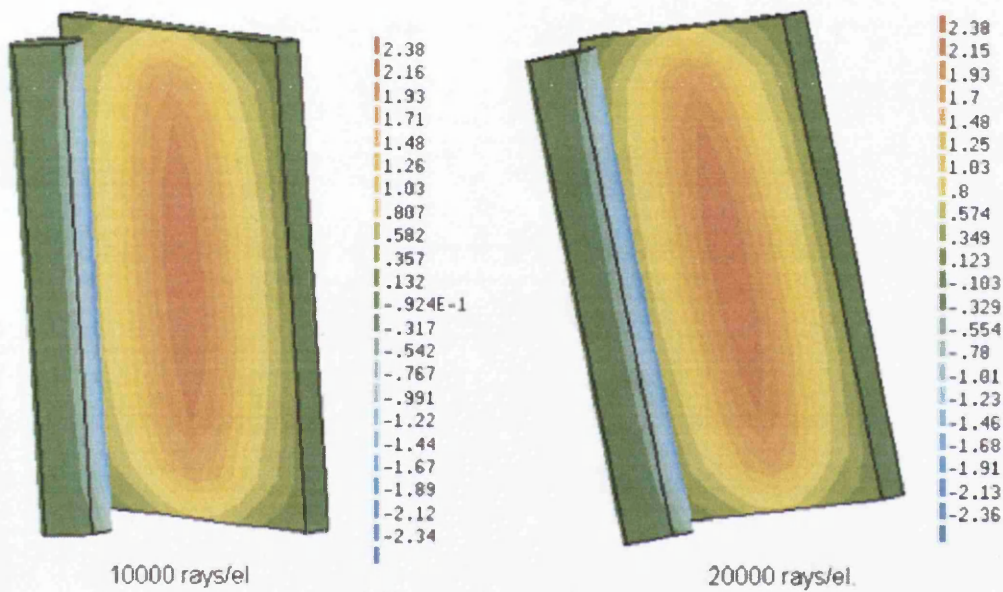
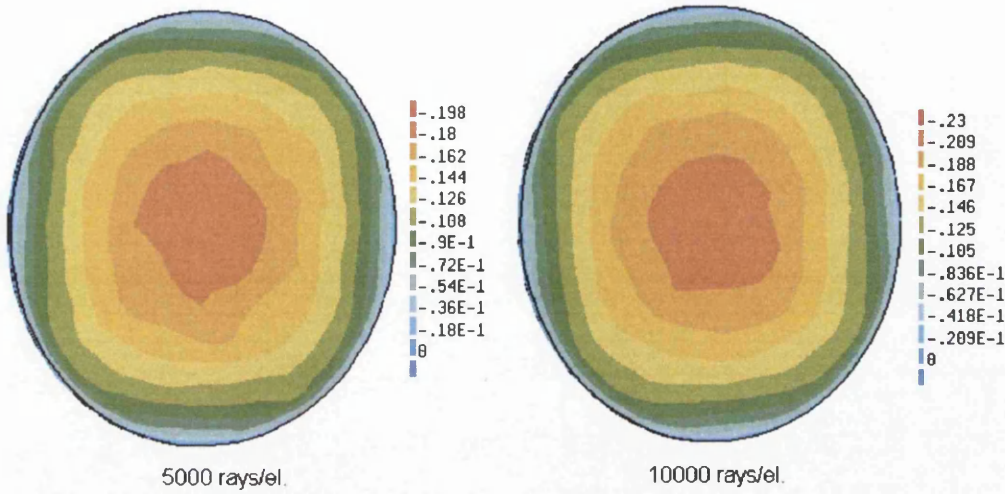Figure 6.52: Net radiative flux exchanged between the emitter and the receiver obtained using the Monte Carlo method with 10000 and 20000 rays/el. for the view factor calculation and equation (2.12) for the radiative heat transfer simulation - Scale in [W/el.]

mesh 20x20x10 - receiver
4x4x20 - emitter
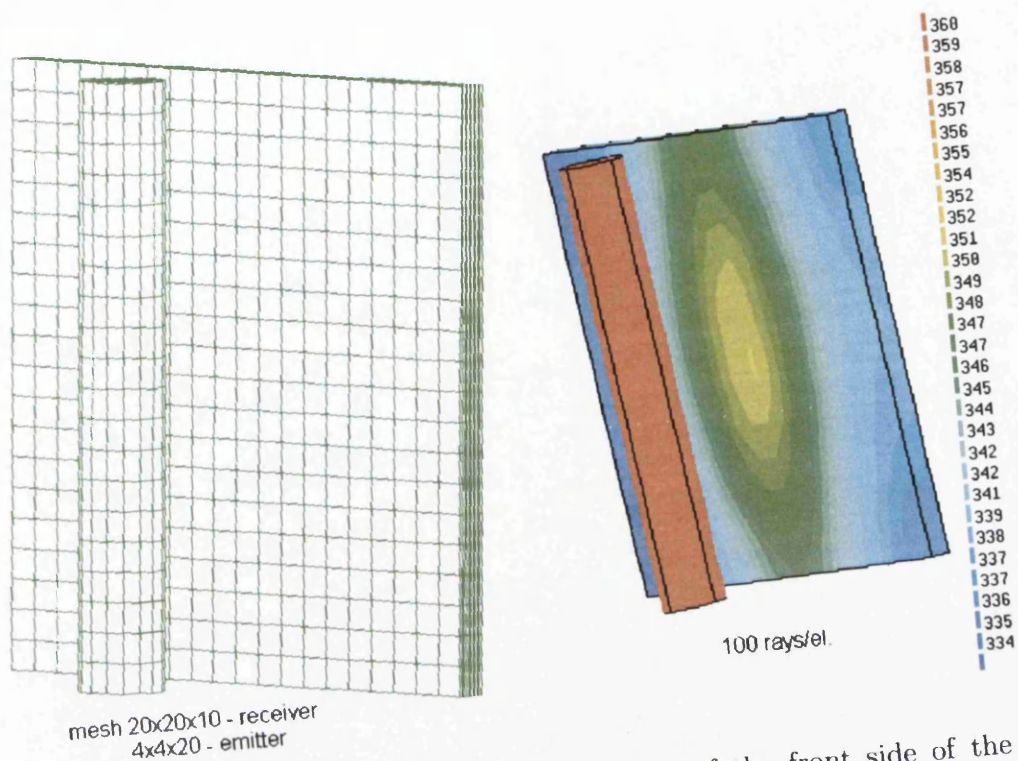
100 rays/el.

Figure 6.53: Mesh and temperature distribution of the front side of the receiver obtained using the Monte carlo method with 100 rays/el. for the view factor calculation and equation (2.12) for the radiative heat transfer simulation - Temperature scale in [K]
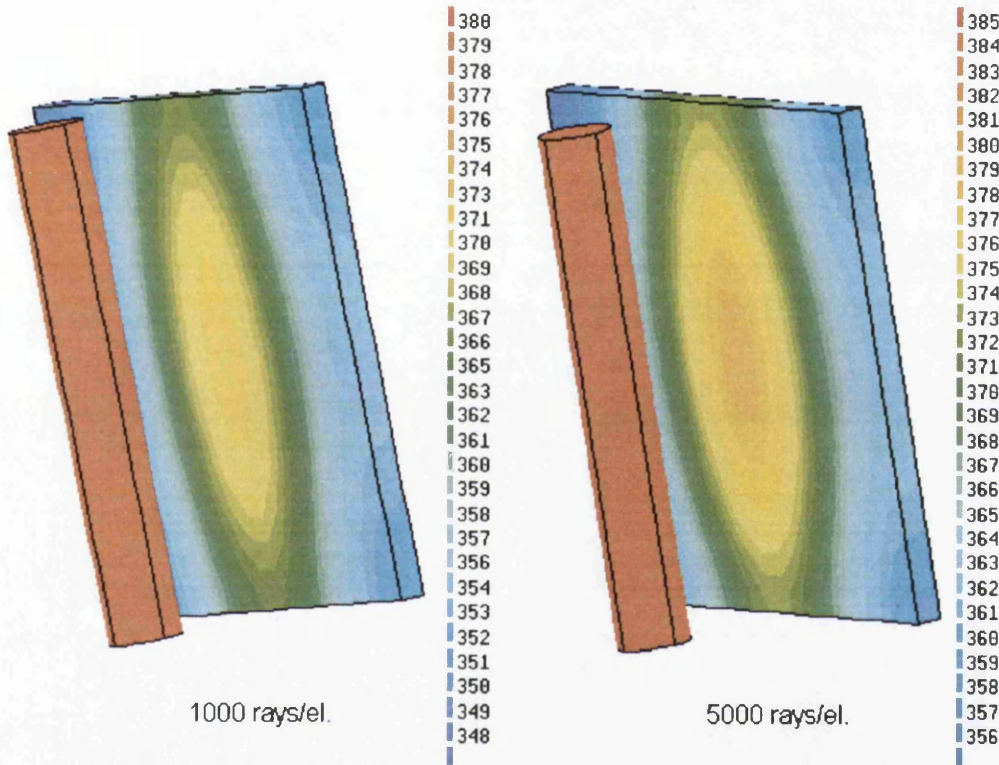
Figure 6.54: Temperature distribution of the front side of the receiver obtained using the Monte carlo method with 1000 and 5000 rays/el. for the view factor calculation and equation (2.12) for the radiative heat transfer simulation - Temperature scale in [K]
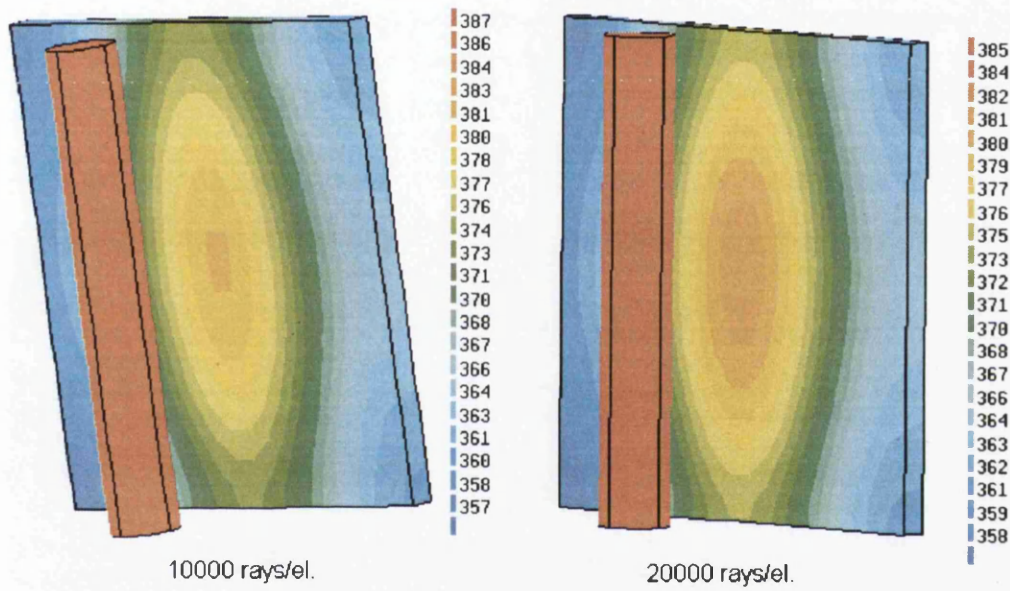
Figure 6.55: Temperature distribution of the front side of the receiver obtained using the Monte carlo method with 10000 and 20000 rays/el. for the view factor calculation and equation (2.12) for the radiative heat transfer simulation - Temperature scale in [K]
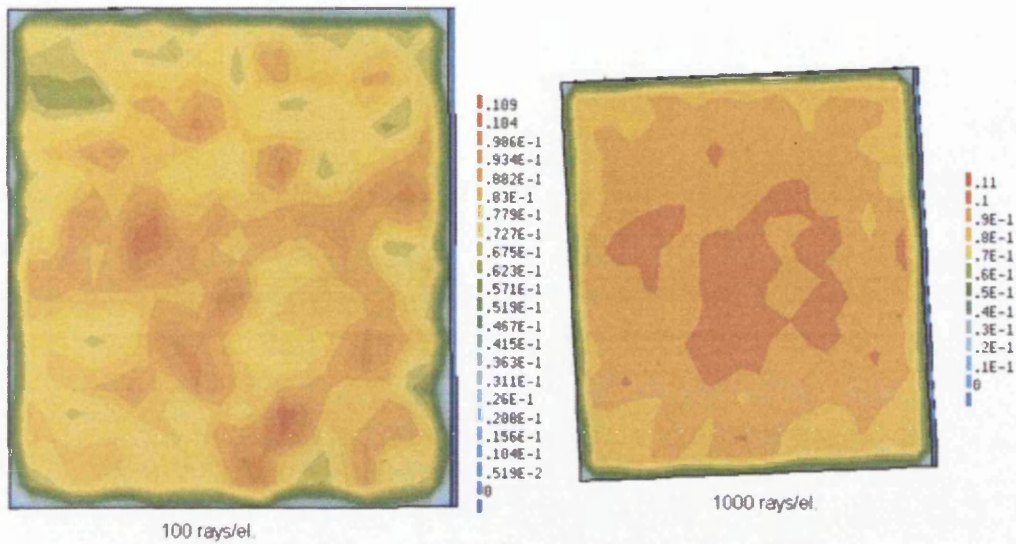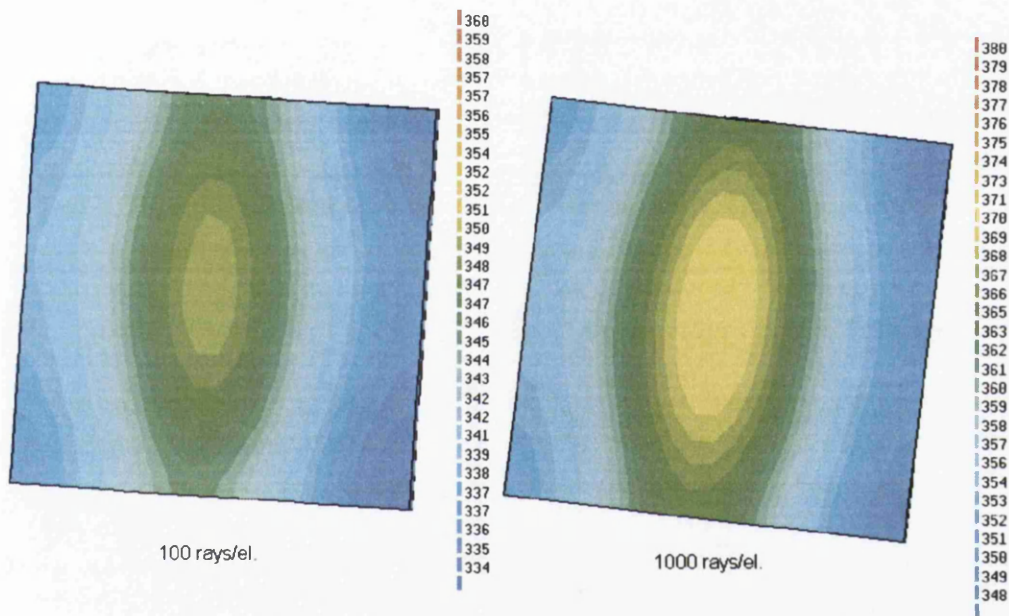
Figure 6.56: Temperature distribution of the back side of the receiver obtained using the Monte carlo method with 100 and 1000 rays/el. for the view factor calculation and equation (2.12) for the radiative heat transfer simulation - Temperature scale in [K]
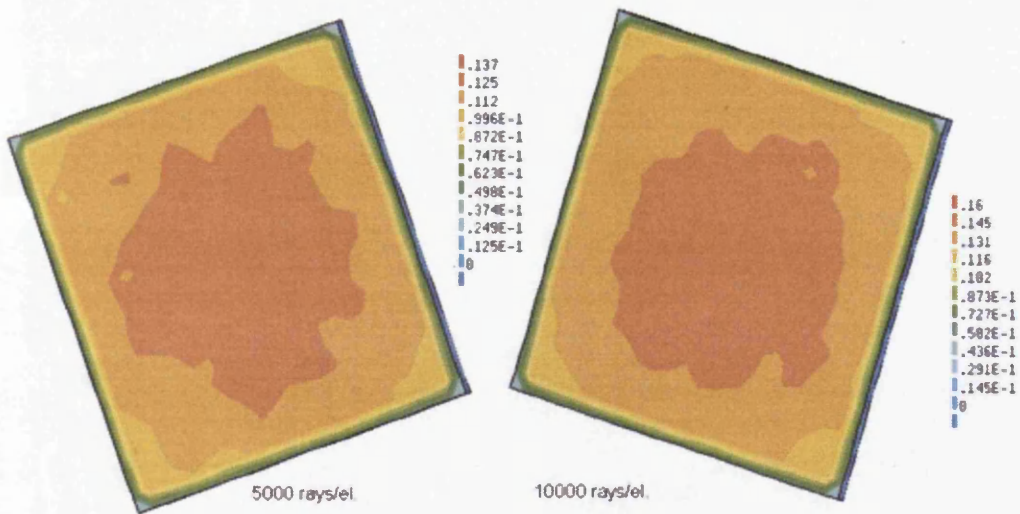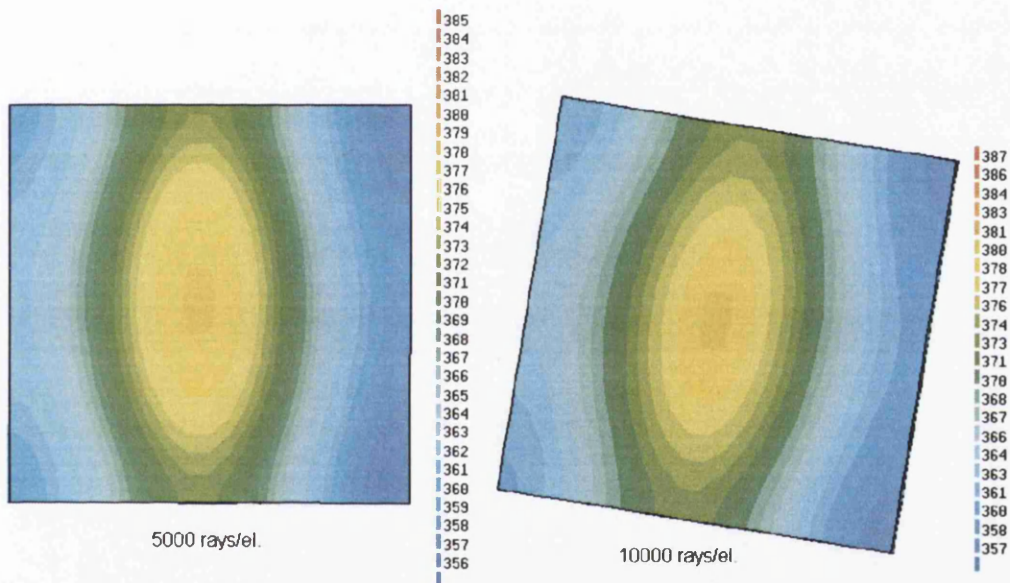
Figure 6.57: Temperature distribution of the back side of the receiver obtained using the Monte carlo method with 5000 and 10000 rays/el. for the view factor calculation and equation (2.12) for the radiative heat transfer simulation - Temperature scale in [K]
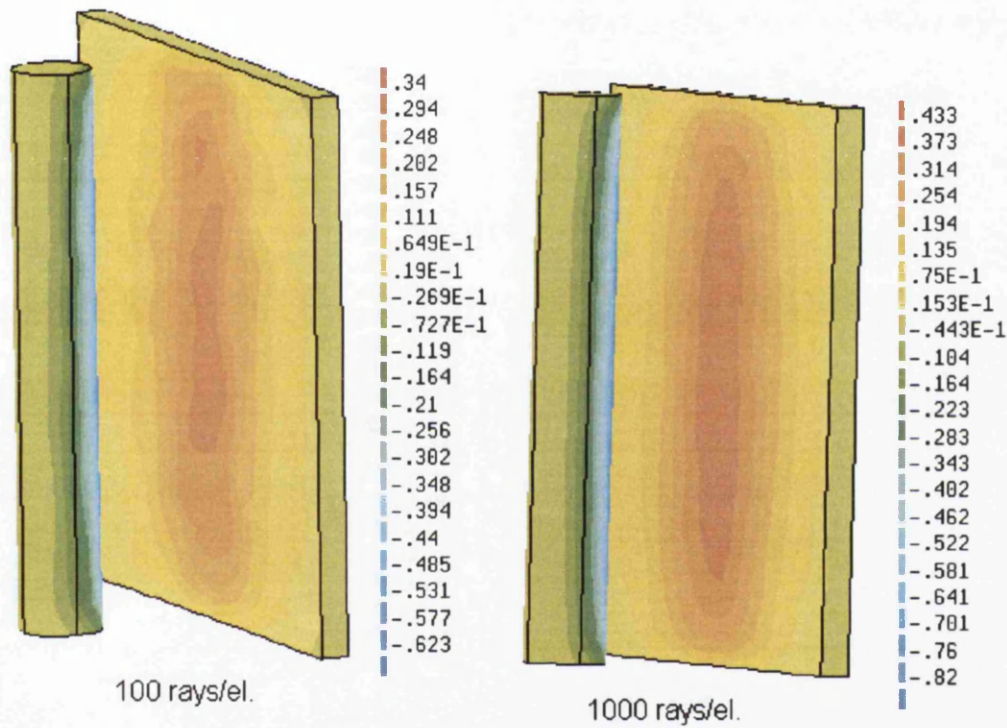
Figure 6.58: Net radiative flux exchanged between the emitter and the receiver obtained using the Monte Carlo method with 100 and 1000 rays/el. for the view factor calculation and equation (2.12) for the radiative heat transfer simulation - Scale in [W/el.]
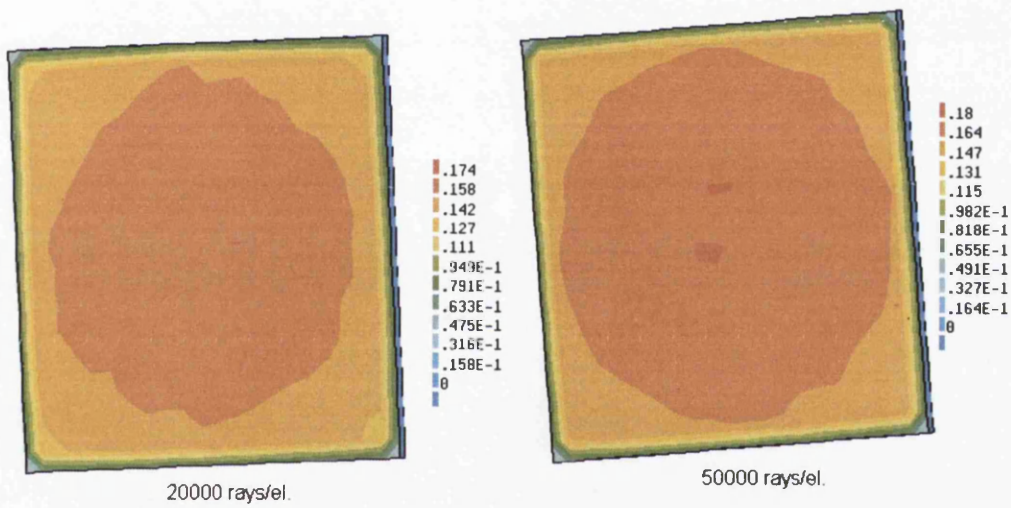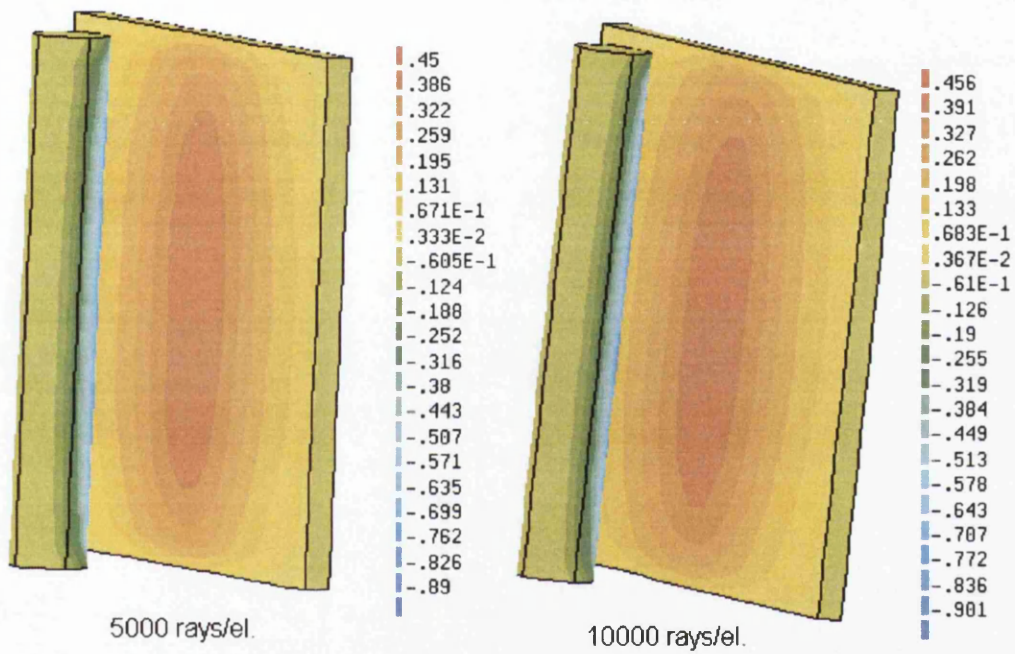
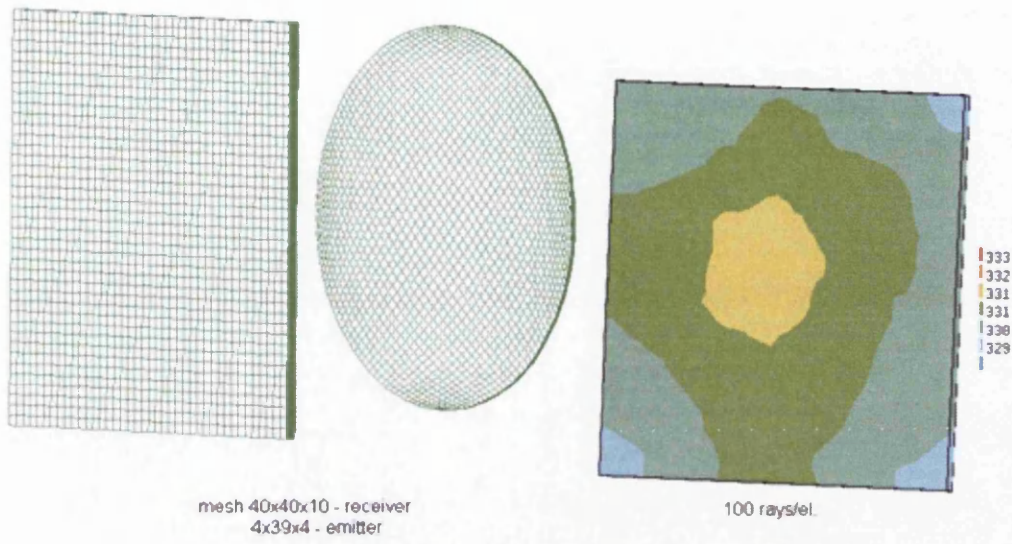Figure 6.59: Net radiative flux exchanged between the emitter and the receiver obtained using the Monte Carlo method with 5000 and 10000 rays/el. for the view factor calculation and equation (2.12) for the radiative heat transfer simulation - Scale in [W/el.]
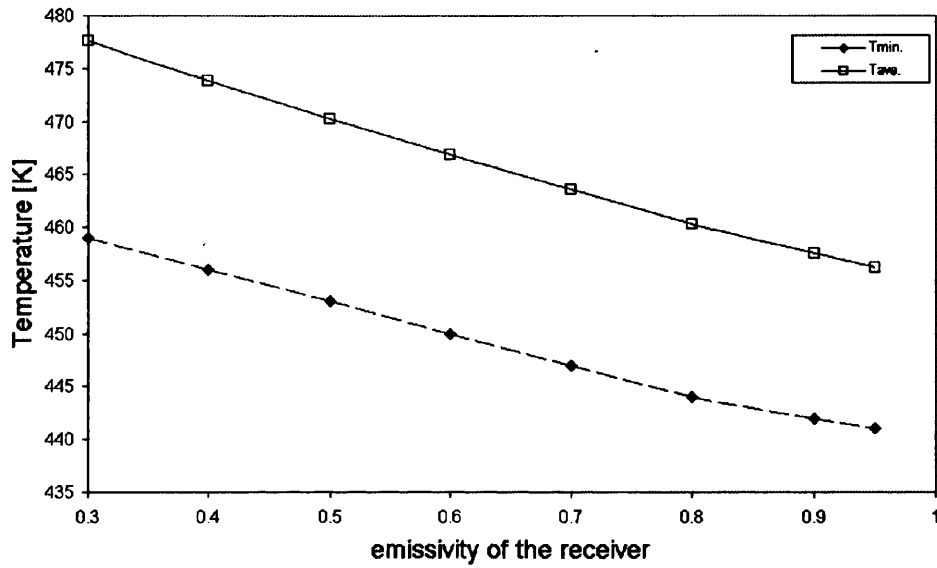
Figure 6.60: Minimum and average temperature of the receiver composed of steel for the different emissivity and the fixed emissivity of the emitter, obtained using the Monte Carlo method with 10000 rays/el. and equation (2.12) for the radiative heat transfer simulation
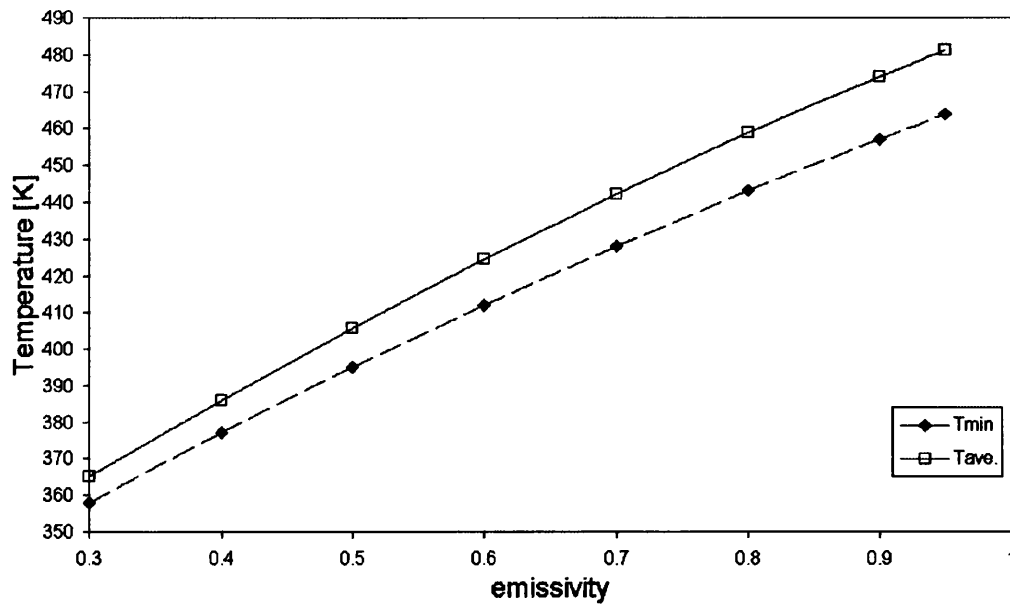
Figure 6.61: Minimum and average temperature of the receiver composed of steel for different emissivity (emissivity of the receiver and the emitter were identical) where the Monte Carlo method was used for the view factor calculation with 10000 rays/el. and equation (2.12) for the radiative heat transfer simulation
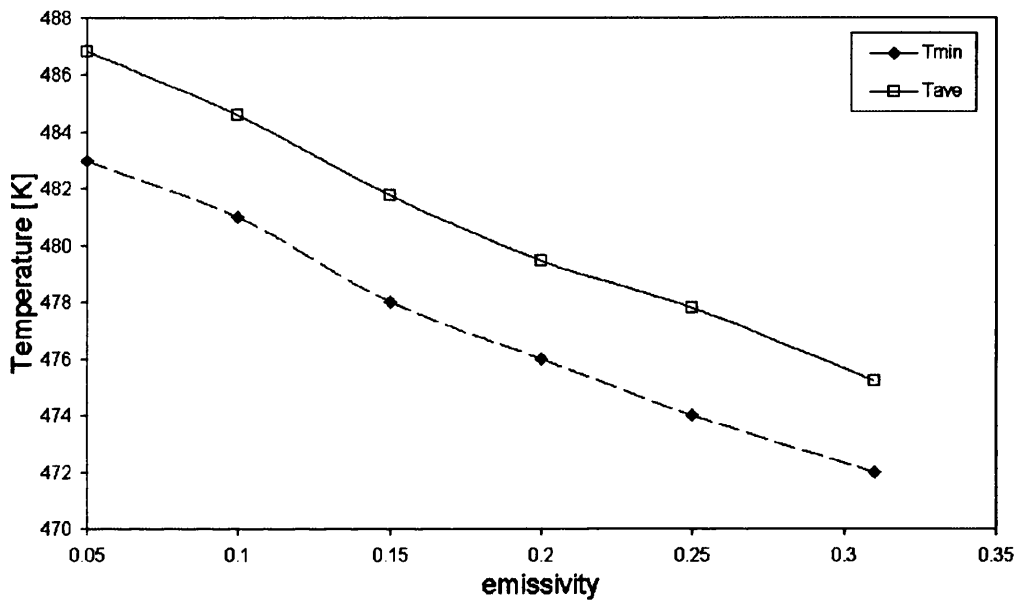
Figure 6.62: Minimum and average temperature of the receiver composed of aluminium for different emissivity where the Monte Carlo method was used for the view factor calculation with 10000 rays/el. and equation (2.12) for the radiative heat transfer simulation
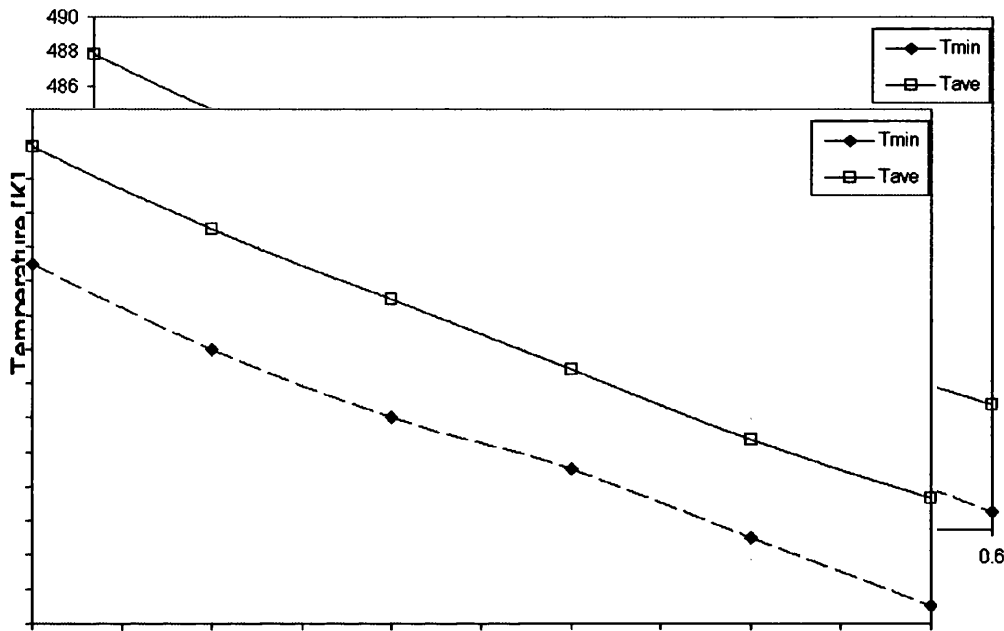
Figure 6.63: Minimum and average temperature of the receiver composed of brass for different emissivity where the Monte Carlo method was used for the view factor calculation with 10000 rays/el. and equation (2.12) for the radiative heat transfer simulation
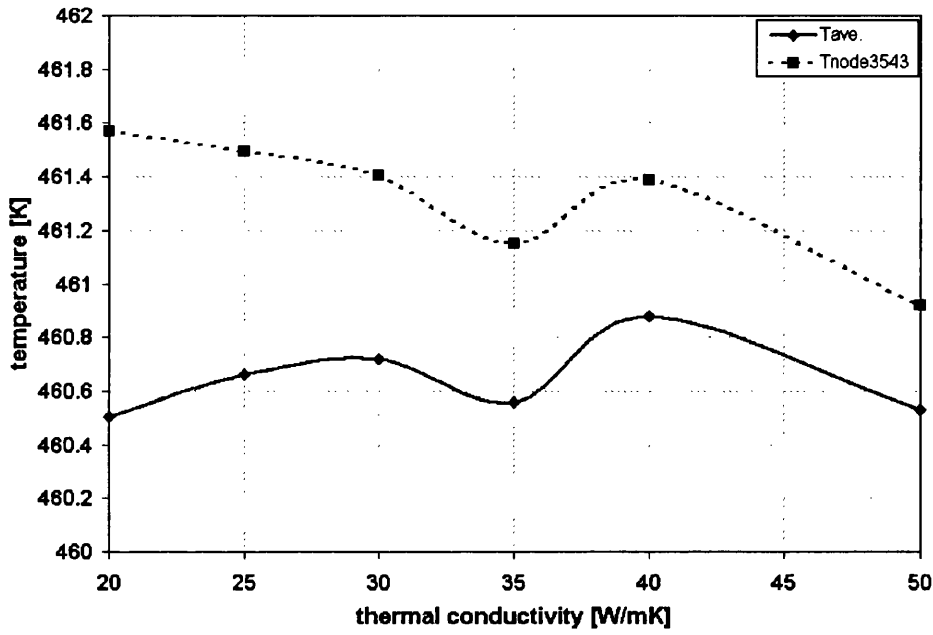
Figure 6.64: Temperatures at node 3543 and the average temperatures of the receiver obtained using the Monte Carlo method with 10000 rays/el. for the view factor calculation and equation (2.12) for the radiative heat transfer simulation
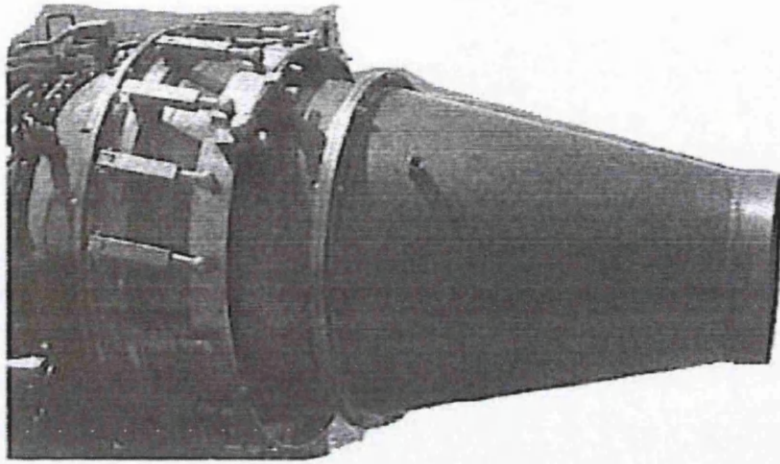
Figure 6.65: GNOME Rolls Royce jet pipe
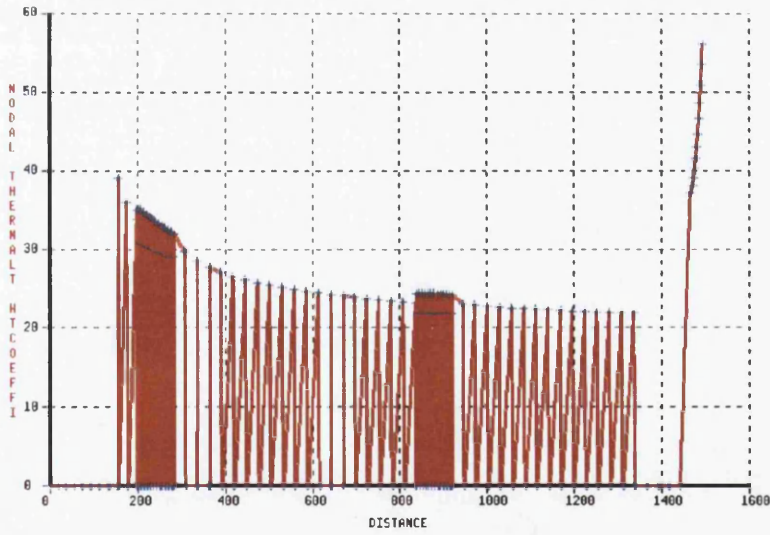

Figure 6.66: Convection heat transfer coefficient along internal cylinder
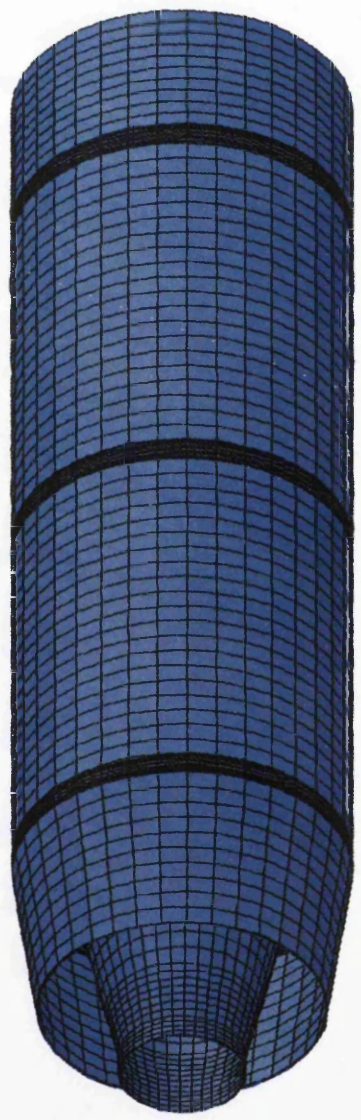
Figure 6.67: Geometry of GNOME Rolls Royce jet pipe
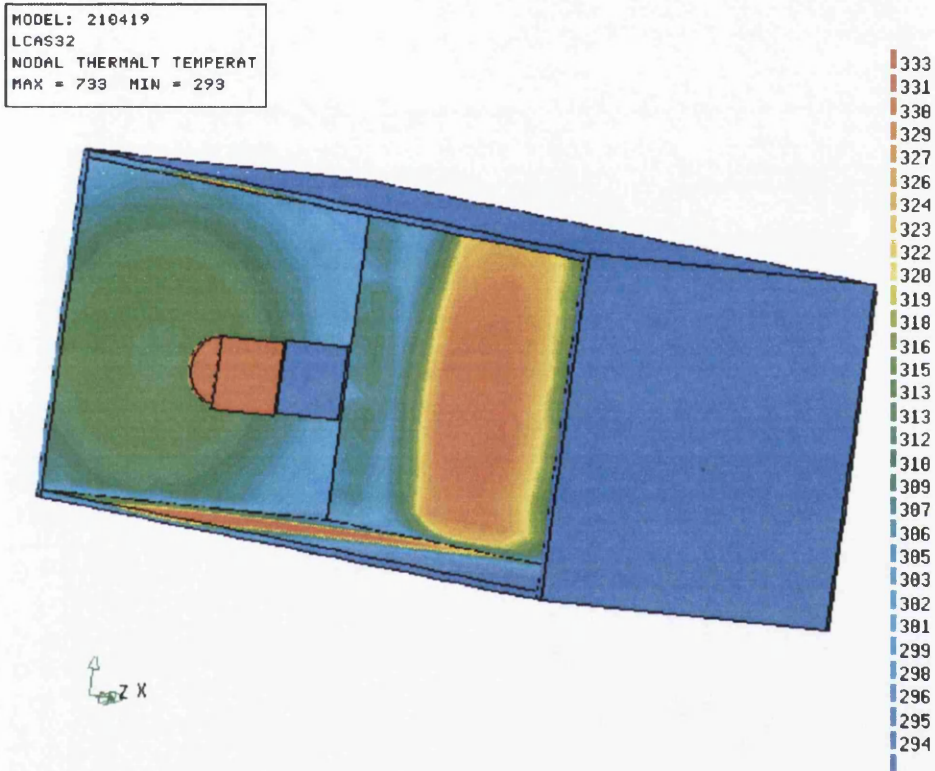
Figure 6.68: Temperatures of enclosure obtained using the Hemi-cube method with 1000 rays per element and equation (2.54) for the calculation of net radiative heat flux exchanged within enclosure - Temperature scale in [K]
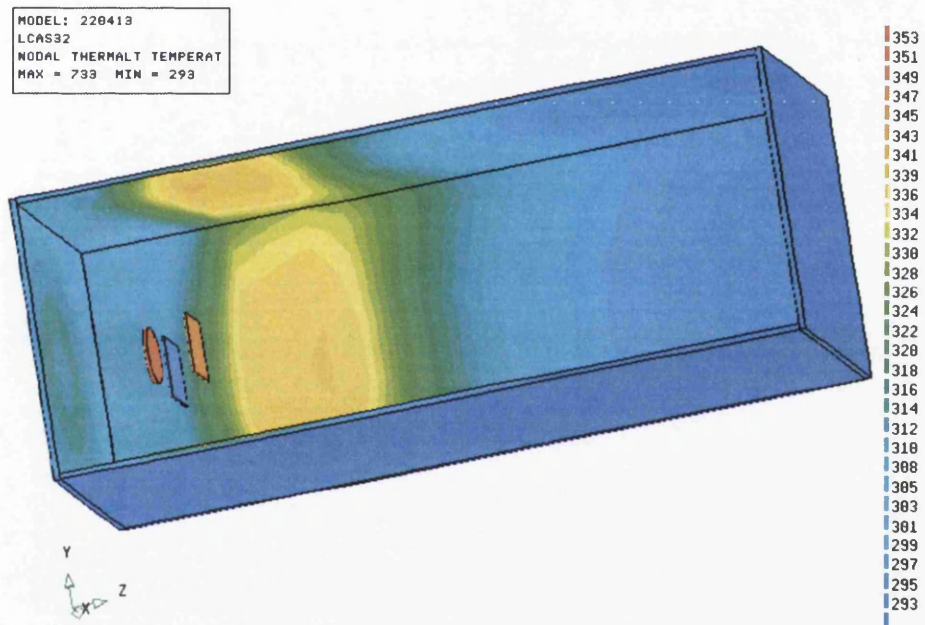
Figure 6.69: Temperatures of enclosure obtained using the Hemi-cube method with 10000 rays per element where equation (2.54) was used for the calculation of net radiative heat flux exchanged within enclosure - Temperature scale in [K]
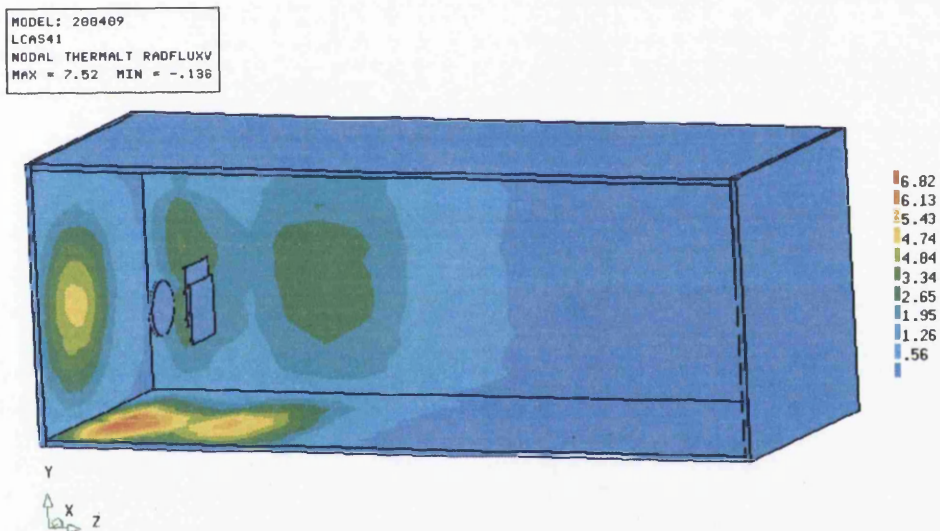
Figure 6.70: Radiative flux exchanged in enclosure obtained using the Hemi-cube method with 100 rays per element for the view factor calculation where equation (2.54) was used for the calculation of net radiative heat flux exchanged within enclosure - Scale in [W/el.]
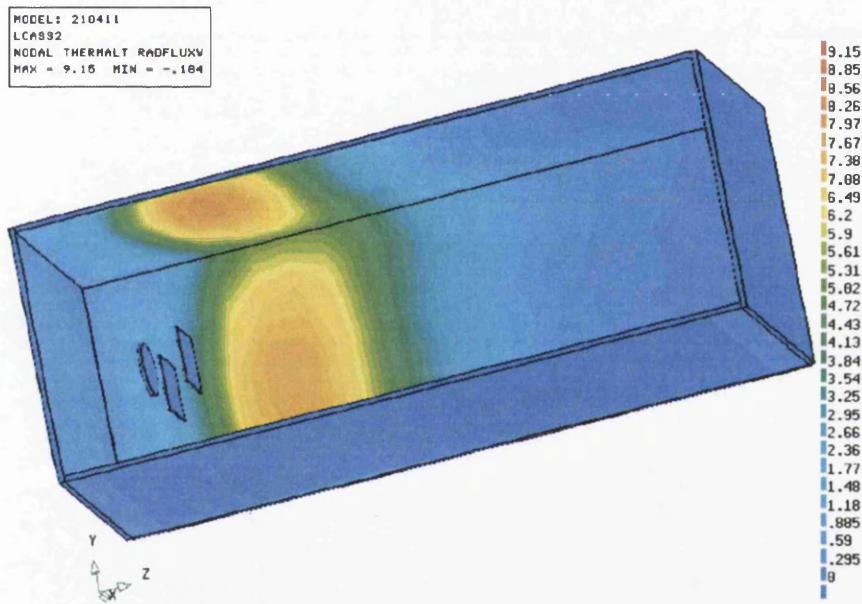
Figure 6.71: Radiative flux exchanged in enclosure obtained using the Hemi-cube method with 1000 rays per element for the view factor calculation where equation (2.54) was used for the calculation of net radiative heat flux exchanged within enclosure - Scale in [W/el.]
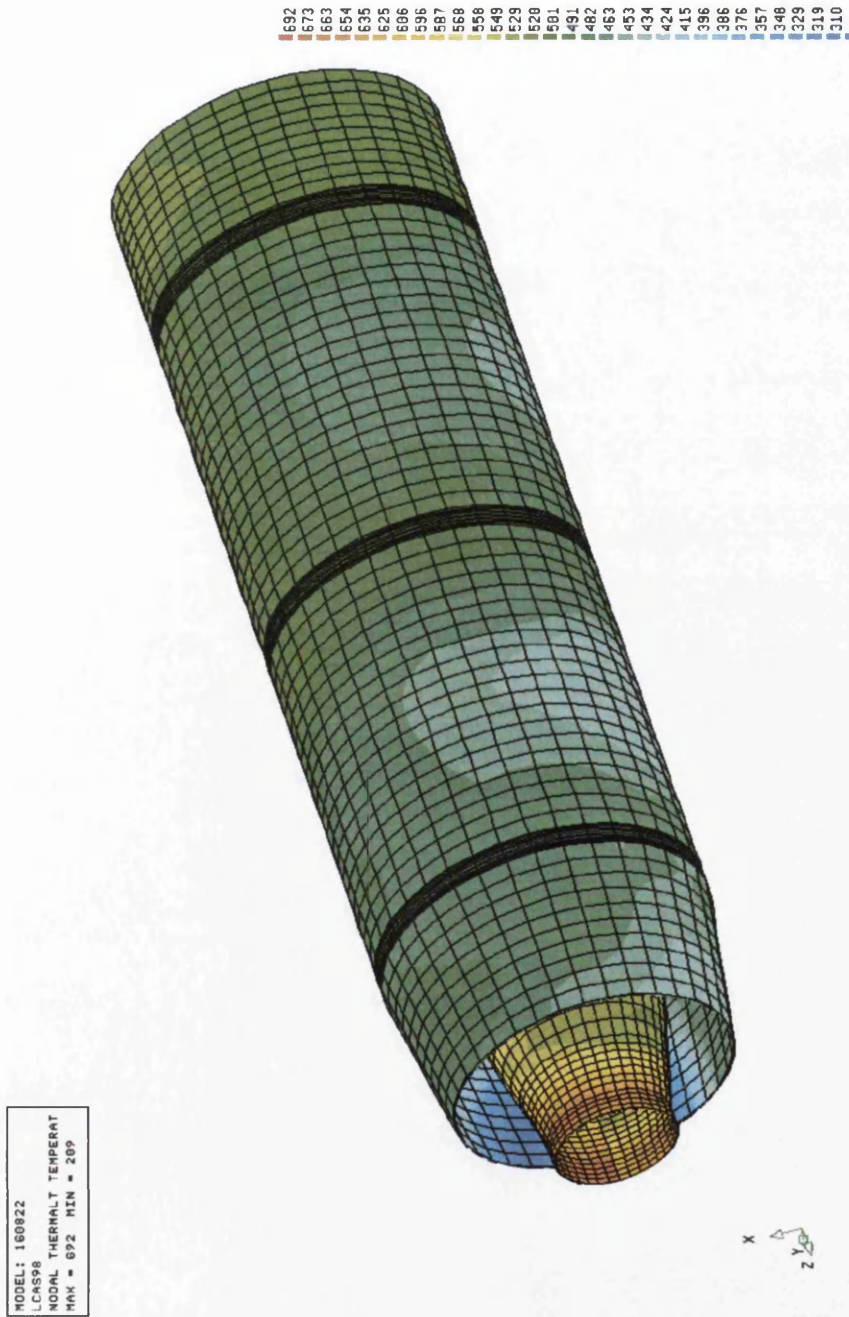
Figure 6.72: Temperatures of GNOME Rolls Royce jet pipe obtained using the Hemi-cube method with 1000 rays per element for the view factor calculation where equation (2.54) was used for the calculation of net radiative heat flux exchanged within enclosure - Temperature scale in [K]
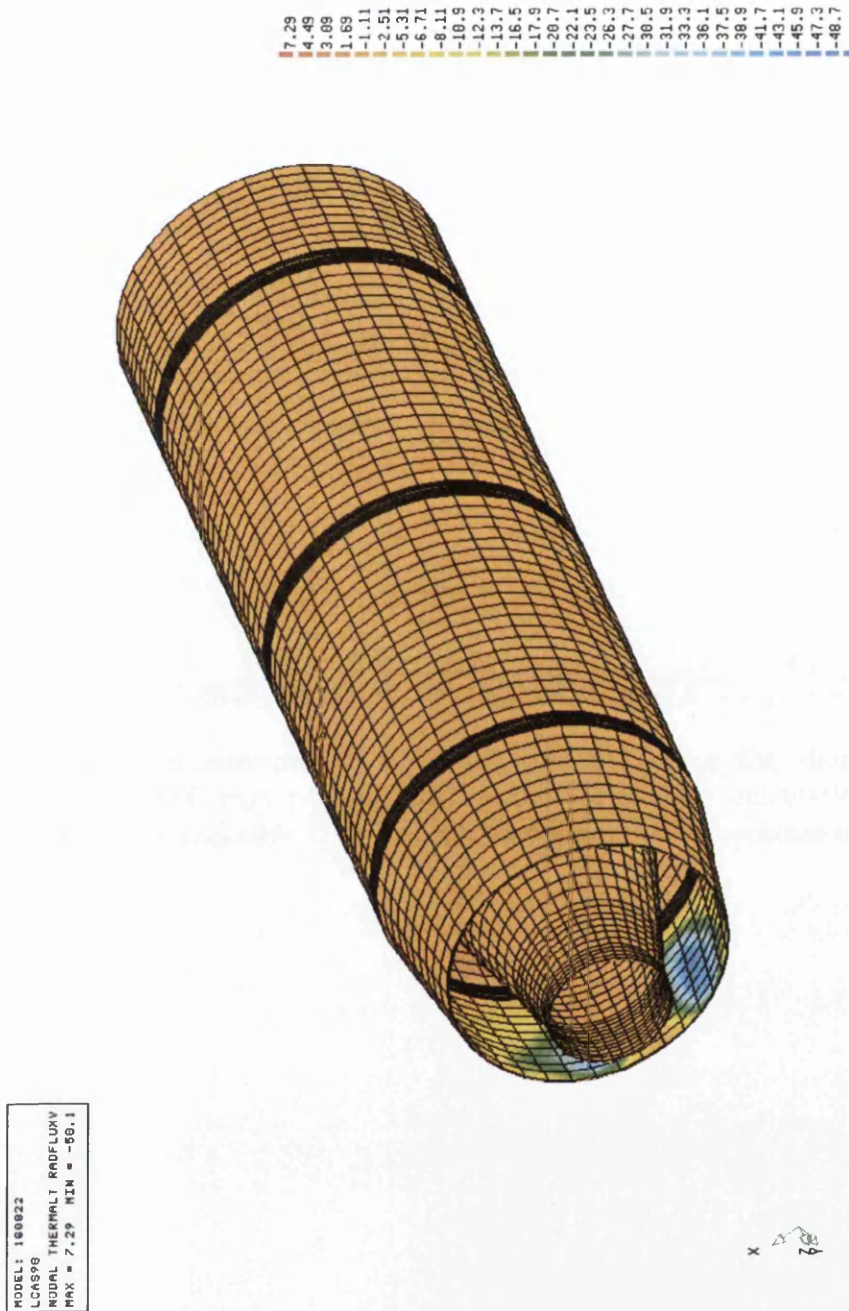
Figure 6.73: Radiative flux exchanged within GNOME Rolls Royce jet pipe obtained using the Hemi-cube method with 1000 rays per element for the view factor calculation where equation (2.54) was used for the calculation of net radiative heat flux exchanged within enclosure - Scale in [W/el.]
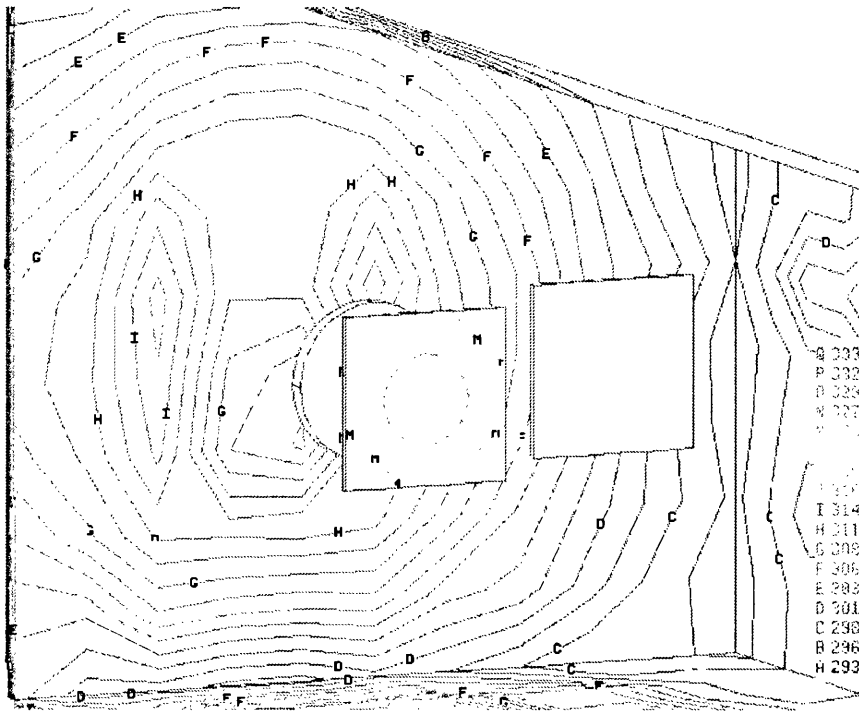
Figure 6.74: Temperatures of enclosure obtained using the Hemi-cube method with 30000 rays per element for the view factor calculation and MRV method for radiative heat transfer simulation - Temperature scale in [K]
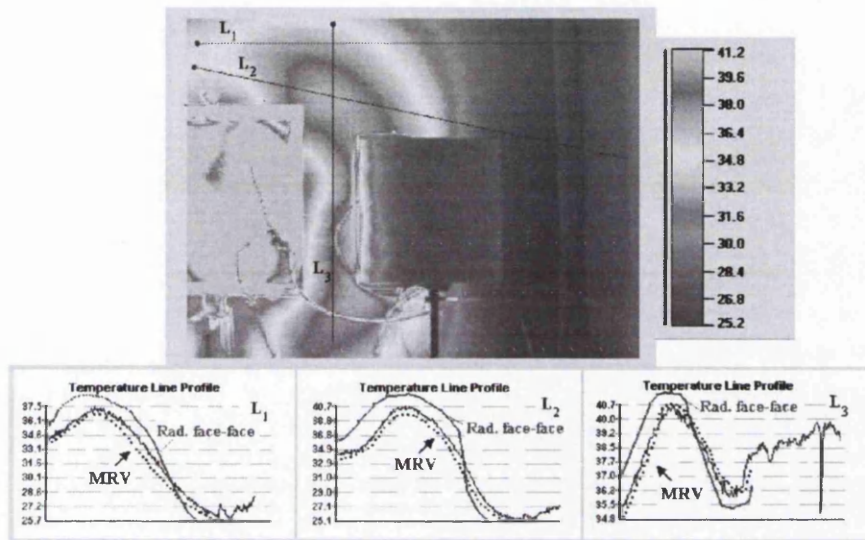
Figure 6.75: Comparison between results obtained using the MRV method (for the view factor calculation the Hemi-cube method with 30000 pixels/el. was used)and Radiosity face to face method with experimental data - Temperature scale in $[^oC]$
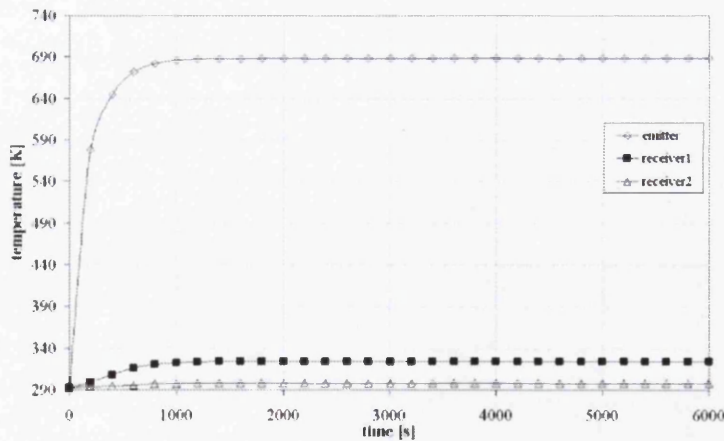
Figure 6.76: Average transient temperatures of the emitter and receivers obtained using MRV method and the Hemi-cube method with 30000 pixels/el. for the view factor calculation
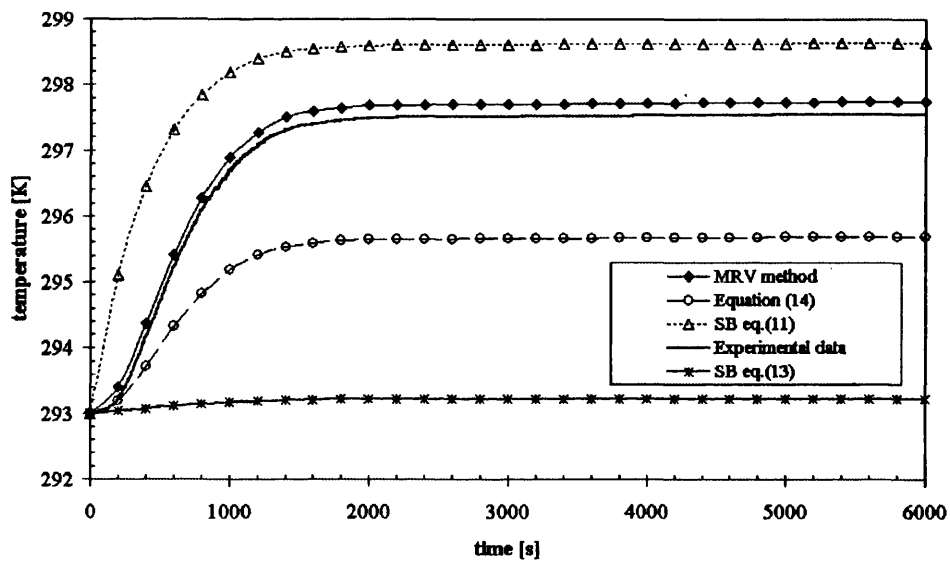
Figure 6.77: Average transient temperatures of receiver 2 obtained using MRV method and the Hemi-cube method with 30000 pixels/el. for the view factor calculation
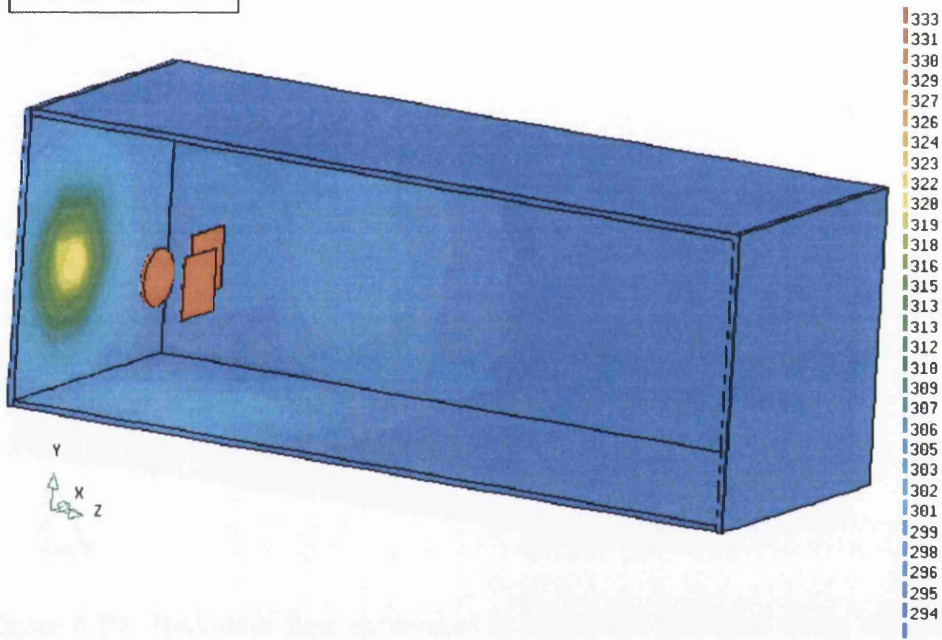
Figure 6.78: Temperatures of enclosure using equation (2.12) for radiative heat transfer simulation and 100 rays per element for the view factor calculation (the Hemi-cube method) - Temperature scale in [K]
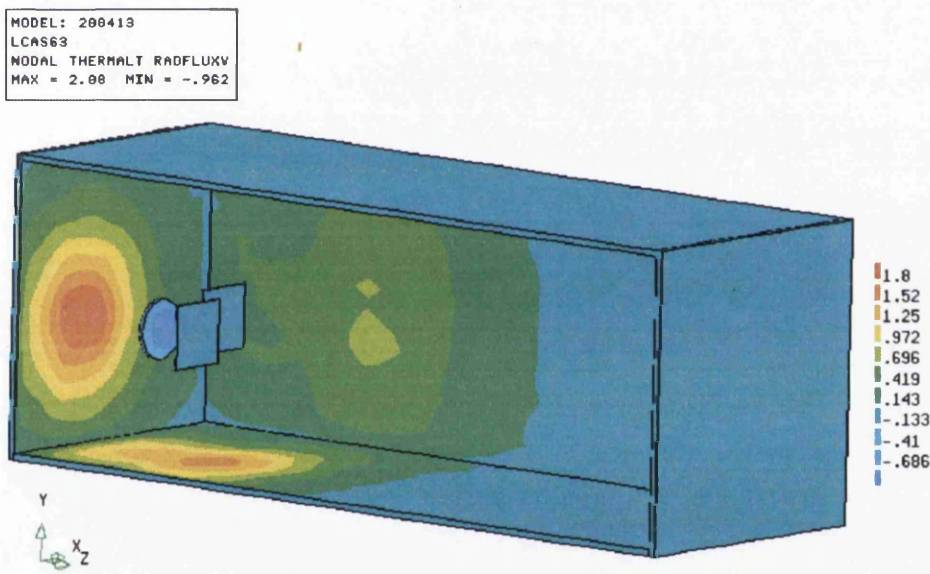
Figure 6.79: Radiative flux exchanged in enclosure obtained using equation (2.12) and 100 rays per element for the view factor calculation (the Hemi-cube method) - Scale in [W/el.]
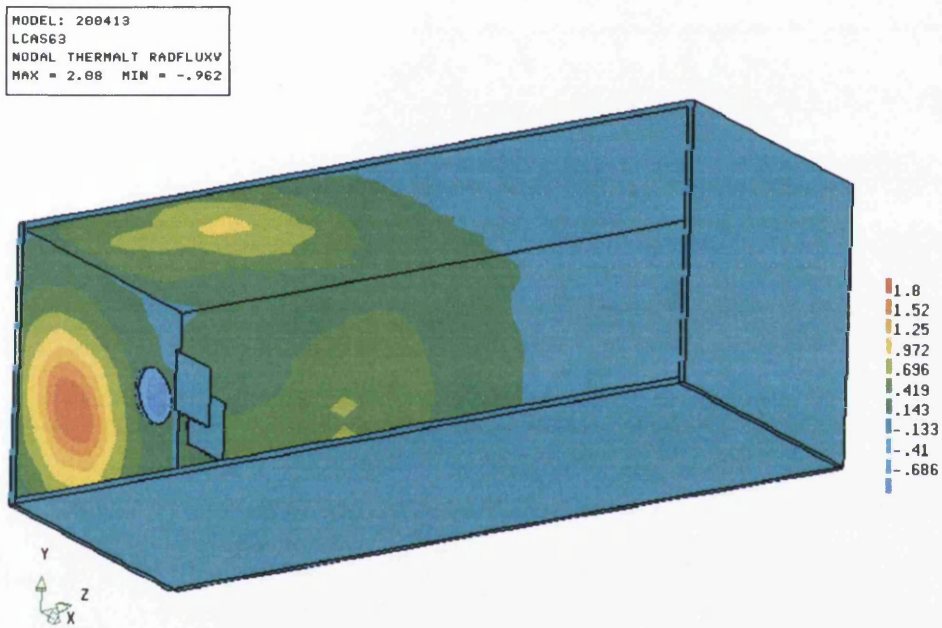
Figure 6.80: Radiative flux exchanged in enclosure obtained using equation (2.12) for radiative heat transfer simulation and 100 rays per element for the view factor calculation (the Hemi-cube method) - Scale in [W/el.]
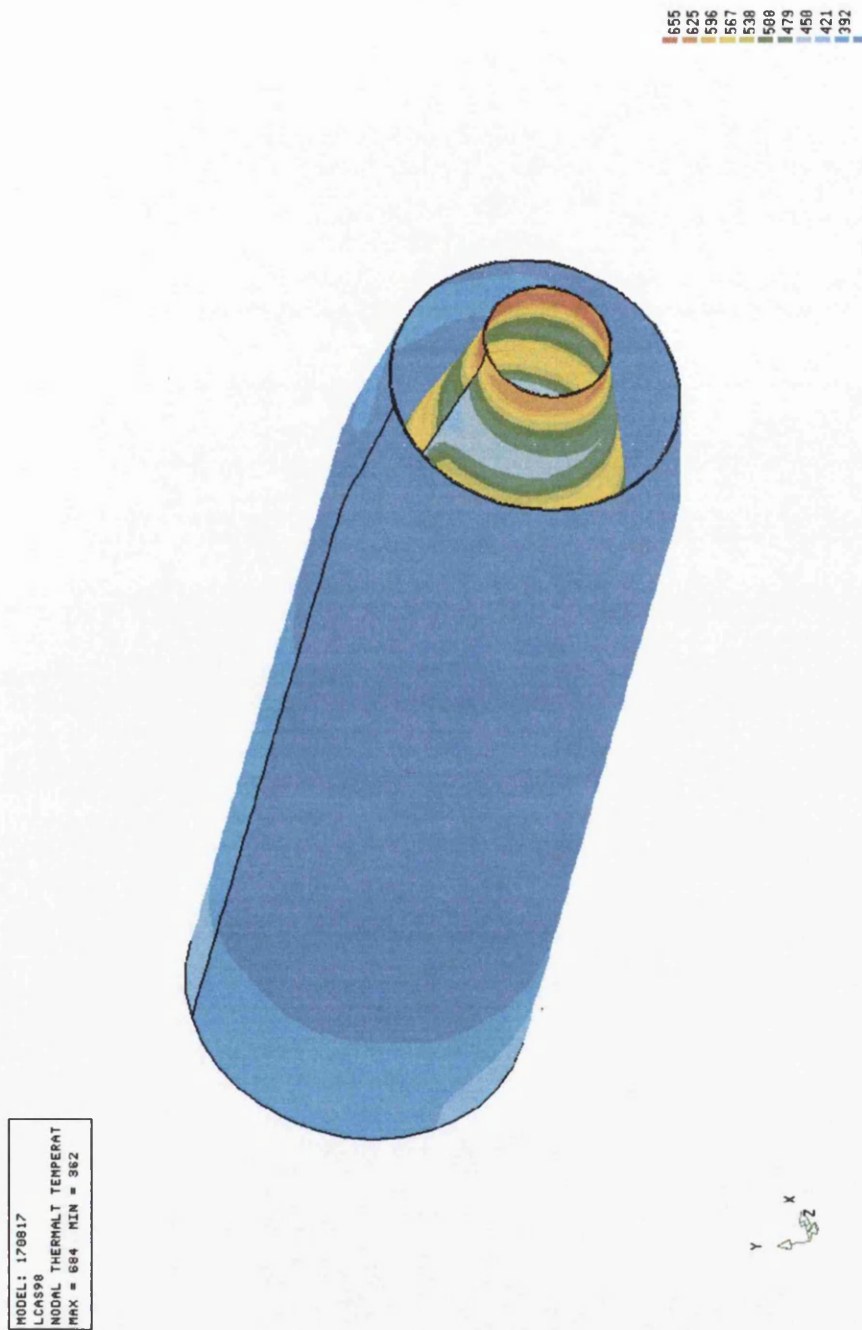
Figure 6.81: Temperature distribution in GNOME Rolls Royce jet pipe using obtained using equation (2.12) for radiative heat transfer simulation and 1000 rays per element for the view factor calculation (the Hemi-cube method) - Temperature scale in [K]
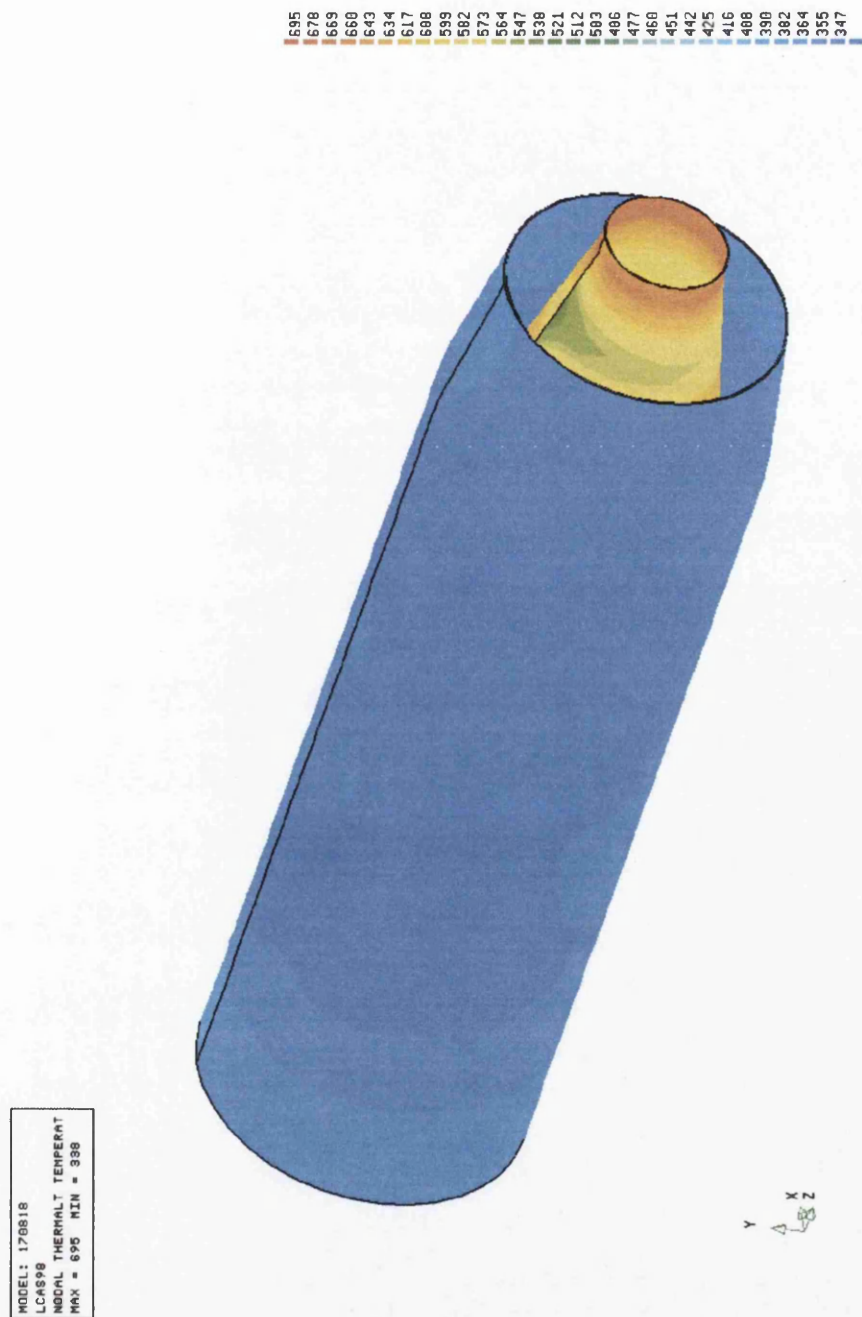
Figure 6.82: Temperature distribution in GNOME Rolls Royce jet pipe obtained using equation (2.51) for radiative heat transfer simulation and 1000 rays per element for the view factor calculation (the Hemi-cube method) - Temperature scale in [K]
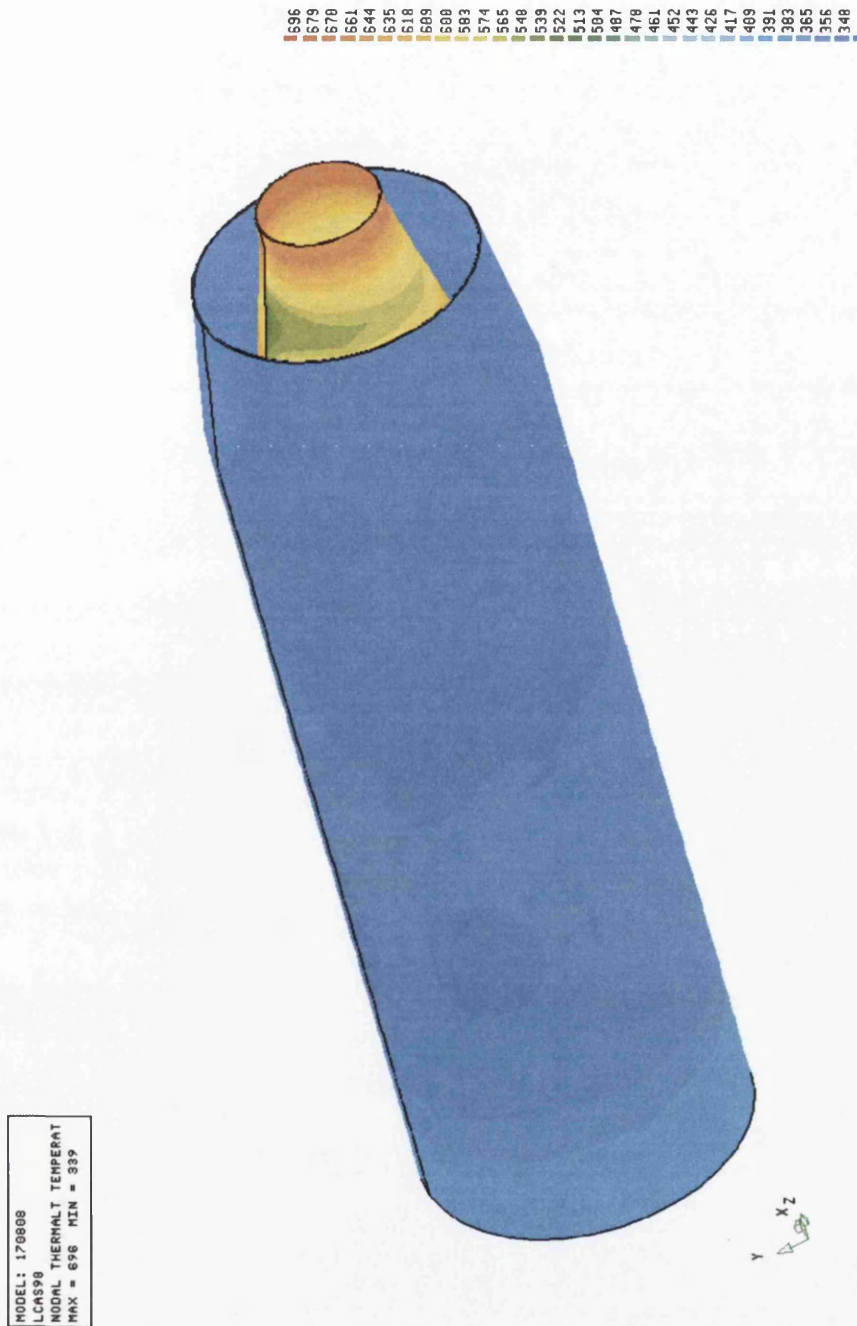
Figure 6.83: Temperature distribution in GNOME Rolls Royce jet pipe obtained using equation (2.52) for radiative heat transfer simulation and 1000 rays per element for the view factor calculation (the Hemi-cube method) - Temperature scale in [K]

Chapter 7

Conclusions with achievements

Through this thesis it has been shown that a knowledge of heat transfer including thermal conduction, convection and thermal radiation presents a crucial tool in the process of designing heat exchangers, boilers, furnaces, car and jet engines etc. All of these heat transfer mechanisms play a very important role, where any error made during calculations reflects very badly on the final results. This is the main reason why a few parallel analyses were made. All the analyses given in the text were made with the aim of finding the best method for the view factor calculation, the best time stepping, the fastest iterative solver etc. In the end, all conclusions given after every section were considered during the writing of the computer code **Pharo**. Therefore, only general conclusions with the most important points will be given in this chapter. Analyses included in this thesis are:

1. Radiative heat transfer with a detailed theoretical explanation of numerical methods for the view factor calculation and the comparison between them. It has been shown that for the view factor calculation the Monte Carlo and the Hemi-cube methods have an advantage over integration methods (shadowing and complex environment). Also, it has been shown that the Monte Carlo method is more accurate than the Hemi-cube method. At the same time the Hemi-cube method is about 20% faster than the Monte Carlo method. Again, attention has to be given to the mesh selection and to be aware of the relationship between it, CPU time and accuracy. It has been shown that an increase in mesh resolution requires more rays to gain the same accuracy as was gained using a lower mesh resolution. Obviously, it requires more rays per element, thereby causing an increase in CPU time.

An optimization of the Monte Carlo method can be made using one of the probability theories, such as Chebyshev inequality, exponential Cheby-

shev inequality, binomial distribution etc. All these methods use a certain confidence in a strip of wanted width and do not take into account a distance ratio between elements. However, it has been shown that distance ratio between acting elements is very important. Therefore, all formulaes obtained using one of above mentioned theories which can be used for optimization have to be reworked thoughtfully. Optimization can only be made where the view factor is calculated between two elements. However, in this thesis the view factor is calculated between one element and all other elements within the enclosure using a certain number of rays in one moment. Therefore, when including different distance ratios between elements it is not possible to make any optimization.

The main achievement in the work presented is the analysis of the relationship between numerical sensitivity and discretization schemes. The results of the analysis are presented earlier in the thesis. Also, the comparison between results obtained using two different origins when the Monte Carlo method is used for view factor calculation does not give any advantage either of them, but one special case with partial shadowing eliminates the centre of an element as an origin. As it is known, the Hemi-cube method uses the centre of an element as an origin and struggles with this this type of problem.

The second achievement of this work is the robustness and flexibility of **Pharo**. Different numerical methods for view factor calculation have been built in the code and they can work without difficulty in any environment, i.e. with or without obstacles.

2. New, specially generated benchmark experimental data for several test cases including simple plate (a square plate, a disc and a cylinder as an emitter) to plate cases, shadowing and a reflectivity effect was analyzed. Also a theoretical analysis of surface properties such as emissivity and reflectivity is given. Temperatures measured using thermocouples in combination with thermal image camera were of a great importance in the process of validation of the computer code. Temperature distributions of surfaces obtained using thermal image camera were used to compare with temperature distributions obtained using **Pharo**. As was expected plates with higher absorptivity reached higher temperatures (black painted steel plate). Also, it was shown that with an increase of distance ratio between an emitter and a receiver caused the temperatures of the receivers to decrease with a similar trend as the view factors.

Information presented in Chapter 3 has, for the first time, been analyzed systematically. This is the main achievement of this experimental work.

3. Thermal conduction with special attention to the transient heat conduction and different time stepping. The effect of different numerical schemes as well as different finite element types on the transient heat transfer was also analyzed. This analysis was made to help in the process of selecting which time stepping regime is the most appropriate to be used. It was shown that an increase in mesh resolution will give better results. Also, the Crank-Nicolson method (the second order of accuracy) for time stepping appears to be the most appropriate of all presented.

The analysis of transient heat conduction includes ten different iterative solvers and five different time stepping. One of the main findings is that PCG method is the fastest of all analyzed for this type of problem.

4. Heat transfer simulations using different approaches such as different variations of the Stefan-Boltzmann equation, the MRV method and as well as radiosity (face to face) method. Experimental results have shown that reflectivity effect can be very important, especially when distances between surfaces are very small and one of the surfaces has a high reflectivity. It was shown that the temperatures of the emitter increased with a decrease of distance ratios between it and receivers (50%).

This is the main reason for consideration of radiosity method. By involving the radiosity method a new problem appears, which involves a solution of a non symmetric, no sparse system of matrix equations.

To avoid a work with a non-symmetric, non-sparse system of matrix equations, a new approach called MRV (Multiple Reflection of View Factors) method has been proposed.

One of the main achievements of the whole work presented in this thesis is the proposition of the MRV method. It was shown that results obtained using the MRV method have an excellent agreement with experimental data. Also, possibilities to use the MRV method when bidirectional surface properties take place give a great advantage to this method. The calculation procedure for this case will appear in a future paper.

There are some instances where the assumptions presented in Chapter 1 do not give good results which can be explained as follows:

1. spectral emissivity depends to wavelength and varies with it causing different spectral distributions and failure of grey assumption $\epsilon(T_A) \neq \alpha(T_A)$;

2. The presence of any polished surface will invalidate the diffuse reflection assumption (an application of the MRV method can be useful).

Postscript

After all work has been completed one question appears: Did it make **Pharo** better or similar to the existing commercial codes. Of course, there is no 'right' answer, as there is no 'right' answer to the question is this one the best or which one heat transfer code is the best? It all depends on what features are important to the user. Even trying to solve a problem or group of problems, using the same methods in different commercial codes will give different results. There are many reason which can cause different results such as different grids, non-demonstrated grid convergence, different implementation of the models and different boundary conditions. But defining the criteria, e.g. speed, interface to CAD, meshing, linear analysis, non-linear analysis, maintenance and support, cost, etc should be helpful to evaluate the codes against these criteria and rank-order them against the criteria.

Chapter 8

Future work

There are many tasks which have engaged me during my PhD study. The first task was writing subroutines for the view factor calculations (the Monte Carlo and the Hemi-cube methods). This task has been finished successfully and in my opinion no significant further improvement can be made.

The second task was designing an experimental rig and doing series of experiments including simple plate to plate cases to more complex enclosures involving third plate with and without shadowing. A huge amount of experimental data was obtained to help in the process of the validation of computer codes. However, further research can be made in coupling all three heat transfer mechanisms (conduction, convection and thermal radiation).

The third task was heat transfer simulation. A few different variations of the Stefan-Boltzmann equation and simple face to face radiosity method were used. The results obtained when compared with the experimental data show that radiosity method has to be fully employed. This will cause other problems such as a huge view factor matrix on the left side of the system of matrix equations. One of the options is to test which of the iterative solvers explained in Appendix B can be used to solve the problem. As was mentioned earlier (Chapter 1) radiation exchange in an enclosure composed of diffuse-grey surfaces containing radiatively *nonparticipating* media was analyzed in this thesis.

Therefore, there are at least two directions in which this work can go:
1. radiation exchange in enclosure with specular reflective surfaces;
2. radiation exchange in enclosure containing *participating* media.

Radiative heat transfer prediction within exhaust gas flow which involves participating media with a special application to jet engine can be a subject of an interest.

Appendix A

Comparison between radiation methods

A simple geometry including four plates is analyzed in this appendix (see Figure A.1). View factors between plates are calculated and they are:

$$
\begin{aligned}
F_{1-2} &= 0.034 \\
F_{1-3} &= 0.033 \\
F_{1-4} &= 0.034 \\
F_{2-3} &= 0.034 \\
F_{2-4} &= 0.199825 \\
F_{3-4} &= 0.034 \\
F_{2-1} &= F_{1-2} \\
F_{3-1} &= F_{1-3} \\
F_{4-1} &= F_{1-4} \\
F_{3-2} &= F_{2-3} \\
F_{4-2} &= F_{2-4} \\
F_{4-3} &= F_{3-4}
\end{aligned}
\tag{A.1}
$$

Emissivity of the surfaces are chosen:

$$
\begin{aligned}
\varepsilon_1 &= 0.8 \\
\varepsilon_2 &= 0.3 \\
\varepsilon_3 &= 0.4 \\
\varepsilon_4 &= 0.5
\end{aligned}
\tag{A.2}
$$

Surface temperatures are also specified:

$$T_1 = 900 \ [K]$$
$$T_2 = 600 \ [K]$$
$$T_3 = 300 \ [K]$$
$$T_4 = 500 \ [K] \tag{A.3}$$

For the calculation simplicity the areas of elements are chosen to be same $1 \ [m^2]$.

A.1 Radiosity method

Considering the enclosure as presented in Figure A.1, and temperatures as boundary conditions, an application of equation (2.55) for surface 1 gives:

$$q_1(\frac{1}{\varepsilon_1} - F_{1-1}\frac{1-\varepsilon_1}{\varepsilon_1}) - q_2 F_{1-2}\frac{1-\varepsilon_2}{\varepsilon_2} - q_3 F_{1-3}\frac{1-\varepsilon_3}{\varepsilon_3} - q_4 F_{1-4}\frac{1-\varepsilon_4}{\varepsilon_4}$$
$$= F_{1-2}\sigma(T_1^4 - T_2^4) + F_{1-3}\sigma(T_1^4 - T_3^4) + F_{1-4}\sigma(T_1^4 - T_4^4) \tag{A.4}$$

for surface 2:

$$q_2(\frac{1}{\varepsilon_2} - F_{2-2}\frac{1-\varepsilon_2}{\varepsilon_2}) - q_1 F_{2-1}\frac{1-\varepsilon_1}{\varepsilon_1} - q_3 F_{2-3}\frac{1-\varepsilon_3}{\varepsilon_3} - q_4 F_{2-4}\frac{1-\varepsilon_4}{\varepsilon_4}$$
$$= F_{2-1}\sigma(T_2^4 - T_1^4) + F_{2-3}\sigma(T_2^4 - T_3^4) + F_{2-4}\sigma(T_2^4 - T_4^4) \tag{A.5}$$

for surface 3:

$$q_3(\frac{1}{\varepsilon_3} - F_{3-3}\frac{1-\varepsilon_3}{\varepsilon_3}) - q_3 F_{3-1}\frac{1-\varepsilon_1}{\varepsilon_1} - q_2 F_{3-2}\frac{1-\varepsilon_2}{\varepsilon_2} - q_4 F_{3-4}\frac{1-\varepsilon_4}{\varepsilon_4}$$
$$= F_{3-1}\sigma(T_3^4 - T_1^4) + F_{3-2}\sigma(T_3^4 - T_2^4) + F_{3-4}\sigma(T_3^4 - T_4^4) \tag{A.6}$$

and finally for surface 4:

$$q_4(\frac{1}{\varepsilon_4} - F_{4-4}\frac{1-\varepsilon_4}{\varepsilon_4}) - q_1 F_{4-1}\frac{1-\varepsilon_1}{\varepsilon_1} - q_2 F_{4-2}\frac{1-\varepsilon_2}{\varepsilon_2} - q_3 F_{4-3}\frac{1-\varepsilon_3}{\varepsilon_3}$$
$$= F_{4-1}\sigma(T_4^4 - T_1^4) + F_{4-2}\sigma(T_4^4 - T_2^4) + F_{4-3}\sigma(T_4^4 - T_3^4) \tag{A.7}$$

Finally, a system of four equations with four unknowns (q_1, q_2, q_3 and q_4) is obtained, and is solved using Gaussian elimination ($q_1 = 2598.31 \ [W/m^2]$, $q_2 = -519.662 \ [W/m^2]$, $q_3 = -779.493 \ [W/m^2]$, $q_4 = -1299.12 \ [W/m^2]$).

Overall heat balance $\sum_{k=1}^{4} q_k = 0$ is used as a check.

A.2 MRV method

An application of the MRV method for the enclosure between surfaces 1 and 3, considering only one reflection, gives the view factor value as:

$$F_{1-3}^{Iref} = F_{1-3}^0 + F_{1-2} * (1 - \varepsilon_2) * F_{2-3} + F_{1-4} * (1 - \varepsilon_4) * F_{4-3} \qquad (A.8)$$

while the second reflection view factor value becomes:

$$F_{1-3}^{IIref} = F_{1-3}^{Iref} + F_{1-2}*(1-\varepsilon_2)*F_{2-4}*(1-\varepsilon_4)*F_{4-3} + F_{1-4}*(1-\varepsilon_4)*F_{4-2}*(1-\varepsilon_2)*F_{2-3} \qquad (A.9)$$

The same procedure can be applied to calculate view factors between elements 1 and 2 and 4.

Putting the view factor value obtained using equations (A.8) and (A.9) in the equation (2.54) gives the net heat exchanged between elements 1 and 3 as $q_{1-3} = 1240 \ [W/m^2]$ and $q_{1-3} = 1279 \ [W/m^2]$ respectively.

The net heat exchanged between surfaces 1 and 3 using full radiosity method is $q_{1-3} = 1299 \ [W/m^2]$. A comparison between results obtained using the MRV and radiosity methods shows a very good agreement. The difference between these methods is that the radiosity method can be engaged to solve problems with diffuse properties of materials only, while the MRV method can be used for both bi-directional and diffuse surface properties. This is the main advantage of the MRV method over the radiosity method.
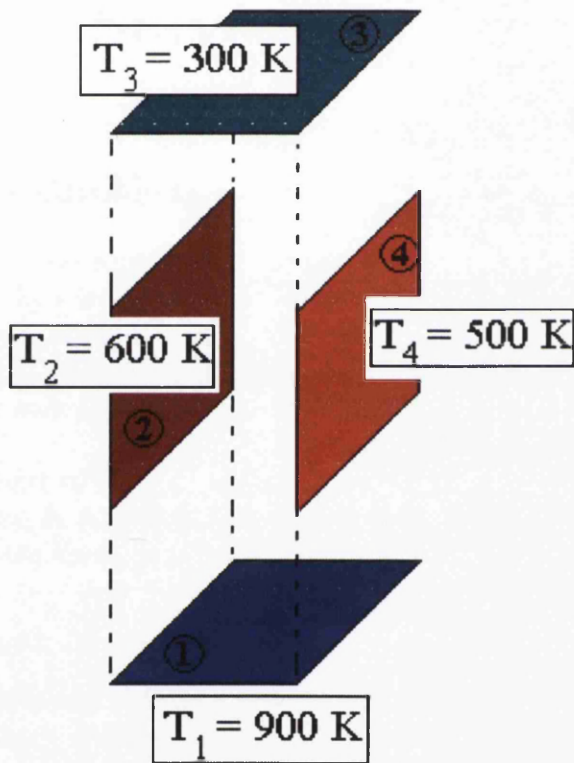
Figure A.1: A simple enclosure with four plates

Appendix B

Iterative Solvers

B.1 Introduction

A discretization (finite difference, boundary element, finite element or finite volume) of the partial differential equation (Laplace, Navier-Stokes etc.) gives a set of linear or nonlinear (symmetric or non symmetric) algebraic (matrix) equations. Generally speaking there are two families of methods that can be used for solving systems of algebraic equations: direct and iterative methods.

From the point of view of accuracy, CPU time and robustness, it is of great importance as to which solver is going to be used. Therefore, great attention has been given in this thesis to solvers.

B.1.1 Direct Methods

All methods which are included into direct methods are based on Gaussian elimination. There are the profile solver, the band solver and the frontal solver.

In the following text a short explanation of Gaussian elimination with a modification called pivoting will be given. Sometimes it may be necessary to swap two rows if a diagonal entry, which is intended for use as a pivot, turns out to be zero. In any case, inaccuracy may arise if the pivot is too small, so the row with the largest possible entry in the pivot position is chosen and used as the pivot. In the following Figure B.1 the algorithm for Gaussian elimination with pivoting is presented.

The result of the Gaussian elimination is a upper triangular matrix which

has only one unknown in the right lower corner.

$$
\begin{aligned}
A_{1,1}x_1 + A_{1,2}x_2 + \cdots + A_{1,n}x_n &= b_1 \\
A_{2,2}x_2 + \cdots + A_{2,n}x_n &= b_2 \\
\cdots \\
A_{n,n}x_n &= b_n
\end{aligned}
\tag{B.1}
$$

Solutions of this matrix (B.1) are obtained using back substitution which is given in the next equation:

$$
\begin{aligned}
do\ i &= n, 1, -1 \\
x_i &= (b_i - A_{i,i+1}x_{i+1} - \cdots - A_{i,n}x_n)/A_{n,n} \\
end\ do
\end{aligned}
\tag{B.2}
$$

Gaussian elimination requires approximately $n^3/3$ operations (where n is the size of the system). In the case when n is very large this method, according to the one of the criteria such as computation time, becomes very expensive.

A second disadvantage of Gaussian elimination is that all coefficients of the matrix $A_{i,j}$ have to be stored in core memory. In many real applications, the matrix $\mathbf{A}$ is sparse, most of its elements are zero, keeping track of the whole matrix is wasteful. This is the main reason why the frontal solver has been evolved. In the frontal solver only certain element stiffness matrices $A_{i,j}$ are stored at any one time in the core.

B.1.2 Iterative Methods

As problem sizes grow, the storage requirement becomes a burden, even on a modern computer. For this reason, alternative solution strategies have been developed - iterative methods. This family includes the following methods: Jacobi iteration, Gauss-Seidel, Line Relaxation, Successive Over-relaxation, Multigrid and Conjugate Gradient.

In the text that follows a short overview of the Jacobi iteration, Gauss-Seidel and Successive Over-relaxation method is given.

Splitting the Matrix

Many methods involve splitting the matrix $\mathbf{A}$ that is given in equation (B.13) into the difference between two new matrices $\mathbf{M}$ and $\mathbf{N}$:

$$
\mathbf{A} = \mathbf{M} - \mathbf{N}
\tag{B.3}
$$

Substituting matrix $\mathbf{A}$ in equation(B.13) with its definition (B.3) gives equation:

$$\mathbf{M}\mathbf{x} = \mathbf{N}\mathbf{x} + \mathbf{b} \tag{B.4}$$

that is solved iteratively:

$$\mathbf{M}\mathbf{x}^{k+1} = \mathbf{N}\mathbf{x}^k + \mathbf{b} \tag{B.5}$$

There are many different ways to split the matrix $\mathbf{A}$. To make the right choice two main conditions have to be satisfied, such as:
a) matrix $\mathbf{M}$ should be easily invertible;
b) the scheme should converge as rapidly as possible towards the true solution.
These conditions are in conflict: the fastest convergence is gained when $\mathbf{M} = \mathbf{A}$ but the matrix $\mathbf{A}$ is not easy to invert; while on the other hand, if a matrix that is easy to invert is chosen it may not converge especially rapidly (or at all). A matrix could be split as in the following equation:

$$\mathbf{A} = \mathbf{L} + \mathbf{D} + \mathbf{U} \; (= \mathbf{M} - \mathbf{N}) \tag{B.6}$$

where $\mathbf{L}$ is strictly lower triangular,
$\mathbf{D}$ is diagonal,
$\mathbf{U}$ is strictly upper triangular matrix.
As an example it could be writen,

$$\mathbf{A} = \begin{pmatrix} 4 & 5 & 6 \\ 7 & 8 & 9 \\ 1 & 2 & 3 \end{pmatrix}$$

where

$$\mathbf{L} = \begin{pmatrix} 0 & 0 & 0 \\ 7 & 0 & 0 \\ 1 & 2 & 0 \end{pmatrix}, \mathbf{D} = \begin{pmatrix} 4 & 0 & 0 \\ 0 & 8 & 0 \\ 0 & 0 & 3 \end{pmatrix}, \mathbf{U} = \begin{pmatrix} 0 & 5 & 6 \\ 0 & 0 & 9 \\ 0 & 0 & 0 \end{pmatrix}$$

Jacobi Iteration

In Jacobi's iteration there is $\mathbf{M} = \mathbf{D}$ and $\mathbf{N} = -(\mathbf{L} + \mathbf{U})$
The main disadvantage of Jacobi method is that it requires us to store all the components of $\mathbf{x}^k$ until the computing of the next iteration $\mathbf{x}^{k+1}$ has been finished. This method requires significant memory for solving very large systems, which may become a problem. This problem is eliminated in the following method.

Gauss-Seidel Method

Instead of storing all the components of $\mathbf{x}^k$ it makes more sense to use the "new" values of the first unknown to calculate next unknown. For the general $(n \times n)$ system, and it begins by using the first equation to update x_1:

$$(x_1)_{new} = \frac{1}{a_{11}} \left[b_1 - \sum_{j=2}^{n} a_{1j} x_j \right] \qquad (B.7)$$

Next step is to use the second equation to update x_2:

$$(x_2)_{new} = \frac{1}{a_{22}} \left[b_2 - \sum_{j=3}^{n} a_{2j} x_j \right] - \frac{a_{21}}{a_{22}} x_1 \qquad (B.8)$$

The right-hand side of this equation can be rearranged to:

$$(x_2)_{new} = (x_2)_{old} + \frac{1}{a_{22}} \left[b_2 - \sum_{j=1}^{n} a_{2j} x_j \right] \qquad (B.9)$$

Finally, the general formula for updating x_i is:

$$(x_i)_{new} = (x_i)_{old} + \frac{1}{a_{ii}} \left[b_i - \sum_{j=1}^{n} a_{ij} x_j \right] \qquad (B.10)$$

Gauss-Seidel method has one condition that all diagonal coefficients a_{ii} are nonzero. In Gauss-Seidel method matrix $\mathbf{A}$ is split in the following way: $\mathbf{M} = \mathbf{L} + \mathbf{D}$ and $\mathbf{N} = -(\mathbf{U})$.

Successive Over-relaxation Method-SOR

In this method a combination of the previous methods is used, such as:

$$(\mathbf{D} + \omega\mathbf{L})\mathbf{x}^{k+1} = [(1 - \omega)\mathbf{D} - \omega\mathbf{U}]\mathbf{x}^k + \omega\mathbf{b} \qquad (B.11)$$

where ω-is an over-relaxation or acceleration parameter. This parameter depends on the problem being solved, but it always lies between 1 and 2 for over-relaxation. Applying the same procedure for a general system of equations as for Gauss-Seidel method the following equation will be obtained:

$$(x_i)_{new} = (x_i)_{old} + \frac{\omega}{a_{ii}} \left[b_i - \sum_{j=1}^{n} a_{ij} x_j \right] \qquad (B.12)$$

After this short overview a more systematic analysis which considers conjugate gradient method and its derivations will be presented in the text that follows. These methods are conjugate gradient (CG), preconditioned conjugate gradient (PCG), least squared conjugate gradient (LSCG), conjugate gradient squared (CGS), preconditioned conjugate squared (PCGS), bi-conjugate gradient (BCG), preconditioned bi-conjugate gradient (PBCG), bi-conjugate gradient stabilized (BCGSTAB), preconditioned bi-conjugate gradient stabilized (PBCGSTAB).

B.2   Conjugate Gradient Method

The Conjugate gradient method is an old and well-known non stationary method discovered independently by **Hestenes** and **Stiefel** in the early fifties (Hestenes (1952)). Also it is the most popular iterative method for solving large, symmetric and positive definite systems of linear equations. Actually, conjugate gradient method (as well as preconditioned conjugate method) can only be used for solving symmetric linear equations obtained after discretization of Laplace or Poisson equation. Other iterative methods can be used for solving both symmetric and non symmetric equations (e.g. Navier-Stokes equations).

Finite element discretization gives a system of the form

$$\mathbf{Ax} = \mathbf{b} \tag{B.13}$$

where $\mathbf{x}$ is an unknown vector, $\mathbf{b}$ is a known vector and $\mathbf{A}$ is a known, square matrix. Symmetry and positive definiteness are properties of $\mathbf{A}$.

$\mathbf{A}$ matrix is positive definite if, for every nonzero vector $\mathbf{x}$,

$$\mathbf{x}^T \mathbf{Ax} > 0 \tag{B.14}$$

A *quadric* form is simply a vector, quadratic function of a vector with the form:

$$f(x) = \frac{1}{2} x^T \mathbf{A} x - \mathbf{b}^T x + c = \frac{1}{2} \sum_{j=1}^{n} \sum_{i=1}^{n} A_{ij} x_i x_j - \sum_{i=1}^{n} x_i b_i + c \tag{B.15}$$

where c is a scalar constant.

With a little bit of tedious mathematics it can be shown, in the case that $\mathbf{A}$ is symmetric and positive definite, $f(x)$ is minimized by the solution to $\mathbf{Ax} = \mathbf{b}$.

As an example a simple sample problem was chosen (Figure B.2):

$$\begin{aligned} 3x_1 + 2x_2 &= 2 \\ 2x_1 + 6x_2 &= -8. \end{aligned} \tag{B.16}$$

For this problem, the solution is $x = [2, -2]^T$ and the corresponding quadratic form $f(x)$ is presented in Figure B.3. This (paraboloid bowl) shape of the quadratic form is because $\mathbf{A}$ is positive definite.

In case that $\mathbf{A}$ is a negative definite matrix the shape of quadratic form $f(x)$ will be as in Figure B.4, or for an indefinite matrix as in Figure B.5.

The *gradient* of the quadratic form is defined to be:

$$f'(x) = \begin{vmatrix} \frac{\partial}{\partial x_1} f(x) \\ \frac{\partial}{\partial x_2} f(x) \\ \frac{\partial}{\partial x_n} f(x) \end{vmatrix} \tag{B.17}$$

A minimum of the function can be found when the first derivative is set to zero.

In the analyzed case

$$f'(x) = \frac{1}{2}\mathbf{A}^T x + \frac{1}{2}\mathbf{A}x - \mathbf{b} \tag{B.18}$$

Symmetric matrix has that characteristic that $\mathbf{A}^T = \mathbf{A}$, and it reduces this equation to:

$$f'(x) = \mathbf{A}x - \mathbf{b} \tag{B.19}$$

Setting the gradient to zero, equation (B.13) is obtained. So, $\mathbf{A}x = \mathbf{b}$ can be solved by finding an $\mathbf{x}$ that minimizes $f(x)$.

In the following text *Steepest Descent* method will be explained which is intuitively understood in terms of minimization problems like Figure B.3, not in terms of hyperplanes such as Figure B.5.

B.2.1 The Method of Steepest Descent

In this method, which is an old method for seeking the minimum of a function, firstly the solution process will start at an arbitrary point $x^{(0)}$ and slide down to the bottom of the paraboloid. The iterative process will run until it comes close enough to the solution x.

According to equation (B.19) there is:

$$-f'(x^{(i)}) = \mathbf{b} - \mathbf{A}\mathbf{x}^{(i)} \tag{B.20}$$

Equation (B.20) gives the direction in which f decreases most quickly.

A vector that indicates how far the current result is from the solution is called the error $e^{(i)} = x^{(i)} - x$.

The residual

$$r^{(i)} = \mathbf{b} - \mathbf{A}x^{(i)} \tag{B.21}$$

indicates how far is current value of $\mathbf{b}$ from the correct value of $\mathbf{b}$. It can easily be seen that $r^{(i)} = -\mathbf{A}e^{(i)}$. Also, more importantly, that $r^{(i)} = -f'(x^{(i)})$ and could be seen as the direction of *steepest descent*.

Starting the calculation at $x^{(0)} = [-2, -2]^T$, the first step, along the direction of steepest descent, will fall somewhere on the solid line at point,

$$\mathbf{x}^{(1)} = \mathbf{x}^{(0)} + \alpha \mathbf{r}^{(0)} \tag{B.22}$$

in Figure B.6. Applying a line search α should be chosen to minimize f along a line.

From basic calculus, α minimizes f when the *directional derivative* $\frac{d}{d\alpha} f(x^{(1)})$ is equal to zero.

This expression could be written as:

$$\frac{df(x^{(1)})^T}{dx} \frac{dx^{(1)}}{d\alpha} = f'(x^{(1)})^T r^{(0)} \tag{B.23}$$

Setting it to zero, it is found that α should be chosen so that $r^{(0)}$ and $f'(x^{(1)})$ are orthogonal (Figure B.6).

There is an intuitive reason why it should be expected for these vectors to be orthogonal at the minimum. Figure B.7 shows the gradient vectors at various points along the search line.

To find α it will start that the expression (B.23) is equal zero. Already, it has be known that $f'(x^{(1)}) = -r^{(1)}$, and the result is:

$$\mathbf{r}^{(1)T} \mathbf{r}^{(0)} = 0 \tag{B.24}$$

Involving equation (B.21) yields:

$$(\mathbf{b} - \mathbf{A}\mathbf{x}^{(1)})^T \mathbf{r}^{(0)} = 0 \tag{B.25}$$

Putting equation (B.22) into the previous equation gives:

$$
\begin{aligned}
(\mathbf{b} - \mathbf{A}(\mathbf{x}^{(0)} + \alpha \mathbf{r}^{(0)}))^T \mathbf{r}^{(0)} &= 0 \\
(\mathbf{b} - \mathbf{A}\mathbf{x}^{(0)})^T \mathbf{r}^{(0)} - \alpha(\mathbf{A}\mathbf{r}^{(0)})^T \mathbf{r}^{(0)} &= 0 \\
(\mathbf{b} - \mathbf{A}\mathbf{x}^{(0)})^T \mathbf{r}^{(0)} &= \alpha(\mathbf{A}\mathbf{r}^{(0)})^T \mathbf{r}^{(0)}
\end{aligned} \tag{B.26}
$$

Finally, α is obtained as:

$$\alpha = \frac{\mathbf{r}^{(0)T}\mathbf{r}^{(0)}}{\mathbf{r}^{(0)}(\mathbf{A}\mathbf{r}^{(0)})^T} \tag{B.27}$$

The following equations present the method of *Steepest Descent*:

$$\mathbf{r}^{(i)} = b - \mathbf{A}x^{(i)} \tag{B.28}$$

$$\alpha^{(i)} = \frac{\mathbf{r}^{(i)T}\mathbf{r}^{(i)}}{\mathbf{r}^{(i)}(\mathbf{A}\mathbf{r}^{(i)})^T} \tag{B.29}$$

$$\mathbf{x}^{(i+1)} = \mathbf{x}^{(i)} + \alpha^{(i)}\mathbf{r}^{(i)} \tag{B.30}$$

The example is run until it converges, Figure B.8. As can be seen in Figure B.8, a new gradient is orthogonal to the previous gradient which causes a zigzag path.

Unfortunately, the steepest descent method often converges slowly and in the case that the magnitude of the function f has a narrow valley, the method tends to oscillate back and forth across that valley and many steps may be required to find the solution.

As it has seen earlier (Jacobi Iteration) the matrix $\mathbf{A}$ could be split into two parts: $\mathbf{D}$,which has only diagonal elements and they are identical to those of $\mathbf{A}$; and $\mathbf{T}$ whose diagonal elements are zero and non-diagonal elements are identical to those of $\mathbf{A}$. Applying this it becomes:

$$\begin{aligned}
\mathbf{A}\mathbf{x} &= \mathbf{b} \\
\mathbf{D}\mathbf{x} &= -\mathbf{N}\mathbf{x} + \mathbf{b} \\
\mathbf{x} &= -\mathbf{D}^{-1}\mathbf{N}\mathbf{x} + \mathbf{D}^{-1}\mathbf{b} \\
\mathbf{x} &= \mathbf{B}\mathbf{x} + \mathbf{z} \tag{B.31}
\end{aligned}$$

where $\mathbf{B} = -\mathbf{D}^{-1}\mathbf{N}$, $\mathbf{z} = \mathbf{D}^{-1}\mathbf{b}$. Matrix $\mathbf{D}$ is diagonal and it is easy to invert. Identity (B.31) can be converted into an iterative method as

$$\mathbf{x}^{(i+1)} = \mathbf{B}\mathbf{x}^{(i)} \tag{B.32}$$

The hope is that after starting with a vector $\mathbf{x}^{(0)}$ the solution process is getting closer and closer to the solution $\mathbf{x}$. $\mathbf{x}$ is called a *stationary point* of equation (B.32). This is the reason why this method is called the **Stationary iterative method**.

Each iterate $\mathbf{x}^{(i)}$ could be expressed as the sum of the exact solution $\mathbf{x}$ and the error $\mathbf{e}^{(i)}$:

$$\begin{aligned}
\mathbf{x}^{(i+1)} &= \mathbf{B}\mathbf{x}^{(i)} + \mathbf{z} \\
&= \mathbf{B}(\mathbf{x} + \mathbf{e}^{(i)}) + \mathbf{z} \\
&= \mathbf{B}\mathbf{x} + \mathbf{z} + \mathbf{B}\mathbf{e}^{(i)} \\
&= \mathbf{x} + \mathbf{B}\mathbf{e}^{(i)} \tag{B.33}
\end{aligned}$$

According to the equation (B.33) the error term for the new iteration $\mathbf{e}^{(i+1)}$ can be defined as

$$\mathbf{e}^{(i+1)} = \mathbf{B}\mathbf{e}^{(i)} \tag{B.34}$$

Equation (B.34) says that the error vector is affected in every iteration. Unfortunately, *Jacobi Method* does not converge for every $\mathbf{A}$, even when $\mathbf{A}$ is a positive definite matrix.

In order to give a complete view of the **Conjugate Gradient Method** and its history in the next section the **Method of Conjugate Directions** will be explained.

B.2.2 The Method of Conjugate Directions

As could be seen from Figure B.8 the problem of the Steepest Descent method is that this method finds a solution taking steps in the same direction as earlier steps. This problem is solved by taking a set of orthogonal *search directions* $d^{(0)}$, $d^{(1)}, \ldots, d^{(n-1)}$. In fact, it could be seen that is possible to minimize a function with respect to several directions simultaneously while searching in one direction at a time.

Generally, for each step a point is chosen:

$$\mathbf{x}^{(i+1)} = \mathbf{x}^{(i)} + \alpha^{(i)}\mathbf{d}^{(i)} \tag{B.35}$$

In equation (B.35) $\alpha^{(i)}$ could be found if $\mathbf{e}^{(i+1)}$ and $\mathbf{d}^{(i)}$ are orthogonal. This means that the inner product is equal to zero.

$$\begin{aligned}
\mathbf{d}^{T(i)}\mathbf{e}^{(i+1)} &= 0 \\
\mathbf{d}^{T(i)}(\mathbf{e}^{(i)} + \alpha^{(i)}\mathbf{d}^{(i)}) &= 0 \\
\alpha^{(i)} = -\frac{\mathbf{d}^{T(i)}\mathbf{e}^{(i)}}{\mathbf{d}^{T(i)}\mathbf{d}^{(i)}} & \tag{B.36}
\end{aligned}$$

Therefore, before calculating $\alpha^{(i)}$ $\mathbf{e}^{(i+1)}$ is already known. At the same time if $\mathbf{e}^{(i+1)}$ is known the problem is already solved.

This is solved by involving A-orthogonality instead orthogonality. That means the search directions (vectors) are A-orthogonal instead of orthogonal. Two vectors $\mathbf{d}^{(i)}$ and $\mathbf{d}^{(j)}$ are A-orthogonal, or *conjugate*, if

$$\mathbf{d}^{T(i)}\mathbf{A}\mathbf{d}^{(j)} = 0 \tag{B.37}$$

In the case that the search directions are A-orthogonal further derivation of equation (B.36) gives the new expression for $\alpha^{(i)}$ and it is

$$\alpha^{(i)} = -\frac{\mathbf{d}^{T(i)}\mathbf{r}^{(i)}}{\mathbf{d}^{T(i)}\mathbf{A}\mathbf{d}^{(i)}} \tag{B.38}$$

Expressions of $\alpha^{(i)}$ in equations (B.28) and (B.38) are identical in case that the search direction is the residual.

Gram-Schmidt Conjugation

The *conjugate Gram-Schmidt process* is a simple way to generate a set of A-orthogonal search directions $\mathbf{d}^{(i)}$. Also, there is a set of n linearly independent vectors $u_0, u_1, \ldots, u_{n-1}$. A search direction $\mathbf{d}^{(i)}$ could be constructed by taking u_i and subtracting out any components that are not A-orthogonal to the previous $\mathbf{d}$ vectors.

$$\mathbf{d}^{(i)} = u_i + \sum_{k=0}^{i-1} \beta_{ik} \mathbf{d}^{(k)} \tag{B.39}$$

where β_{ik} are defined for $i > k$. Multiplying equation (B.39) by $\mathbf{Ad}^{(j)}$ gives:

$$\begin{aligned}
\mathbf{d}^{T(i)} \mathbf{Ad}^{(j)} &= u_i^T \mathbf{Ad}^{(j)} + \sum_{k=0}^{i-1} \beta_{ik} \mathbf{d}^{T(k)} \mathbf{Ad}^{(j)} \\
0 &= u_i^T \mathbf{Ad}^{(j)} + \beta_{ij} \mathbf{d}^{T(j)} \mathbf{Ad}^{(j)} \\
\beta_{ij} &= -\frac{u_i^T \mathbf{Ad}^{(j)}}{\mathbf{d}^{T(j)} \mathbf{Ad}^{(j)}}
\end{aligned} \tag{B.40}$$

The number of matrix-vector products per iteration can be reduced to one by using a recurrence to find the residual:

$$\begin{aligned}
\mathbf{r}^{(i+1)} &= -\mathbf{Ae}^{(i+1)} \\
&= -\mathbf{A}(\mathbf{e}^{(i)} + \alpha^{(i)} \mathbf{d}^{(i)}) \\
&= \mathbf{r}^{(i)} - \alpha^{(i)} \mathbf{Ad}^{(i)}
\end{aligned} \tag{B.41}$$

B.2.3 The Conjugate Gradient Method

The Conjugate Gradient (CG) method appeared after the Steepest Descent method and the Conjugate Direction method. Defacto, the CG method is the Conjugate Direction method where the search directions are constructed by conjugation of the residuals.

The residual has the desirable property that it is orthogonal to the previous search directions, so a new, linearly independent search direction is produced. At the same time the residual is orthogonal to the previous residuals:

$$\mathbf{r}^{T(i)} \mathbf{r}^{(j)} = 0, \; i \neq j \tag{B.42}$$

The Conjugate Gradient strategy is presented in the following pseudocode.

$$Pseudocode : CG$$

1. *initial guess* $\mathbf{x}^{(0)}$ (*for example* $\mathbf{x}^{(0)} = 0$)

2. *compute* $\mathbf{r}^{(0)} = \mathbf{b} - \mathbf{A}\mathbf{x}^{(0)}$

3. $\mathbf{p}^{(0)} = \mathbf{r}^{(0)}$

do for $i = 1, 2, ..., iterations\ limit$

$$\mathbf{q}^{(i)} = \mathbf{A}\mathbf{p}^{(i-1)}$$

$$\alpha^{(i)} = \frac{(\mathbf{r}^{(i-1)}, \mathbf{r}^{(i-1)})}{(\mathbf{p}^{(i-1)}, \mathbf{q}^{(i)})}$$

$$\mathbf{x}^{(i)} = \mathbf{x}^{(i-1)} + \alpha^{(i)}\mathbf{p}^{(i-1)}$$

$$\mathbf{r}^{(i)} = \mathbf{r}^{(i-1)} - \alpha^{(i)}\mathbf{q}^{(i)}$$

$$\beta^{(i)} = \frac{(\mathbf{r}^{(i)}, \mathbf{r}^{(i)})}{(\mathbf{r}^{(i-1)}, (\mathbf{r}^{(i-1)}))}$$

$$\mathbf{p}^{(i)} = \mathbf{r}^{(i)} + \beta^{(i)}\mathbf{p}^{(i-1)}$$

check convergence, continue if necessary

end

B.2.4   Preconditioned Conjugate Gradient Method

An increase in the number of elements obtained after a discretization causes the standard Conjugate Gradient method to converge slowly. The rate of convergence of this method (CG) depends on the *condition number k* of the matrix,

$$k = \frac{\lambda_{(max)}}{\lambda_{(min)}} \tag{B.43}$$

where $\lambda_{(max)}$ and $\lambda_{(min)}$ are the largest and the smallest eigenvalues of the matrix.

The slow convergency problem of the standard Conjugate Gradient method can be eliminated by replacing the problem whose solution is going to be solved by another one with the same solution but a smaller condition number. This process is called **preconditioning**.

A matrix $\mathbf{M}$ which is a symmetric, positive definite that approximates matrix $\mathbf{A}$ could be taken. Instead solving a system of equations (B.13) the new system of equations (B.44) will be solved:

$$\mathbf{M}^{-1}\mathbf{A}\mathbf{x} = \mathbf{M}^{-1}\mathbf{b} \qquad (\text{B.44})$$

or

$$\mathbf{A}\mathbf{M}^{-1}\mathbf{u} = \mathbf{b}, \ \mathbf{x} = \mathbf{M}^{-1}\mathbf{u} \qquad (\text{B.45})$$

The system which has the same solution as the original system is called a pre-conditioned system and $\mathbf{M}$ is the preconditioning matrix or preconditioner.

There are a few different techniques for preconditioning, three of them are: splitting, left preconditioning, and right preconditioning. **Splitting** method is explained earlier and in the text that follow preconditioning matrices for the Jacobi, Gauss-Seidel, SOR and SSOR iterations, (according to Saad (2000)) are given respectively:

$$
\begin{aligned}
\mathbf{M}_{JA} &= \mathbf{D} \\
\mathbf{M}_{GS} &= \mathbf{D} - \mathbf{L} \\
\mathbf{M}_{SOR} &= \frac{1}{\omega}(\mathbf{D} - \omega\mathbf{L}) \\
\mathbf{M}_{SSOR} &= \frac{1}{\omega(2-\omega)}(\mathbf{D} - \omega\mathbf{L})\mathbf{D}^{-1}(\mathbf{D} - \omega\mathbf{U}) \qquad (\text{B.46})
\end{aligned}
$$

When $\mathbf{M}$ is formed using an incomplete Cholesky factorization, where

$$\mathbf{M} = \mathbf{L}\mathbf{L}^T \qquad (\text{B.47})$$

then in order to preserve symmetry the preconditioner is split between left and right, to solve

$$\mathbf{L}^{-1}\mathbf{A}\mathbf{L}^{-T}\mathbf{u} = \mathbf{L}^{-1}\mathbf{b}, \ \mathbf{x} = \mathbf{L}^{-T}\mathbf{u} \qquad (\text{B.48})$$

If the condition number of $\mathbf{M}^{-1}\mathbf{A}$ is much smaller than the condition number of $\mathbf{A}$ $k(\mathbf{M}^{-1}\mathbf{A}) \ll k(\mathbf{A})$, equation (B.44) could be solved iteratively and more quickly than the original problem (Smith (1998)).

Pseudocode : PCG

1. *initial guess* $\mathbf{x}^{(0)}(for\ example\ \mathbf{x}^{(0)} = 0)$

2. *compute* $\mathbf{r}^{(0)} = \mathbf{b} - \mathbf{A}\mathbf{x}^{(0)}$

3. $\mathbf{p}^{(0)} = \mathbf{d}^{(0)} = \mathbf{M}^{-1}\mathbf{r}^{(0)}$

$$do \ for \ i = 1, 2, ..., iterations \ limit$$

$$\mathbf{q}^{(i)} = \mathbf{A}\mathbf{p}^{(i-1)}$$

$$\alpha^{(i)} = \frac{(\mathbf{d}^{(i-1)}, \mathbf{r}^{(i-1)})}{(\mathbf{p}^{(i-1)}, \mathbf{q}^{(i)})}$$

$$\mathbf{x}^{(i)} = \mathbf{x}^{(i-1)} + \alpha^{(i)}\mathbf{p}^{(i-1)}$$

$$\mathbf{r}^{(i)} = \mathbf{r}^{(i-1)} - \alpha^{(i)}\mathbf{q}^{(i)}$$

$$\mathbf{d}^{(i)} = \mathbf{M}^{-1}\mathbf{r}^{(i)}$$

$$\beta^{(i)} = \frac{(\mathbf{q}^{(i)}, \mathbf{r}^{(i)})}{(\mathbf{q}^{(i-1)}, (\mathbf{r}^{(i-1)}))}$$

$$\mathbf{p}^{(i)} = \mathbf{d}^{(i)} + \beta^{(i)}\mathbf{p}^{(i-1)}$$

check convergence, continue if necessary

end

In the case that an incomplete Cholesky factorization is used and **M** is obtained as in equation (B.47), there are two options: the split preconditioning option (B.48); or the pseudocode written above. The following pseudocode describes split preconditioner conjugate gradient (Saad (2000)).

Pseudocode : Split Preconditioner Conjugate Gradient

1. *initial guess* $\mathbf{x}^{(0)}$ (*for example* $\mathbf{x}^{(0)} = 0$)

2. *compute* $\mathbf{r}^{(0)} = \mathbf{b} - \mathbf{A}\mathbf{x}^{(0)}$

3. $\tilde{\mathbf{r}}^{(0)} = \mathbf{L}^{-1}\mathbf{r}^{(0)}$

4. $\mathbf{p}^{(0)} = \mathbf{L}^{-T}\tilde{\mathbf{r}}^{(0)}$

$$do \ for \ i = 1, 2, ..., iterations \ limit$$

$$\mathbf{q}^{(i)} = \mathbf{A}\mathbf{p}^{(i-1)}$$

$$\alpha^{(i)} = \frac{(\tilde{\mathbf{r}}^{(i-1)}, \tilde{\mathbf{r}}^{(i-1)})}{(\mathbf{p}^{(i-1)}, \mathbf{q}^{(i)})}$$

$$\mathbf{x}^{(i)} = \mathbf{x}^{(i-1)} + \alpha^{(i)}\mathbf{p}^{(i-1)}$$

$$\tilde{\mathbf{r}}^{(i)} = \tilde{\mathbf{r}}^{(i-1)} - \alpha^{(i)}\mathbf{L}^{-1}\mathbf{q}^{(i)}$$

$$\beta^{(i)} = \frac{(\tilde{\mathbf{r}}^{(i)}, \tilde{\mathbf{r}}^{(i)})}{(\tilde{\mathbf{r}}^{(i-1)}, (\tilde{\mathbf{r}}^{(i-1)}))}$$

$$\mathbf{p}^{(i)} = \mathbf{L}^{-T}\tilde{\mathbf{r}}^{(i)} + \beta^{(i)}\mathbf{p}^{(i-1)}$$

check convergence, continue if necessary

end

B.3 Least Squares Conjugate Gradient Method

In the case that matrix $\mathbf{A}$ is nonsymmetric the conjugate gradient method cannot be used for solving system of equations (B.13). Multiplying both sides of equation (B.13) by $\mathbf{A}^T$ gives:

$$\mathbf{A}^T\mathbf{r} = \mathbf{A}^T\mathbf{b} - \mathbf{A}^T\mathbf{A}\mathbf{x} \qquad (B.49)$$

The new matrix $\mathbf{A}^T\mathbf{A}$ is always symmetric.

Pseudocode : LSCG

1. *initial guess* $\mathbf{x}^{(0)}$ *(for example* $\mathbf{x}^{(0)} = 0$*)*

2. *compute* $\mathbf{r}^{(0)} = \mathbf{b} - \mathbf{A}\mathbf{x}^{(0)}$

3. $\mathbf{p}^{(0)} = \mathbf{s}^{(0)} = \mathbf{A}^T\mathbf{r}^{(0)}$

do for $i = 1, 2, ..., iterations\ limit$

$$\mathbf{q}^{(i)} = \mathbf{A}\mathbf{p}^{(i-1)}$$

$$\alpha^{(i)} = \frac{(\mathbf{s}^{(i-1)}, \mathbf{s}^{(i-1)})}{(\mathbf{q}^{(i)}, \mathbf{q}^{(i)})}$$

$$\mathbf{x}^{(i)} = \mathbf{x}^{(i-1)} + \alpha^{(i)}\mathbf{p}^{(i-1)}$$

$$\mathbf{r}^{(i)} = \mathbf{r}^{(i-1)} - \alpha^{(i)}\mathbf{q}^{(i)}$$

$$\mathbf{s}^{(i)} = \mathbf{A}^T\mathbf{r}^{(i)}$$

$$\beta^{(i)} = \frac{(\mathbf{s}^{(i)}, \mathbf{s}^{(i)})}{(\mathbf{s}^{(i-1)}, (\mathbf{s}^{(i-1)})}$$

$$\mathbf{p}^{(i)} = \mathbf{s}^{(i)} + \beta^{(i)}\mathbf{p}^{(i-1)}$$

check convergence, continue if necessary

end

B.4 Bi-conjugate Gradient Method

The conjugate gradient method is not suitable for nonsymmetric systems of equations because the residual vectors cannot be made orthogonal with short recurrences. This is the main reason for introducing the bi-conjugate gradient method, which takes a different approach in replacing the orthogonal sequence of residuals by two mutually orthogonal sequences (Barrett (1994)). The minimization is no longer provided.

Instead, solving system equations (B.13), using this method involves solving the following system equations (Lavery (1996)):

$$
\begin{aligned}
\mathbf{Ax} &= \mathbf{b} \\
\mathbf{A}^T \widetilde{\mathbf{x}} &= \mathbf{b}
\end{aligned}
\tag{B.50}
$$

As was mentioned above two sequences of residuals are updated:

$$
\begin{aligned}
\mathbf{r}^{(i)} &= \mathbf{r}^{(i-1)} - \alpha^{(i)} \mathbf{A} \mathbf{p}^{(i)} \\
\widetilde{\mathbf{r}}^{(i)} &= \widetilde{\mathbf{r}}^{(i-1)} - \alpha^{(i)} \mathbf{A}^T \widetilde{\mathbf{p}}^{(i)}
\end{aligned}
\tag{B.51}
$$

and two sequences of search directions:

$$
\begin{aligned}
\mathbf{p}^{(i)} &= \mathbf{r}^{(i-1)} + \beta^{(i-1)} \mathbf{p}^{(i-1)} \\
\widetilde{\mathbf{p}}^{(i)} &= \widetilde{\mathbf{r}}^{(i-1)} + \beta^{(i-1)} \widetilde{\mathbf{p}}^{(i-1)}
\end{aligned}
\tag{B.52}
$$

The pseudocode is given in the text written below.

Pseudocode : BCG

1. *initial guess* $\mathbf{x}^{(0)}$ *(for example,* $\mathbf{x}^{(0)} = 0$*)*

2. *compute* $\mathbf{r}^{(0)} = \mathbf{b} - \mathbf{Ax}^{(0)}$

3. *choose* $\widetilde{\mathbf{r}}^{(0)}$ *(for example,* $\widetilde{\mathbf{r}}^{(0)} = \mathbf{r}^{(0)}$*)*

4. $\rho^{(0)} = 1.$

do for $i = 1, 2, ..., iterations\ limit$

$$\rho^{(i)} = (\widetilde{\mathbf{r}}^{(i-1)}, \mathbf{r}^{(i-1)})$$

$$\beta^{(i)} = \frac{\rho^{(i)}}{\rho^{(i-1)}}$$

$$\rho^{(i-1)} = \rho^{(i)}$$

$$\mathbf{p}^{(i)} = \mathbf{r}^{(i)} + \beta^{(i)} \mathbf{p}^{(i-1)}$$

$$\widetilde{\mathbf{p}}^{(i)} = \widetilde{\mathbf{r}}^{(i)} + \beta^{(i)} \widetilde{\mathbf{p}}^{(i-1)}$$

$$\sigma^{(i)} = (\widetilde{\mathbf{p}}^{(i)}, \mathbf{A}\mathbf{p}^{(i)})$$

$$\alpha^{(i)} = \frac{\rho^{(i)}}{\sigma^{(i)}}$$

$$\mathbf{r}^{(i)} = \mathbf{r}^{(i-1)} - \alpha^{(i)} \mathbf{A}\mathbf{p}^{(i)}$$

$$\widetilde{\mathbf{r}}^{(i)} = \widetilde{\mathbf{r}}^{(i-1)} - \alpha^{(i)} \mathbf{A}^T \widetilde{\mathbf{p}}(i)$$

$$\mathbf{x}^{(i)} = \mathbf{x}^{(i-1)} + \alpha^{(i)} \mathbf{p}^{(i)}$$

check convergence, continue if necessary

end

For symmetric positive definite systems, this method give the same results as the conjugate gradient method, but at twice the cost per iteration. For nonsymmetric matrices, it could be shown that convergence behavior may be quite irregular, and the method may break down. The breakdown situation, which may occur when $\rho^{(i)} = (\widetilde{\mathbf{r}}^{(i-1)}, \mathbf{r}^{(i-1)}) \approx 0$, can be avoided by so-called look-ahead strategies. Also, the problem can appear if chosen decomposition fails. However, this problem can repaired using another decomposition.

B.4.1 Preconditioned Bi-conjugate Gradient Method

The difference between PBCG method and BCG method is two new steps which involve the preconditioner. The preconditioner must be chosen with care because similar problems arise during the two solvers involving the preconditioning matrix as it was with BCG method. The pseudocode of PBCG method is given in the text that follows (Perić (2002)):

Pseudocode : PBCG

1. *initial guess* $\mathbf{x}^{(0)}$ *(for example,* $\mathbf{x}^{(0)} = 0$*)* .

2. *compute* $\mathbf{r}^{(0)} = b - \mathbf{A}\mathbf{x}^{(0)}$

3. *choose* $\widetilde{\mathbf{r}}^{(0)}$ *(for example,* $\widetilde{\mathbf{r}}^{(0)} = \mathbf{r}^{(0)}$*)*

4. $\rho^{(0)} = 1$.

do for $i = 1, 2, ..., iterations\ limit$

solve $\mathbf{M}\mathbf{z}^{(i-1)} = \mathbf{r}^{(i-1)}$

solve $\mathbf{M}^T \widetilde{\mathbf{z}}^{(i-1)} = \widetilde{\mathbf{r}}^{(i-1)}$

$$\rho^{(i)} = (\mathbf{z}^{(i-1)T}, \widetilde{\mathbf{r}}^{(i-1)})$$

$$\beta^{(i)} = \frac{\rho^{(i)}}{\rho^{(i-1)}}$$

$$\rho^{(i-1)} = \rho^{(i)}$$

$$\mathbf{p}^{(i)} = \mathbf{z}^{(i)} + \beta^{(i)}\mathbf{p}^{(i-1)}$$

$$\widetilde{\mathbf{p}}^{(i)} = \widetilde{\mathbf{z}}^{(i)} + \beta^{(i)}\widetilde{\mathbf{p}}^{(i-1)}$$

$$\sigma^{(i)} = (\widetilde{\mathbf{p}}^{(i)}, \mathbf{A}\widetilde{\mathbf{p}}^{(i)})$$

$$\alpha^{(i)} = \frac{\rho^{(i)}}{\sigma^{(i)}}$$

$$\mathbf{r}^{(i)} = \mathbf{r}^{(i-1)} - \alpha^{(i)}\mathbf{A}\mathbf{p}^{(i)}$$

$$\widetilde{\mathbf{r}}^{(i)} = \widetilde{\mathbf{r}}^{(i-1)} - \alpha^{(i)}\mathbf{A}^T\widetilde{\mathbf{p}}(i)$$

$$\mathbf{x}^{(i)} = \mathbf{x}^{(i-1)} + \alpha^{(i)}\mathbf{p}^{(i)}$$

check convergence, continue if necessary

end

B.5   Conjugate Gradient Squared Method

Conjugate gradient squared method developed by **Sonneveld** (Sonneveld (1989))has been derived from the bi-conjugate gradient method to deal with nonsymmetric, non positive real systems of equations.

The main idea for introducing this method is to avoid using the transpose of **A** as it is in the **BCG** and to gain faster convergence for roughly the same computation cost.

In this method the residual and direction vectors are chosen according to:

$$
\begin{aligned}
\mathbf{r}^{(i)} &= \phi^{(i)2}(\mathbf{A})\mathbf{r}^{(0)} \\
\mathbf{p}^{(i)} &= \psi^{(i)2}(\mathbf{A})\mathbf{p}^{(0)}
\end{aligned}
\tag{B.53}
$$

Convergence is usually twice as fast as for the BCG method, but it is very often highly irregular behavior. The CGS method works quite well in many cases. The only problem is that the polynomials are squared and rounding errors tend to be more damaging than in the standard BCG method.

The pseudocode of this method is given below.

Pseudocode : CGS

1. *initial guess* $\mathbf{x}^{(0)}$ *(for example,* $\mathbf{x}^{(0)} = 0$*)*

$$2.\ compute\ \mathbf{r}^{(0)} = \mathbf{b} - \mathbf{A}\mathbf{x}^{(0)}$$

$$3.\ choose\ \tilde{\mathbf{r}}^{(0)}(for\ example,\ \tilde{\mathbf{r}}^{(0)} = \mathbf{r}^{(0)})$$

$$4.\ \mathbf{q}^{(0)} = \mathbf{p}^{(0)} = 0$$

$$5.\ \rho^{(0)} = 1.$$

do for $i = 1, 2, ..., iterations\ limit$

$$\rho^{(i)} = (\tilde{\mathbf{r}}^{(i-1)}, \mathbf{r}^{(i-1)})$$

$$\beta^{(i)} = \frac{\rho^{(i)}}{\rho^{(i-1)}}$$

$$\rho^{(i-1)} = \rho^{(i)}$$

$$\mathbf{z}^{(i)} = \mathbf{r}^{(i-1)} + \beta^{(i)}\mathbf{q}^{(i-1)}$$

$$\mathbf{p}^{(i)} = \mathbf{z}^{(i)} + \beta^{(i)}(\mathbf{q}^{(i-1)} + \beta^{(i)}\mathbf{p}^{(i-1)})$$

$$\mathbf{v}^{(i)} = \mathbf{A}\mathbf{p}^{(i)}$$

$$\sigma^{(i)} = (\tilde{\mathbf{r}}^{(i)}, \mathbf{v}^{(i)})$$

$$\alpha^{(i)} = \frac{\rho^{(i)}}{\sigma^{(i)}}$$

$$\mathbf{q}^{(i)} = \mathbf{z}^{(i)} - \alpha^{(i)}\mathbf{v}^{(i)}$$

$$\mathbf{r}^{(i)} = \mathbf{r}^{(i-1)} - \alpha^{(i)}\mathbf{A}(\mathbf{z}^{(i)} + \mathbf{q}^{(i)})$$

$$\mathbf{x}^{(i)} = \mathbf{x}^{(i-1)} + \alpha^{(i)}(\mathbf{z}^{(i)} + \mathbf{q}^{(i)})$$

check convergence, continue if necessary

end

B.5.1 Preconditioned Conjugate Gradient Squared Method

Everything that has been written about preconditioning in the explanation of the preconditioned conjugate gradient method can be used in this section. This means that any theoretical explanation is avoided and the pseudocode of this method is given in the text that follows.

Pseudocode : PCGS

$$1.\ initial\ guess\ \mathbf{x}^{(0)}(for\ example,\ \mathbf{x}^{(0)} = 0)$$

$$2.\ compute\ \mathbf{r}^{(0)} = \mathbf{b} - \mathbf{A}\mathbf{x}^{(0)}$$

$$3.\ choose\ \tilde{\mathbf{r}}^{(0)}(for\ example,\ \tilde{\mathbf{r}}^{(0)} = \mathbf{r}^{(0)})$$

4. $\mathbf{q}^{(0)} = \mathbf{p}^{(0)} = 0$

5. $\rho^{(0)} = 1.$

do for $i = 1, 2, ..., iterations\ limit$

$$\rho^{(i)} = (\widetilde{\mathbf{r}}^{(i-1)}, \mathbf{r}^{(i-1)})$$

$$\beta^{(i)} = \frac{\rho^{(i)}}{\rho^{(i-1)}}$$

$$\rho^{(i-1)} = \rho^{(i)}$$

$$\mathbf{z}^{(i)} = \mathbf{r}^{(i-1)} + \beta^{(i)}\mathbf{q}^{(i-1)}$$

$$\mathbf{p}^{(i)} = \mathbf{z}^{(i)} + \beta^{(i)}(\mathbf{q}^{(i-1)} + \beta\mathbf{p}^{(i-1)})$$

solve $\mathbf{M}\hat{\mathbf{p}} = \mathbf{p}^{(i)}$

$$\hat{\mathbf{v}}^{(i)} = \mathbf{A}\hat{\mathbf{p}}^{(i)}$$

$$\sigma^{(i)} = (\widetilde{\mathbf{r}}^{(i)}, \hat{\mathbf{v}}^{(i)})$$

$$\alpha^{(i)} = \frac{\rho^{(i)}}{\sigma^{(i)}}$$

$$\mathbf{q}^{(i)} = \mathbf{z}^{(i)} - \alpha^{(i)}\hat{\mathbf{v}}^{(i)}$$

solve $\mathbf{M}\hat{\mathbf{z}} = \mathbf{z}^{(i)} + \mathbf{q}^{(i)}$

$$\mathbf{x}^{(i)} = \mathbf{x}^{(i-1)} + \alpha^{(i)}\hat{\mathbf{z}}$$

$$\hat{\mathbf{q}} = \mathbf{A}\hat{\mathbf{z}}^{(i)}$$

$$\mathbf{r}^{(i)} = \mathbf{r}^{(i-1)} - \alpha^{(i)}\hat{\mathbf{q}}$$

check convergence, continue if necessary

end

It can be noted that pseudocode of PCGS method has two new steps involving the preconditioning matrix. Obviously, preconditioning will accelerate CGS method, but the problem with convergence behavior is same as in CGS method. The problem occurs if $\rho^{(i)} = (\widetilde{\mathbf{r}}^{(i-1)}, \mathbf{r}^{(i-1)}) = 0$. In this case the method will fail.

B.6   Bi-conjugate Gradient Stabilized Method

The bi-conjugate gradient stabilized method was developed by **Van der Vorst** Van der Vorst (1992) to solve nonsymmetric linear systems avoiding the often irregular convergence patterns of the conjugate gradient squared method. Instead of computing the conjugate gradient squared method sequence (B.53) the following equations will be solved:

$$\mathbf{r}^{(i)} = \phi^{(i)}(\mathbf{A})\psi^{(i)}(\mathbf{A})\mathbf{r}^{(0)}$$
$$\psi^{(i)}(\mathbf{A}) = (\mathbf{I} - \omega^{(1)}\mathbf{A})(\mathbf{I} - \omega^{(2)}\mathbf{A})\cdots(\mathbf{I} - \omega^{(i)}\mathbf{A}) \qquad (\text{B.54})$$

where $\omega^{(i)}$ is chosen to minimize $r^{(i)}$. The pseudocode of this method is given below.

Pseudocode : BCGSTAB

1. *initial guess* $\mathbf{x}^{(0)}$ (*for example,* $\mathbf{x}^{(0)} = 0$)

2. *compute* $\mathbf{r}^{(0)} = \mathbf{b} - \mathbf{A}\mathbf{x}^{(0)}$

3. $\mathbf{p} = \mathbf{r}^{(0)}$

4. $\hat{\omega}^{(0)} = \beta^{(0)} = \alpha^{(0)} = 1$

5. $\mathbf{q}^{(0)} = \mathbf{v}^{(0)} = 0$

do for $i = 1, 2, ..., iterations\ limit$

$$\hat{\beta} = (\mathbf{p}, \mathbf{r}^{(i-1)})$$

$$\omega^{(i)} = \frac{\hat{\beta}}{\beta} \times \frac{\hat{\omega}^{(i-1)}}{\alpha^{(i-1)}}$$

$$\beta = \hat{\beta}$$

$$\mathbf{q}^{(i)} = \mathbf{r}^{(i-1)} - \hat{\omega}^{(i)}(\mathbf{q}^{(i-1)} - \alpha^{(i-1)}\mathbf{v}^{(i-1)})$$

$$\mathbf{v}^{(i)} = \mathbf{A}\mathbf{q}^{(i)}$$

$$\hat{\omega}^{(i)} = \frac{\hat{\beta}}{(\mathbf{p}, \mathbf{v}^{(i)})}$$

$$\mathbf{s} = \mathbf{r}^{(i-1)} - \hat{\omega}^{(i)}\mathbf{v}^{(i)}$$

$$\mathbf{t} = \mathbf{A}\mathbf{s}$$

$$\alpha^{(i)} = \frac{(\mathbf{t}, \mathbf{s})}{(\mathbf{t}, \mathbf{t})}$$

$$\mathbf{x}^{(i)} = \mathbf{x}^{(i-1)} + \hat{\omega}^{(i)}\mathbf{q}^{(i)} + \alpha^{(i)}\mathbf{s}$$

$$\mathbf{r}^{(i)} = \mathbf{s} - \alpha^{(i)}\mathbf{t}$$

check convergence, continue if necessary

end

B.6.1 Preconditioned Bi-conjugate Gradient Stabilized Method

$$Pseudocode : \; PBCGSTAB$$

1. *initial guess* $\mathbf{x}^{(0)} (for \; example, \; \mathbf{x}^{(0)} = 0)$

2. *compute* $\mathbf{r}^{(0)} = \mathbf{b} - \mathbf{A}\mathbf{x}^{(0)}$

3. $\mathbf{p} = \mathbf{r}^{(0)}$

4. $\hat{\omega}^{(0)} = \beta^{(0)} = \alpha^{(0)} = 1$

5. $\mathbf{q}^{(0)} = \mathbf{v}^{(0)} = 0$

do for $i = 1, 2, ..., iterations \; limit$

$$\hat{\beta} = (\mathbf{p}, \mathbf{r}^{(i-1)})$$

$$\omega^{(i)} = \frac{\hat{\beta}}{\beta} \times \frac{\hat{\omega}^{(i-1)}}{\alpha^{(i-1)}}$$

$$\beta = \hat{\beta}$$

$$\mathbf{q}^{(i)} = \mathbf{r}^{(i-1)} - \hat{\omega}^{(i)}(\mathbf{q}^{(i-1)} - \alpha^{(i-1)}\mathbf{v}^{(i-1)})$$

solve $\mathbf{M}\hat{\mathbf{q}} = \mathbf{q}^{(i)}$

$$\mathbf{v}^{(i)} = \mathbf{A}\hat{\mathbf{q}^{(i)}}$$

$$\hat{\omega}^{(i)} = \frac{\hat{\beta}}{(\mathbf{p}, \mathbf{v}^{(i)})}$$

$$\mathbf{s} = \mathbf{r}^{(i-1)} - \hat{\omega}^{(i)}\mathbf{v}^{(i)}$$

solve $\mathbf{M}\hat{\mathbf{s}} = \mathbf{s}$

$$\mathbf{t} = \mathbf{A}\hat{\mathbf{s}}$$

$$\alpha^{(i)} = \frac{(\mathbf{t}, \mathbf{s})}{(\mathbf{t}, \mathbf{t})}$$

$$\mathbf{x}^{(i)} = \mathbf{x}^{(i-1)} + \hat{\omega}^{(i)}\mathbf{q}^{(i)} + \alpha^{(i)}\mathbf{s}$$

$$\mathbf{r}^{(i)} = \mathbf{s} - \alpha^{(i)}\mathbf{t}$$

check convergence, continue if necessary

end
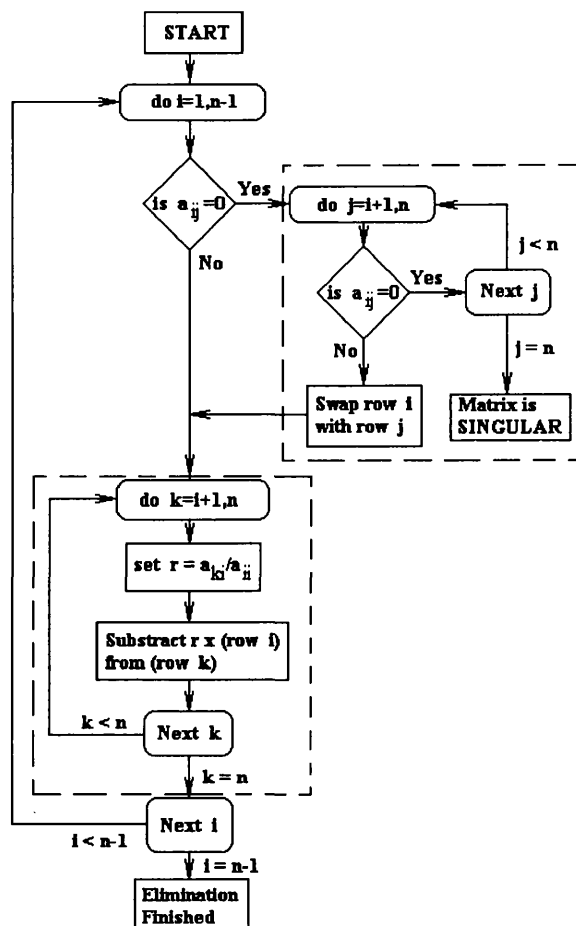
Figure B.1: Algorithm for Gaussian elimination
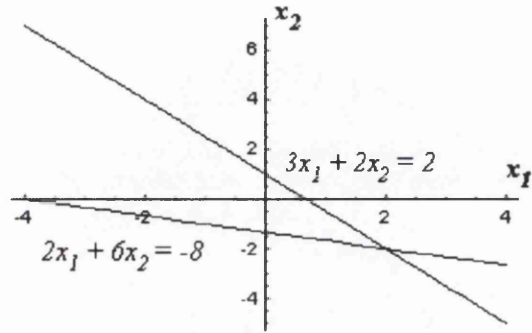
Figure B.2: Sample two-dimensional linear system
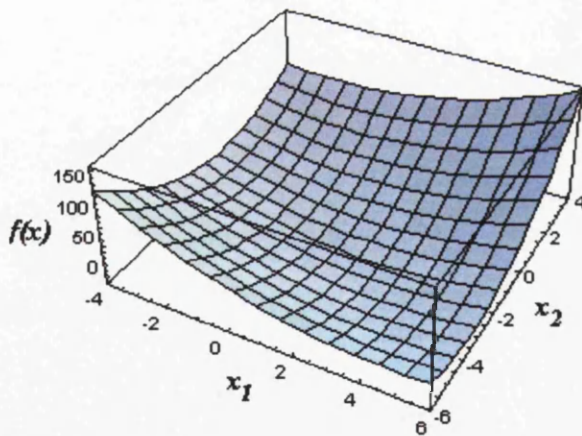
Figure B.3: Graph of quadratic form $f(x)$
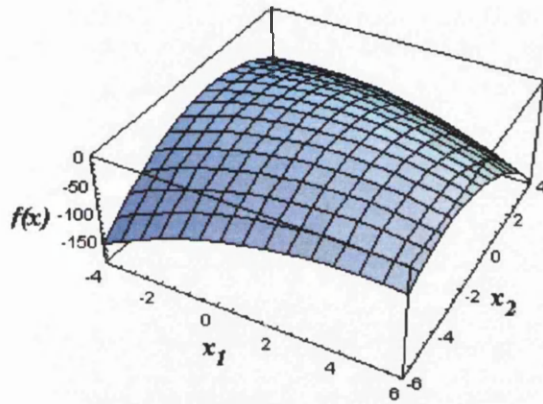
Figure B.4: A negative definite matrix
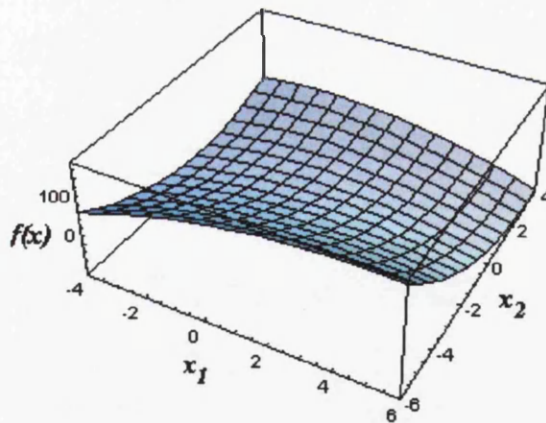
Figure B.5: An indefinite matrix
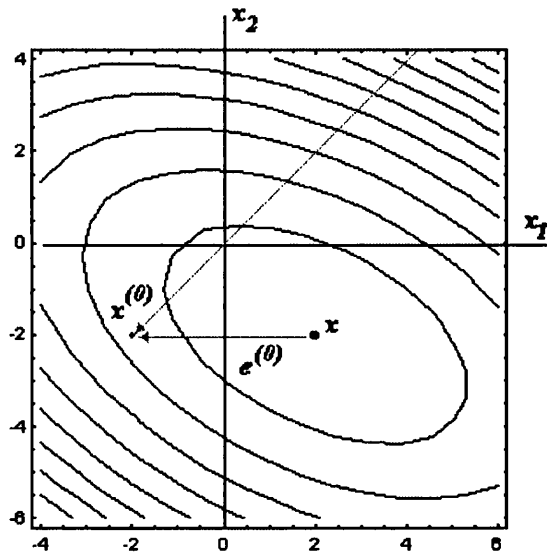
Figure B.6: Starting at $[-2, -2]^T$, take a step in the direction of steepest descent of f
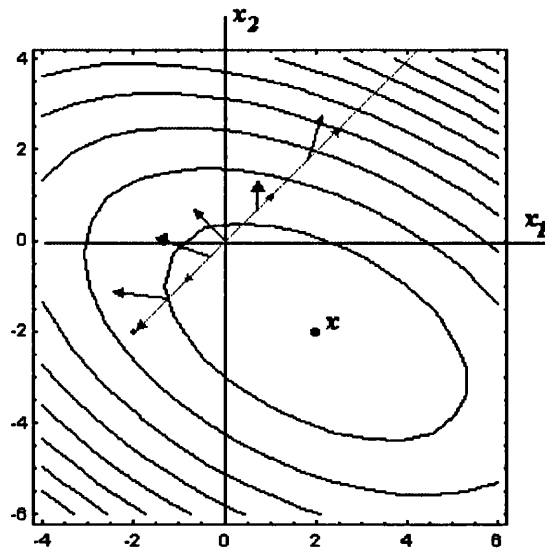
Figure B.7: Gradient f at several locations along the search line (blue arrow) and gradient's projection onto the line (grey arrow)
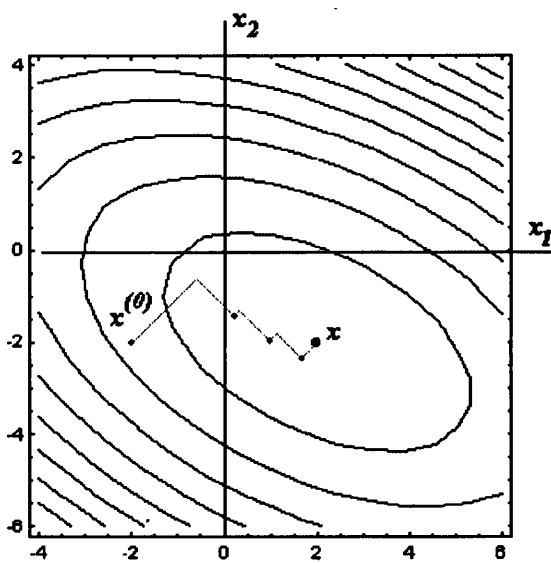
Figure B.8: Convergence of results from the starting point $[-2, 2]^T$ to the solution $[2, -2]^T$

Appendix C

PBiCG method

The Fortran 90 code to solve transient heat conduction using the Preconditioned Bi-conjugate Gradient method with an analysis of time being used during calculations is presented in the text that follows. The algorithm of this method is explained earlier in Appendix B. The diagonal preconditioner is used for preconditioning. Time discretization methods including θ method are presented in Chapter 5.

```fortran
                        program bcg1
!----------------------------------------------------------------

   ! transient conduction equation on rectangular area using 8 - node

   ! hexahedron elements : iterative PBCG method, implicit integration

                ! in time using 'theta' method
!----------------------------------------------------------------
              use library ! (subroutine library)
              use geometry ! (geometry library)
                  implicit none
integer :: nels, nxe, nze, neq, nn, nr, nip, nodof = 1, nod = 8, ndof, ndim = 3,
            i, j, k, l, iel, nstep, npri, iters, limit, m, n,
   real :: aa, bb, cc, permx, permy, permz, det, theta, dtim, val0, time, tol,
          alpha, beta, up, big, rho, time begin, time end, ro,
        tro, sigma, omega, bata, omegat, alpa, alpha1, alpha2
                logical :: converged
```

$character(len = 15) \; :: \; element =' hexahedron'$

$- - - - - - - - - - - -dynamic\ arrays - - - - - - - - - - - - - - -$

$real, allocatable \; :: \; loads(:), u(:), p(:), points(:,:),$

$kay(:,:), coord(:,:), fun(:), jac(:,:), der(:,:), v(:),$

$deriv(:,:), weights(:), d(:), ks(:,:), mm(:,:), funny(:,:),$

$g\ coord(:,:), ploads(:), qvo(:), pro(:), ka(:,:), kb(:,:),$

$x(:), xnew(:), g\ pmul(:,:), g\ utemp(:,:), diag\ precon(:), svo(:)$

$integer, allocatable \; :: \; nf(:,:), g(:), num(:), g\ num(:,:), g\ g(:,:)$

$!- - - - - - - - - -input\ and\ initialization -$

$open(10, file =' bcg1.dat', status = \; 'old', action =' read')$

$open(11, file =' bcg1.res', status =' replace', action =' write')$

$write(*,*)''$

$write(*,*)'TRANSIENT\ HEAT\ CONDUCTION'$

$write(*,*)'Preconditioned\ Bi - conjugate\ Gradient\ Method'$

$write(*,*)'Implicit\ Integration\ in\ Time'$

$write(*,*)'Using\ "Theta"\ Method'$

$write(*,*)''$

$read(10,*)nels, nxe, nze, nip, aa, bb, cc, permx,$

$permy, permz, dtim, nstep, theta, npri, tol, limit$

$ndof = nod * nodof$

$nn = (nxe + 1) * *2 * (nze + 1) \; !total\ number\ of\ nodes$

$$allocate(nf(nodof, nn), points(nip, ndim), weights(nip), kay(ndim, ndim),$$

$$coord(nod, ndim), fun(nod), jac(ndim, ndim),$$

$$g\ coord(ndim, nn), der(ndim, nod), deriv(ndim, nod),$$

$$mm(ndof, ndof), g\ num(nod, nels), ks(ndof, ndof), g(ndof),$$

$$funny(1, nod), num(nod), g_g(ndof, nels), ka(ndof, ndof),$$

$$kb(ndof, ndof), g\ utemp(ndof, nels), g\ pmul(ndof, nels))$$

$$kay = .0$$

$$kay(1, 1) = permx$$

$$kay(2, 2) = permy$$

$$kay(3, 3) = permz$$

$$call\ cpu\ time(time\ begin)\ ; call\ sample(element, points, weights)$$

$$nf = 1$$

$$call\ formnf(nf); q = maxval(nf)$$

$$!----loop\ the\ elements\ to\ set\ up\ global\ arrays--------------$$

$$loop\ 1 : do\ iel = 1, nels$$

$$call\ geometry\ 8bxz(iel, nxe, nze, aa, bb, cc, coord, num)$$

$$g\ num(:, iel) = num; g\ coord(:, num) = transpose(coord)$$

$$call\ num\ to\ g(num, nf, g); g\ g(:, iel) = g$$

$$end\ do\ loop\ 1$$

$$write(11,'(a)')"Global\ coordinates"$$

$$do\ k = 1, nn$$

$$write(11,'(a, i8, a, 3e12.4)')"Node", k, "", g\ coord(:, k)$$

$$end\ do$$

$$write(11,'(a)')"Global\ node\ numbers"$$

$$do\ k = 1, nels$$

$$write(11,'(a, i8, a, 8i8)')"Element", k, "", g\ num(:, k)$$

$$end\ do$$

$$allocate(loads(0:neq), diag\ precon(0:neq),$$

$$u(0:neq), d(0:neq), p(0:neq), x(0:neq), xnew(0:neq),$$

$$qvo(0:neq), v(0:neq), ploads(0:neq), pro(0:neq), svo(0:neq))$$

$$write(11,'(a, i8, a)')"There\ are\ ", neq, "equations\ to\ b\ solved"$$

$$p = .0; pro = .0; q = .0; qvo = .0; svo = .0; xnew = .0$$

$$diag\ precon = .0$$

$$!--element\ integration, storage\ and\ build\ preconditioner---------$$

$$loop\ 2: do\ iel = 1, nels$$

$$num = g\ num(:, iel)$$

$$coord = transpose(g\ coord(:, num))$$

$$g = g\ g(:, iel)$$

$$ks = .0; mm = .0$$

$$gauss\ pts: do\ i = 1, nip$$

$$call\ shape\ der(der, points, i)$$

$$call\ shape\ fun(fun, points, i)$$

$$funny(1,:) = fun(:)$$

$$jac = matmul(der, coord)$$

$$det = determinant(jac)$$

$$call\ invert(jac)$$

$$deriv = matmul(jac, der)$$

$$ks = ks + matmul(matmul(transpose(deriv), kay), deriv) * det * weights(i)$$

$$mm = mm + matmul(transpose(funny), funny) * det * weights(i)$$

$$end\ do\ gauss\ pts$$

$$ka = mm + ks * theta * dtim$$

$$kb = mm - ks * (1. - theta) * dtim$$

$$do\ k = 1, ndof$$

$$diag\ precon(g(k)) = diag\ precon(g(k)) + ka(k, k)$$

$$end\ do$$

$$end\ do\ loop\ 2$$

$$!------initial\ conditions-------------------------$$

$$read(10, *)val0; loads = val0; loads(0) = .0$$

$$!--------time\ stepping\ recursion-------------------$$

$$write(11,' (a, 7x, a, 7x, a, 2x, a)')"Time", "Temp.atnode", "node", "Iterations"$$

$$!--------now\ PBCG\ method---------------------------$$

$$timesteps\ pbcg : do\ j = 1, nstep$$

$$time = j * dtim$$

$$u = .0$$

$$loop\ 3 : do\ iel = 1, nels\ !\ rhs$$

$$g\ pmul(:, iel) = loads(g\ g(:, iel))$$

$$end\ do\ loop\ 3$$

$$g\ utemp = matmul(kb, g\ pmul)$$

$$loop\ 4 : do\ iel = 1, nels$$

$$u(g\ g(:, iel)) = u(g\ g(:, iel)) + g\ utemp(:, iel)$$

$$end\ do\ loop\ 4$$

! in slower version this matrix product was made in the following order

! loop 3a : do iel = 1, nels ! rhs

! g = g g(:, iel)

! ks = kb(:, :, iel)

! pmul = loads(g)

! utemp = matmul(ks, pmul)

! u(g) = u(g) + utemp

! end do loop 3a

$$u(0) = .0; loads = u; ploads = loads; ro = 1.; x = .0$$

$$iters = 0$$

$$iterations\ pbcg : do$$

$$iters = iters + 1$$

$$loop\ 5 : do\ iel = 1, nels$$

$$g = g\ g(:, iel)$$

$$qvo(g) = loads(g)/diag\ precon(g)$$

$$end\ do\ loop\ 5$$

$$qvo(0) = .0$$

$$loop\ 6 : do\ iel = 1, nels$$

$$g = g\ g(:, iel)$$

$$svo(g) = ploads(g)/diag\ precon(g)$$

$$end\ do\ loop\ 6$$

$$svo(0) = .0$$

$$tro = dot\ product(qvo, ploads)$$

$$beta = tro/ro$$

$$ro = tro$$

$$p = qvo + p * beta$$

$$pro = svo + pro * beta$$

$$u = 0.$$

$$loop\ 7 : do\ iel = 1, nels\ !\ again\ matrix\ product\ A * p$$

$$g\ pmul(:, iel) = p(g\ g(:, iel))$$

$$end\ do\ loop\ 7$$

$$g\ utemp = matmul(ka, g\ pmul)$$

$$loop\ 8 : do\ iel = 1, nels$$

$$u(g\ g(:, iel)) = u(g\ g(:, iel)) + g\ utemp(:, iel)$$

$$end\ do\ loop\ 8$$

$$u(0) = .0$$

$$sigma = dot\ product(pro, u)$$

$$alpha = tro/sigma$$

$$loads = loads - alpha * u$$

$$v = .0$$

$$loop\ 9 : do\ iel = 1, nels$$

$$g\ pmul(:, iel) = p(g\ g(:, iel))$$

$$end\ do\ loop\ 9$$

$$g\ utemp = matmul(transpose(ka), g\ pmul)$$

$$loop\ 10 : do\ iel = 1, nels\ !\ matrix\ product\ A^T * p$$

$$v(g\ g(:, iel)) = v(g\ g(:, iel)) + g\ utemp(:, iel)$$

$$end\ do\ loop\ 10$$

$$v(0) = .0$$

$$ploads = ploads - alpha * v$$

$$xnew = x + p * alpha$$

$$big = .0$$

$$converged = .true.$$

$$do\ i = 1, neq$$

$$if(abs(xnew(i)) > big)big = abs(xnew(i))$$

$$end\ do$$

$$do\ i = 1, neq$$

$$if(abs(xnew(i) - x(i))/big > tol)converged = .false.$$

$$end\ do$$

$$x = xnew$$

$$if(converged.or.iters == limit)exit$$

$$end\ do\ iterations\ pbcg$$

$$xnew(1211 : 1331) = 0.$$

$$loads = xnew$$

$$loop\ 11 : do\ l = 1, 1211, 121$$

$$if(j/npri * npri == j)then$$

$$write(11,'(2e12.4, 7x, i5, 4x, i5)')time, loads(nf(:, l)), l, iters$$

$$endif$$

$$end\ do\ loop\ 11$$

$$end\ do\ timesteps\ pbcg$$

$$call\ cpu\ time(time\ end)$$

$$write(11, *)'Time\ of\ calculation\ was', time\ end - time\ begin,' seconds'$$

$$write(11, *)'There\ are\ results\ of\ calculation\ by'$$

$$write(11, *)'PBCG\ method'$$

$$!----------------end\ of\ PBCG\ method------------------------$$

$$end\ program\ bcg1$$

The most time consuming operation in the program presented above is *MATMUL*. It has been noted that on vector computers it runs slower than the peak machine speed. Two different *MATMUL* operations are presented: matrix-vector and matrix-matrix. The difference between them is that matrix-matrix operation collects all the *pmul* vectors into a global matrix *g pmul*. As it was mentioned earlier using matrix-matrix operation about three times less time was needed for the same calculation.

Appendix D

Brass microstructure and roughness of samples

Brass microstructure

Figure D.1: Microstructure of brass specimen, magnification ×16

Figure D.2: Microstructure of brass specimen, magnification ×80
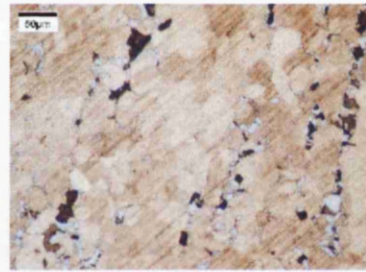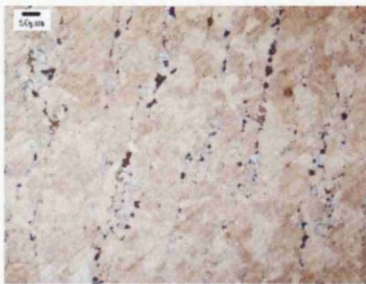

Figure D.3: Microstructure of brass specimen, magnification ×160
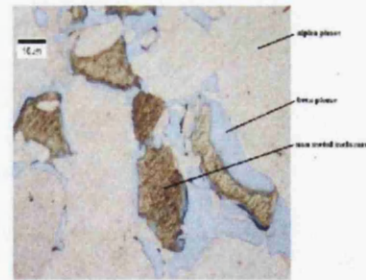
Figure D.4: Microstructure of brass specimen, magnification ×800
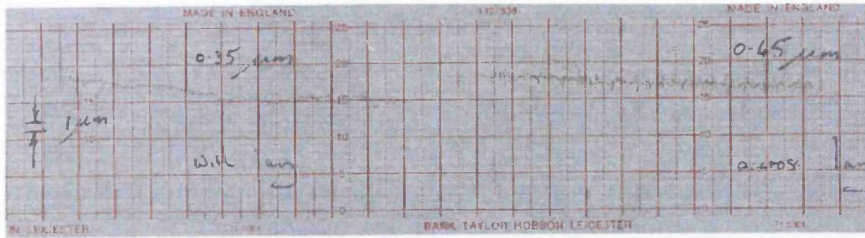
Roughness

Figure D.5: Surface roughness of the sample composed of brass
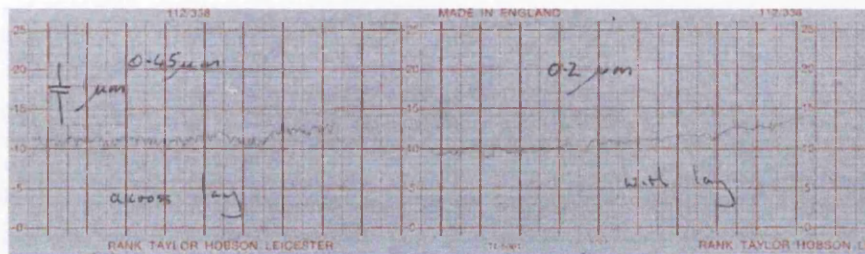
Figure D.6: Surface roughness of the sample composed of aluminium

Figure D.7: Surface roughness of the sample composed of black painted steel

References

ALFANO, G., SARN A. 1975. Normal and Hemispherical Thermal Emittances of Cylindrical Cavities. *Journal of Heat Transfer*, **96**(August), 387–390.

AMERI, A., FELSKE J.D. 1982. Radiation Configuration Factors for Obliquely Oriented Finite Length Circular Cylinders. *International Journal of Heat and Mass Transfer*, **33**, 728–736.

AMRIT, A., VENKATESHAN S.P. 1993. Accurate Determination of Diffuse View Factors Between Planar Surfaces. *International Journal of Heat and Mass Transfer*, **36**, 2203–2208.

ANDRE, S., DEGIOVANNI A. 1998. A New Way of Solving Transient Radiative-Conductive Heat Transfer Problems. *Journal of Heat Transfer*, **120**(November), 943–953.

ANTAL, G., SZIRMAY-KALOS L. CSONKA F. Hemicube Shooting for Non-Diffuse Global Illumination. *In: Spring Conference on Computer Graphics.*

BALLANCE, J.O., DONOVAN-J. 1973. Radiation Configuration Factors for Annular Rings and Hemispherical Sectors. *Journal of Heat Transfer*, **95**(May), 275–276.

BARANOSKI, G.V.G., ROKNE-J.G. GUANGWU X. 2001. Applying the Exponential Chebyshev Inequality to the Nondeterministic Computation of Form Factors. *Journal of Quantitative Stectroscopy and Radiative Transfer*, **69**, 447–467.

BARRETT, R., BERRY-M. CHAN T.F. DEMMEL J. DONATO J. DONGARRA J. EIJKHOUT V. POZO R. ROMINE C. VAN DER VOST H. 1994. *Templates for the Solution of Linear Systems: Building Blocks for Iterative Methods.*

BRANDENBURG, W. M. 1983. *The Reflectivity of Solids at Grazing Angles.* Tech. rept.

BYRD, L.W. 1993. View Factor Algebra for Two Arbitrary Sized Nonopposing Parallel Rectangles. *Journal of Heat Transfer*, **115**, 517–518.

CAREN, R.P. 1972. Radiation Energy Density and Radiation Heat Flux in Small Restangular Cavities. *Journal of Heat Transfer*, August, 289–294.

CARPENTER, J.R., BRIGGS-D.G. SERNAS V. 1976. Combined Radiation and Developing Laminar Free Convection Between Vertical Flat Plates With Asymmetric Heating. *Journal of Heat Transfer*, February, 95–100.

CHOI, A.S. 2002. Practical Applications of Form Factor Computation in Lighting Calculations. *Elseiver*, 117–125.

CHUNG, T.J., KIM-J.Y. 1982a. Radiation View Factors by Finite Elements. *Journal of Heat Transfer*, **104**(February), 792–795.

CHUNG, B.T.F., NARAGHI-M.H.N. 1982b. Radiation Configuration Between Disks and a Class of Axisymmetric Bodies. *Journal of Heat Transfer*, **104**(August), 426–431.

CHUNG, B.T.F., NARAGHI-M.H.N. 1982c. A Simpler Formulation for Radiative View Factors from Spheres to a Class of Axisymmetric Bodies. *Journal of Heat Transfer*, **104**(February), 201–204.

CHUNG, B.T. F., SUMITRA P. S. 1972. Radiation Shape Factors from Plane Point Sources. *Journal of Heat Transfer*, August, 328–330.

COHEN, M.F., GREENBERG D.P. 1985. The Hemicube: A Radiosity Solution for Complex Environment. *Computer Graphics(SIGGRAPH 85)*, 31–40.

CONCUS, P., GOLUB G. MEURANT G. 1989. Block Preconditioning for the Conjugate Gradient Method. *SIAM J. Sci. Stat. Comput.*, **6**(1), 220–252.

CROFT, D.R., LILLEY D.G. 1977. *Heat Transfer Calculation Using Finite Difference Equations*. Applied Science Publishers.

DAUN, K.J., HOLLANDS K.G.T. 2001. Infinitesimal-Area Radiative Analysis Using Parametric Surface Representation, Through NURBS. *Journal of Heat Transfer*, **123**(April), 249–256.

DUNKLE, R.V. 1963. Configuration Factors for Radiant Heat-transfer Calculations Involving People. *Journal of Heat Transfer*, February, 71–76.

EDDY, T.L. NIELSSON, G.E. 1988. Radiation Shape Factors for Channels with Varying Cross-section. *Journal of Heat Transfer*, **110**(February), 264–266.

EDSON, P., GENBERG V. 1997. *Use of Finite Element Models for Determining Radiation Geometric View Factors*. Tech. rept. Eastman Kodak Company.

EMERY, A.F., JOHANSSON O. LOBO M. ABROUS A. 1991. A Comparative Study of Methods for Computing the Diffuse Radiation View Factors for Complex Structures. *Journal of Heat Transfer*, **113**(May), 413–422.

FARRELL, A. 1976. Determination of Configuration Factors of Irregular Shape. *Journal of Heat Transfer*, May, 311–313.

FEINGOLD, A. 1978. A New Look at Radiation Configuration Factors Between Disks. *Journal of Heat Transfer*, **100**(November), 742–744.

FEINGOLD, A., GUPTA K.G. 1970. New Analytical Approach to the Evaluation of Configuration Factors in Radiation from Spheres and Infinitely Long Cylinders. *Journal of Heat Transfer*, **92**(February), 69–76.

FELSKE, A. 1978. Approximate Radiation Shape Factors Between Spheres. *Journal of Heat Transfer*, **100**(August), 547–548.

FERZIGER, J.H. 1998. *Numerical Methods for Engineering Application*. John Willey and Sons.

FLETCHER, R. 1976. Conjugate Gradient Methods for Indefinite Systems. *Springer*, 73–89.

GEBHART, B. 1961. Surface Temperature Calculations in Radiant Surroundings of Arbitrary Complexity - for Gray, Diffuse Radiation. *International Journal of Heat and Mass Transfer*, **3**, 341–346.

GIRAULT, V., RAVIART P.A. 1979. *Finite Element Approximation of the Navier-Stokes Equations*. Springer.

GOLUB, G., VAN LOAN C. 1996. *Matrix Computations*. John Hopkins University Press.

GOULD, D.C. 2000 (19-22 June). Radiation Heat Transfer Between Diffuse-Gray Surfaces Using Higher Order Finite Elements. *In: 34th AIAA Thermophysics Conference*.

GRAY, D.E. 1957. *American Institute of Physics Handbook.* McGraw-Hill.

GUELZIM, A., SOUIL J.M. VANTELON J.P. 1993. Suitable Configuration Factors for Radiation Calculation Concerning Tilted Flames. *Journal of Heat Transfer,* 115(May), 489–492.

GUTKNECHT, M.H. 1993. Variants of BI-CGSTAB for Matrices with Complex Spectrum. *SIAM J. Sci. Stat. Comput.,* 14, 1020–1033.

HAGEMAN, L.H., YOUNG D.M. 1981. *Applied Iterative Methods.* Academic Press.

HAHN, G.J., SHAPIRO S.S. 1967. *Statistical models in engineering.* John Willey and Sons.

HALLER, H.C., STOCKMAN N.O. 1963. A Note on Fin-tube View Factors. *Journal of Heat Transfer,* November, 380–381.

HENWOOD, D., BONET J. 1996. *Finite Elements-A Gentle Introduction.* Macmillan Press.

HESTENES, M., STIEFFEL E. 1952. Methods of Conjugate Gradients for Solving Linear Systems. *J. Res. Nat. Bur. Stan.,* 49, 409–435.

HIRSCH, C. 1997. *Numerical Computation of Internal and External Flow.* Vol. 1. John Willey and Sons.

HOLCHENDLER, J., LAVERTY W.F. 1974. Configuration Factors for Radiant Heat Exchange in Cavities Bounded at the Ends by Parallel Disks and Having Conical Centerbodies. *Journal of Heat Transfer,* 96(May), 254–257.

HOLLANDS, K.G.T. 1995. On the Superposition Rule for Configuration Factors. *Journal of Heat Transfer,* 117(February), 241–245.

JONES, L.R. 1965. Diffuse Radiation View Factors Between two Spheres. *Journal of Heat Transfer,* 87(August), 421–422.

JUUL, N.H. 1979. Diffuse Radiation View Factors from Differential Plane Sources to Spheres. *Journal of Heat Transfer,* 101(August), 558–560.

JUUL, N.H. 1982. View Factors in Radiation Between Two Parallel Oriented Cylinders of Finite Length. *Journal of Heat Transfer,* 104(May), 384–388.

KANGRO, H. 1976. *Early History of Plank's RadiationLaw.* Taylor and Francis Ltd.

KERMANI, M.M., CHUNG B.T.F. 1989. Radiation View Factors from a Finite Rectangular Plate. *Journal of Heat Transfer*, **111**(November), 1115–1117.

LARSEN, M.E., HOWELL J.R. 1986. Least-squares Smoothing of Direct Exchange Factors in Zonal Analysis. *Journal of Heat Transfer*, **108**, 239–242.

LAVERY, N.P. 1996. *Iterative Methods for the Finite Element Solution of Turbulent and Incompressible Flow*. PhD Thesis.

LAVERY, N.P., VUJIČIĆ M.R. BROWN S.G.R. 2005. Thermal Benchmark Experimental Investigation of Radiative Heat Transfer. *Pages 251–261 of: 12th International Conference on Computational Methods and Experimental Measurements*, vol. 41. Wessex Institute of Technology, Malta.

LEWIS, R.W., MORGAN K. 1985. *Numerical Methods in Heat Transfer*. Vol. III. John Willey and Sons.

LEWIS, R.W., MORGAN K. SCHREFLER B.A. 1983. *Numerical Methods in Heat Transfer*. Vol. II. John Willey and Sons.

LEWIS, R.W., MORGAN K. THOMAS H.R. SEETHARAMU K.N. 1996. *The Finite Element Method in Heat Transfer Analysis*. John Willey and Sons.

LIN, S., LEE P.M. WANG J.C.Y. DAI Y.L. LOU Y.S. 1986. Radiant-interchange Configuration Factors Between Disk and Segment of Parallel Concentric Disk. *Journal of Heat Transfer*, **29**, 501–503.

LOEHRKE, R.I., DOLAGHAN J.S. BURNS P.J. 1995. Smoothing Monte Carlo Exchange Factors. *Journal of Heat Transfer*, **117**, 524–526.

LOPES, R., MOURA L. BAILLIS D. SACADURA J.F. 2001. Directional Spectral Emittance of a Packed Bed: Correlation Between Theoretical Prediction and Experimental Data. *Journal of Heat Transfer*, **123**(April), 240–248.

MAHAN, J.R. 2002. *Radiation Heat Transfer: A Statistical Approach*. John Wiley & Sons. Inc.

MAHBOD, B., ADAMS R.L. 1984. Radiation View Factors Between Axisymmetric Subsurfaces Within a Cylinder with Spherical Centerbody. *Journal of Heat Transfer*, **106**(February), 244–248.

MAVROULAKIS, A., TROMBE A. 1998. A New Semianalytical Algorithm for Calculating Diffuse Plane View Factors. *Journal of Heat Transfer*, **120**(February), 279–282.

MINNING, C.P. 1977. Calculation of Shape Factors Between Rings and Inverted Cones Sharing a Common Axis. *Journal of Heat Transfer*, **99**(August), 492–494.

MITALAS, G.P., STEPHENSON D.G. 1966. *FORTRAN IV Programs to Calculate Radiant Interchange Factors*. Tech. rept.

M.O. DEVILLE, T.H. LE, & MORCHOISNE, Y. 1992. The Challenges of the Numerical Integration of the Transient Three-Dimensional Navier-Stokes Equations. *VIEWEG*, **36**, 7–13.

MODEST, M.F. 2003. Backward Monte Carlo Simulations in Radiative Heat Transfer. *Journal of Heat Transfer*, **125**(February), 57–62.

MORGAN, K., TAYLOR C. BREBBIA C.A. 1980. *Computer Methods in Fluids*. Pentech Press.

NARAGHI, M.H.N. WARNA, J.P. 1988. Radiation Configuration Factors from Axisymmetric Bodies to Plane Surfaces. *International Journal of Heat and Mass Transfer*, **31**, 1537– 1539.

NARAGHI, M.H.N., SALTIEL C. 1990. Radiative Configuration Factors from Cylinders to Coaxial Axisymmetric Bodies. *International Journal of Heat and Mass Transfer*, **33**, 215–218.

NEUMANN, L., NEUMANN A. 1995. Radiosity and Hybrid Methods. *ACM Transaction on Graphics*, **14**(3), 233–265.

NISHITA, T., NAKAMAE E. 1985. Continuous Tone Representation of Three-Dimensional Objects Account of Shadows and Interreflection. *Computer Graphics(SIGGRAPH 85)*, 23–27.

PAINTER, J.F. 1994. *Finite element radiation transport in one dimension (U)*. Tech. rept. Lawrence Livermore National Laboratory.

PARTHASARATHY, G., LEE H.S. CHAI J.C. PATANKAR S.V. 1995. Monte Carlo Solutions for Radiative Heat Transfer in Irregular Two-Dimensional Geometries. *Journal of Heat Transfer*, **117**, 792–794.

PATCZAK, T. 1997. *The Finite Element Method and Thermal Desktop*. Tech. rept. Cullimore and Ring Technologies.

PATTANAIK, S.N., MUDUR S.P. 1993. Computation of Global Illumination in a Participating Meadium by Monte Carlo Simulation. *Journal of Visualization and Computer Animation*, 4(3), 133–152.

PERIĆ, M., FERZIGER J.H. 2002. *Computational Methods for Fluid Dynamics.* Springer.

RUAN, L.M., TAN H.P. 2002. Solutions of Radiative Heat Transfer in Three-Dimensional Inhomogeneous, Scattering Media. *Journal of Heat Transfer*, **124**, 985–988.

RUSHMEIER, H.E., BAUM D.R. HALL D.E. 1991. Accelerating the Hemicube Algotithm for Calculating Radiation Form Factors. *Journal of Heat Transfer*, **113**(November), 1044–1047.

SAAD, Y. 2000. *Iterative Methods for Spars Linear Systems.* SIAM 2003 (PWS 1996).

SCHAFER, S. 2000. *Efficient Object-Based Hierarchical Radiosity Methods.* EngD Thesis.

SHAPIRO, A.B. 1983. *FACET-A radiation view factor computer code for axisymmetric, 2D planar, and 3D geometries with shadowing.* Tech. rept.

SHAPIRO, A.B. 1985. Computer Implementation, Accuracy, and Timing of Radiation View Factor Algorithms. *Journal of Heat Transfer*, **107**(August), 730–732.

SIEGEL, R., HOWELL J. 2002. *Thermal Radiation Heat Transfer.* Taylor and Francis .

SIKA, J. 1991. Evaluation of Direct-Exchange Areas for a Cylindrical Enclosure. *Journal of Heat Transfer*, **113**(November), 1040–1044.

SLEIJPEN, G.L.G., FOKKEMA D.R. 1993. BI-CGSTAB(I) for Linear Equations Involving Unsymmetric Matrices with Complex Spectrum. *Elec. Trans. Numer. Anal.*, **1**, 11–32.

SMETANA, W., REICHER R. 1998. A New Measuring Method to Determine Material Spectral Emissivity. *Measuring Science Technology*, **9**, 797–802.

SMITH, I.M., GRIFFITHS D.V. 1998. *Programming-The Finite Element Method.* John Willey and Sons.

SMITH, I.M. 1993. BI-CGSTAB(I) for Linear Equations Involving Unsymmetric Matrices with Complex Spectrum. *Elec. Trans. Numer. Anal.*, **1**, 11–32.

SOMMERS, R.D., GRIER N.T. 1969. Radiation View Factors for a Toroid: Comparison of Eckert's Technique and Direct Computation. *Journal of Heat Transfer*, **91**(August), 459–461.

SONNEVELD, P. 1989. CGS:A Fast Lanczos-Type Solver for Nonsymmetric Linear Systems. *SIAM J. Sci. Stat. Comput.*, **10**, 36–52.

SOWELL, E.F., O'BRIEN P.F. 1972. Efficient Computation of Radiant-Interchange Factors Within an Enclosure. *Journal of Heat Transfer*, **49**(November), 326–328.

SPARROW, E.M., ALBERS L.U. ECKERT E.R.G. 1962. Thermal Radiation Characteristics of Cylindrical Heat Transfer. *Journal of Heat Transfer*, 73–81.

SPARROW, E.M. 1963. A New and Simpler Formulation for Radiative Angle Factors. *Journal of Heat Transfer*, May, 81–87.

THOMASSET, F. 1981. *Implementation of Finite Element Methods for Navier-Stokes Equations.* Springer.

TOOR, J.S., VISKANTA R. 1972. Experiment and Analysis of Directional Effects on Radiant Heat Transfer. *Journal of Heat Transfer*, November, 459–465.

TSENG, J.W.C., STRIEDER W. 1990. View Factors from Wall to Random Dispersed Solid Bed Transport. *Journal of Heat Transfer*, **112**, 816–819.

VAN DER VORST, H.A. 1992. BI-CGSTAB: A Fast and Smoothly Converging Variant of BI-CG for the Solution of Non-Symmetric Linear Systems. *SIAM J. Sci. Stat. Comput*, **13**, 631–644.

VAN DER VORST, H.A., SONNEVELD P. 1990. *CGSTAB, a more smoothly converging variant of CGS.* Technical Report 90-50. Delft University of Technology.

VUJIČIĆ, M.R., LAVERY N.P. BROWN S.G.R. 2003. Thermal Benchmark Experimentation Data for Numerical Simulation of Radiative Heat Transfer. *In: 8th UK Heat Transfer Conference.* University of Oxford, Oxford.

VUJIČIĆ, M.R., LAVERY N.P. BROWN S.G.R. 2005a. Benchmark Experimental Data for Radiative Heat Transfer Prediction. *Pages 932–935 of: 3rd MIT Conference on Computational Fluid and Solid Mechanics.* Massachusetts Institute of Technology, Cambridge.

VUJIČIĆ, M.R., LAVERY N.P. BROWN S.G.R. 2005b. View Factor Calculation Using Monte Carlo Method and Experimental Validation in Radiative Heat Transfer. *In: 9th National UK Heat Transfer Conference.* UMIST, Manchester.

VUJIČIĆ, M.R., LAVERY N.P. BROWN S.G.R. 2005c. View Factor Calculation Using the Monte Carlo Method and Numerical Sensitivity. *Communications in Numerical Methods in Engineering,* accepted.

WAKAO, N., KATO K. FURUYA N. 1969. View Factor Between Two Hemispheres in Contact and Radiation Heat Transfer Coefficient in Packed Beds. *International Journal of Heat and Mass Transfer,* **12,** 118–120.

WANG, Y., BAYAZITOGLU Y. 2002. Wavelets and the Discrete Ordinate Method for Radiative Heat Transfer in a Two-Dimensional Restangular Enclosure With a Nongray Medium. *Journal of Heat Transfer,* **124**(October), 971–974.

WESSELING, P. 1992. *An introduction to multigrid method.* John Willey and Sons.

WIEBELT, J.A., RUO S.Y. 1963. Radiant-interchange Configuration Factors for Finite Right Circular Cylinder to Rectangular Plane. *International Journal of Heat and Mass Transfer,* **6,** 143–146.

YAJIMA, D., OHNISHI A. NAGASAKA Y. 2003. Simultaneous Measurement Method of Normal Spectral Emissivity and Optical Constant at High Temperatures. *In: 15th Symposium on Thermophysical Properties.*

ZENG, M., TAO W.Q. 2000. A Comparison Study of the Convergence Characteristics and Robustness for Four Variations of SIMPLE. *Engineering Computations,* **20,** 320–340.